

UNIVERSIDADE DE LISBOA
FACULDADE DE CIÊNCIAS
DEPARTAMENTO DE FÍSICA



Multi Singlet Scalar Dark Matter Extensions of the Standard Model

Tomás Carrilho Escarameia Trindade Henriques

Mestrado em Física e Astrofísica

Dissertação orientada por:
Dr. Rui Alberto Serra Ribeiro dos Santos

Agradecimentos Acknowledgments

Em primeiro lugar, gostaria de agradecer ao meu orientador, professor Dr. Rui Santos, por me ter ensinado (e continuar a ensinar) muitos dos conceitos presentes nesta dissertação. Agradeço também pelo tempo que disponibiliza para ajudar, e para discutir Física, a qualquer hora do dia. Aproveito para agradecer também aos meus colegas do seu grupo de trabalho, formalmente conhecidos por “Físicos que Gostam de Matéria Escura” (FiGoMatEs), pelo ambiente saudável e propenso a discussões interessantes. Um agradecimento especial à minha colega Maria Gonçalves, pela sua colaboração e amizade.

Agradeço aos meus professores da Faculdade de Ciências da Universidade de Lisboa, tanto da Licenciatura em Física como do Mestrado em Física e Astrofísica, por terem sido fundamentais na minha formação, nomeadamente o professor Dr. Luís Bento.

Agradeço aos meus pais, Sofia e Miguel, e aos meus segundos pais, Eunice e Diogo, por sempre me terem apoiado, cada um à sua maneira. Um agradecimento especial à minha mãe Sofia, que mais acompanhou o meu dia-a-dia, e que tantas vezes me ajudou para maximizar o meu tempo de trabalho. Quero também agradecer ao meu avô José, a quem dedico esta dissertação, pela grande pessoa que é.

Por fim, não só agradeço aos meus amigos, mas sobretudo à minha querida namorada Filipa, que me acompanha sempre nos bons e maus momentos, e de quem eu gosto muito.

Nota: Parte do trabalho desenvolvido nesta dissertação deu origem a um artigo científico [1].

Resumo Extended Abstract

O Modelo Standard (SM) da física de partículas é uma teoria quântica de campo, matematicamente consistente e renormalizável, que descreve todas as interações não-gravitacionais (i.e., as interações eletromagnética, fraca e forte) com enorme sucesso (Capítulo 2). No entanto, mesmo quando combinado com a teoria da Relatividade Geral (que descreve a gravitação), não consegue explicar todos os fenómenos físicos que observamos. Um possível exemplo, entre vários outros (Secção 3.1), é o mistério da natureza da matéria escura (DM), uma forma não-bariónica de matéria que apesar de invisível, constitui cerca de 26% da matéria-energia total (o que corresponde a 84% da matéria total) do Universo observável. A vasta gama de evidências experimentais para a existência de matéria escura (e.g., desde curvas de rotação de galáxias “espirais” a medições da radiação cósmica de fundo em micro-ondas (CMB)), provêm exclusivamente dos efeitos gravitacionais produzidos pela mesma (Secção 3.1.1). Estas evidências experimentais de natureza gravítica fornecem informação acerca das propriedades da matéria escura, como o facto de interagir de forma fraca, e ser “fria”, eletricamente neutra e estável (Secção 3.2). Mas para percebermos o que é matéria escura, precisamos de a observar a interagir não-gravitacionalmente com matéria visível (i.e., bariónica). Apesar de um grande esforço internacional por via de inúmeras experiências de deteção direta, deteção indireta e buscas em aceleradores (Secção 3.2.2), esta ainda não foi detetada.

Neste trabalho assumimos que matéria escura corresponde a uma ou mais partículas elementares que ainda não foram descobertas, o que necessariamente exige a extensão do Modelo Standard, que (por si só) não contém nenhuma partícula candidata a matéria escura. Em particular, apenas vamos considerar a classe de candidatos “weakly interactive massive particle” (WIMP), que são termicamente produzidas de acordo com o mecanismo “freeze-out” (Secção 3.2.1). Existem muitas extensões do Modelo Standard que fornecem um candidato viável a matéria escura, que além de satisfazer as propriedades acima referidas, terá que reproduzir a densidade de relíquia observada de $\Omega_{\text{DM}}^{\text{obs}} h^2 = 0.120 \pm 0.001$, e não ser excluída pelas experiências de deteção. Uma das formas mais simples de estender o Modelo Standard com uma partícula candidata a matéria escura, sem quebrar a simetria de gauge $\text{SU}(3)_c \times \text{SU}(2)_L \times \text{U}(1)_Y$ ou a renormalizabilidade da teoria, consiste em introduzir um campo singlete de $\text{SU}(3)_c \times \text{SU}(2)_L \times \text{U}(1)_Y$ escalar real $S(x) \sim (\mathbf{1}, \mathbf{1}, 0)$ e uma simetria discreta $\mathcal{Z}_2 : S(x) \rightarrow -S(x)$, $\text{SM} \rightarrow +\text{SM}$ não-quebrada (ou exata) que garante a estabilidade (i.e., impede o decaimento) da nova partícula S (Secção 3.3). No entanto, como verificámos após aplicarmos os mais recentes constrangimentos experimentais ao espaço de parâmetros livres (Secção 3.3.1), este modelo está excluído para massas de matéria escura inferiores a 3535 GeV (não considerando o cenário ressonante $m_S \approx m_h/2$). Assim, é impossível testar esta extensão do SM singlete-escalar-real (SM+RSS) através de buscas no Large Hadron Collider (LHC), que opera a uma energia do centro-de-massa de $\sqrt{s} = 13.6$ TeV (Run 3), e nunca ultrapassará um valor máximo de $\sqrt{s} = 14$ TeV (HL-LHC). Esta é a principal motivação por detrás da subsequente investigação.

Este trabalho dedica-se ao estudo de extensões do SM $n = 2, 3$ multi-singlete-escalar-real (SM+ n RSS) com simetrias discretas $\times_{r=1}^n \mathcal{Z}_2^{(r)} \equiv \mathcal{Z}_2^{(1)} \times \dots \times \mathcal{Z}_2^{(n)}$ não-quebradas (Capítulos 4 e 5). Debaixo deste produto direto de grupos discretos de simetria, os campos transformam-se tal que $S_r(x) \xrightarrow{\mathcal{Z}_2^{(r)}} -S_r(x)$,

$S_{r'}(x) \xrightarrow{\mathcal{Z}_2^{(r)}} +S_{r'}(x)$, $\text{SM} \xrightarrow{\mathcal{Z}_2^{(r)}} +\text{SM} (r, r' = 1, \dots, n \wedge r' \neq r)$. Ao permanecerem não-quebradas, as simetrias dão origem a $n = 2, 3$ partículas estáveis S_r candidatas a matéria escura e zero extra partículas tipo-Higgs (não há mistura de sabores nos termos de massa escalares). As partículas de matéria escura acoplam ao bóson de Higgs através dos termos de portal $\mathcal{L}_{\text{portal}(r)} = -\kappa_{Hr}/2S_r^2\Phi^\dagger\Phi$ (que ligam os setores “escuros” ao setor do SM), mas também entre si através dos termos de interação $\mathcal{L}_{\text{int}(r,r')} = -\lambda_{rr'}/4S_r^2S_{r'}^2$ (que ligam os setores “escuros” entre si).

Começamos por estudar o caso $n = 2$, i.e., a extensão dois-singlete-escalar-real com uma simetria discreta $\mathcal{Z}_2^{(1)} \times \mathcal{Z}_2^{(2)}$ não-quebrada (Capítulo 4). Antes de aplicar constrangimentos no espaço de parâmetros livres, determinamos expressões analíticas para as secções eficazes relevantes para a detecção direta e densidade de relíquia (Secção 4.2), sendo estas, respetivamente, a secção eficaz spin-independente (SI) $\sigma^{\text{SI}}(S_r N \rightarrow S_r N)$, $N = p, n$ de dispersão elástica de uma partícula de matéria escura num nucleão (Secção 4.2.1), e as secções eficazes $\sigma(S_r S_r \rightarrow X \bar{X})$, $X = \text{SM}, S_{r' \neq r}$ de processos de aniquilação de matéria escura (Secção 4.2.2). De seguida, impusemos analiticamente (Secção 4.3) os constrangimentos teóricos e experimentais que qualquer extensão do Modelo Standard é obrigada a satisfazer (i.e., não-específicos de matéria escura), nomeadamente: condições para o potencial escalar ser limitado por baixo, condições de unitariedade perturbativa (dois teóricos), limite superior para o “branching ratio” (BR) do decaimento do bóson de Higgs para produtos invisíveis e medições de precisão de observáveis eletrofracos (dois experimentais). Obtidas as condições analíticas, ficámos prontos para impor os constrangimentos provenientes de experiências de matéria escura através de uma análise numérica.

Como os constrangimentos experimentais da densidade de relíquia observada e da detecção direta, combinados, conseguem dar conta (sem as restantes experiências) de todo o espaço de parâmetros livres que é excluído na extensão singlete-escalar-real; fizemos o scan do espaço de parâmetros da extensão dois-singlete-escalar-real, (novamente) com o código `micrOMEGAS 6.0`, para estes dois constrangimentos experimentais específicos de matéria escura (Secção 4.4). Tomando S_1 (S_2) como a WIMP mais leve (pesada) – sem perda de generalidade, devido à simetria $S_1 \leftrightarrow S_2$ do modelo – encontramos três regiões não-excluídas (ou permitidas) principais: 1) o caso $m_{S_1} \sim m_{S_2} > 1 \text{ TeV}$, onde ambas as partículas DM são pesadas; 2) o caso $m_h/2 < m_{S_1} < 1 \text{ TeV} < m_{S_2}$, onde uma das partículas DM é mais leve (do que 1 TeV) e a outra é pesada; 3) o caso de ressonância $m_h/2 \approx m_{S_1} < m_{S_2}$. Destas regiões permitidas, o caso $m_h/2 < m_{S_1} < 1 \text{ TeV} < m_{S_2}$ é o único que não estava já (analogamente) presente na extensão ($n = 1$) singlete-escalar-real. Além disso, ao fornecer uma partícula DM mais leve que pode ser alvo de buscas no LHC, esta região permitida tornou-se o nosso foco de interesse. A nossa subsequente análise numérica (Secção 4.4.1) mostra que, neste caso não-excluído, a partícula DM mais pesada S_2 é responsável por (quase) toda a densidade de relíquia observada, e consequentemente, a sua massa m_{S_2} e coeficiente de portal κ_{H2} estão (juntamente) altamente constrangidos (limitados por baixo e por cima) devido à “tensão” entre sobre-densidade de relíquia e exclusão por detecção direta associada a S_2 , esta última sendo determinada pela secção eficaz SI em $\sigma^{\text{SI}}(S_2 N \rightarrow S_2 N) \times \Omega_{S_2}/\Omega_{\text{DM}} \approx \sigma^{\text{SI}}(S_2 N \rightarrow S_2 N)$. Em contraste, a partícula DM mais leve S_1 faz uma contribuição virtual de $\Omega_{S_1} h^2 \sim 10^{-7}$ para a densidade de relíquia total de matéria escura, de forma a que m_{S_1} e κ_{H1} apenas estão constrangidos (limitados por baixo e por cima, e por baixo, respetivamente) devido à exclusão por detecção direta associada a S_1 , que é agora determinada pela fração de abundância em $\sigma^{\text{SI}}(S_1 N \rightarrow S_1 N) \times \Omega_{S_1}/\Omega_{\text{DM}}$. Também se concluiu que o coeficiente “inter-escuro” λ_{12} que regula a aniquilação (dominante) $S_2 S_2 \rightarrow S_1 S_1$ não influencia a densidade de relíquia total de forma tão significativa quanto m_{S_2} e κ_{H2} , não sendo por isso constrangida pela mesma. Mas como afeta a fração de abundância $\Omega_{S_1}/\Omega_{\text{DM}}$, é limitado por cima devido à exclusão por detecção direta associada a S_1 .

No entanto, esta região permitida do caso uma-leve-uma-pesada $m_{S_1} < m_{S_2}$ está quase excluída pelos novos resultados LUX-ZEPLIN (LZ) de 2024. Estes constrangimentos recentes não estão (ainda) incorporados no código micrOMEGAs 6.0, pelo que tivemos que fazer a correspondente exclusão por detecção direta (Secção 4.4.2) à parte da análise numérica anterior. Os valores $\sigma^{\text{SI}}(S_r N \rightarrow S_r N) \times \Omega_{S_r}/\Omega_{\text{DM}}$ ($r = 1, 2$) previstos pelo modelo, para os pontos permitidos (de espaço de parâmetros) do caso $m_{S_1} < m_{S_2}$, excedem o limite superior estabelecido pela experiência LZ 2024 para a secção eficaz SI da dispersão elástica WIMP-núcleo, com parte destas previsões contidas na banda de incerteza experimental para ambas as partículas DM.

Isto levou-nos a estudar a extensão $n = 3$, i.e., a três-singlete-escalar-real com uma simetria discreta $\mathcal{Z}_2^{(1)} \times \mathcal{Z}_2^{(2)} \times \mathcal{Z}_2^{(3)}$ não-quebrada (Capítulo 5). Por via de uma análise numérica semelhante (mas com scans locais, em regiões alvo do espaço de parâmetros), identificámos duas regiões permitidas de interesse: 1) o caso duas-leves-uma-pesada $m_{S_3} < m_{S_1} < 1 \text{ TeV} < m_{S_2}$, onde S_3 assume o papel de uma partícula DM leve adicional; 2) o caso uma-leve-duas-pesadas $m_{S_1} < 1 \text{ TeV} < m_{S_2} < m_{S_3}$, onde S_3 assume o papel de uma partícula DM pesada adicional (Secção 5.4). O primeiro destes casos é idêntico ao caso (uma-leve-uma-pesada) $m_{S_1} < m_{S_2}$ do modelo SM+2RSS, excepto pela (desnecessária) partícula DM leve extra. No entanto, o segundo caso tem a característica (até agora, única) de ter duas partículas DM pesadas que são simultaneamente responsáveis pela densidade de relíquia total, tal que $\sum_{r=1}^3 \Omega_{S_r} \approx \Omega_{S_2} + \Omega_{S_3}$, com $\Omega_{S_2} \sim \Omega_{S_3}$. Adicionalmente, a exclusão por detecção direta associada às partículas DM pesadas $S_{2,3}$ é agora também determinada pelas frações de abundância $\Omega_{S_{2,3}}/\Omega_{\text{DM}}$, e não apenas pelas secções eficazes SI. Assim, a “tensão” entre sobre-densidade de relíquia e exclusão por detecção direta associada às partículas DM pesadas $S_{2,3}$ é “aliviada”, enfraquecendo os (fortes) constrangimentos dos valores permitidos para as massas $m_{S_{2,3}}$ e coeficientes de portal $\kappa_{H2,3}$ das partículas DM pesadas. Consequentemente, esta região permitida do caso uma-leve-duas-pesadas $m_{S_1} < m_{S_2} < m_{S_3}$ contém pontos que prevêem valores $\sigma^{\text{SI}}(S_r N \rightarrow S_r N) \times \Omega_{S_r}/\Omega_{\text{DM}}$ que não estão acima do limite superior LZ 2024 para as três partículas DM $S_{r=1,2,3}$ (Secção 5.4.1).

Por fim, identificámos as experiências do LHC mais relevantes para determinar se os nossos pontos permitidos (pela densidade de relíquia e detecção direta) estavam experimentalmente excluídos por buscas em aceleradores (Secções 4.5 e 5.5). As buscas seleccionadas são as chamadas buscas jato, mono-Higgs e mono-Z, realizadas com o detetor ATLAS, que estabeleceram limites superiores “model-independent” para a secção eficaz visível dos processos de produção de matéria escura correspondentes. As nossas previsões para as secções eficazes visíveis estão pelo menos cerca de uma ordem de grandeza abaixo dos limites de exclusão destas três análises experimentais, em todos os pontos permitidos do espaço de parâmetros de ambos os modelos ($n = 2, 3$). No entanto, estão suficientemente próximas de serem excluídas pelas buscas jato e mono-Higgs, o que sugere que uma WIMP escalar poderá ser detetada durante o restante período de operação do LHC, especialmente na fase HL-LHC.

Palavras-chave: além do Modelo Standard, física Higgs, partícula matéria escura, WIMP escalar

Abstract

Despite extensive experimental evidence supporting the existence of dark matter (DM), its fundamental nature remains unknown. A common assumption is that DM consists of one or more undiscovered elementary particles. One of the simplest ways of extending the Standard Model (SM) of particle physics with a dark matter particle candidate, without breaking the $SU(3)_c \times SU(2)_L \times U(1)_Y$ gauge symmetry of the SM or spoiling renormalizability, is by adding a real scalar singlet (RSS) field and imposing an additional unbroken \mathbb{Z}_2 discrete symmetry that ensures the stability of the corresponding new spin 0 particle. However, this minimal Higgs-portal extension is highly constrained by the observed relic density and direct detection experiments. Being experimentally excluded for DM masses below 3535 GeV, this model cannot be probed through collider searches at the Large Hadron Collider (LHC). In this work, after re-constraining the real scalar singlet SM extension (SM+RSS) with the most recent experiments, we study multi-real-scalar-singlet SM extensions (SM+ n RSS) featuring $n = 2, 3$ real scalar $SU(3)_c \times SU(2)_L \times U(1)_Y$ singlets and unbroken $\times_{r=1}^n \mathbb{Z}_2^{(r)} \equiv \mathbb{Z}_2^{(1)} \times \dots \times \mathbb{Z}_2^{(n)}$ discrete symmetries. These models provide $n = 2, 3$ (respectively) stable scalar DM particle candidates that in addition to coupling to the Higgs boson, also couple to each other. In both ($n = 2$ and $n = 3$) cases, we obtain a lower non-excluded mass range for at least one of the DM candidates, well below 1 TeV. The corresponding allowed free parameter space regions are, however, close from being excluded by the most recent (2024) LUX-ZEPLIN results. Therefore, not only can these ($n = 2, 3$) multi-real-scalar-singlet SM extensions be probed in upcoming direct detection experiments, but also through collider searches targeted at the lighter DM particle candidates at the LHC or future colliders.

Keywords: beyond Standard Model, Higgs physics, particle dark matter, scalar WIMP

Contents

1	Introduction	1
2	The Standard Model of Particle Physics	3
2.1	Electroweak Interaction from $SU(2)_L \times U(1)_Y$ Gauge Symmetry	3
2.2	Spontaneous Symmetry Breaking and the Higgs Mechanism	7
2.2.1	The Vacuum and its Spontaneous Symmetry Breaking	7
2.2.2	Higgs Mass, Self-Interactions and Goldstone Bosons	9
2.2.3	Masses of the Electroweak Gauge Bosons and the Higgs Mechanism	10
2.2.4	Higgs Interactions with the Electroweak Gauge Bosons	11
2.3	The Yukawa Sector	12
2.3.1	Flavour Space Rotations: Weak and Mass Eigenstates	13
2.3.2	Lepton Masses and Mixing	14
2.3.3	Quark Masses, Mixing and the CKM Matrix	16
2.3.4	Yukawa Interactions	17
2.4	Strong Interaction from $SU(3)_c$ Gauge Symmetry	18
2.5	Lagrangian and Parameters of the Standard Model	19
3	Particle DM and the Real Scalar Singlet SM Extension	20
3.1	Problems with the Standard Model of Particle Physics	20
3.1.1	Experimental Evidence for Dark Matter	22
3.2	The Particle Physics Approach to Dark Matter	23
3.2.1	Relic Density of Dark Matter	24
3.2.2	Dark Matter (Particle) Detection	25
3.3	The SM+RSS DM Model with an Unbroken \mathcal{Z}_2 Symmetry	26
3.3.1	Parameter Space Scans and Numerical Analysis	29
4	The Two-Real-Scalar-Singlet SM Extension	31
4.1	The SM+2RSS DM Model with an Unbroken $\mathcal{Z}_2^{(1)} \times \mathcal{Z}_2^{(2)}$ Symmetry	31
4.2	Cross Sections for Direct Detection and Relic Density of DM	34
4.2.1	Spin-Independent Cross Section of DM-Nucleon Elastic Scattering	35
4.2.2	Cross Section of Dark Matter Annihilation Processes	40
4.3	Theoretical and Pre-Scan Experimental Constraints	44
4.4	Parameter Space Scans and Numerical Analysis	46
4.4.1	Analysis of the $(m_h/2 <) \mathbf{m}_{S_1} < \mathbf{m}_{S_2}$ Case	48
4.4.2	LZ 2024 Results and Future Prospects for Direct Detection	54
4.5	Searches for the Lighter DM Particle at the LHC	55

4.5.1	Jet Searches	60
4.5.2	Mono-Higgs Searches	62
4.5.3	Mono- Z Searches	63
5	The Three-Real-Scalar-Singlet SM Extension	66
5.1	The SM+3RSS DM Model with an Unbroken $\mathcal{Z}_2^{(1)} \times \mathcal{Z}_2^{(2)} \times \mathcal{Z}_2^{(3)}$ Symmetry	66
5.2	Cross Sections for Direct Detection and Relic Density of DM	70
5.3	Theoretical and Pre-Scan Experimental Constraints	70
5.4	Parameter Space Scans and Numerical Analysis	71
5.4.1	LZ 2024 Results and Future Prospects for Direct Detection	74
5.5	Searches for the Lighter DM Particle(s) at the LHC	77
6	Conclusions	79
	References	81
A	Principles in Field Theory	88
A.1	The Variational Principle of Least Action	88
A.2	The Gauge Symmetry Principle and Non-Abelian Gauge Theories	89
B	Scale Invariance Breaking and the Trace Anomaly in QCD	94
B.1	A Generalization of Noether's Theorem	94
B.2	Canonical EMT and the Belinfante Symmetrization Procedure	96
B.3	Dilatations and Scale Invariance in QCD	98
B.4	The Trace Anomaly of QCD	99
B.5	Nucleon Mass and the Heavy Quark Contribution	101
C	Explicit $\mathcal{Z}_2^{(1)} \times \mathcal{Z}_2^{(2)} \rightarrow \mathcal{Z}_2^{(1,2)}$ Symmetry Breaking in the Two-Real-Scalar-Singlet	102
C.1	The SM+2RSS DM Model with an Unbroken $\mathcal{Z}_2^{(1,2)}$ Symmetry	102
C.2	Parameter Space Scans and Numerical Analysis	104

List of Figures

3.1	Diagrammatic “make it, shake it, break it” illustration of dark matter particle detection, with arrows indicating the direction of the process and corresponding detection experiment.	25
3.2	Feynman rules for the interaction vertices involving the S dark matter particle candidate. The decays $S \rightarrow \text{SM SM}$ are forbidden by “dark parity” (or \mathcal{Z}_2 charge) conservation, as a consequence of the \mathcal{Z}_2 discrete symmetry.	28
3.3	Experimental constraints on the SM+RSS model (3.4), obtained by scanning the free parameter space with micrOMEGAs 6.0 for the freeze-out mechanism. The grey, purple, green and orange regions are respectively excluded by DM relic (over-)density, direct detection, indirect detection and $\text{BR}(h \rightarrow \text{inv})$; while the red region corresponds to the observed DM relic density.	29
4.1	Feynman rules for the interaction vertices involving the S_1 and S_2 dark matter particle candidates. The decays $S_{1,2} \rightarrow \text{SM SM}$ and $S_{1,2} \rightarrow S_{2,1} S_{2,1}$ are forbidden by “dark parity” (or $\mathcal{Z}_2^{(r)}$ charge, $r = 1, 2$) conservation, as a consequence of the $\mathcal{Z}_2^{(1)} \times \mathcal{Z}_2^{(2)}$ discrete symmetry.	35
4.2	Experimental constraints on the SM+2RSS model (4.4), obtained by scanning the free parameter space with micrOMEGAs 6.0 for the freeze-out mechanism. The left panel shows parameter space points that correspond to the observed DM relic density, and the right panel displays the points that are <i>also</i> not excluded by direct detection. Columns share the x -axis, and rows share the y -axis and the colour bar.	47
4.3	Experimental constraints on the SM+2RSS model (4.4), obtained by scanning the free parameter space with micrOMEGAs 6.0 for the freeze-out mechanism. The left panel shows parameter space points that correspond to the observed DM relic density, and the right panel displays the points that are <i>also</i> not excluded by direct detection. The y -axis and the colour bar are shared. The figure is similar to the first row of Figure 4.2, but here the colour bar displays the relic density of the DM particle S_1 .	48
4.4	Scanned free parameter space points that correspond to the observed DM relic density and are not excluded by direct detection, just like in the right panel of Figure 4.2 (except here all coupling constants are taken as positive). The $m_{S_1} < m_{S_2}$ case points are coloured, while the other allowed parameter space points are grey (each colour bar has its grey version “twin”). Columns share the x -axis.	49
4.5	Analysis of the $m_{S_1} < m_{S_2}$ case with all parameters but m_{S_1} (light DM mass) fixed. Each row shows one fixed parameter – between m_{S_2} , κ_{H1} , κ_{H2} and λ_{12} – taking five different fixed values. Only green points are not excluded by direct detection. Columns share the x -axis.	51

- 4.6 Analysis of the $m_{S_1} < m_{S_2}$ case with all parameters (but one) fixed. Each row scans one parameter – m_{S_1} , m_{S_2} , κ_{H1} , κ_{H2} and λ_{12} , in this order – with all the remaining parameters fixed. Only green points are not excluded by direct detection. 52
- 4.7 Spin-independent cross section of DM-nucleon elastic scattering $S_r N \rightarrow S_r N$ ($N = p, n$) multiplied by the corresponding fraction of DM relic density $\Omega_{S_r}/\Omega_{\text{DM}}$ ($r = 1, 2$), for both the lighter S_1 (left panel) and the heavier S_2 (right panel) DM particle candidates. The presented points correspond to the model's theoretical predictions for the $m_{S_1} < m_{S_2}$ case points, for both proton (p) and neutron (n) elastic scattering. The blue and green (solid) lines correspond to the LUX-ZEPLIN (LZ) experimental upper limits on the WIMP-nucleon elastic scattering spin-independent cross section from 2022 [2] and 2024 [3] results, respectively. The (shaded green) experimental uncertainty band from the LZ 2024 results is displayed. The legend is shared by both panels. 55
- 4.8 Feynman diagrams contributing to mono-jet production processes $pp \rightarrow S_1 S_1 j$ at tree-level, where $j = q, \bar{q}, b, \bar{b}, g$ are jets and $q = u, d, c, s$ are light quarks. The vertices for the ggh and $gggh$ effective couplings arise from top quark loops in gluon fusion processes (in the heavy top quark limit, $m_t^2 \gg s$). 56
- 4.9 Feynman diagrams contributing to the mono-Higgs production process $pp \rightarrow S_1 S_1 h$ at tree-level, where $q = u, d, c, s$ are light quarks. The third and last diagrams each represent two distinct contributions, due to the interchange of the external legs with coloured four-momenta $k_{3,4}^\mu$ and $k_{4,3}^\mu$. The vertex for the ggh effective coupling (arising from the top quark loop in gluon fusion) is explicitly shown in Figure 4.8. 57
- 4.10 Feynman diagrams contributing to the mono- Z production process $pp \rightarrow S_1 S_1 Z$ at tree-level, where $q = u, d, c, s$ are light quarks. 57
- 4.11 Cross section of jet production processes $pp \rightarrow S_1 S_1 + N j$ ($N = 1, 2, 3, 4$), where $j = q, \bar{q}, b, \bar{b}, g$ and $q = u, d, c, s$, at a center-of-mass energy of $\sqrt{s} = 13$ TeV. The presented points correspond to the model's theoretical predictions for the $m_{S_1} < m_{S_2}$ case points, and the red (solid) line is the ATLAS (2021) [4] model-independent experimental upper limit on the visible cross section (σ^{vis}) of $pp \rightarrow N j + \text{DM}$ ($N = 1, 2, 3, 4$) processes. Left panel: model predictions of the cross section for all $m_{S_1} < m_{S_2}$ case points without momentum cuts. Right panel: model predictions of the cross section for six benchmark $m_{S_1} < m_{S_2}$ case points with different missing transverse momentum (p_T^{miss}) cuts, along with the corresponding ATLAS upper limits. The legend is shared by both panels. 61
- 4.12 Cross section of mono-Higgs production processes $pp \rightarrow S_1 S_1 h$ at a center-of-mass energy of $\sqrt{s} = 13$ TeV. The presented points correspond to the model's theoretical predictions for the $m_{S_1} < m_{S_2}$ case points, and the red (solid) line is the ATLAS (2021) [5] model-independent experimental upper limit on $\sigma^{\text{vis}}/\text{BR}(h \rightarrow b\bar{b}) \equiv \sigma \times A \times \epsilon$ of $pp \rightarrow Z + \text{DM}$ processes. Left panel: model predictions of the cross section for all $m_{S_1} < m_{S_2}$ case points without momentum cuts. Right panel: model predictions of the cross section for six benchmark $m_{S_1} < m_{S_2}$ case points with different missing transverse momentum (p_T^{miss}) ranges, along with the corresponding ATLAS upper limits. The legend is shared by both panels. 63

4.13	Cross section of mono- Z production processes $pp \rightarrow S_1 S_1 Z$ at a center-of-mass energy of $\sqrt{s} = 13$ TeV. The presented points correspond to the model's theoretical predictions for the $m_{S_1} < m_{S_2}$ case points, and the red (solid) line is the ATLAS (2018) [6] model-independent experimental upper limit on the cross section (σ) of $pp \rightarrow Z + \text{DM}$ processes. Left panel: model predictions of the cross section for all $m_{S_1} < m_{S_2}$ case points without momentum cuts. Right panel: model predictions of the cross section for six benchmark $m_{S_1} < m_{S_2}$ case points with different missing transverse momentum (p_T^{miss}) ranges, along with the corresponding ATLAS upper limits. The legend is shared by both panels.	64
5.1	Feynman rules for the interaction vertices involving the S_r ($r = 1, 2, 3$) dark matter particle candidates. The decays $S_r \rightarrow \text{SM SM}$ and $S_r \rightarrow S_{r'} S_{r'}$ ($r' \neq r$) are forbidden by “dark parity” (or $\mathcal{Z}_2^{(r)}$ charge) conservation, as a consequence of the $\mathcal{Z}_2^{(1)} \times \mathcal{Z}_2^{(2)} \times \mathcal{Z}_2^{(3)}$ discrete symmetry.	70
5.2	Experimental constraints on the SM+3RSS model (5.4), obtained by scanning the free parameter space with micrOMEGAs 6.1 for the freeze-out mechanism. Both panels show free parameter space points that correspond to the observed DM relic density and are not excluded by direct detection. Columns share the x -axis, and rows share the colour bar.	72
5.3	Experimental constraints on the SM+3RSS model (5.4), obtained by scanning the free parameter space with micrOMEGAs 6.1 for the freeze-out mechanism. All panels show free parameter space points that correspond to the observed DM relic density and are not excluded by direct detection. Each colour bar displays the relic density of one of the DM particles S_r ($r = 1, 2, 3$).	73
5.4	Spin-independent cross section of DM-nucleon elastic scattering $S_r N \rightarrow S_r N$ ($N = p, n$) multiplied by the corresponding fraction of DM relic density $\Omega_{S_r}/\Omega_{\text{DM}}$ ($r = 1, 2, 3$). The presented points correspond to the model's theoretical predictions for the $m_{S_3} < m_{S_1} < m_{S_2}$ (two light one two heavy) case points of Figure 5.2, for both proton (p) and neutron (n) elastic scattering. The blue and green (solid) lines correspond to the LUX-ZEPLIN (LZ) experimental upper limits on the WIMP-nucleon elastic scattering spin-independent cross section from 2022 [2] and 2024 [3] results, respectively. The (shaded green) experimental uncertainty band from the LZ 2024 results is displayed. The legend is shared by both panels.	75
5.5	Spin-independent cross section of DM-nucleon elastic scattering $S_r N \rightarrow S_r N$ ($N = p, n$) multiplied by the corresponding fraction of DM relic density $\Omega_{S_r}/\Omega_{\text{DM}}$ ($r = 1, 2, 3$). The presented points correspond to the model's theoretical predictions for the $m_{S_1} < m_{S_2} < m_{S_3}$ (one-light-two-heavy) case points of Figure 5.2, for both proton (p) and neutron (n) elastic scattering. The blue and green (solid) lines correspond to the LUX-ZEPLIN (LZ) experimental upper limits on the WIMP-nucleon elastic scattering spin-independent cross section from 2022 [2] and 2024 [3] results, respectively. The (shaded green) experimental uncertainty band from the LZ 2024 results is displayed. The legend is shared by all panels.	76
C.1	Feynman rules of the SM+2RSS model for the interaction vertices involving the χ_1, χ_2 scalar particles. The coloured vertices emerge upon $\mathcal{Z}_2^{(1)} \times \mathcal{Z}_2^{(2)} \rightarrow \mathcal{Z}_2^{(1,2)}$ explicit symmetry breaking.	104

C.2	Experimental constraints on the $\mathcal{Z}_2^{(1,2)}$ invariant SM+2RSS model (C.1), obtained by scanning the free parameter space with micrOMEGAs 6.1 for the freeze-out mechanism. All panels show the parameter space points that correspond to the observed DM relic density and are not excluded by direct detection.	105
C.3	Spin-independent cross section of DM-nucleon elastic scattering $\chi_1 N \rightarrow \chi_1 N$ ($N = p, n$). The presented points correspond to the model's theoretical predictions for the points of Figure C.2, for both proton (p) and neutron (n) elastic scattering. The blue and green (solid) lines correspond to the LUX-ZEPLIN (LZ) experimental upper limits on the WIMP-nucleon elastic scattering spin-independent cross section from 2022 [2] and 2024 [3] results, respectively. The (shaded green) experimental uncertainty band from the LZ 2024 results is displayed. The legend is shared by all panels, which differ only in the colour bar.	105

List of Tables

4.1	Experimental constraints responsible for each boundary of the free parameters' allowed ranges in the $m_{S_1} < m_{S_2}$ case region. If a particular boundary does not exist, the corresponding table entry displays “—”. The m_{S_2} and κ_{H2} parameters are interdependently constrained by the relic-DD “tension”, and the grey bounds on m_{S_2} (κ_{H2}) are only exhibited for fixed κ_{H2} (m_{S_2}) values.	54
4.2	Model predictions of the cross section $\sigma(pp \rightarrow S_1 S_1 j)$ and corresponding number of events (NE) for six benchmark $m_{S_1} < m_{S_2}$ case points, at three distinct center-of-mass energies. The NE's were computed for the following integrated luminosities: $L = 190 \text{ fb}^{-1}$ at $\sqrt{s} = 13 \text{ TeV}$, $L = 450 \text{ fb}^{-1}$ at $\sqrt{s} = 13.6 \text{ TeV}$ and $L = 3000 \text{ fb}^{-1}$ at $\sqrt{s} = 14 \text{ TeV}$	58
4.3	Model predictions of the cross section $\sigma(pp \rightarrow S_1 S_1 h)$ and corresponding number of events (NE) for six benchmark $m_{S_1} < m_{S_2}$ case points, at three distinct center-of-mass energies. The NE's were computed for the following integrated luminosities: $L = 190 \text{ fb}^{-1}$ at $\sqrt{s} = 13 \text{ TeV}$, $L = 450 \text{ fb}^{-1}$ at $\sqrt{s} = 13.6 \text{ TeV}$ and $L = 3000 \text{ fb}^{-1}$ at $\sqrt{s} = 14 \text{ TeV}$	58
4.4	Model predictions of the cross section $\sigma(pp \rightarrow S_1 S_1 Z)$ and corresponding number of events (NE) for six benchmark $m_{S_1} < m_{S_2}$ case points, at three distinct center-of-mass energies. The NE's were computed for the following integrated luminosities: $L = 190 \text{ fb}^{-1}$ at $\sqrt{s} = 13 \text{ TeV}$, $L = 450 \text{ fb}^{-1}$ at $\sqrt{s} = 13.6 \text{ TeV}$ and $L = 3000 \text{ fb}^{-1}$ at $\sqrt{s} = 14 \text{ TeV}$	58
4.5	Model predictions of the cross section $\sigma(pp \rightarrow S_1 S_1 b\bar{b})$ and corresponding number of events (NE) for six benchmark $m_{S_1} < m_{S_2}$ case points, at three distinct center-of-mass energies. The NE's were computed for the following integrated luminosities: $L = 190 \text{ fb}^{-1}$ at $\sqrt{s} = 13 \text{ TeV}$, $L = 450 \text{ fb}^{-1}$ at $\sqrt{s} = 13.6 \text{ TeV}$ and $L = 3000 \text{ fb}^{-1}$ at $\sqrt{s} = 14 \text{ TeV}$	59
A.1	Summary of the different gauge theory conventions found in the literature, both for active/passive transformations (which are inverse to each other, with their correspondence obtained through a change of sign in the $\vec{\alpha}$ parameters) and for the sign of the gauge coupling constant in the covariant derivative.	92

List of Abbreviations

BR	Branching Ratio
BSM	Beyond Standard Model
CC	Charged Current
CKM	Cabibbo–Kobayashi–Maskawa
CMB	Cosmic Microwave Background
DD	Direct Detection
DM	Dark Matter
EFT	Effective Field Theory
EMT	Energy-Momentum Tensor
ESB	Explicit Symmetry Breaking
EW	Electroweak
FIMP	Feebly Interactive Massive Particle
GR	General Relativity
h.c.	Hermitian Conjugate
ID	Indirect Detection
LHC	Large Hadron Collider
LZ	LUX-ZEPLIN
MET	Missing Transverse Energy
NC	Neutral Current
PMNS	Pontecorvo–Maki–Nakagawa–Sakata
QCD	Quantum Chromodynamics
QED	Quantum Electrodynamics
QFT	Quantum Field Theory
RGE	Renormalization Group Equation
SI	Spin-Independent
SM	Standard Model
SM+2RSS	Two-Real-Scalar-Singlet Extension of the Standard Model
SM+3RSS	Three-Real-Scalar-Singlet Extension of the Standard Model
SM+CSS	Complex Scalar Singlet Extension of the Standard Model
SM+RSS	Real Scalar Singlet Extension of the Standard Model
SM+nRSS	n -Real-Scalar-Singlet Extension of the Standard Model
SSB	Spontaneous Symmetry Breaking
TAC	Thermally Averaged Cross Section
VEV	Vacuum Expectation Value
WIMP	Weakly Interactive Massive Particle
ΛCDM	Lambda Cold Dark Matter

Chapter 1

Introduction

The Standard Model (SM) of particle physics is a mathematically self-consistent, renormalizable quantum field theory that describes all known non-gravitational (electromagnetic, weak and strong) interactions between all known elementary particles with remarkable success, making it the closest we have to a fundamental theory. However, even when combined with general relativity (GR), it fails to explain all the physical phenomena we observe. One of the most fundamental questions in physics concerns the nature of dark matter (DM), an invisible non-baryonic form of matter that constitutes about 26% of the total matter-energy and 84% of the total matter of the observable Universe. From the rotation curves of spiral galaxies to Cosmic Microwave Background (CMB) observations [7] at the cosmological scale, the overwhelming experimental evidence for the existence of dark matter arises solely from the gravitational effects it produces. These gravitational probes provide valuable information on the properties of DM – such as it being cold, weakly interactive, electrically neutral and stable – but understanding the nature of DM requires the observation of its non-gravitational interactions with ordinary visible matter. Despite the global effort to search for DM through numerous direct, indirect and collider detection experiments, it has never been detected so far.

The most popular approach to this problem relies on the common assumption of DM consisting of a new elementary particle (or particles) that has yet to be discovered [8, 9, 10], thus requiring an extension of the Standard Model of particle physics. These extension models introduce new symmetries to ensure the stability of potential DM particle candidates. The most common choice – although not unique (e.g., $U(1)$ symmetries are also widely used) – is a \mathbb{Z}_2 discrete symmetry under which all the SM fields transform trivially (\mathbb{Z}_2 -even), while the DM field does not (\mathbb{Z}_2 -odd). This prevents interaction terms that are linear in the DM field and subsequent DM decay, thereby ensuring the stability (and viability) of the candidate. One of the first models to be proposed was the real scalar singlet SM extension (SM+RSS) with an unbroken \mathbb{Z}_2 symmetry $S(x) \rightarrow -S(x)$, $\text{SM} \rightarrow +\text{SM}$ which prevents the real scalar $SU(3)_c \times SU(2)_L \times U(1)_Y$ singlet DM particle candidate S from decaying [11, 12, 13]. The appeal of this model lies in its simplicity and minimalism: 1) The singlet field $S(x) \sim (\mathbf{1}, \mathbf{1}, 0)$ cannot (explicitly or spontaneously) break the SM gauge symmetry. 2) The singlet $S(x)$ couples exclusively to the Higgs doublet $\Phi(x)$, through a portal term $\mathcal{L}_{\text{portal}} \propto S^2 \Phi^\dagger \Phi$ linking the SM and dark sectors. 3) The model introduces only three extra free parameters beyond the SM: the DM mass, the portal coefficient, and the quartic self-interaction coefficient (the latter being irrelevant at tree-level in perturbation theory). However (as we shall see), the observed DM relic density and direct detection experiments exclude this model for DM masses below about 3.5 TeV, making it impossible to probe at the Large Hadron Collider (LHC).

There are many generalizations of the real scalar singlet SM extension that despite being more elaborate (e.g., increased number of free parameters), still retain some of its features. One possible alternative

is the complex scalar singlet SM extension (SM+CSS) with a softly broken $U(1)$ global (dark) symmetry, that provides a pseudo-Goldstone boson DM candidate [14]. Another approach is to study Higgs-portal effective interactions under the framework of effective field theory (EFT) [15, 16, 17]. Finally, and amongst many other possible alternatives, one can just consider an increased number of real scalar singlets (and possibly, but not necessarily, of independent \mathcal{Z}_2 symmetries).

These $n = 1, 2, \dots$ multi-real-scalar-singlet SM extensions (SM+ n RSS) will be the main focus of our work. In particular, we shall study the $n = 2, 3$ cases and impose a symmetry with respect to the discrete direct product group $\times_{r=1}^n \mathcal{Z}_2^{(r)} \equiv \mathcal{Z}_2^{(1)} \times \dots \times \mathcal{Z}_2^{(n)}$, under which the fields transform as

$$\mathcal{Z}_2^{(r)} : S_r(x) \rightarrow -S_r(x), \quad S_{r'}(x) \rightarrow +S_{r'}(x), \quad \text{SM} \rightarrow +\text{SM}, \quad (1.1)$$

$r, r' = 1, \dots, n \wedge r' \neq r$. The symmetry remains unbroken, thus leading to $n = 2, 3$ stable DM candidates S_r (and zero extra Higgs-like particles, because there is no mixing), that we assume are weakly interactive massive particles (WIMPs) [18] that were thermally produced according to the freeze-out mechanism. The $n = 2$ case (i.e., the SM+2RSS model) with a $\mathcal{Z}_2^{(1)} \times \mathcal{Z}_2^{(2)}$ symmetry has already been studied [19, 20], but for different scenarios than ours (which to our knowledge, has not been proposed in the literature). In Ref. [19], the $\mathcal{Z}_2^{(1)} \times \mathcal{Z}_2^{(2)}$ symmetry is spontaneously broken down to no residual symmetry (i.e., both symmetries are spontaneously broken), thus leading to two extra Higgs-like particles and zero DM candidates. In Ref. [20], on the other hand, the symmetry also remains unbroken, but one of the (two) DM candidates is a feebly interactive massive particle (FIMP) that was produced according to the freeze-in mechanism.¹ The SM+3RSS model ($n = 3$ case) with an unbroken $\mathcal{Z}_2^{(1)} \times \mathcal{Z}_2^{(2)} \times \mathcal{Z}_2^{(3)}$ symmetry has never been studied.

This work is organized as follows. In Chapter 2, we construct the SM of particle physics from the local gauge symmetry principle, by imposing $SU(3)_c \times SU(2)_L \times U(1)_Y$ gauge invariance without mentioning experimental motivations or historical perspectives. In Chapter 3, we give a brief introduction to the field of particle dark matter, and then proceed to re-study the real scalar singlet SM extension – our starting point, and motivation for what follows. Chapter 4 is dedicated to the two-real-scalar-singlet SM extension. First, we present the model, compute relevant cross sections and perform an analytical analysis for the theoretical and experimental constraints related to particle physics. We then perform a numerical analysis for the experimental constraints related to DM – specifically, the observed relic density, direct detection experiments and LHC searches – and identify the allowed free parameter space regions of interest. Chapter 5 is analogous to the previous Chapter 4, but for the three-real-scalar-singlet SM extension. Finally, we present our conclusions and final remarks in Chapter 6.

¹Ref. [20] also briefly considers an alternative (unbroken) symmetry group $\mathcal{Z}_2^{(1,2)}$ under which both singlets transform non-trivially, thus leading to the $S_1 S_2$ mixing scenario (which excludes the Higgs boson).

Chapter 2

The Standard Model of Particle Physics

Before extending the Standard Model of particle physics with new physics phenomena, one must understand how this quantum field (gauge) theory is constructed. Therefore, we shall build the SM from scratch, by imposing the local $SU(3)_c \times SU(2)_L \times U(1)_Y$ gauge symmetry to a free massless spinor field theory. Both the variational principle of least action and the local gauge symmetry principle are discussed in detail in Appendix A. Our treatment will not cover historical developments nor experimental motivations, and many important details will be left out.

There is a vast literature on the topics of quantum field theory [21, 22, 23, 24, 25, 26, 27], group theory [28, 29] and – more relevant to this chapter – Standard Model and beyond [30, 31], which have directly or indirectly impacted this work. The textbook by P. Langacker [32], the lectures on *Standard Model* by Filipe Joaquim [33] and the (respective) lecture notes by Luís Lavoura [34] were the most influential to this chapter. Nevertheless, we follow our own conventions.

2.1 Electroweak Interaction from $SU(2)_L \times U(1)_Y$ Gauge Symmetry

We start by introducing the chiral projection operators $P_{L,R} \equiv (\mathbb{1} \mp \gamma^5)/2$, where $\gamma^5 \equiv i\gamma^0\gamma^1\gamma^2\gamma^3$ has the following properties: $(\gamma^5)^2 = \mathbb{1}$, $\gamma^{5\dagger} = \gamma^5$, $\{\gamma^\mu, \gamma^5\} = 0$. The matrices γ^μ ($\mu = 0, 1, 2, 3$) are the usual 4×4 Dirac matrices, satisfying $\{\gamma^\mu, \gamma^\nu\} = 2g^{\mu\nu}\mathbb{1}$ and $\gamma^{\mu\dagger} = \gamma^0\gamma^\mu\gamma^0$. The first two properties of γ^5 imply that its eigenvalues are ∓ 1 , the so-called chirality values. Eigenstates of γ^5 have well-defined chirality $-1(+1)$, and are referred to as left(right)-handed chiral states.¹ Using the first property of γ^5 , it is trivial to show that $P_{L,R}$ satisfy the projection operator algebra: $P_L + P_R = \mathbb{1}$, $P_{L,R}^2 = P_{L,R}$, $P_{L,R}P_{R,L} = 0$. Hence, any spinor ψ can be decomposed into left-handed (LH) and right-handed (RH) chiral components, $\psi = (P_L + P_R)\psi = \psi_L + \psi_R$ (with $\gamma^5\psi_{L,R} = \mp\psi_{L,R}$). The second and third properties of γ^5 imply $P_{L,R}^\dagger = P_{L,R}$ and $\gamma^\mu P_{L,R} = P_{R,L}\gamma^\mu$ (respectively), so that for a Dirac adjoint spinor $\bar{\psi} \equiv \psi^\dagger\gamma^0$, one has

$$\overline{\psi_{L,R}} = (P_{L,R}\psi)^\dagger\gamma^0 = \psi^\dagger P_{L,R}^\dagger\gamma^0 = \psi^\dagger P_{L,R}\gamma^0 = \psi^\dagger\gamma^0 P_{R,L} = \bar{\psi}P_{R,L}. \quad (2.1)$$

Finally, with the previous conditions, we are able to obtain the following relations

$$\begin{aligned} \bar{\psi}\psi &= \bar{\psi}(P_L + P_R)\psi = \bar{\psi}(P_L^2 + P_R^2)\psi = \bar{\psi}_R\psi_L + \bar{\psi}_L\psi_R \\ \bar{\psi}\gamma^\mu\psi &= \bar{\psi}\gamma^\mu(P_L + P_R)\psi = \bar{\psi}\gamma^\mu(P_L^2 + P_R^2)\psi = \bar{\psi}(P_R\gamma^\mu P_L + P_L\gamma^\mu P_R)\psi = \bar{\psi}_L\gamma^\mu\psi_L + \bar{\psi}_R\gamma^\mu\psi_R, \end{aligned}$$

¹This is because helicity eigenstates with helicity $\mp 1/2$ correspond to γ^5 eigenstates (or chiral states) with chirality ∓ 1 in the relativistic (massless fermion) limit ($m \ll E$).

which will be widely used throughout this Chapter 2 (without further demonstration). We are now prepared to introduce the electroweak theory of interactions.

Our starting point is a theory $\mathcal{L}_{\text{kin}}^{(f)} = \sum_{\psi} i\bar{\psi}\not{\partial}\psi \equiv \sum_{\psi} i\bar{\psi}\gamma^{\mu}\partial_{\mu}\psi$ of free massless matter (or fermion) fields ψ . The Standard Model of particle physics – the final goal of this Chapter 2 – is a gauge theory, i.e., a quantum field theory based on the local gauge symmetry principle. For now, we shall focus on the theory of electroweak (EW) interactions (the strong interaction will be later introduced, in Section 2.4). From numerous experimental results (e.g., the observation of parity violation in weak interactions, revealing their chiral structure), we know that the electromagnetic and weak interactions emerge from a gauge symmetry with respect to the continuous direct product group $\text{SU}(2)_L \times \text{U}(1)_Y$ (as a whole, which is why they are said to be “unified”). This symmetry group has dimension $3 + 1 = 4$, with generators T_i ($i = 1, 2, 3$) of $\text{SU}(2)_L$ and Y of $\text{U}(1)_Y$. The definition of direct product group requires the $\text{SU}(2)_L$ and $\text{U}(1)_Y$ transformations to be independent, which implies (via the Baker–Campbell–Hausdorff formula) the commutation $[T_i, Y] = 0$. Finally, the $\text{U}(1)_Y$ charge, known as the weak hypercharge, is defined such that the $\text{U}(1)_Q$ charge of electromagnetism (electric charge) is given by $Q = T_3 + Y$ (implying that $\text{U}(1)_Q$ is a subgroup of $\text{SU}(2)_L \times \text{U}(1)_Y$).

The fermion fields can be placed in **n**-multiplets Ψ of $\text{SU}(2)_L$ with well-defined hypercharge $Y^{(\Psi)}$ which transform under the following $\Psi \sim (\mathbf{n}, Y^{(\Psi)})$ representations of $\text{SU}(2)_L \times \text{U}(1)_Y$

$$L_{\alpha L} = \begin{pmatrix} \nu_{\alpha L} \\ \ell_{\alpha L} \end{pmatrix} = \begin{pmatrix} \nu_{eL} \\ e_L \end{pmatrix}, \begin{pmatrix} \nu_{\mu L} \\ \mu_L \end{pmatrix}, \begin{pmatrix} \nu_{\tau L} \\ \tau_L \end{pmatrix} \sim (\mathbf{2}, -1/2) \quad (2.2)$$

$$Q_{\alpha L} = \begin{pmatrix} u_{\alpha L} \\ d_{\alpha L} \end{pmatrix} = \begin{pmatrix} u_L \\ d_L \end{pmatrix}, \begin{pmatrix} c_L \\ s_L \end{pmatrix}, \begin{pmatrix} t_L \\ b_L \end{pmatrix} \sim (\mathbf{2}, +1/6) \quad (2.3)$$

$$\nu_{\alpha R} = \nu_{eR}, \nu_{\mu R}, \nu_{\tau R} \sim (\mathbf{1}, 0), \quad \ell_{\alpha R} = e_R, \mu_R, \tau_R \sim (\mathbf{1}, -1) \quad (2.4)$$

$$u_{\alpha R} = u_R, c_R, t_R \sim (\mathbf{1}, +2/3), \quad d_{\alpha R} = d_R, s_R, b_R \sim (\mathbf{1}, -1/3), \quad (2.5)$$

where $\alpha = 1, 2, 3$ are generation/family indices, and the leptons $\nu_{\alpha}, \ell_{\alpha}$ and quarks u_{α}, d_{α} (i.e., all fermions) are introduced. The LH and RH components of the fermion fields transform under different representations of this group, and hence, the $\text{SU}(2)_L \times \text{U}(1)_Y$ symmetry is said to be chiral. Our starting theory of free massless fermions $\mathcal{L}_{\text{kin}}^{(f)} = \sum_{\psi} i\bar{\psi}\gamma^{\mu}\partial_{\mu}\psi$ can be expressed in terms of the $\text{SU}(2)_L \times \text{U}(1)_Y$ multiplets (2.2)–(2.5), giving

$$\begin{aligned} \mathcal{L}_{\text{kin}}^{(f)} &= \sum_{\alpha} (i\bar{\ell}_{\alpha}\gamma^{\mu}\partial_{\mu}\ell_{\alpha} + i\bar{\nu}_{\alpha}\gamma^{\mu}\partial_{\mu}\nu_{\alpha}) + \sum_{\alpha} (i\bar{u}_{\alpha}\gamma^{\mu}\partial_{\mu}u_{\alpha} + i\bar{d}_{\alpha}\gamma^{\mu}\partial_{\mu}d_{\alpha}) \quad (2.6) \\ &= \sum_{\alpha} (i\bar{\ell}_{\alpha L}\gamma^{\mu}\partial_{\mu}\ell_{\alpha L} + i\bar{\ell}_{\alpha R}\gamma^{\mu}\partial_{\mu}\ell_{\alpha R} + i\bar{\nu}_{\alpha L}\gamma^{\mu}\partial_{\mu}\nu_{\alpha L} + i\bar{\nu}_{\alpha R}\gamma^{\mu}\partial_{\mu}\nu_{\alpha R}) \\ &\quad + \sum_{\alpha} (i\bar{u}_{\alpha L}\gamma^{\mu}\partial_{\mu}u_{\alpha L} + i\bar{u}_{\alpha R}\gamma^{\mu}\partial_{\mu}u_{\alpha R} + i\bar{d}_{\alpha L}\gamma^{\mu}\partial_{\mu}d_{\alpha L} + i\bar{d}_{\alpha R}\gamma^{\mu}\partial_{\mu}d_{\alpha R}) \\ &= \sum_{\alpha} (i\bar{L}_{\alpha L}\gamma^{\mu}\partial_{\mu}L_{\alpha L} + i\bar{\ell}_{\alpha R}\gamma^{\mu}\partial_{\mu}\ell_{\alpha R} + i\bar{\nu}_{\alpha R}\gamma^{\mu}\partial_{\mu}\nu_{\alpha R}) \\ &\quad + \sum_{\alpha} (i\bar{Q}_{\alpha L}\gamma^{\mu}\partial_{\mu}Q_{\alpha L} + i\bar{u}_{\alpha R}\gamma^{\mu}\partial_{\mu}u_{\alpha R} + i\bar{d}_{\alpha R}\gamma^{\mu}\partial_{\mu}d_{\alpha R}), \quad (2.7) \end{aligned}$$

which is explicitly invariant under $\Psi \rightarrow \Psi' = e^{-i\sum_i \alpha^i T_i} e^{-iY\theta} \Psi$ global (but not local) $\text{SU}(2)_L \times \text{U}(1)_Y$ transformations. The corresponding local gauge symmetry is obtained through the minimal coupling re-

placement procedure $\partial_\mu \hookrightarrow D_\mu$, with the $SU(2)_L \times U(1)_Y$ covariant derivative

$$D_\mu = \partial_\mu + ig_w \sum_{i=1}^3 T_i W_\mu^i + ig' Y B_\mu, \quad (2.8)$$

provided that the $SU(2)_L$ and $U(1)_Y$ gauge boson fields $W_\mu^i(x)$ ($i = 1, 2, 3$) and $B_\mu(x)$ transform as

$$W_\mu^i \xrightarrow{SU(2)_L} W_\mu'^i = W_\mu^i + \sum_{j,k=1}^3 \epsilon_{ijk} \alpha^j(x) W_\mu^k + \frac{\partial_\mu \alpha^i(x)}{g_w} = \left[\vec{W}_\mu + \vec{\alpha}(x) \times \vec{W}_\mu + \frac{\partial_\mu \vec{\alpha}(x)}{g_w} \right]^i \quad (2.9)$$

$$B_\mu \xrightarrow{U(1)_Y} B'_\mu = B_\mu + \frac{\partial_\mu \theta(x)}{g'}, \quad (2.10)$$

where g_w and g' are the EW coupling constants, and ϵ_{ijk} (elements of the Levi-Civita tensor) are the structure constants of the non-Abelian Lie group $SU(2)_L$. As shown in Eq. (2.9), the $SU(2)_L$ gauge bosons $W_\mu^i(x)$ are components $i = 1, 2, 3$ of a vector $\left(W_\mu^1 \ W_\mu^2 \ W_\mu^3 \right)^\top$ which transforms under the adjoint **3** representation of $SU(2)_L$. Defining $W_\mu^\pm = (W_\mu^1 \mp iW_\mu^2)/\sqrt{2}$ and $T^\pm = (T_1 \pm iT_2)/\sqrt{2}$ ($\equiv T_\pm/\sqrt{2}$), we get $T_1 W_\mu^1 + T_2 W_\mu^2 = T^+ W_\mu^+ + T^- W_\mu^-$, which can be introduced in the covariant derivative (2.8) to obtain the charged current weak interactions. However, if W_μ^3 and B_μ were physical bosons, the covariant derivative term $ig_w T_3 W_\mu^3 + ig' Y B_\mu$ would not reproduce the observed neutral current electroweak interactions.² Defining the two physical neutral EW gauge bosons through an $SO(2)$ flavour rotation of the “original” ones, as in the Glashow-Weinberg-Salam model,

$$\begin{pmatrix} Z_\mu \\ A_\mu \end{pmatrix} = \begin{pmatrix} \cos \theta_w & -\sin \theta_w \\ +\sin \theta_w & \cos \theta_w \end{pmatrix} \begin{pmatrix} W_\mu^3 \\ B_\mu \end{pmatrix}, \quad \begin{cases} \cos \theta_w = \frac{g_w}{\sqrt{g_w^2 + g'^2}} \\ \sin \theta_w = \frac{g'}{\sqrt{g_w^2 + g'^2}} \end{cases} \Rightarrow \tan \theta_w = \frac{g'}{g_w}, \quad (2.11)$$

the covariant derivative (2.8) of $SU(2)_L \times U(1)_Y$ is parametrized as

$$D_\mu = \partial_\mu + ieQ A_\mu + i \frac{g_w}{\cos \theta_w} (T_3 - Q \sin^2 \theta_w) Z_\mu + ig_w (T^+ W_\mu^+ + T^- W_\mu^-), \quad (2.12)$$

where $e = g' \cos \theta_w = g_w \sin \theta_w = g_w g' / \sqrt{g_w^2 + g'^2}$ is the electromagnetic gauge coupling. The minimal coupling $\partial_\mu \hookrightarrow D_\mu$ replacement in the kinetic Lagrangian density (2.7) leads to

$$\begin{aligned} \mathcal{L}_{\text{kin}+(ew)\text{int}}^{(f)} &= \sum_\alpha \left(i \bar{L}_{\alpha L} \gamma^\mu D_\mu L_{\alpha L} + i \bar{\ell}_{\alpha R} \gamma^\mu D_\mu \ell_{\alpha R} + i \bar{\nu}_{\alpha R} \gamma^\mu D_\mu \nu_{\alpha R} \right) \\ &\quad + \sum_\alpha \left(i \bar{Q}_{\alpha L} \gamma^\mu D_\mu Q_{\alpha L} + i \bar{u}_{\alpha R} \gamma^\mu D_\mu u_{\alpha R} + i \bar{d}_{\alpha R} \gamma^\mu D_\mu d_{\alpha R} \right) \\ &= \sum_\alpha \left[i \bar{\ell}_\alpha \gamma^\mu \partial_\mu \ell_\alpha + i \bar{\nu}_\alpha \gamma^\mu \partial_\mu \nu_\alpha + e A_\mu \bar{\ell}_\alpha \gamma^\mu \ell_\alpha - \frac{g_w}{2 \cos \theta_w} Z_\mu \bar{\ell}_\alpha \gamma^\mu (-P_L + 2 \sin^2 \theta_w) \ell_\alpha \right. \\ &\quad \left. - \frac{g_w}{2 \cos \theta_w} Z_\mu \bar{\nu}_\alpha \gamma^\mu P_L \nu_\alpha - \frac{g_w}{\sqrt{2}} (W_\mu^+ \bar{\nu}_\alpha \gamma^\mu P_L \ell_\alpha + \text{h.c.}) \right] \\ &\quad + \sum_\alpha \left[i \bar{u}_\alpha \gamma^\mu \partial_\mu u_\alpha + i \bar{d}_\alpha \gamma^\mu \partial_\mu d_\alpha - \frac{2}{3} e A_\mu \bar{u}_\alpha \gamma^\mu u_\alpha + \frac{1}{3} e A_\mu \bar{d}_\alpha \gamma^\mu d_\alpha \right. \\ &\quad \left. - \frac{g_w}{2 \cos \theta_w} Z_\mu \bar{u}_\alpha \gamma^\mu \left(P_L - \frac{4}{3} \sin^2 \theta_w \right) u_\alpha - \frac{g_w}{2 \cos \theta_w} Z_\mu \bar{d}_\alpha \gamma^\mu \left(-P_L + \frac{2}{3} \sin^2 \theta_w \right) d_\alpha \right] \end{aligned} \quad (2.13)$$

²It would reproduce an electromagnetic-type interaction mediated by B_μ and another neutral current interaction, mediated by W_μ^3 , where RH fermions ($SU(2)_L$ singlets) do not participate – thus contradicting experiment.

$$-\frac{g_w}{\sqrt{2}} \left(W_\mu^+ \bar{u}_\alpha \gamma^\mu P_L d_\alpha + \text{h.c.} \right) \Big] , \quad (2.14)$$

where h.c. stands for “hermitian conjugate”. These are the observed electroweak interactions. It should be noted that this Lagrangian density can be written in the more compact form

$$\begin{aligned} \mathcal{L}_{\text{kin}+(\text{ew})\text{int}}^{(f)} = & \sum_\psi \left(i\bar{\psi} \not{\partial} \psi - e A_\mu j_{\text{em}}^\mu[\psi] - \frac{g_w}{2 \cos \theta_w} Z_\mu j_{\text{NC}(w)}^\mu[\psi] \right) \\ & + \sum_{(\psi_{(u)}, \psi_{(d)})} -\frac{g_w}{\sqrt{2}} \left(W_\mu^+ j_{\text{CC}(w)}^{-\mu}[\psi_{(u)}, \psi_{(d)}] + \text{h.c.} \right) , \end{aligned} \quad (2.15)$$

where the electromagnetic (EM) and weak neutral currents (NC) are given by

$$j_{\text{em}}^\mu[\psi] = Q^{(\psi)} \bar{\psi} \gamma^\mu \psi \quad (2.16)$$

$$j_{\text{NC}(w)}^\mu[\psi] = \bar{\psi} \gamma^\mu \left(2I_{w3}^{(\psi_L)} P_L - 2Q^{(\psi)} \sin^2 \theta_w \right) \psi = \bar{\psi} \gamma^\mu \left(g_V^{(\psi)} - g_A^{(\psi)} \gamma^5 \right) \psi , \quad (2.17)$$

$\forall \psi = \ell_\alpha, \nu_\alpha, u_\alpha, d_\alpha$ (all SM fermions), with $g_V^{(\psi)} = I_{w3}^{(\psi_L)} - 2Q^{(\psi)} \sin^2 \theta_w$ and $g_A^{(\psi)} = I_{w3}^{(\psi_L)}$ being the vector and axial-vector neutral current coefficients; and the weak charged current (CC) is given by

$$j_{\text{CC}(w)}^{-\mu}[\psi_{(u)}, \psi_{(d)}] = \bar{\psi}_{(u)} \gamma^\mu P_L \psi_{(d)} , \quad \forall \begin{pmatrix} \psi_{(u)} \\ \psi_{(d)} \end{pmatrix} = \begin{pmatrix} \nu_\alpha \\ \ell_\alpha \end{pmatrix} , \begin{pmatrix} u_\alpha \\ d_\alpha \end{pmatrix} , \quad (2.18)$$

with the corresponding h.c. $j_{\text{CC}(w)}^{+\mu}[\psi_{(u)}, \psi_{(d)}] = j_{\text{CC}(w)}^{-\dagger\mu}[\psi_{(u)}, \psi_{(d)}] = \bar{\psi}_{(d)} \gamma^\mu P_L \psi_{(u)}$.

Additionally, the electroweak gauge bosons W_μ^\pm, Z^μ, A^μ are not external/auxiliary, but rather dynamical fields, thus requiring kinetic terms. The missing $\text{SU}(2)_L \times \text{U}(1)_Y$ gauge invariant and renormalizable terms are the usual “pure gauge” terms of any gauge theory,

$$\mathcal{L}_{\text{gauge}}^{\text{SU}(2)_L \times \text{U}(1)_Y} = -\frac{1}{4} \sum_{i=1}^3 W_{\mu\nu}^i W^{i\mu\nu} - \frac{1}{4} B_{\mu\nu} B^{\mu\nu} , \quad (2.19)$$

where

$$W_{\mu\nu}^i \equiv \partial_\mu W_\nu^i - \partial_\nu W_\mu^i - g_w \sum_{j,k=1}^3 \epsilon_{ijk} W_\mu^j W_\nu^k = [\partial_\mu \vec{W}_\nu - \partial_\nu \vec{W}_\mu - g_w \vec{W}_\mu \times \vec{W}_\nu]^i \quad (2.20)$$

$$B_{\mu\nu} \equiv \partial_\mu B_\nu - \partial_\nu B_\mu \quad (2.21)$$

are the so-called field strength tensors. The (supposedly) physical gauge bosons are obtained through unitary transformations of the “original” gauge bosons, thus yielding correctly normalized kinetic terms; additionally, the non-Abelian nature of $\text{SU}(2)_L$ leads to self-interactions of the gauge bosons,

$$\begin{aligned} \mathcal{L}_{\text{gauge}}^{\text{SU}(2)_L \times \text{U}(1)_Y} = & -\frac{1}{2} \sum_{i=1}^3 [(\partial_\mu W_\nu^i) \partial^\mu W^{i\nu} - (\partial_\mu W_\nu^i) \partial^\nu W^{i\mu}] - \frac{1}{2} [(\partial_\mu B_\nu) \partial^\mu B^\nu - (\partial_\mu B_\nu) \partial^\nu B^\mu] \\ & + g_w \sum_{i,j,k=1}^3 \epsilon_{ijk} (\partial^\mu W^{i\nu}) W_\mu^j W_\nu^k - \frac{g_w^2}{4} \sum_{i,j,k,l,m=1}^3 \epsilon_{ijk} \epsilon_{ilm} W_\mu^j W_\nu^k W^{l\mu} W^{m\nu} \\ = & -[(\partial_\mu W_\nu^-) \partial^\mu W^{+\nu} - (\partial_\mu W_\nu^-) \partial^\nu W^{+\mu}] - \frac{1}{2} [(\partial_\mu Z_\nu) \partial^\mu Z^\nu - (\partial_\mu Z_\nu) \partial^\nu Z^\mu] \end{aligned} \quad (2.22)$$

$$\begin{aligned}
 & -\frac{1}{2} [(\partial_\mu A_\nu) \partial^\mu A^\nu - (\partial_\mu A_\nu) \partial^\nu A^\mu] \\
 & + g_w (\partial^\mu \vec{W}^\nu) \cdot (\vec{W}_\mu \times \vec{W}_\nu) - \frac{g_w^2}{4} [(\vec{W}_\mu \cdot \vec{W}^\mu)^2 - (\vec{W}_\mu \cdot \vec{W}_\nu)(\vec{W}^\mu \cdot \vec{W}^\nu)] . \quad (2.23)
 \end{aligned}$$

Finally, we still lack the mass terms for both weak gauge bosons and fermions. Vector gauge boson mass terms explicitly break the symmetry of any gauge theory, and in the case of a chiral symmetry (where LH and RH fermion fields transform under different representations), fermion mass terms are also forbidden. Nevertheless, since both are (in general) known to be massive, this must be addressed.

2.2 Spontaneous Symmetry Breaking and the Higgs Mechanism

There are two different types of symmetry breaking: *explicit symmetry breaking* (ESB) occurs when a symmetry of the Lagrangian density is broken,³ and *spontaneous symmetry breaking* (SSB) occurs when a symmetry of the vacuum is broken, so that the vacuum ends up having a smaller symmetry group than that of the Lagrangian density. In order to generate gauge boson mass terms without explicitly breaking the respective local gauge symmetry, one needs the so-called *Higgs Mechanism*, which relies on SSB. As we shall see, when SSB occurs, quantum fields acquire a non-zero *vacuum expectation value* (VEV). However, only scalar fields can have non-zero VEVs without breaking Lorentz invariance. Hence, the simplest way to spontaneously break the local $SU(2)_L \times U(1)_Y$ gauge symmetry is to insert a complex⁴ scalar $SU(2)_L$ doublet field

$$\Phi(x) = \begin{pmatrix} \phi_1(x) \\ \phi_2(x) \end{pmatrix} = \begin{pmatrix} \frac{1}{\sqrt{2}}(\varphi_1(x) + i\varphi_2(x)) \\ \frac{1}{\sqrt{2}}(\varphi_3(x) + i\varphi_4(x)) \end{pmatrix} \sim (\mathbf{2}, Y^{(\Phi)}) \quad (2.24)$$

with well-defined $U(1)_Y$ hypercharge $Y^{(\Phi)}$ in our theory, by adding the most general renormalizable⁵ and local $SU(2)_L \times U(1)_Y$ gauge invariant⁶ scalar sector,

$$\mathcal{L}_H = (D_\mu \Phi)^\dagger D^\mu \Phi - V(|\Phi|), \quad \text{with} \quad V(|\Phi|) = \mu_H^2 \Phi^\dagger \Phi + \lambda_H (\Phi^\dagger \Phi)^2. \quad (2.25)$$

The scalar potential $V[\Phi]$ is bounded from below if and only if $\lambda_H > 0$.

2.2.1 The Vacuum and its Spontaneous Symmetry Breaking

The vacuum state (or ground state) is the state of minimum energy, and corresponds to a constant value $\langle \Phi \rangle_0$ (so that $\partial_\mu \langle \Phi \rangle_0 = 0$) which minimizes the scalar potential $V[\Phi] \leq V[\langle \Phi \rangle_0]$. This value is, of course, the vacuum expectation value $\langle \Phi \rangle_0 \equiv \langle 0 | \Phi(x) | 0 \rangle$, obtained by the usual minimization

$$\begin{cases} \frac{\partial V}{\partial \Phi} \big|_{\Phi=\langle \Phi \rangle_0} = \langle \Phi \rangle_0^\dagger (\mu_H^2 + 2\lambda_H \langle \Phi \rangle_0^\dagger \langle \Phi \rangle_0) = 0 \\ \frac{\partial V}{\partial \Phi^\dagger} \big|_{\Phi=\langle \Phi \rangle_0} = (\mu_H^2 + 2\lambda_H \langle \Phi \rangle_0^\dagger \langle \Phi \rangle_0) \langle \Phi \rangle_0 = 0 \end{cases} \Leftrightarrow \underbrace{\langle \Phi \rangle_0 = 0}_{\text{trivial sol.}} \vee \underbrace{\langle \Phi \rangle_0^\dagger \langle \Phi \rangle_0 = \frac{-\mu_H^2}{2\lambda_H} \equiv \frac{v^2}{2}}_{\text{non-trivial sol.}}. \quad (2.26)$$

³Typically done by introducing terms that break this symmetry.

⁴The doublet components are necessarily complex, since the fundamental $\mathbf{2}$ representation of $SU(2)$, defined by the mapping $T_i \mapsto \sigma_i/2$ ($\sigma_i, i = 1, 2, 3$ being the Pauli matrices), is complex.

⁵A theory $\mathcal{L}(\varphi_r, \partial_\mu \varphi_r) = \sum_i c_i \mathcal{O}_i(\varphi_r, \partial_\mu \varphi_r)$ of fields φ_r is renormalizable if and only if $[\mathcal{O}_i(\varphi_r, \partial_\mu \varphi_r)] \leq [m]^4 = [E]^4$ (in natural units). Since $[\Phi] = [m]$, we can go up to quartic terms in Φ, Φ^\dagger in the scalar potential V .

⁶The only possible terms are $(\Phi^\dagger \Phi)^n, n = 1, 2$ (for $n = 0$ we get a constant term without physical meaning, and for $n > 2$ the theory is no longer renormalizable).

The trivial solution $\langle \Phi \rangle_0 = 0$ – which corresponds to a minimum for $\mu_H^2 > 0$, and a maximum for $\mu_H^2 < 0$ – although invariant under local $SU(2)_L \times U(1)_Y$ gauge transformations, is non-degenerate, and therefore does not allow SSB to occur. On the other hand, the non-trivial solution $\langle \Phi \rangle_0^\dagger \langle \Phi \rangle_0 = v^2/2 \in \mathbb{R}^+$ is possible if and only if $\mu_H^2 < 0$, and corresponds to an infinitely degenerate vacuum

$$\left\{ \langle \Phi \rangle_0 : \langle \Phi \rangle_0^\dagger \langle \Phi \rangle_0 = \frac{-\mu_H^2}{2\lambda_H} \equiv \frac{v^2}{2} \right\} \quad (2.27)$$

that is also invariant under local $SU(2)_L \times U(1)_Y$ gauge transformations, since

$$\langle \Phi \rangle_0^\dagger \langle \Phi \rangle_0 \rightarrow \langle \Phi' \rangle_0^\dagger \langle \Phi' \rangle_0 = \langle \Phi \rangle_0^\dagger e^{+iY\theta(x)} e^{+i\sum_i \alpha^i(x)T_i} e^{-i\sum_i \alpha^i(x)T_i} e^{-iY\theta(x)} \langle \Phi \rangle_0 = \langle \Phi \rangle_0^\dagger \langle \Phi \rangle_0.$$

Hence, SSB occurs when (μ_H transitions from $\mu_H^2 > 0$ to) $\mu_H^2 < 0$, because Nature *realizes* a particular VEV out of the possible continuous set (2.27), and the vacuum no longer contains the (full) symmetry of the Lagrangian density. Let us take, without loss of generality, the conventional VEV

$$\langle \Phi \rangle_0 \equiv \langle 0 | \Phi(x) | 0 \rangle := \begin{pmatrix} 0 \\ \frac{v}{\sqrt{2}} \end{pmatrix}, \quad \text{with } v = +\sqrt{\frac{-\mu_H^2}{\lambda_H}} > 0, \quad (2.28)$$

which corresponds to choosing a direction and complex phase of (2.27) so that $\langle \phi_1 \rangle_0 = 0$, $\langle \phi_2 \rangle_0 = \frac{v}{\sqrt{2}}$; or equivalently, $\langle \varphi_1 \rangle_0 = \langle \varphi_2 \rangle_0 = \langle \varphi_4 \rangle_0 = 0$, $\langle \varphi_3 \rangle_0 = v$ (with $v \in \mathbb{R}^+$). Notice that the $SU(2)_L$ and $U(1)_Y$ generators do not annihilate the vacuum, i.e.

$$T_i \langle \Phi \rangle_0 = \frac{\sigma_i}{2} \begin{pmatrix} 0 \\ \frac{v}{\sqrt{2}} \end{pmatrix} \neq \begin{pmatrix} 0 \\ 0 \end{pmatrix}, \quad Y \langle \Phi \rangle_0 = Y^{(\Phi)} \mathbb{1}_{2 \times 2} \begin{pmatrix} 0 \\ \frac{v}{\sqrt{2}} \end{pmatrix} \neq \begin{pmatrix} 0 \\ 0 \end{pmatrix}, \quad (2.29)$$

so that $\langle \Phi \rangle_0 \rightarrow \langle \Phi' \rangle_0 = e^{-i\sum_i \alpha^i(x)T_i} e^{-iY\theta(x)} \langle \Phi \rangle_0 \neq \langle \Phi \rangle_0$. However, we do not want to spontaneously break the local $U(1)_Q$ gauge symmetry of electromagnetism.⁷ Hence, the $U(1)_Q$ generator must annihilate the vacuum (or equivalently, the VEV must be neutrally charged)

$$\begin{aligned} Q \langle \Phi \rangle_0 &= (T_3 + Y) \langle \Phi \rangle_0 = \left(\frac{\sigma_3}{2} + Y^{(\Phi)} \mathbb{1}_{2 \times 2} \right) \begin{pmatrix} 0 \\ \frac{v}{\sqrt{2}} \end{pmatrix} = \begin{pmatrix} +1/2 + Y^{(\Phi)} & 0 \\ 0 & -1/2 + Y^{(\Phi)} \end{pmatrix} \begin{pmatrix} 0 \\ \frac{v}{\sqrt{2}} \end{pmatrix} \\ &= \begin{pmatrix} 0 \\ (-1/2 + Y^{(\Phi)}) \frac{v}{\sqrt{2}} \end{pmatrix} := \begin{pmatrix} 0 \\ 0 \end{pmatrix} \Leftrightarrow Y^{(\Phi)} := +\frac{1}{2}, \end{aligned} \quad (2.30)$$

so that $\langle \Phi \rangle_0 \rightarrow \langle \Phi' \rangle_0 = e^{-iQ\alpha(x)} \langle \Phi \rangle_0 = e^{-i\alpha(x)T_3} e^{-iY\alpha(x)} \langle \Phi \rangle_0 = \langle \Phi \rangle_0$, i.e. the VEV remains invariant under local $U(1)_Q \subset SU(2)_L \times U(1)_Y$ gauge transformations. With the previous imposition,

$$Q\Phi(x) = \begin{pmatrix} 1 & 0 \\ 0 & 0 \end{pmatrix} \begin{pmatrix} \phi_1(x) \\ \phi_2(x) \end{pmatrix} = \begin{pmatrix} +\phi_1(x) \\ 0 \end{pmatrix}, \quad (2.31)$$

and changing notations to $G^+(x) \leftrightarrow \phi_1(x)$, $\phi^0(x) \leftrightarrow \phi_2(x)$, one concludes that the complex scalar G^+ ($\equiv \phi_1$) has electric charge +1 and the complex scalar ϕ^0 ($\equiv \phi_2$) has electric charge 0.

Quantum fields that correspond to physical particles are perturbations (or excitations) around the state of minimum energy (the vacuum), and therefore have zero VEV (necessary condition, yet not sufficient).

⁷The reason for this will later become clear. For now, we simply state that the $U(1)_Q$ gauge symmetry is observed in Nature, where $Q = T_3 + Y$ is the electric charge operator.

Hence, we expand the scalar doublet around the VEV $\langle \Phi \rangle_0 \equiv \langle 0 | \Phi(x) | 0 \rangle$,

$$\Phi(x) = \begin{pmatrix} G^+(x) \\ \phi^0(x) \end{pmatrix} = \begin{pmatrix} G^+(x) \\ \frac{v+h(x)+iG^0(x)}{\sqrt{2}} \end{pmatrix} \sim (\mathbf{2}, +1/2), \quad (2.32)$$

where $h(x) \equiv \varphi_3(x) - v$ is the perturbation of $\varphi_3(x)$ around its VEV $\langle \varphi_3 \rangle_0 \equiv \langle 0 | \varphi_3(x) | 0 \rangle = v$, and we made an additional change of notation $G^0(x) \leftrightarrow \varphi_4(x)$.

2.2.2 Higgs Mass, Self-Interactions and Goldstone Bosons

Expanding the scalar potential $V[\Phi]$ around the VEV $\langle \Phi \rangle_0 \equiv \langle 0 | \Phi(x) | 0 \rangle$ one obtains (using the minimum condition $v^2 = -\mu_H^2/\lambda_H \Leftrightarrow \mu_H^2 = -\lambda_H v^2$)

$$\begin{aligned} V(|\Phi|) &= \frac{1}{2} \overbrace{(2\lambda_H v^2)}^{=m_h^2} h^2 + \lambda_H v h^3 + \frac{\lambda_H}{4} h^4 + \frac{\lambda_H}{4} G^{04} + \lambda_H (G^- G^+)^2 + \lambda_H v h G^{02} + \frac{\lambda_H}{2} h^2 G^{02} \\ &\quad + 2\lambda_H v h G^- G^+ + \lambda_H h^2 G^- G^+ + \lambda_H G^{02} G^- G^+ - \underbrace{\frac{\lambda_H v^4}{4}}_{=\text{const.}}, \end{aligned} \quad (2.33)$$

which means that we have a massive real scalar $h(x)$ with $m_h = \sqrt{2\lambda_H v^2}$, a massless real scalar $G^0(x)$ and two massless complex scalars $G^+(x)$, $G^-(x) \equiv G^{+\dagger}(x)$ ($m_{G^0} = m_{G^\pm} = 0$). Ignoring the unphysical constant term, and writing the interaction terms in terms of m_h , we get

$$\begin{aligned} -\mathcal{L}_H \supset V(|\Phi|) &= \frac{1}{2} m_h^2 h^2 + \frac{m_h^2}{2v} h^3 + \frac{m_h^2}{8v^2} h^4 + \frac{m_h^2}{8v^2} G^{04} + \frac{m_h^2}{2v^2} (G^- G^+)^2 + \frac{m_h^2}{2v} h G^{02} \\ &\quad + \frac{m_h^2}{4v^2} h^2 G^{02} + \frac{m_h^2}{v} h G^- G^+ + \frac{m_h^2}{2v^2} h^2 G^- G^+ + \frac{m_h^2}{2v^2} G^{02} G^- G^+, \end{aligned} \quad (2.34)$$

which contains all the scalar interactions and self-interactions. We now state an important theorem regarding SSB.

Theorem 1 (Nambu-Goldstone Theorem) *For each (“broken”) generator of a spontaneously broken continuous global symmetry (of the vacuum), a corresponding massless scalar boson emerges. These are known as Nambu-Goldstone (NG) bosons.*

If the spontaneously broken symmetry concerned the 4-dimensional⁸ $\text{SU}(2)_L \times \text{U}(1)_Y$ group, there would be 4 Nambu-Goldstone bosons. However, the $\text{U}(1)_Q \subset \text{SU}(2)_L \times \text{U}(1)_Y$ residual symmetry remains unbroken,⁹ as imposed by Eq. (2.30). Hence, the spontaneously broken symmetry concerns the $4 - 1 = 3$ dimensional $\{\text{SU}(2)_L \times \text{U}(1)_Y\}/\text{U}(1)_Q$ coset space [35, 24], and we end up with $4 - 1 = 3$ massless Nambu-Goldstone bosons: G^0 , G^+ and G^- .

The Goldstone Theorem has an important nuance. If the global symmetry that is spontaneously broken is a consequence (particular case) of the (more general) respective local symmetry, then we can locally transform the Lagrangian density (under the symmetry group) so that the Nambu-Goldstone bosons vanish. In this case, the Nambu-Goldstone fields do not correspond to physical particles, and are referred to as *would-be* Goldstone bosons. In our particular case, one can make an $\text{SU}(2)_L \times \text{U}(1)_Y$ local

⁸One should remember that the dimension of a continuous (or *Lie*) group is given by the number of generators.

⁹Some authors phrase it as the $\text{SU}(2)_L \times \text{U}(1)_Y$ symmetry being spontaneously “broken down to” $\text{U}(1)_Q$, or just $\text{SU}(2)_L \times \text{U}(1)_Y \rightarrow \text{U}(1)_Q$. Another popular phrasing is to say that one $\text{SU}(2)_L \times \text{U}(1)_Y$ generator, $Q \equiv T_3 + Y$, was not “broken”; therefore leaving $4 - 1 = 3$ Nambu-Goldstone bosons for the $4 - 1 = 3$ “broken generators”.

transformation (consistently, in the entire Lagrangian density) which sets $\Phi(x) \rightarrow \frac{1}{\sqrt{2}} \begin{pmatrix} 0 & v + h(x) \end{pmatrix}^\top$, resulting in the so-called unitary gauge. Hence, we are left with just 1 (out of 4) scalar h with physical meaning: the Higgs boson, discovered at the LHC in 2012 [36, 37].

2.2.3 Masses of the Electroweak Gauge Bosons and the Higgs Mechanism

The Higgs mechanism, in its most general form, is a mass term generation mechanism for fields that bilinearly couple to a scalar field that acquires a non-zero VEV upon the SSB of a given symmetry (discrete, global continuous or local continuous). In the particular case of SSB of a local gauge symmetry, the scalar acquiring a VEV necessarily transforms under the corresponding gauge symmetry group,¹⁰ and therefore, the respective gauge bosons are bilinearly coupled to the scalar through the minimally coupled scalar kinetic term (thus gaining mass). This is precisely what happens in the SM with the electroweak gauge bosons, which bilinearly couple to the Higgs doublet field through the minimally coupled Higgs kinetic terms

$$(D_\mu \Phi)^\dagger D^\mu \Phi = (D_\mu \langle 0 | \Phi | 0 \rangle)^\dagger D^\mu \langle 0 | \Phi | 0 \rangle + \left[(D_\mu \Phi)^\dagger D^\mu \Phi - (D_\mu \langle 0 | \Phi | 0 \rangle)^\dagger D^\mu \langle 0 | \Phi | 0 \rangle \right] \quad (2.35)$$

$$= \mathcal{L}_{\text{mass}}^{(\text{ew})\text{gauge}} + \mathcal{L}_{\text{kin}+(\text{ew})\text{int}}^{(H)} \quad (2.36)$$

The EW gauge boson mass terms are generated in the pure Higgs VEV $\langle 0 | \Phi(x) | 0 \rangle = \begin{pmatrix} 0 & v/\sqrt{2} \end{pmatrix}^\top$ contribution after EW SSB, i.e.¹¹

$$\mathcal{L}_{\text{mass}}^{(\text{ew})\text{gauge}} = (D_\mu \langle 0 | \Phi | 0 \rangle)^\dagger D^\mu \langle 0 | \Phi | 0 \rangle \quad (2.37)$$

$$= \underbrace{\frac{g_w^2 v^2}{4} W_\mu^- W^{+\mu}}_{=m_W^2} + \frac{1}{2} \left(\frac{g_w^2 v^2}{4} W_\mu^3 W^{3\mu} - \underbrace{\frac{g_w g' v^2}{2} W_\mu^3 B^\mu + \frac{g'^2 v^2}{4} B_\mu B^\mu}_{\text{mixing mass term}} \right), \quad (2.38)$$

where $\frac{1}{2}(W_\mu^1 W^{1\mu} + W_\mu^2 W^{2\mu}) = W_\mu^- W^{+\mu}$ was used. As explicitly shown, the mass of the W_μ^\pm weak charged bosons is given by $m_W = g_w v/2$. Additionally, there is a mass term where the fields W_μ^3 and B_μ mix, thus revealing they are not physical fields (associated to physical particles), since they do not satisfy the “correct” equation of motion of the massive vector field (Proca equation).¹² Hence, W_μ^3, B_μ must be a linear combination of two physical fields Z_μ, A_μ (and vice-versa), such that the mass terms no longer contain flavour mixing when expressed in terms of these fields. Adopting a matrix notation, we have

$$\mathcal{L}_{\text{mass}}^{(\text{ew})\text{gauge}} \supset \frac{1}{2} \begin{pmatrix} W_\mu^3 & B_\mu \end{pmatrix} M^2 \begin{pmatrix} W^{3\mu} \\ B^\mu \end{pmatrix}, \quad \text{with} \quad M^2 = \begin{pmatrix} \frac{g_w^2 v^2}{4} & -\frac{g_w g' v^2}{4} \\ -\frac{g_w g' v^2}{4} & \frac{g'^2 v^2}{4} \end{pmatrix}. \quad (2.39)$$

The symmetric non-diagonal squared-mass matrix $M^2 \in \mathbb{R}^{2 \times 2}$ can be diagonalized by a single matrix $U \in \mathbb{R}^{2 \times 2}$, so that $U^{-1} M^2 U = \text{diag}(m_Z^2, m_A^2) \equiv \mathcal{D}^2$ is diagonal with real positive elements. Solving $(M^2 - m^2 \mathbb{1})\vec{v} = 0$ yields two non-degenerate eigenvalues $m_Z^2 = (g_w^2 + g'^2)v^2/4$ and $m_A^2 = 0$. The two

¹⁰The scalar acquiring a VEV must transform under a given group for the symmetry with respect to that group to be spontaneously broken (otherwise, the vacuum would still be invariant under transformations of that group)!

¹¹For didactic purposes, we use the covariant derivative (2.8) with the “original” gauge bosons $W_\mu^i(x), B_\mu(x)$ which correspond to the T_i, Y generators, respectively; instead of its Glashow-Weinberg-Salam parametrization (2.12) with the physical gauge bosons $W_\mu^\pm(x), Z_\mu(x), A_\mu(x)$.

¹²These fields do not have well-defined masses, and in the absence of interactions, do not propagate as free independent particles (i.e., as eigenstates of the free Hamiltonian).

respective eigenvectors $\vec{v}_Z = (g_w^2 + g'^2)^{-1/2} \begin{pmatrix} g_w & -g' \end{pmatrix}^\top$ and $\vec{v}_A = (g_w^2 + g'^2)^{-1/2} \begin{pmatrix} +g' & g_w \end{pmatrix}^\top$ form an orthonormal basis of the flavour space, so that

$$U = \frac{1}{\sqrt{g_w^2 + g'^2}} \begin{pmatrix} g_w & +g' \\ -g' & g_w \end{pmatrix} = \begin{pmatrix} \cos \theta_w & +\sin \theta_w \\ -\sin \theta_w & \cos \theta_w \end{pmatrix} \in \text{SO}(2), \quad \begin{cases} \cos \theta_w = \frac{g_w}{\sqrt{g_w^2 + g'^2}} \\ \sin \theta_w = \frac{g'}{\sqrt{g_w^2 + g'^2}} \end{cases} \quad (2.40)$$

($\Rightarrow \tan \theta_w = g'/g_w$), and the mass terms (2.39) written in this basis are given by

$$\begin{aligned} \mathcal{L}_{\text{mass}}^{(\text{ew})\text{gauge}} &\supset \frac{1}{2} \begin{pmatrix} W_\mu^3 & B_\mu \end{pmatrix} M^2 \begin{pmatrix} W^{3\mu} \\ B^\mu \end{pmatrix} = \frac{1}{2} \begin{pmatrix} W_\mu^3 & B_\mu \end{pmatrix} U(\theta_w) U^\top(\theta_w) M^2 U(\theta_w) U^\top(\theta_w) \begin{pmatrix} W^{3\mu} \\ B^\mu \end{pmatrix} \\ &= \frac{1}{2} \begin{pmatrix} Z_\mu & A_\mu \end{pmatrix} \mathcal{D}^2 \begin{pmatrix} Z^\mu \\ A^\mu \end{pmatrix} = \frac{1}{2} \frac{g_w^2 + g'^2}{4} v^2 Z_\mu Z^\mu + \frac{1}{2} \times 0^2 \times A_\mu A^\mu, \end{aligned} \quad (2.41)$$

where the physical gauge bosons are given by $\begin{pmatrix} Z_\mu & A_\mu \end{pmatrix}^\top = U^\top(\theta_w) \begin{pmatrix} W_\mu^3 & B_\mu \end{pmatrix}^\top$, where Z_μ is the weak neutral Z boson field and A_μ is the electromagnetic A boson (i.e., the photon γ) field. These results would be directly obtained by using the Glashow-Weinberg-Salam parametrization (2.12), but we have now seen how this parametrization is not arbitrary, but rather necessary for obtaining the physical EW gauge bosons! The only missing relation is $e = g' \cos \theta_w = g_w \sin \theta_w = g_w g' / \sqrt{g_w^2 + g'^2}$, which is readily obtained by inserting the previous relations in the covariant derivative. In summary, the EW gauge boson mass terms (2.38) are

$$\mathcal{L}_{\text{mass}}^{(\text{ew})\text{gauge}} = m_W^2 W_\mu^- W^{+\mu} + \frac{1}{2} m_Z^2 Z_\mu Z^\mu + \frac{1}{2} m_A^2 A_\mu A^\mu, \quad \begin{cases} m_W = \frac{g_w v}{2} \\ m_Z = \frac{\sqrt{g_w^2 + g'^2}}{2} v = \frac{g_w v}{2 \cos \theta_w} \\ m_A = 0 \end{cases} \quad (2.42)$$

As expected, no mass term is generated for the gauge boson of the unbroken (residual) symmetry $U(1)_Q \subset \text{SU}(2)_L \times U(1)_Y$, since it does not couple to the electrically neutral lower component (the one which acquired the VEV) of the Higgs doublet.

2.2.4 Higgs Interactions with the Electroweak Gauge Bosons

Finally, the Higgs kinetic and interaction terms with the $\text{SU}(2)_L \times U(1)_Y$ gauge bosons are given by all remaining terms in $(D_\mu \Phi)^\dagger D^\mu \Phi$ that are not EW gauge boson mass terms, i.e.

$$\mathcal{L}_{\text{kin}+(\text{ew})\text{int}}^{(H)} = (D_\mu \Phi)^\dagger D^\mu \Phi - \mathcal{L}_{\text{mass}}^{(\text{ew})\text{gauge}} = (D_\mu \Phi)^\dagger D^\mu \Phi - (D_\mu \langle 0 | \Phi | 0 \rangle)^\dagger D^\mu \langle 0 | \Phi | 0 \rangle \quad (2.43)$$

$$\begin{aligned} &= \frac{1}{2} (\partial_\mu h) \partial^\mu h + \frac{1}{2} (\partial_\mu G^0) \partial^\mu G^0 + (\partial_\mu G^-) \partial^\mu G^+ \\ &\quad - m_Z Z_\mu \partial^\mu G^0 + m_W (i W_\mu^+ \partial^\mu G^- + \text{h.c.}) \end{aligned} \quad (2.44)$$

$$\begin{aligned} &+ \frac{g_w m_Z}{2 \cos \theta_w} Z_\mu Z^\mu h + g_w m_W W_\mu^- W^{+\mu} h \\ &+ e m_W A^\mu (W_\mu^+ G^- + \text{h.c.}) - g_w m_Z \sin^2 \theta_w Z^\mu (W_\mu^+ G^- + \text{h.c.}) \\ &- \frac{g_w}{2 \cos \theta_w} Z^\mu h \overleftrightarrow{\partial}_\mu G^0 - i e A^\mu G^- \overleftrightarrow{\partial}_\mu G^+ - i \frac{g_w \cos(2\theta_w)}{2 \cos \theta_w} Z^\mu G^- \overleftrightarrow{\partial}_\mu G^+ \\ &+ \frac{g_w}{2} [i W^{+\mu} (h \overleftrightarrow{\partial}_\mu G^-) + \text{h.c.}] - \frac{g_w}{2} [W^{+\mu} (G^0 \overleftrightarrow{\partial}_\mu G^-) + \text{h.c.}] \end{aligned} \quad (2.45)$$

$$\begin{aligned}
 & + \frac{g_w^2}{8 \cos^2 \theta_w} Z_\mu Z^\mu h^2 + \frac{g_w^2}{4} W_\mu^- W^{+\mu} h^2 + \frac{g_w^2}{8 \cos^2 \theta_w} Z_\mu Z^\mu G^{02} + \frac{g_w^2}{4} W_\mu^- W^{+\mu} G^{02} \\
 & + e^2 A_\mu A^\mu G^- G^+ + \frac{g_w^2 (1 - \tan^2 \theta_w)}{4} Z_\mu Z^\mu G^- G^+ + \frac{g_w^2}{2} W_\mu^- W^{+\mu} G^- G^+ \\
 & + \frac{eg_w \cos(2\theta_w)}{\cos \theta_w} A_\mu Z^\mu G^- G^+ + \frac{eg_w}{2} A^\mu (W_\mu^+ G^- + \text{h.c.}) h + \frac{eg_w}{2} A^\mu (iW_\mu^+ G^- + \text{h.c.}) G^0 \\
 & - \frac{g_w^2 \sin^2 \theta_w}{2 \cos \theta_w} Z^\mu (W_\mu^+ G^- + \text{h.c.}) h - \frac{g_w^2 \sin^2 \theta_w}{2 \cos \theta_w} Z^\mu (iW_\mu^+ G^- + \text{h.c.}) G^0, \quad (2.46)
 \end{aligned}$$

where $\overleftrightarrow{\partial}_\mu \equiv \overrightarrow{\partial}_\mu - \overleftarrow{\partial}_\mu$. The two flavour mixing kinetic terms (2.44) have no physical meaning, since the would-be Goldstone bosons $G^0(x)$, $G^\pm(x)$ do not correspond to physical particles. Hence, they can be “gauged away” (unitary gauge), and the same applies to all 3-linear (2.44)–(2.45) and 4-linear (2.45)–(2.46) interaction terms containing these would-be Goldstone bosons. As expected, the gauge boson $A_\mu(x)$ of the unbroken (residual) symmetry $U(1)_Q$ does not couple to the electrically neutral Higgs boson $h(x)$ (or to $G^0(x)$).

2.3 The Yukawa Sector

As already stated, fermion mass terms $\psi = -m\bar{\psi}\psi = -m(\bar{\psi}_L\psi_R + \text{h.c.})$ explicitly break $SU(2)_L \times U(1)_Y$ invariance, since left-handed and right-handed components transform under different representations of the symmetry group. This can be shown by taking $\psi_L \equiv \Psi_{I_3^w L}$ as the $I_3^w \equiv I_{w3}^{(\psi_L)}$ component of an $SU(2)_L \times U(1)_Y$ fermion doublet $\Psi_L = \begin{pmatrix} \psi_{(+L)} & \psi_{(-L)} \end{pmatrix}^\top \sim (\mathbf{2}, Y^{(\Psi_L)})$, so that

$$\bar{\psi}_R \psi_L \equiv \bar{\psi}_R \Psi_{I_3^w L} \rightarrow \bar{\psi}'_R \psi'_L \equiv \bar{\psi}'_R \Psi'_{I_3^w L} = \bar{\psi}_R e^{+iY^{(\psi_R)}\theta} e^{-iY^{(\psi_L)}\theta} \sum_{I'=\pm} U_{I_3^w I'}(\vec{\alpha}) \Psi_{I' L} \quad (2.47)$$

$$= \bar{\psi}_R e^{+iI_3^w \theta} \sum_{I'=\pm} U_{I_3^w I'}(\vec{\alpha}) \Psi_{I' L} \neq \bar{\psi}_R \Psi_{I_3^w L}, \quad (2.48)$$

with $U(\vec{\alpha}) = e^{-i \sum_i \alpha^i T_i}$, and thus $-m(\bar{\psi}_L \psi_R + \text{h.c.}) \rightarrow -m(\bar{\psi}'_L \psi'_R + \text{h.c.}) \neq -m(\bar{\psi}_L \psi_R + \text{h.c.})$ is not invariant under both local and (also) global $SU(2)_L \times U(1)_Y$ transformations.

However, we have not yet introduced all gauge invariant and renormalizable terms of our theory (as one must, in a gauge theory). Since $[\bar{\psi}\phi\psi] = [m]^4$, any $SU(2)_L \times U(1)_Y$ gauge invariant terms of this form allow fermion fields to bilinearly couple to the Higgs doublet field, thereby generating fermion mass terms through the Higgs mechanism after EW SSB. Such terms indeed exist, and are described by the Yukawa Lagrangian density¹³

$$\begin{aligned}
 \mathcal{L}_{\text{Yuk}} &= - \sum_{\alpha, \beta} Y_{\alpha\beta}^{(\ell)} \bar{L}_{\alpha L} \Phi \ell_{\beta R} - \sum_{\alpha, \beta} Y_{\alpha\beta}^{(u)} \bar{Q}_{\alpha L} \tilde{\Phi} u_{\beta R} - \sum_{\alpha, \beta} Y_{\alpha\beta}^{(d)} \bar{Q}_{\alpha L} \Phi d_{\beta R} + \text{h.c.} \\
 &= \mathcal{L}_{\text{mass}}^{(f)} + \mathcal{L}_{\text{int}}^{(\text{Yuk})}, \quad (2.49)
 \end{aligned}$$

where

$$\tilde{\Phi}(x) \equiv i\sigma_2 \Phi^*(x) = \begin{pmatrix} \phi^{0*}(x) \\ -G^-(x) \end{pmatrix} = \begin{pmatrix} \frac{v+h(x)-iG^0(x)}{\sqrt{2}} \\ -G^-(x) \end{pmatrix} \sim (\mathbf{2}, -1/2) \quad (2.50)$$

is an $SU(2)_L$ doublet field with the opposite $U(1)_Y$ hypercharge to that of the Higgs doublet, and the

¹³We do not consider the missing invariant terms $-\sum_{\alpha, \beta} Y_{\alpha\beta}^{(\nu)} \bar{L}_{\alpha L} \tilde{\Phi} \nu_{\beta R} + \text{h.c.}$, since for $Y_{\alpha\beta}^{(\nu)} \neq 0$, they lead to (Dirac) neutrino mass terms. Neutrinos are massless in the SM.

coupling constants $Y_{\alpha\beta}^{(l,u,d)}$ are components of arbitrary 3×3 complex matrices of flavour (or generation/family) space, without any constraint from gauge (or any other) symmetry.

The fermion mass terms are generated by the Higgs VEV $\langle 0 | \Phi(x) | 0 \rangle = \begin{pmatrix} 0 & v/\sqrt{2} \end{pmatrix}^\top$ after SSB,

$$\begin{aligned} \mathcal{L}_{\text{mass}}^{(f)} &= - \sum_{\alpha,\beta} Y_{\alpha\beta}^{(\ell)} \overline{L_{\alpha L}} \langle 0 | \Phi | 0 \rangle \ell_{\beta R} - \sum_{\alpha,\beta} Y_{\alpha\beta}^{(u)} \overline{Q_{\alpha L}} \langle 0 | \tilde{\Phi} | 0 \rangle u_{\beta R} - \sum_{\alpha,\beta} Y_{\alpha\beta}^{(d)} \overline{Q_{\alpha L}} \langle 0 | \Phi | 0 \rangle d_{\beta R} + \text{h.c.} \\ &= - \frac{v}{\sqrt{2}} \sum_{\alpha,\beta} \overline{\ell_{\alpha L}} Y_{\alpha\beta}^{(\ell)} \ell_{\beta R} - \frac{v}{\sqrt{2}} \sum_{\alpha,\beta} \overline{u_{\alpha L}} Y_{\alpha\beta}^{(u)} u_{\beta R} - \frac{v}{\sqrt{2}} \sum_{\alpha,\beta} \overline{d_{\alpha L}} Y_{\alpha\beta}^{(d)} d_{\beta R} + \text{h.c.} \\ &= - \sum_{\alpha,\beta} \overline{\ell_{\alpha L}} M_{\alpha\beta}^{(\ell)} \ell_{\beta R} - \sum_{\alpha,\beta} \overline{u_{\alpha L}} M_{\alpha\beta}^{(u)} u_{\beta R} - \sum_{\alpha,\beta} \overline{d_{\alpha L}} M_{\alpha\beta}^{(d)} d_{\beta R} + \text{h.c.}, \end{aligned} \quad (2.51)$$

with $M_{\alpha\beta}^{(\ell,u,d)} = \frac{v}{\sqrt{2}} Y_{\alpha\beta}^{(\ell,u,d)}$, and the Yukawa interaction terms come from the contribution of the Higgs doublet field around the VEV, $\Phi(x) - \langle 0 | \Phi(x) | 0 \rangle = \begin{pmatrix} G^+(x) & (h(x) + iG^0(x))/\sqrt{2} \end{pmatrix}^\top$,

$$\begin{aligned} \mathcal{L}_{\text{int}}^{(\text{Yuk})} &= - \sum_{\alpha,\beta} \frac{Y_{\alpha\beta}^{(\ell)}}{\sqrt{2}} h \overline{\ell_{\alpha L}} \ell_{\beta R} - \sum_{\alpha,\beta} \frac{Y_{\alpha\beta}^{(u)}}{\sqrt{2}} h \overline{u_{\alpha L}} u_{\beta R} - \sum_{\alpha,\beta} \frac{Y_{\alpha\beta}^{(d)}}{\sqrt{2}} h \overline{d_{\alpha L}} d_{\beta R} \\ &\quad - i \sum_{\alpha,\beta} \frac{Y_{\alpha\beta}^{(\ell)}}{\sqrt{2}} G^0 \overline{\ell_{\alpha L}} \ell_{\beta R} + i \sum_{\alpha,\beta} \frac{Y_{\alpha\beta}^{(u)}}{\sqrt{2}} G^0 \overline{u_{\alpha L}} u_{\beta R} - i \sum_{\alpha,\beta} \frac{Y_{\alpha\beta}^{(d)}}{\sqrt{2}} G^0 \overline{d_{\alpha L}} d_{\beta R} \\ &\quad - \sum_{\alpha,\beta} Y_{\alpha\beta}^{(\ell)} G^+ \overline{\nu_{\alpha L}} \ell_{\beta R} + \sum_{\alpha,\beta} Y_{\alpha\beta}^{(u)} G^- \overline{d_{\alpha L}} u_{\beta R} - \sum_{\alpha,\beta} Y_{\alpha\beta}^{(d)} G^+ \overline{u_{\alpha L}} d_{\beta R} + \text{h.c.}, \end{aligned} \quad (2.52)$$

where the last six terms (and respective h.c.) can be “gauged away” into the unitary gauge, since the would-be Goldstone bosons $G^0(x)$, $G^\pm(x)$ do not correspond to physical particles.

2.3.1 Flavour Space Rotations: Weak and Mass Eigenstates

From now on, rather than carrying the generation/family indices α, β throughout our derivations, we will adopt the more convenient matrix notation, since

$$\nu_{\alpha L,R} = \begin{pmatrix} \nu_{eL,R} \\ \nu_{\mu L,R} \\ \nu_{\tau L,R} \end{pmatrix}_\alpha, \quad \ell_{\alpha L,R} = \begin{pmatrix} e_{L,R} \\ \mu_{L,R} \\ \tau_{L,R} \end{pmatrix}_\alpha, \quad u_{\alpha L,R} = \begin{pmatrix} u_{L,R} \\ c_{L,R} \\ t_{L,R} \end{pmatrix}_\alpha, \quad d_{\alpha L,R} = \begin{pmatrix} d_{L,R} \\ s_{L,R} \\ b_{L,R} \end{pmatrix}_\alpha \quad (2.53)$$

can be expressed in terms of 3-dimensional vectors of the flavour (or generation/family) space.

Since the mass matrices in Eq. (2.51) are not constrained by gauge symmetry (i.e., are arbitrary), they are (in general, for $M^{(l,u,d)} \neq \mathbb{1}_{3 \times 3}$) non-diagonal, thus leading to flavour mixing mass terms. These mixing fermion fields are not physical (i.e., associated to particles), and shall be denoted with a $^{(w)}$ superscript from now on (explanation below).

Being square matrices, $M^{(\ell,u,d)} \in \mathbb{C}^{3 \times 3}$ can each be bi-diagonalized by two unitary matrices $V_L^{(\ell,u,d)}$ and $V_R^{(\ell,u,d)}$, so that

$$V_L^{(\ell)\dagger} M^{(\ell)} V_R^{(\ell)} = \text{diag}(m_e, m_\mu, m_\tau) \equiv \mathcal{D}^{(\ell)} \quad (2.54)$$

$$V_L^{(u)\dagger} M^{(u)} V_R^{(u)} = \text{diag}(m_u, m_c, m_t) \equiv \mathcal{D}^{(u)} \quad (2.55)$$

$$V_L^{(d)\dagger} M^{(d)} V_R^{(d)} = \text{diag}(m_d, m_s, m_b) \equiv \mathcal{D}^{(d)} \quad (2.56)$$

are diagonal matrices with real positive elements. Thus, the fermion mass terms (2.51) can be written as

$$\mathcal{L}_{\text{mass}}^{(f)} = -\overline{\ell_L^{(w)}} M^{(\ell)} \ell_R^{(w)} - \overline{u_L^{(w)}} M^{(u)} u_R^{(w)} - \overline{d_L^{(w)}} M^{(d)} d_R^{(w)} + \text{h.c.} \quad (2.57)$$

$$\begin{aligned} &= -\overline{\ell_L^{(w)}} V_L^{(\ell)} V_L^{(\ell)\dagger} M^{(\ell)} V_R^{(\ell)} V_R^{(\ell)\dagger} \ell_R^{(w)} - \overline{u_L^{(w)}} V_L^{(u)} V_L^{(u)\dagger} M^{(u)} V_R^{(u)} V_R^{(u)\dagger} u_R^{(w)} \\ &\quad - \overline{d_L^{(w)}} V_L^{(d)} V_L^{(d)\dagger} M^{(d)} V_R^{(d)} V_R^{(d)\dagger} d_R^{(w)} + \text{h.c.} \\ &= -\overline{\ell_L^{(m)}} \mathcal{D}^{(\ell)} \ell_R^{(m)} - \overline{u_L^{(m)}} \mathcal{D}^{(u)} u_R^{(m)} - \overline{d_L^{(m)}} \mathcal{D}^{(d)} d_R^{(m)} + \text{h.c.}, \end{aligned} \quad (2.58)$$

where

$$\ell_{L,R}^{(m)} = V_{L,R}^{(\ell)\dagger} \ell_{L,R}^{(w)}, \quad u_{L,R}^{(m)} = V_{L,R}^{(u)\dagger} u_{L,R}^{(w)}, \quad d_{L,R}^{(m)} = V_{L,R}^{(d)\dagger} d_{L,R}^{(w)}. \quad (2.59)$$

are the flavour space vectors in the mass eigenstate basis $^{(m)}$ – the basis in which the mass matrices are (real, positive and) diagonal ($\mathcal{D}_{\alpha\beta}^{(\Psi)} = \delta_{\alpha\beta} m_{\Psi_\alpha} \in \mathbb{R}_0^+$), thus leaving the mass terms without flavour mixing:

$$\mathcal{L}_{\text{mass}}^{(\Psi=\ell,u,d)} = -\overline{\Psi_L^{(m)}} \mathcal{D}^{(\Psi)} \Psi_R^{(m)} + \text{h.c.} = -\sum_{\alpha} \left(\overline{\Psi_{\alpha L}^{(m)}} \underbrace{\mathcal{D}_{\alpha\alpha}^{(\Psi)}}_{=m_{\Psi_\alpha}} \Psi_{\alpha R}^{(m)} + \overline{\Psi_{\alpha R}^{(m)}} \underbrace{\mathcal{D}_{\alpha\alpha}^{(\Psi)\dagger}}_{=m_{\Psi_\alpha}} \Psi_{\alpha L}^{(m)} \right) \quad (2.60)$$

$$= -\sum_{\alpha} m_{\Psi_\alpha} \left(\overline{\Psi_{\alpha L}^{(m)}} \Psi_{\alpha R}^{(m)} + \overline{\Psi_{\alpha R}^{(m)}} \Psi_{\alpha L}^{(m)} \right) = -\sum_{\alpha} m_{\Psi_\alpha} \overline{\Psi_{\alpha}^{(m)}} \Psi_{\alpha}^{(m)}, \quad (2.61)$$

$\forall \Psi_\alpha = \ell_\alpha, u_\alpha, d_\alpha$. Therefore, Eq. (2.58) gives

$$\mathcal{L}_{\text{mass}}^{(f)} = -\sum_{\alpha} m_{\ell_\alpha} \overline{\ell_\alpha^{(m)}} \ell_\alpha^{(m)} - \sum_{\alpha} m_{u_\alpha} \overline{u_\alpha^{(m)}} u_\alpha^{(m)} - \sum_{\alpha} m_{d_\alpha} \overline{d_\alpha^{(m)}} d_\alpha^{(m)}. \quad (2.62)$$

These field components of the flavour space vectors in the mass eigenstate basis are the physical fields (associated to particles), and particle physicists simply call them “mass eigenstates”.

Prior to this change of basis (or rotation) in flavour space, we were working in the (weak) interaction eigenstate basis $^{(w)}$, where there was no fermion generation mixing in the interaction terms (2.14) with the EW gauge bosons. The field components of the flavour space vectors in the interaction eigenstate basis are referred to as “interaction eigenstates”. The question now is what happens to the fermion interaction terms (2.14) when written in terms of the physical fields (i.e., in the mass basis).

2.3.2 Lepton Masses and Mixing

As we have just seen in Eqs. (2.57), (2.58), (2.62) the lepton mass terms

$$\mathcal{L}_{\text{mass}}^{(\ell)} = -\overline{\ell_L^{(w)}} M^{(\ell)} \ell_R^{(w)} + \text{h.c.} = -\overline{\ell_L^{(m)}} \mathcal{D}^{(\ell)} \ell_R^{(m)} + \text{h.c.} = -\sum_{\alpha} m_{\ell_\alpha} \overline{\ell_\alpha^{(m)}} \ell_\alpha^{(m)} \quad (2.63)$$

are diagonal in the mass eigenstate basis $\ell_{L,R}^{(m)} = V_{L,R}^{(\ell)\dagger} \ell_{L,R}^{(w)}$. The kinetic and interaction terms of the massive charged leptons in Eq. (2.14), at the time written in the weak eigenstate basis, are

$$\mathcal{L}_{\text{kin}+(\text{ew})\text{int}}^{(\ell)} = i\overline{\ell}^{(w)} \not{\partial} \ell^{(w)} - eA_\mu j_{\text{em}}^\mu[\ell] - \frac{g_w}{2\cos\theta_w} Z_\mu j_{\text{NC}(w)}^\mu[\ell] - \frac{g_w}{\sqrt{2}} \left(W_\mu^+ j_{\text{CC}(w)}^{-\mu}[\nu, \ell] + \text{h.c.} \right), \quad (2.64)$$

where the kinetic terms

$$\mathcal{L}_{\text{kin}}^{(\ell)} = i\overline{\ell}^{(w)} \gamma^\mu \partial_\mu \ell^{(w)} = i\overline{\ell_L^{(w)}} \gamma^\mu \partial_\mu \ell_L^{(w)} + i\overline{\ell_R^{(w)}} \gamma^\mu \partial_\mu \ell_R^{(w)} \quad (2.65)$$

2.3. The Yukawa Sector

$$\begin{aligned}
&= i\overline{\ell_L^{(m)}} V_L^{(\ell)\dagger} \gamma^\mu \partial_\mu V_L^{(\ell)} \ell_L^{(m)} + i\overline{\ell_R^{(m)}} V_R^{(\ell)\dagger} \gamma^\mu \partial_\mu V_R^{(\ell)} \ell_R^{(m)} \\
&= i\overline{\ell_L^{(m)}} \gamma^\mu \partial_\mu \ell_L^{(m)} + i\overline{\ell_R^{(m)}} \gamma^\mu \partial_\mu \ell_R^{(m)} = i\overline{\ell^{(m)}} \gamma^\mu \partial_\mu \ell^{(m)} ;
\end{aligned} \tag{2.66}$$

the EM interaction terms $\mathcal{L}_{\text{int}}^{(\text{QED})}[\ell, A_\mu] = -e A_\mu j_{\text{em}}^\mu[\ell]$, with

$$j_{\text{em}}^\mu[\ell] = -\overline{\ell^{(w)}} \gamma^\mu \ell^{(w)} = -\left(\overline{\ell_L^{(w)}} \gamma^\mu \ell_L^{(w)} + \overline{\ell_R^{(w)}} \gamma^\mu \ell_R^{(w)} \right) \tag{2.67}$$

$$\begin{aligned}
&= -\left(\overline{\ell_L^{(m)}} V_L^{(\ell)\dagger} \gamma^\mu V_L^{(\ell)} \ell_L^{(m)} + \overline{\ell_R^{(m)}} V_R^{(\ell)\dagger} \gamma^\mu V_R^{(\ell)} \ell_R^{(m)} \right) \\
&= -\left(\overline{\ell_L^{(m)}} \gamma^\mu \ell_L^{(m)} + \overline{\ell_R^{(m)}} \gamma^\mu \ell_R^{(m)} \right) = -\overline{\ell^{(m)}} \gamma^\mu \ell^{(m)} ;
\end{aligned} \tag{2.68}$$

and the NC weak interaction terms $\mathcal{L}_{\text{int}}^{\text{NC}(w)}[\ell, Z_\mu] = -\frac{g_w}{2\cos\theta_w} Z_\mu j_{\text{NC}(w)}^\mu[\ell]$, with

$$\begin{aligned}
j_{\text{NC}(w)}^\mu[\ell] &= \overline{\ell^{(w)}} \gamma^\mu (-P_L + 2\sin^2\theta_w) \ell^{(w)} \\
&= 2\sin^2\theta_w \left(\overline{\ell_L^{(w)}} \gamma^\mu \ell_L^{(w)} + \overline{\ell_R^{(w)}} \gamma^\mu \ell_R^{(w)} \right) - \overline{\ell_L^{(w)}} \gamma^\mu \ell_L^{(w)} \\
&= 2\sin^2\theta_w \left(\overline{\ell_L^{(m)}} V_L^{(\ell)\dagger} \gamma^\mu V_L^{(\ell)} \ell_L^{(m)} + \overline{\ell_R^{(m)}} V_R^{(\ell)\dagger} \gamma^\mu V_R^{(\ell)} \ell_R^{(m)} \right) - \overline{\ell_L^{(m)}} V_L^{(\ell)\dagger} \gamma^\mu V_L^{(\ell)} \ell_L^{(m)} \\
&= 2\sin^2\theta_w \left(\overline{\ell_L^{(m)}} \gamma^\mu \ell_L^{(m)} + \overline{\ell_R^{(m)}} \gamma^\mu \ell_R^{(m)} \right) - \overline{\ell_L^{(m)}} \gamma^\mu \ell_L^{(m)} \\
&= \overline{\ell^{(m)}} \gamma^\mu (-P_L + 2\sin^2\theta_w) \ell^{(m)}
\end{aligned} \tag{2.69}$$

remain diagonal (without flavour mixing) in the mass eigenstate basis. Conversely, the CC weak interaction terms $\mathcal{L}_{\text{int}}^{\text{CC}(w)}[\nu, \ell, W_\mu^\pm] = -\frac{g_w}{\sqrt{2}} \left(W_\mu^- j_{\text{CC}(w)}^{+\mu}[\nu, \ell] + \text{h.c.} \right)$, with

$$j_{\text{CC}(w)}^{+\mu}[\nu, \ell] = \overline{\ell^{(w)}} \gamma^\mu P_L \nu = \overline{\ell_L^{(w)}} \gamma^\mu \nu_L = \overline{\ell_L^{(m)}} V_L^{(\ell)\dagger} \gamma^\mu \nu_L \tag{2.71}$$

are non-diagonal in the mass eigenstate basis – there is flavour mixing. Notice, however, that neutrinos are *massless* in the SM, and therefore neutrino fields can be arbitrarily rotated!¹⁴ Redefining the physical neutrinos as

$$\nu_L' = V_L^{(\ell)\dagger} \nu_L \quad \Leftrightarrow \quad \nu_L = V_L^{(\ell)} \nu_L', \tag{2.72}$$

the lepton weak charged current (2.71) is given by

$$j_{\text{CC}(w)}^{+\mu}[\nu, \ell] = \overline{\ell_L^{(m)}} \gamma^\mu \nu_L' = \overline{\ell^{(m)}} \gamma^\mu P_L \nu', \tag{2.73}$$

and the CC weak interaction terms also remain diagonal in the mass eigenstate basis.

All lepton (both kinetic and EW interaction) terms $\mathcal{L}_{\text{kin}+(\text{ew})\text{int}}^{(\ell)}$ in Eq. (2.14) are diagonal (without flavour mixing) in the mass eigenstate basis. Therefore, in the SM, the lepton mass eigenstates *necessarily* correspond to weak gauge eigenstates – there is no need to distinguish between them, and we shall drop the $^{(m)}$ superscript from now on.

It is worth reminding that this happens because the SM considers neutrinos to be massless, allowing for the neutrino flavour rotations (2.72) that are responsible for the diagonalization of the lepton

¹⁴This is because neutrino fields only appear in kinetic and NC interaction terms, which are invariant under flavour space rotations. Neutrino mass terms (like any other fermion mass term) would not be invariant, but they do not exist in the SM!

weak charged current in Eq. (2.73). However, the discovery of neutrino flavour oscillations (between weak eigenstates) showed that neutrinos are in fact massive, with mass eigenstates $\nu_L^{(m)} = U_{\text{PMNS}}^\dagger \nu_L^{(w)}$ ($U_{\text{PMNS}} \neq \mathbb{1}$ is the lepton mixing matrix) that do not correspond to weak eigenstates (more details in Section 3.1)

2.3.3 Quark Masses, Mixing and the CKM Matrix

As we have just seen in Eqs. (2.57), (2.58), (2.62) the quark mass terms

$$\mathcal{L}_{\text{mass}}^{(q)} = -\overline{u_L^{(w)}} M^{(u)} u_R^{(w)} - \overline{d_L^{(w)}} M^{(d)} d_R^{(w)} + \text{h.c.} = -\overline{u_L^{(m)}} \mathcal{D}^{(u)} u_R^{(m)} - \overline{d_L^{(m)}} \mathcal{D}^{(d)} d_R^{(m)} + \text{h.c.} \quad (2.74)$$

$$= -\sum_{\alpha} m_{u_{\alpha}} \overline{u_{\alpha}^{(m)}} u_{\alpha}^{(m)} - \sum_{\alpha} m_{d_{\alpha}} \overline{d_{\alpha}^{(m)}} d_{\alpha}^{(m)} \quad (2.75)$$

are diagonal in the mass eigenstate basis $u_{L,R}^{(m)} = V_{L,R}^{(u)\dagger} u_{L,R}^{(w)}$, $d_{L,R}^{(m)} = V_{L,R}^{(d)\dagger} d_{L,R}^{(w)}$. The kinetic and interaction terms of the quarks in Eq. (2.14), at the time written in the weak eigenstate basis, are

$$\begin{aligned} \mathcal{L}_{\text{kin}+(\text{ew})\text{int}}^{(q)} &= i\overline{u^{(w)}} \not{\partial} u^{(w)} + i\overline{d^{(w)}} \not{\partial} d^{(w)} - eA_{\mu} (j_{\text{em}}^{\mu}[u] + j_{\text{em}}^{\mu}[d]) \\ &\quad - \frac{g_w}{2\cos\theta_w} Z_{\mu} (j_{\text{NC}(w)}^{\mu}[u] + j_{\text{NC}(w)}^{\mu}[d]) - \frac{g_w}{\sqrt{2}} (W_{\mu}^{+} j_{\text{CC}(w)}^{-\mu}[u, d] + \text{h.c.}), \end{aligned} \quad (2.76)$$

where, performing the analogous computations that we did for the leptons in the previous section (now leaving them as exercise), the kinetic terms

$$\mathcal{L}_{\text{kin}}^{(u)} = i\overline{u^{(w)}} \gamma^{\mu} \partial_{\mu} u^{(w)} = i\overline{u^{(m)}} \gamma^{\mu} \partial_{\mu} u^{(m)}, \quad \mathcal{L}_{\text{kin}}^{(d)} = i\overline{d^{(w)}} \gamma^{\mu} \partial_{\mu} d^{(w)} = i\overline{d^{(m)}} \gamma^{\mu} \partial_{\mu} d^{(m)}; \quad (2.77)$$

the EM interaction terms $\mathcal{L}_{\text{int}}^{(\text{QED})}[u, d, A_{\mu}] = -eA_{\mu} (j_{\text{em}}^{\mu}[u] + j_{\text{em}}^{\mu}[d])$, with

$$j_{\text{em}}^{\mu}[u] = +\frac{2}{3}\overline{u^{(w)}} \gamma^{\mu} u^{(w)} = +\frac{2}{3}\overline{u^{(m)}} \gamma^{\mu} u^{(m)}, \quad j_{\text{em}}^{\mu}[d] = -\frac{1}{3}\overline{d^{(w)}} \gamma^{\mu} d^{(w)} = -\frac{1}{3}\overline{d^{(m)}} \gamma^{\mu} d^{(m)}; \quad (2.78)$$

and the NC weak interaction terms $\mathcal{L}_{\text{int}}^{\text{NC}(w)}[u, d, Z_{\mu}] = -\frac{g_w}{2\cos\theta_w} Z_{\mu} (j_{\text{NC}(w)}^{\mu}[u] + j_{\text{NC}(w)}^{\mu}[d])$, with

$$j_{\text{NC}(w)}^{\mu}[u] = \overline{u^{(w)}} \gamma^{\mu} \left(P_L - \frac{4}{3} \sin^2 \theta_w \right) u^{(w)} = \overline{u^{(m)}} \gamma^{\mu} \left(P_L - \frac{4}{3} \sin^2 \theta_w \right) u^{(m)}, \quad (2.79)$$

$$j_{\text{NC}(w)}^{\mu}[d] = \overline{d^{(w)}} \gamma^{\mu} \left(-P_L + \frac{2}{3} \sin^2 \theta_w \right) d^{(w)} = \overline{d^{(m)}} \gamma^{\mu} \left(-P_L + \frac{2}{3} \sin^2 \theta_w \right) d^{(m)} \quad (2.80)$$

remain diagonal (without flavour mixing) in the mass eigenstate basis. Conversely, the CC weak interaction terms $\mathcal{L}_{\text{int}}^{\text{CC}(w)}[u, d, W_{\mu}^{\pm}] = -\frac{g_w}{\sqrt{2}} (W_{\mu}^{+} j_{\text{CC}(w)}^{-\mu}[u, d] + \text{h.c.})$, with

$$j_{\text{CC}(w)}^{-\mu}[u, d] = \overline{u^{(w)}} \gamma^{\mu} P_L d^{(w)} = \overline{u_L^{(w)}} \gamma^{\mu} d_L^{(w)} = \overline{u_L^{(m)}} V_L^{(u)\dagger} \gamma^{\mu} V_L^{(d)} d_L^{(m)} \quad (2.81)$$

$$= \overline{u^{(m)}} \gamma^{\mu} P_L \left[V_L^{(u)\dagger} V_L^{(d)} \right] d^{(m)} \quad (2.82)$$

are non-diagonal in the mass eigenstate basis – there is flavour mixing. Defining the so-called Cabibbo-Kobayashi-Maskawa (CKM) matrix as

$$V_{\text{CKM}} \equiv V_L^{(u)\dagger} V_L^{(d)} \quad \Leftrightarrow \quad V_{\text{CKM}}^{\dagger} \equiv V_L^{(d)\dagger} V_L^{(u)} = V_{\text{CKM}}^{-1}, \quad (2.83)$$

the quark CC weak interaction terms are given by

$$\mathcal{L}_{\text{int}}^{\text{CC}(w)}[u, d, W_\mu^\pm] = -\frac{g_w}{\sqrt{2}} \left(\underbrace{W_\mu^+ \overline{u^{(m)}} \gamma^\mu P_L V_{\text{CKM}} d^{(m)}}_{=j_{\text{CC}(w)}^\mu[u, d]} + \underbrace{W_\mu^- \overline{d^{(m)}} V_{\text{CKM}}^\dagger \gamma^\mu P_L u^{(m)}}_{=j_{\text{CC}(w)}^{+\mu}[u, d]} \right) \quad (2.84)$$

$$= -\frac{g_w}{\sqrt{2}} \sum_{\alpha, k} \left(W_\mu^+ \overline{u_\alpha^{(m)}} \gamma^\mu P_L V_{\alpha k} d_k^{(m)} + W_\mu^- \overline{d_k^{(m)}} V_{\alpha k}^* \gamma^\mu P_L u_\alpha^{(m)} \right). \quad (2.85)$$

Therefore, in the SM, the quark mass eigenstates *may not* correspond to weak gauge eigenstates. To state it precisely, it should be clear from Eq. (2.83) that $V_{\text{CKM}} = \mathbb{1} \Leftrightarrow V_L^{(u)} = V_L^{(d)}$ is necessary and sufficient condition for the mass eigenstates to correspond to weak eigenstates; and conversely, $V_{\text{CKM}} \neq \mathbb{1} \Leftrightarrow V_L^{(u)} \neq V_L^{(d)}$ is necessary and sufficient condition for the mass eigenstates to not correspond to weak eigenstates. This is something that can only be determined experimentally, since we have considered the most general mass matrices $M^{(\ell, u, d)} = \frac{v}{\sqrt{2}} Y^{(\ell, u, d)}$ for the fermion mass terms (2.51) in the weak eigenstate basis, without any particular constraint.

Experiment confirmed Nature's choice: $|(V_{\text{CKM}})_{\alpha k}| \neq \delta_{\alpha k}$, and thus, there is flavour mixing in the quark CC weak interaction. The standard convention is to define the quark mass eigenstates as $u_\alpha^{(m)} = u_\alpha^{(w)} \wedge d_k^{(m)} = \sum_\alpha (V_{\text{CKM}}^\dagger)_{k\alpha} d_\alpha^{(w)}$, which is just a convenient choice. For $n_g = 3$ generations of quarks, the CKM (complex) matrix starts with $2n_g^2$ real parameters. Unitarity and re-phasing invariance impose n_g^2 and $2n_g - 1$ constraints, respectively, leaving $2n_g^2 - n_g^2 - (2n_g - 1) = (n_g - 1)^2 = 4$ independent real parameters. A popular parametrization convention is [38]

$$V_{\text{CKM}} = \begin{pmatrix} c_{12}c_{13} & s_{12}c_{13} & s_{13}e^{-i\delta} \\ -s_{12}c_{23} - c_{12}s_{23}s_{13}e^{i\delta} & c_{12}c_{23} - s_{12}s_{23}s_{13}e^{i\delta} & s_{23}c_{13} \\ s_{12}s_{23} - c_{12}c_{23}s_{13}e^{i\delta} & -c_{12}s_{23} - s_{12}c_{23}s_{13}e^{i\delta} & c_{23}c_{13} \end{pmatrix}. \quad (2.86)$$

with $c_{ij} \equiv \cos \theta_{ij}$, $s_{ij} \equiv \sin \theta_{ij}$, and it is possible to show that invariance of the quark mixing CC weak interaction terms (2.84) under charge conjugation \times parity (CP) transformations would imply $\delta = 0$. But experimental measurements determine $\delta \neq 0$, thus showing that the quark mixing CC weak interaction is CP-violating (with phase parameter δ regulating the “amount” of CP violation).

2.3.4 Yukawa Interactions

Finally, the Yukawa interaction terms in Eq. (2.52) (at the time written in the weak basis), are now given in the mass basis by

$$\begin{aligned} \mathcal{L}_{\text{int}}^{(\text{Yuk})} &= -h \overline{\ell_L^{(m)}} \frac{\mathcal{D}^{(l)}}{v} \ell_R^{(m)} - h \overline{u_L^{(m)}} \frac{\mathcal{D}^{(u)}}{v} u_R^{(m)} - h \overline{d_L^{(m)}} \frac{\mathcal{D}^{(d)}}{v} d_R^{(m)} \\ &\quad - iG^0 \overline{\ell_L^{(m)}} \frac{\mathcal{D}^{(l)}}{v} \ell_R^{(m)} + iG^0 \overline{u_L^{(m)}} \frac{\mathcal{D}^{(u)}}{v} u_R^{(m)} - iG^0 \overline{d_L^{(m)}} \frac{\mathcal{D}^{(d)}}{v} d_R^{(m)} \\ &\quad - G^+ \overline{\nu_L^{(m)}} \frac{\sqrt{2}\mathcal{D}^{(l)}}{v} \ell_R^{(m)} + G^- \overline{d_L^{(m)}} V_{\text{CKM}}^\dagger \frac{\sqrt{2}\mathcal{D}^{(u)}}{v} u_R^{(m)} - G^+ \overline{u_L^{(m)}} \frac{\sqrt{2}\mathcal{D}^{(d)}}{v} V_{\text{CKM}} d_R^{(m)} + \text{h.c.} \\ &= -\sum_\alpha \frac{m_{\ell_\alpha}}{v} h \overline{\ell_\alpha^{(m)}} \ell_\alpha^{(m)} - \sum_\alpha \frac{m_{u_\alpha}}{v} h \overline{u_\alpha^{(m)}} u_\alpha^{(m)} - \sum_\alpha \frac{m_{d_\alpha}}{v} h \overline{d_\alpha^{(m)}} d_\alpha^{(m)} \\ &\quad - i \sum_\alpha \frac{m_{\ell_\alpha}}{v} G^0 \overline{\ell_\alpha^{(m)}} \gamma^5 \ell_\alpha^{(m)} + i \sum_\alpha \frac{m_{u_\alpha}}{v} G^0 \overline{u_\alpha^{(m)}} \gamma^5 u_\alpha^{(m)} - i \sum_\alpha \frac{m_{d_\alpha}}{v} G^0 \overline{d_\alpha^{(m)}} \gamma^5 d_\alpha^{(m)} \end{aligned}$$

$$\begin{aligned}
 & - \sum_{\alpha} \frac{\sqrt{2}m_{\ell_{\alpha}}}{v} \left(G^{+} \overline{\nu'_{\alpha}} P_R \ell_{\alpha}^{(m)} + G^{-} \overline{\ell_{\alpha}^{(m)}} P_L \nu'_{\alpha} \right) \\
 & + \sum_{\alpha,k} \frac{\sqrt{2}m_{u_{\alpha}}}{v} \left(G^{-} \overline{d_k^{(m)}} V_{\alpha k}^{*} P_R u_{\alpha}^{(m)} + G^{+} \overline{u_{\alpha}^{(m)}} P_L V_{\alpha k} d_k^{(m)} \right) \\
 & - \sum_{\alpha,k} \frac{\sqrt{2}m_{d_k}}{v} \left(G^{+} \overline{u_{\alpha}^{(m)}} P_R V_{\alpha k} d_k^{(m)} + G^{-} \overline{d_k^{(m)}} V_{\alpha k}^{*} P_L u_{\alpha}^{(m)} \right), \tag{2.87}
 \end{aligned}$$

where the last six terms (and respective h.c.) can be “gauged away” into the unitary gauge, as the would-be Goldstone bosons G^0 , G^{\pm} do not correspond to physical particles. The remaining first three terms can be written in a compact form: $\sum_{\psi} \mathcal{L}_{\text{int}}^{(\text{Yuk})}[h, \psi] = \sum_{\psi} -\frac{m_{\psi}}{v} h \bar{\psi} \psi$.

2.4 Strong Interaction from $\text{SU}(3)_c$ Gauge Symmetry

The strong interaction arises from imposing an additional (and independent) local $\text{SU}(3)_c$ (or colour) gauge symmetry, thus completing the $\text{SU}(3)_c \times \text{SU}(2)_L \times \text{U}(1)_Y$ gauge symmetry group of the SM. Quark fields $q = u_{\alpha}, d_{\alpha}$ are colour triplets, thus transforming under the fundamental **3** representation of $\text{SU}(3)_c$, so that $q \rightarrow q' = e^{-i \sum_{a=1}^8 \vartheta^a T_a^s} q$ with $T_a^s \mapsto \lambda_a/2$ (Gell-Mann 3×3 matrices). The remaining (so far introduced) SM fields are $\text{SU}(3)_c$ singlets, thus transforming trivially under this colour group. The local symmetry is obtained through the usual minimal coupling procedure $\partial_{\mu} \hookrightarrow D_{\mu}$, which can be performed with the $\text{SU}(3)_c$ covariant derivative

$$D_{\mu} = \partial_{\mu} + i g_s \sum_{a=1}^8 T_a^s G_{\mu}^a \tag{2.88}$$

in the quark kinetic terms, where g_s is the strong coupling constant and $G_{\mu}^a(x)$ are the gluon fields (the $\text{SU}(3)_c$ gauge bosons), components $a = 1, \dots, 8$ of a vector $\begin{pmatrix} G_{\mu}^1 & \dots & G_{\mu}^8 \end{pmatrix}^{\top}$ which transforms under the adjoint **8** representation of $\text{SU}(3)_c$, so that $G_{\mu}^a \rightarrow G_{\mu}^{\prime a} = G_{\mu}^a + \sum_{b,c=1}^8 f_{abc} \vartheta^b G_{\mu}^c + \partial_{\mu} \vartheta^a / g_s$. Alternatively, we could have directly imposed the full $\text{SU}(3)_c \times \text{SU}(2)_L \times \text{U}(1)_Y$ local symmetry in the fermion kinetic terms (2.7) via the SM gauge symmetry group covariant derivative

$$\begin{aligned}
 D_{\mu} &= \partial_{\mu} + i g_s \sum_{a=1}^8 T_a^s G_{\mu}^a + i g_w \sum_{i=1}^3 T_i W_{\mu}^i + i g' Y B_{\mu} \\
 &= \partial_{\mu} + i e Q A_{\mu} + i \frac{g_w}{\cos \theta_w} (T_3 - Q \sin^2 \theta_w) Z_{\mu} + i g_w (T^{+} W_{\mu}^{+} + T^{-} W_{\mu}^{-}) + i g_s \sum_{a=1}^8 T_a^s G_{\mu}^a.
 \end{aligned} \tag{2.89}$$

Either way, the emergent strong interaction terms are given by¹⁵

$$\mathcal{L}_{\text{int}}^{(\text{QCD})} = \sum_q -g_s \sum_{a=1}^8 G_{\mu}^a \bar{q} \gamma^{\mu} \frac{\lambda_a}{2} q = \sum_q -g_s \sum_{j,k=1}^3 \sum_{a=1}^8 G_{\mu}^a \bar{q}_j \gamma^{\mu} \frac{(\lambda_a)_{jk}}{2} q_k, \tag{2.90}$$

where $j, k = 1, 2, 3$ are colour indices. Additionally, the gluons G_{μ}^a are not external/auxiliary, but rather dynamical fields, thus requiring kinetic terms. The missing $\text{SU}(3)_c$ gauge invariant and renormalizable

¹⁵These interaction terms are (obviously) invariant under changes of basis (or rotations) in flavour space, thus taking this form in both interaction and mass eigenstate basis.

terms are the usual “pure gauge” terms of any gauge theory, containing both kinetic and self-interaction terms of the gauge bosons,

$$\mathcal{L}_{\text{gauge}}^{\text{SU}(3)_c} = -\frac{1}{4} \sum_{a=1}^8 G_{\mu\nu}^a G^{a\mu\nu}, \quad G_{\mu\nu}^a \equiv \partial_\mu G_\nu^a - \partial_\nu G_\mu^a - g_s \sum_{b,c=1}^8 f_{abc} G_\mu^b G_\nu^c \quad (2.91)$$

$$\begin{aligned} &= -\frac{1}{2} \sum_{a=1}^8 [(\partial_\mu G_\nu^a) \partial^\mu G^{a\nu} - (\partial_\mu G_\nu^a) \partial^\nu G^{a\mu}] \\ &\quad + g_s \sum_{a,b,c=1}^8 f_{abc} (\partial^\mu G^{a\nu}) G_\mu^b G_\nu^c - \frac{g_s^2}{4} \sum_{a,b,c,d,e=1}^8 f_{abc} f_{ade} G_\mu^b G_\nu^c G^{d\mu} G^{e\nu}, \end{aligned} \quad (2.92)$$

where $f_{abc} (\neq 0, \text{ in general})$ are the structure constants of the non-Abelian Lie group $\text{SU}(3)_c$.

2.5 Lagrangian and Parameters of the Standard Model

Having completed the construction of the Standard Model from a local $\text{SU}(3)_c \times \text{SU}(2)_L \times \text{U}(1)_Y$ gauge symmetry principle, it is time to assemble all the pieces together. The Lagrangian density of the SM, expanded in the mass eigenstate basis of the physical fields (unless otherwise specified), is given by

$$\begin{aligned} \mathcal{L}_{\text{SM}} &= \overbrace{\mathcal{L}_{\text{gauge}}^{\text{SU}(2)_L \times \text{U}(1)_Y} + \mathcal{L}_{\text{gauge}}^{\text{SU}(3)_c}}^{\equiv \mathcal{L}_{\text{gauge}}} + \overbrace{\mathcal{L}_{\text{kin}+(\text{ew})\text{int}}^{(f)} + \mathcal{L}_{\text{int}}^{(\text{QCD})}}^{\equiv \mathcal{L}_{\text{kin}+\text{int}}^{(f)}} + \overbrace{\mathcal{L}_{\text{mass}}^{(\text{ew})\text{gauge}} + \mathcal{L}_{\text{kin}+(\text{ew})\text{int}}^{(H)}}^{= (D_\mu \Phi)^\dagger D^\mu \Phi \text{ (2.35)}} - V(|\Phi|) \\ &\quad + \underbrace{\mathcal{L}_{\text{mass}}^{(f)} + \mathcal{L}_{\text{int}}^{(\text{Yuk})}}_{= \mathcal{L}_{\text{Yuk}} \text{ (2.49)}}, \end{aligned} \quad (2.93)$$

where $\mathcal{L}_{\text{gauge}}^{\text{SU}(2)_L \times \text{U}(1)_Y}$ is given in Eq. (2.23); $\mathcal{L}_{\text{gauge}}^{\text{SU}(3)_c}$ is given in Eq. (2.92); $\mathcal{L}_{\text{kin}+(\text{ew})\text{int}}^{(f)}$ is given in Eq. (2.14), with the replacement of the quark CC weak interaction terms by the expression (2.85) written in the mass basis; $\mathcal{L}_{\text{int}}^{(\text{QCD})}$ is given in Eq. (2.90); $\mathcal{L}_{\text{mass}}^{(\text{ew})\text{gauge}}$ is given in Eq. (2.42); $\mathcal{L}_{\text{kin}+(\text{ew})\text{int}}^{(H)}$ is given in Eqs. (2.44)–(2.46); $V(|\Phi|)$ is given in Eq. (2.34); $\mathcal{L}_{\text{mass}}^{(f)}$ is given in Eq. (2.62); and $\mathcal{L}_{\text{int}}^{(\text{Yuk})}$ is given in Eq. (2.87).

Finally, we must count the number of free (or independent) parameters of the theory:

- Three coupling constants: e, g_w, g_s .
- Mass of the Higgs boson and electroweak VEV: m_h and v .
- Masses of the nine charged fermions: $m_e, m_\mu, m_\tau, m_u, m_d, m_c, m_s, m_t, m_b$ (massless neutrinos).
- Four independent parameters of the CKM matrix: $\theta_{12}, \theta_{23}, \theta_{31}$ and δ .

Therefore, the Standard Model has $3 + 2 + 9 + 4 = 18$ free parameters that require measurement. The remaining parameters are internal, and their dependence on the free parameters was established throughout this Chapter 2. The choice of free parameters is not unique (e.g., one can choose μ_H, λ_H as the two parameters describing the Higgs potential, instead of m_h, v), but the number of degrees of freedom (18) remains unchanged. Consult the Particle Data Group review [38] for experimental values.

It should be noted that we are considering the most conservative version of the Standard Model. There is an additional QCD term, related to the strong CP problem, that was not considered (more details in Section 3.1), and increases the number of free parameters by 1 ($18 \rightarrow 19$). Additionally, the inclusion of Dirac neutrino masses and lepton mixing (more details in Section 3.1) increases the number by $3+4=7$ ($18 \rightarrow 19 \rightarrow 26$); and Majorana neutrino masses can add an arbitrary number of extra parameters.

Chapter 3

Particle DM and the Real Scalar Singlet SM Extension

As we shall see, the Standard Model (SM) of particle physics has a few problems, or at the very least, is incomplete. Now that we have constructed the SM (and understood how to build a model in particle physics), we will dive in the area of Beyond the Standard Model (BSM) physics. Our work addresses the dark matter (DM) problem, which strictly speaking, is not a problem of the SM itself, but a physical mystery that could be solved under the framework of particle physics.

This chapter is devoted to understanding the particle physics approach to dark matter. Additionally, we motivate the investigation of the following chapters by discussing a Standard Model extension with a real scalar $SU(3)_c \times SU(2)_L \times U(1)_Y$ singlet field and an unbroken Z_2 symmetry, which represents one of the simplest DM particle models that can be constructed without breaking the SM gauge symmetry or spoiling renormalizability [11, 12, 13, 15].

There are many reviews on the subject of particle dark matter, e.g. Refs. [8, 9, 39, 40, 41]. The recent and comprehensive review by M. Cirelli et al. [10] and the lectures on *Dark Matter, Phase Transitions and Gravitational Waves* by Rui Santos [42] were the most influential to this chapter.

3.1 Problems with the Standard Model of Particle Physics

The Standard Model of particle physics is a mathematically self-consistent renormalizable quantum field theory which either predicts or agrees with almost all experimental observables. Despite its remarkable success, there are many reasons to believe that it is not a “final” fundamental theory, but rather an effective field theory that is valid up to the electroweak scale. While some of these reasons may be subjective (to the opinion of the particle physicist), others are undeniable issues that the SM has not been able to solve. We present a few of the most prominent unsolved problems.

- **Neutrino Masses:** The recent discovery of neutrino flavour oscillations implies that neutrinos have different masses, and hence, at least two of them are massive. As discussed in Section 2.3.2, neutrinos are massless in the SM, which necessarily prevents flavour mixing in the lepton charged current weak interaction. Neutrino masses opened the possibility of lepton mixing, which was confirmed by the measurement of the parameters of the lepton mixing matrix U_{PMNS} . In the mass basis, the SM correction of the lepton CC weak interaction terms is $\mathcal{L}_{\text{int}}^{\text{CC}(w)}[\nu, \ell, W_\mu^\pm] = -\frac{g_w}{\sqrt{2}} \sum_{\alpha, k} (W_\mu^- \bar{\ell}_\alpha \gamma^\mu P_L (U_{\text{PMNS}})_{\alpha k} \nu_k + \text{h.c.})$, analogously to the quark mixing case. The problem arises in the neutrino mass terms. Neutrinos are the only electrically neutral fermions, thus

allowing for the possibility of being a Majorana fermion $\nu = \nu_L + \nu_L^C \equiv \nu_L + C\bar{\nu}_L^\top$ (which is its own antiparticle), instead of the standard Dirac fermion $\nu = \nu_L + \nu_R$. Whether neutrinos are Dirac or Majorana fermions is unknown, thus preventing us to determine the neutrino mass sector with certainty. It is common practice to consider the most general neutrino mass sector, with both Dirac and Majorana neutrino mass terms. Neutrino physics is an interesting BSM area of research with many new physics applications (see textbooks [43, 44] for more details).

- **Strong CP Problem:** There is an additional $SU(3)_c$ gauge invariant term which was not previously (in Section 2.4) considered, $\frac{\theta_{\text{QCD}}}{32\pi^2} g_s^2 \frac{1}{2} \epsilon^{\mu\nu\lambda\rho} \sum_{a=1}^8 G_{\mu\nu}^a G_{\lambda\rho}^a$, that can (and should) be added to the QCD (and thus, SM) Lagrangian density. This term is not invariant under parity (P), time reversal (T) or charge conjugation \times parity (CP) transformations. Moreover, for $\theta_{\text{QCD}} \neq 0$, it induces an electric dipole moment for the neutron, which has stringent experimental limits, thus leading to an upper bound $|\theta_{\text{QCD}}| \lesssim 10^{-10}$. But why is (the magnitude of) θ_{QCD} so small? This fine-tuning problem is known as the strong CP problem (see Refs. [45, 46] for more details). A popular solution is the Peccei-Quinn mechanism [47, 48], which relies on the spontaneous breaking of a new global $U(1)_{PQ}$ symmetry, resulting in the emergence of a pseudo-Goldstone boson – a light pseudo-scalar new particle named axion [49, 50].
- **Gravity:** Gravitation is described by Einstein’s classical theory of general relativity (GR). If gravity is an interaction, can it be unified with the other (strong, weak and electromagnetic) interactions of the SM? A fundamental “final theory” should incorporate all known interactions of Nature. But is it possible to quantize general relativity? In a quantum field theory of gravity, the gravitational interaction is mediated by a massless spin-2 gauge boson, the graviton. However, many problems arise. For example, unlike the dimensionless SM gauge coupling constants, the gravitational coupling constant has mass dimensions of -2 , i.e. $[G_N] = [m]^{-2}$, leading to higher-mass-dimensional operators, and thus, quantum gravity is not renormalizable. There are many theories of quantum gravity, such as loop quantum gravity, string theory and supergravity (see didactic reviews [51, 52] for more details).
- **Baryon-Antibaryon Asymmetry:** It is evident from observation that the Universe contains an excessive amount of matter (protons, neutron and electrons) in comparison to the almost negligible amount of antimatter. The measurement of today’s baryon to photon ratio $\eta \equiv \frac{n_B}{n_\gamma} \approx \frac{n_B - n_{\bar{B}}}{n_\gamma} \approx 6 \times 10^{-10}$ ($n_{\bar{B}} \ll n_B$) corresponds to a small asymmetry of $\frac{n_B - n_{\bar{B}}}{n_B} \sim 10^{-9}$ in the early Universe. Assuming this matter-antimatter asymmetry is not due to an initial condition of the Big Bang (the theorized period of cosmological inflation rules out this scenario), then it must have developed during the expansion of the Universe, which is dynamically possible if the three Sakharov conditions [53] are satisfied: 1) baryon number (B) violation; 2) C and CP violation; 3) a departure from thermal equilibrium. The only CP violating terms of the SM are the quark mixing CC interaction terms, where the “amount” of CP violation is regulated by the phase parameter $\delta \neq 0$ of the CKM matrix (Chapter 2), but the matter asymmetry they are able to produce is much lower than the observed value (by several orders of magnitude). Hence, other sources of CP violation are needed. Two popular solutions are leptogenesis, a right-handed neutrino mass mechanism sourcing CP violation, and electroweak baryogenesis, which relies on the occurrence of a strong first-order EW phase transition by the nucleation of vacuum bubbles (see short review [54] for more details).
- **Dark Matter:** There is vast evidence (discussed below, in Section 3.1.1), e.g. from rotation curves of spiral galaxies, motion of galaxies in clusters, weak gravitational lensing and cosmic microwave

background (CMB) measurements (in increasing order of (a wide) astronomical scale), for the existence of a non-baryonic type of matter – a cold, weakly interacting (except gravitationally), invisible, stable matter called dark matter (DM) – which presumably constitutes about 26.4% of the total matter-energy density of today’s Universe, thus corresponding to about 84% of the total (baryonic¹ and dark) matter content. Unlike baryonic matter, DM cannot (be one of, or in general) be made of SM particles, which means that we do not know the origin or nature of 84% of the matter of the Universe. The most popular approach to this problem is to assume that DM is a new (undetected) elementary particle (with specific properties, as we shall discuss in Section 3.2), which requires extending the SM. However, there are other possible solutions based on primordial black holes or modified gravity theories (e.g. modified Newtonian dynamics, known as MOND).

There are many other open questions in particle physics, as reviewed e.g. in Refs. [32, 55, 56]. We shall focus on the dark matter problem, under the assumption of DM being an elementary particle (or particles) that has (have) not been discovered yet.

3.1.1 Experimental Evidence for Dark Matter

Until now, all experimental evidence for the existence of dark matter has arisen solely from its gravitational effects. These effects are observed in a wide range of astronomical scales, which can be categorized into three main groups: the galactic scale, the galaxy cluster scale and the cosmological scale. In turn, these scale categories are not of equal status: experimental evidence from smaller scales (galaxies) are more intuitive and based on simple classical physics, but provide least useful or rigorous measurements; conversely, experimental evidence from larger scales (cosmology) rely on the GR description of an expanding Universe in the context of the Λ CDM model of cosmology, thus delivering preciser measurements [10]. Let us now briefly summarize some experimental evidence for dark matter, categorized by astronomical scale.

1. **Galactic Scale:** Spiral galaxies rotate around their vertical axis, and it is possible to measure the circular velocity of stars and other tracers around them. Assuming a spherical symmetric galactic mass distribution $\rho(r)$, the average circular velocity of a test particle (at this scale, e.g. a star) of mass m at a fixed radial distance r of the galactic center is directly obtained from Newton’s second law, giving $v_{\parallel}(r) = \sqrt{G_N M(r)/r}$, where $M(r) = \int d\Omega \int_0^r \rho(r') r'^2 dr'$ is the galactic mass contained within a distance r from the center. Most of the observed (visible) mass is concentrated in a dense central bulge and in the arms of the disk, so that for sufficiently large r , all galactic visible mass is contained within the orbit and we should obtain $M(r) \approx M_{\text{gal}} \Rightarrow v_{\parallel}(r) = \sqrt{G_N M_{\text{gal}}/r} \propto 1/\sqrt{r}$. But observations show that rotation curves instead remain flat, which is only possible for a mass distribution $\rho(r) \propto 1/r^2$ that leads to $M(r) = \frac{M_{\text{gal}} r}{R_{\text{gal}}} \propto r \Rightarrow v_{\parallel}(r) = \sqrt{G_N \frac{M_{\text{gal}}}{R_{\text{gal}}}} \propto 1$. This implies the existence of an invisible (dark) matter halo that accounts for this galactic mass distribution.
2. **Galaxy Cluster Scale:** Galaxy clusters are the largest gravitationally bound systems in the Universe. In 1933, Fritz Zwicky compared the observed velocity dispersion in the Coma galaxy cluster with a simple prediction of the Virial theorem $\langle T \rangle = (-1/2) \langle V \rangle$ of classical mechanics (which yields $M_{\text{cluster}} \propto v_{\text{gal}}^2$), and concluded that the total mass in the cluster was larger than the visible mass, thus implying the existence of an invisible (dark) mass. In the 1980s decade, X-ray observations emerged as a more efficient method of measuring the amount of ordinary (visible) and dark

¹Here, baryonic matter means (ordinary) matter made of SM particles (a standard cosmology convention).

matter within galaxy clusters (check section 1.2 of Ref. [10] for a description). Nowadays, perhaps the most striking evidence for the presence of DM at the galaxy cluster scale comes from observations of a pair of colliding galaxy clusters known as the Bullet Cluster. Most of the baryonic mass in the Bullet Cluster is in the form of hot gas whose distribution can be traced through its X-ray emissions, and the DM distribution is inferred by comparing the gas mass distribution to an independent measurement of the total (visible and dark) mass distribution via weak gravitational lensing. The spatial separation between visible and dark matter implies that, in contrast to visible matter, dark matter experienced negligible collisions (with both itself and visible matter), thus interacting weakly.

3. **Cosmological Scale:** Nowadays, the most precise evidence for the existence of dark matter come from cosmological observations. The main point is that the Universe would not have evolved to “our” observable Universe if not for dark matter, with the two main probes being large scale structure formation and CMB temperature anisotropies (check section 1.3 of Ref. [10] or cosmology textbooks [57, 58] for comprehensive descriptions). The primordial density inhomogeneities of the (almost perfectly smooth) early Universe were tiny. However, unlike baryonic matter, dark matter did not couple to radiation, enabling these density perturbations to grow in time and form the large scale structures we observe today, such as galaxies, galaxy clusters, and the cosmic web. The precise measurements of the CMB temperature anisotropies are typically described by the CMB power spectrum, which presents peaks due to acoustic oscillations of the photon and baryon (but not dark) matter fluid. These acoustic peaks’ positions depend on the abundance of DM (where less DM implies a later radiation-matter equality), and their amplitudes depend on the relative amount of DM with respect to baryonic matter (if the Universe contained baryonic matter only, the 3rd acoustic peak would be suppressed). Global fits (consistent with the Λ CDM model of cosmology) allow for a precise determination of cosmological parameters such as the abundance of DM, which according to Planck [7] observations is given by $\Omega_{\text{DM}}^{\text{obs}} h^2 = 0.120 \pm 0.001$.²

For other DM probes and more detailed descriptions, we recommend the comprehensive review [10] (first chapter) of M. Cirelli et al., which we closely followed in this section.

3.2 The Particle Physics Approach to Dark Matter

From now on, we will treat DM as an undiscovered elementary particle (or particles). Just like for any other new physics topic, the particle physics approach to dark matter requires extending the SM with new fields and symmetries, without breaking the already existing $\text{SU}(3)_c \times \text{SU}(2)_L \times \text{U}(1)_Y$ gauge symmetry. Moreover, the theory must be renormalizable, except for an effective field theory (EFT). In this particular BSM problem, the model must contain (explicitly or implicitly, through any given mechanism) at least one field that is associated to a DM particle candidate. A viable DM particle candidate must align with the experimental evidence discussed in Section 3.1.1, and consequently, exhibit the following properties:

- DM must be a **massive** particle, in order to account for all the observed gravitational effects it produces. There are practically no (a priori) limits for the DM mass.³

²This translates into a present abundance of $\Omega_{\text{DM}} \equiv \frac{8\pi G_N}{3H_0^2} \rho_{\text{DM},0} = 0.264 \pm 0.003$ (i.e., DM constitutes about 26.4% of the total matter-energy density of today’s Universe, which corresponds to about 84% of the total matter content), where the present Hubble parameter is $H_0 \equiv h \times 100 \text{ km s}^{-1} \text{ Mpc}^{-1}$, with $h = 0.674 \pm 0.005$ (values from Ref. [7]).

³Only fermionic DM masses have a bound $m_{\text{DM}} \gtrsim 1 \text{ keV}$, due to Pauli’s exclusion principle.

- DM must be **cold** (or not too hot), i.e., it must be non-relativistic ($|\vec{p}| \ll m_{\text{DM}}$) in order to be consistent with the cosmological probes.
- DM must be **electrically neutral**, i.e., it must have null (or virtual) electric charge $Q \simeq 0$ in order to be invisible (dark) and consistent with the cosmological probes.⁴
- DM must be **weakly interactive**, in order to account for its collisionless behavior that is observed in both galaxy cluster and cosmological probes.⁵
- DM must be **stable** (or have a lifetime $\Gamma_{\text{DM}}^{(\text{total})}$ much longer than the age of the Universe, $\Gamma_{\text{DM}}^{(\text{total})} \gg 13.8 \text{ Gyr} = 4.35 \times 10^{17} \text{ s}$), in order to account for the time evolution (behavior) of its abundance (as the Universe expanded) that is observed in cosmological probes.

Furthermore, there must be a production mechanism that is able to reproduce the observed DM abundance of $\Omega_{\text{DM}}^{\text{obs}} h^2 = 0.120 \pm 0.001$ [7] (Section 3.2.1). The appropriate production mechanism depends on the nature of the DM particle candidate (WIMP, axion, fuzzy, etc.). Finally, the DM model must not be excluded by any of the other experimental constraints, namely from DM particle detection experiments (Section 3.2.2).

3.2.1 Relic Density of Dark Matter

In this work we will consider the most popular class of DM particle candidates, the so called weakly interactive massive particles (WIMPs), here defined by masses around [1 GeV, 10 TeV] and weak scale interactions with the SM particles. Moreover, WIMPs are produced as a thermal relic via the freeze-out mechanism, described as follows. In the earliest stages of the Universe there is a large abundance of (WIMP) DM, which is able to annihilate into SM particles through $\text{DM DM} \rightarrow \text{SM SM}$ collisions. DM is in thermal equilibrium with the thermal bath, colliding (i.e., annihilating) faster than the expansion of the Universe: $\mathfrak{R}(T) \gg H(T)$, where $\mathfrak{R}(T)$ and $H(T)$ are the total DM annihilation rate and the Hubble function, respectively, at temperature T . DM density is always dropping during this period. As the Universe expands and cools (with time), DM eventually decouples from the thermal bath at some decoupling temperature T_d where $\mathfrak{R}(T_d) \simeq H(T_d)$, after which it no longer collides: $\mathfrak{R}(T) < H(T) \forall T < T_d \Leftrightarrow t > t_d$. Having stopped annihilating, the DM number density (or equivalently, abundance) asymptotically approaches a constant value – the thermal relic density, a “left-over” of a “frozen” process – which is the value we observe today.⁶

This process is quantitatively described by a Boltzmann equation $\hat{L}[f] = \hat{C}[f]$, which can be written in terms of the number density of DM particles $n(t)$, taking the form [39, 41]

$$\dot{n}(t) + 3H(t)n(t) = - \langle \sigma v_{\text{rel}} \rangle [n^2(t) - n_{\text{eq}}^2] , \quad (3.1)$$

where $\sigma \equiv \sum_{\{f\}} \sigma(\text{DM DM} \rightarrow \{f\})$ is the total annihilation cross section, $v_{\text{rel}} \equiv \frac{\sqrt{(p_1 \cdot p_2)^2 - m_1^2 m_2^2}}{E_1 E_2}$ is the Lorentz invariant effective relative velocity between initial state particles 1 and 2 (known as Møller velocity) which allows one to write a Lorentz invariant interaction rate $\mathfrak{R} = n_1 n_2 \sigma v_{\text{rel}}$ in a similar way to

⁴For a weak scale DM mass $m_{\text{DM}} \lesssim 1 \text{ TeV}$, the experimental upper bound is $|Q| \lesssim 10^{-10}$.

⁵Self-interaction cross sections must be smaller than a typical QCD cross section, $\sigma \ll 1/m_\pi^2$ for $m_{\text{DM}} \sim m_\pi$ ($m_\pi = 135 \text{ MeV}$ is the pion mass). In this context, “interactions” never includes gravity.

⁶Two important points: i) If DM had not decoupled from the thermal bath, it would continue to annihilate until it completely vanished, instead of “freezing-out”. ii) An unstable particle would decay into lighter particles after decoupling, causing its number density to drop to zero – that is why DM must be stable.

the non-relativistic formula [39, 41]. Finally, the thermally averaged cross section (TAC) is given by [18]

$$\langle \sigma v_{\text{rel}} \rangle \equiv \frac{\int d^3p_1 d^3p_2 f_{\text{eq}}(|\vec{p}_1|) f_{\text{eq}}(|\vec{p}_2|) \sigma v_{\text{vel}}}{\int d^3p_1 d^3p_2 f_{\text{eq}}(|\vec{p}_1|) f_{\text{eq}}(|\vec{p}_2|)} = \frac{\int_{4m_{\text{DM}}^2}^{\infty} ds \sqrt{s} (s - 4m_{\text{DM}}^2) K_1(\sqrt{s}/T) \sigma(s)}{8m_{\text{DM}}^4 T K_2^2(m_{\text{DM}}/T)}, \quad (3.2)$$

where $s \equiv (p_1 + p_2)^2$ is the squared total energy in the center-of-mass reference frame, $K_{1,2}$ are the modified Bessel functions of the second kind of orders 1, 2 and the equilibrium DM distribution was taken as the Maxwell-Boltzmann distribution $f_{\text{eq}}(|\vec{p}_i|) = e^{-E_{\vec{p}_i}/T}$ ($i = 1, 2$) in the second equality.

The Boltzmann equation (3.1) is challenging to solve analytically without approximations, and is thus typically solved numerically. A DM particle model can influence the (predicted) DM relic density through the TAC (3.2), and must be able to reproduce the precise measurement $\Omega_{\text{DM}}^{\text{obs}} h^2 = 0.120 \pm 0.001$ from the Planck satellite [7], otherwise it is excluded.

3.2.2 Dark Matter (Particle) Detection

As discussed in Section 3.1.1, all experimental evidence for the existence of DM stems solely from its gravitational effects. Nevertheless, these gravitational probes (alone) can establish a set of properties that any DM particle candidate must satisfy, as well as the precisely measured DM relic density (a powerful constraint on DM models), as we have just seen in this Section 3.2.

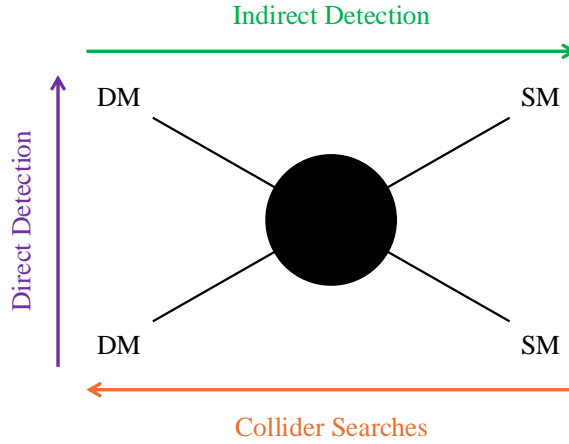


Figure 3.1: Diagrammatic “make it, shake it, break it” illustration of dark matter particle detection, with arrows indicating the direction of the process and corresponding detection experiment.

But in order to understand the nature of DM (i.e., what it really is), we also need to observe it interact (non-gravitationally) with ordinary (visible) matter (i.e., with SM particles). This leads us to the experimental methods of DM detection, which are divided in three main categories, as diagrammatically illustrated in Figure 3.1. Following Ref. [10], these are:

1. **Direct Detection** experiments, designed to detect the recoil events produced by passing (galactic) DM particles that scatter off a nucleus or electron of the material of a shielded and monitored underground detector (made of ultra-pure semiconductors, noble gasses, pristine crystals, etc.). The relevant process are $\text{DM SM} \rightarrow \text{DM SM}$ ($\text{SM} = N, e^-$ ($N = p, n$)) elastic scatterings, represented by the Feynman diagram in Figure 3.1 for the upward direction (\uparrow).
2. **Indirect Detection** experiments, designed to detect DM annihilations in our galaxy (or other astrophysical systems) through searches for signatures in cosmic rays (stable SM particles arriving at Earth: charged (anti)particles, photons, neutrinos, etc.). The relevant processes are $\text{DM DM} \rightarrow$

SM SM annihilations, represented by the Feynman diagram in Figure 3.1 for the left-to-right direction (\rightarrow).

3. **Collider Searches** refer to the production of DM particles in a controlled environment (the collider) via collision of SM particles (e.g., proton-proton collisions at the LHC), in order to “detect” the presence of DM through the missing energy-momentum in the final state of the process.⁷ The relevant processes are SM SM \rightarrow DM DM productions, represented by the Feynman diagram in Figure 3.1 for the right-to-left direction (\leftarrow).

To this day, DM has never been detected through any of these experiments. However, they still provide important constraints that can be applied to our DM particle models, usually in the form of (in general, model-independent) experimental upper limits to cross sections or other cross section dependent observables (the only quantities a DM particle model can predict). This will later be explained for direct detection and collider search experiments in Sections 4.4 and 4.5, respectively.

3.3 The SM+RSS DM Model with an Unbroken \mathcal{Z}_2 Symmetry

We consider an extension of the Standard Model with a real scalar $SU(3)_c \times SU(2)_L \times U(1)_Y$ singlet field $S(x) \sim (\mathbf{1}, \mathbf{1}, 0)$, and impose (in addition to the SM $SU(3)_c \times SU(2)_L \times U(1)_Y$ gauge invariance) an additional symmetry with respect to the discrete group \mathcal{Z}_2 , under which the fields transform as

$$\mathcal{Z}_2 : \quad S(x) \rightarrow -S(x), \quad \text{SM} \rightarrow +\text{SM}, \quad (3.3)$$

i.e., only $S(x)$ is \mathcal{Z}_2 -odd, while the remaining fields are \mathcal{Z}_2 -even and transform trivially under \mathcal{Z}_2 . The \mathcal{Z}_2 charge can be interpreted as a *dark* (intrinsic) parity quantum number. Therefore, the most general renormalizable Lagrangian density invariant under $SU(3)_c \times SU(2)_L \times U(1)_Y \times \mathcal{Z}_2$ transformations is given by

$$\mathcal{L}_{\text{SM+RSS}} = \mathcal{L}_{\text{SM}} + \frac{1}{2}(\partial_\mu S)\partial^\mu S - \frac{1}{2}\mu_S^2 S^2 - \frac{\lambda_S}{4!}S^4 - \underbrace{\frac{\kappa_{HS}}{2}S^2\Phi^\dagger\Phi}_{=\mathcal{L}_{\text{portal}}} \supset -V(|\Phi|, S), \quad (3.4)$$

where $\Phi(x) = \begin{pmatrix} G^+(x) & \phi^0(x) \end{pmatrix}^\top \sim (\mathbf{1}, \mathbf{2}, +1/2)$ is the Higgs doublet, and the scalar potential is now given by

$$V(|\Phi|, S) = \mu_H^2 \Phi^\dagger \Phi + \lambda_H (\Phi^\dagger \Phi)^2 + \frac{1}{2}\mu_S^2 S^2 + \frac{\lambda_S}{4!}S^4 + \frac{\kappa_{HS}}{2}S^2\Phi^\dagger\Phi. \quad (3.5)$$

The singlet $S(x)$ couples to the Higgs doublet $\Phi(x)$ (and no other field) through the portal term $\mathcal{L}_{\text{portal}} = -\kappa_{HS}S^2\Phi^\dagger\Phi/2$, which links the dark sector with the SM sector.

The vacuum (or ground) state is obtained by the usual minimization procedure

$$\begin{cases} \frac{\partial V}{\partial \Phi} \big|_{\Phi=\langle\Phi\rangle_0, S=\langle S\rangle_0} = \left(\mu_H^2 + 2\lambda_H \langle\Phi\rangle_0^\dagger \langle\Phi\rangle_0 + \frac{\kappa_{HS}}{2} \langle S\rangle_0^2 \right) \langle\Phi\rangle_0^\dagger = 0 \\ \frac{\partial V}{\partial \Phi^\dagger} \big|_{\Phi=\langle\Phi\rangle_0, S=\langle S\rangle_0} = \left(\mu_H^2 + 2\lambda_H \langle\Phi\rangle_0^\dagger \langle\Phi\rangle_0 + \frac{\kappa_{HS}}{2} \langle S\rangle_0^2 \right) \langle\Phi\rangle_0 = 0 \\ \frac{\partial V}{\partial S} \big|_{\Phi=\langle\Phi\rangle_0, S=\langle S\rangle_0} = \left(\mu_S^2 + \frac{\lambda_S}{3!} \langle S\rangle_0^2 + \kappa_{HS} \langle\Phi\rangle_0^\dagger \langle\Phi\rangle_0 \right) \langle S\rangle_0 = 0 \end{cases} \quad (3.6)$$

⁷The final state of the DM production process must include at least one visible (detectable) particle in addition to the invisible (undetectable) DM particles, as this makes it possible to identify the occurrence of the event (and thus confirm the presence of missing energy-momentum).

$$\Leftrightarrow \left(\langle \Phi \rangle_0 = 0 \vee \langle \Phi \rangle_0^\dagger \langle \Phi \rangle_0 = -\frac{\mu_H^2 + \kappa_{HS} \langle S \rangle_0^2 / 2}{2\lambda_H} \right) \wedge \left(\langle S \rangle_0 = 0 \vee \langle S \rangle_0^2 = -\frac{\mu_S^2 + \kappa_{HS} \langle \Phi \rangle_0^\dagger \langle \Phi \rangle_0}{\lambda_S / 3!} \right),$$

corresponding to four $SU(3)_c \times SU(2)_L \times U(1)_Y \times \mathcal{Z}_2$ invariant stationary solution sets (which can be minima by requiring the Hessian matrix to have positive eigenvalues)

$$\langle \Phi \rangle_0 = 0 \quad \wedge \quad \langle S \rangle_0 = 0, \quad (3.7)$$

$$\langle \Phi \rangle_0^\dagger \langle \Phi \rangle_0 = -\frac{\mu_H^2}{2\lambda_H} \equiv \frac{v^2}{2} \quad \wedge \quad \langle S \rangle_0 = 0, \quad (3.8)$$

$$\langle \Phi \rangle_0 = 0 \quad \wedge \quad \langle S \rangle_0^2 = -\frac{6\mu_S^2}{\lambda_S} \equiv v_S^2, \quad (3.9)$$

$$\langle \Phi \rangle_0^\dagger \langle \Phi \rangle_0 = -\frac{\mu_H^2 + \kappa_{HS} v_S'^2 / 2}{2\lambda_H} \equiv \frac{v'^2}{2} \quad \wedge \quad \langle S \rangle_0^2 = -\frac{\mu_S^2 + \kappa_{HS} v'^2 / 2}{\lambda_S / 3!} \equiv v_S'^2. \quad (3.10)$$

Let us now analyse these vacuum configurations in more detail. Since the $\Phi(x)$ and $S(x)$ fields are both singlets of $SU(3)_c$ – i.e., they are not coloured and thus transform trivially under this gauge group – the local $SU(3)_c$ symmetry cannot be spontaneously broken. Therefore, it is sufficient to consider only the $SU(2)_L \times U(1)_Y \times \mathcal{Z}_2$ symmetry for this discussion.

- For the minimum solution sets (3.7) and (3.9), the Higgs doublet does not acquire a VEV, i.e. $\langle \Phi \rangle_0 = 0$, and thus electroweak $SU(2)_L \times U(1)_Y \rightarrow U(1)_Q$ SSB does not occur. Consequently, no mass terms for the electroweak gauge bosons and fermions are generated via the SM Higgs mechanism, and therefore, these vacuum configurations do not correspond to what is physically observed in Nature. This leaves us with vacuum configurations (3.8) and (3.10) left to consider, where the Higgs doublet acquires a non-zero VEV $\langle \Phi \rangle_0 \neq 0$ (out of the possible $SU(2)_L \times U(1)_Y$ gauge invariant solution set), thus spontaneously breaking the $SU(2)_L \times U(1)_Y$ gauge symmetry of the vacuum down to $U(1)_Q$. Without loss of generality, we can take the conventional VEV

$$\langle \Phi \rangle_0 = \begin{pmatrix} 0 \\ \frac{v}{\sqrt{2}} \end{pmatrix}, \quad \text{so that} \quad \Phi(x) = \begin{pmatrix} G^+(x) \\ \frac{v+h(x)+iG^0(x)}{\sqrt{2}} \end{pmatrix}, \quad (3.11)$$

where $v \in \mathbb{R}^+$ is determined by the choice of vacuum configuration (between (3.8) and (3.10)). As usual, the fields $G^0(x)$ and $G^\pm(x)$ are would-be Goldstone bosons that can be “gauged away” into the unitary gauge.

- For the minimum solution set (3.10), the singlet also acquires a non-zero VEV out of the possible \mathcal{Z}_2 invariant (discrete) solution set $\langle S \rangle_0 = \pm v'_S$ ($v'_S \in \mathbb{R}^+$), thus also spontaneously breaking the \mathcal{Z}_2 symmetry of the vacuum. After $SU(2)_L \times U(1)_Y \times \mathcal{Z}_2 \rightarrow U(1)_Q$ SSB, $h(x)$ and the field perturbation around the singlet’s VEV $\xi(x) \equiv S(x) - \langle S \rangle_0$ mix in the hSS coupling (contained in the portal term). Hence, $h(x)$ and $\xi(x)$ are interaction eigenstates, while the mass eigenstates (physical fields) are given by an $SO(2)$ rotation in flavour space

$$\begin{pmatrix} h_1(x) \\ h_2(x) \end{pmatrix} = U^\top(\alpha) \begin{pmatrix} h(x) \\ \xi(x) \end{pmatrix}, \quad \text{where} \quad U(\alpha) = \begin{pmatrix} \cos \alpha & +\sin \alpha \\ -\sin \alpha & \cos \alpha \end{pmatrix} \in SO(2) \quad (3.12)$$

diagonalizes the scalar squared-mass matrix M^2 from the interaction eigenstate basis to the mass eigenstate basis, i.e.

$$U^\top(\alpha) M^2 U(\alpha) = \text{diag}(m_{h_1}^2, m_{h_2}^2) \equiv \mathcal{D}^2, \quad (3.13)$$

so that the scalar mass terms are diagonal (without flavour mixing) in the mass basis,

$$\mathcal{L}_{\text{mass}}^{(\text{scalar})} = -\frac{1}{2} \begin{pmatrix} h & \xi \end{pmatrix} M^2 \begin{pmatrix} h \\ \xi \end{pmatrix} = -\frac{1}{2} \begin{pmatrix} h_1 & h_2 \end{pmatrix} \mathcal{D}^2 \begin{pmatrix} h_1 \\ h_2 \end{pmatrix} = -\frac{1}{2} m_{h_1}^2 h_1^2 - \frac{1}{2} m_{h_2}^2 h_2^2. \quad (3.14)$$

In this scenario, h_1 and h_2 are Higgs-like particles (with one of them being the 125 GeV Higgs boson discovered at the LHC), and therefore, both are able to decay (unstable particles). The spontaneously (but not explicitly) broken \mathcal{Z}_2 symmetry

$$S \rightarrow -S \quad \Leftrightarrow \quad \xi = -\sin \alpha h_1 + \cos \alpha h_2 \rightarrow -2v'_S - \xi = -2v'_S + \sin \alpha h_1 - \cos \alpha h_2 \quad (3.15)$$

is now *hidden* in the Lagrangian density. For the minimum solution set (3.10), the model does not contain a DM particle candidate, and hence, this vacuum configuration does not hold any interest in the context of this work.

We are left with minimum solution set (3.8), which is the vacuum configuration we will consider for this model. The singlet does not acquire a VEV, i.e. $\langle S \rangle_0 = 0$, so that the \mathcal{Z}_2 symmetry is not spontaneously broken and there is no flavour mixing with $h(x)$. Hence, $h(x)$ and $S(x)$ are mass eigenstates – i.e., these fields correspond to physical particles – where h is the Higgs boson and S is a new spin 0 massive particle. Using the minimum condition in (3.8), $v^2 = -\mu_H^2/\lambda_H \Leftrightarrow \mu_H^2 = -\lambda_H v^2$ (the same as that of the SM), the (expanded) scalar potential, in the unitary gauge $\Phi(x) \rightarrow \frac{1}{\sqrt{2}} \begin{pmatrix} 0 & v + h(x) \end{pmatrix}^\top$, is given by

$$V(|\Phi|, S) = \frac{1}{2} \overbrace{(2\lambda_H v^2)}^{=m_h^2} h^2 + \lambda_H v h^3 + \frac{\lambda_H}{4} h^4 + \frac{1}{2} \overbrace{(\mu_S^2 + \frac{\kappa_{HS} v^2}{2})}^{=m_S^2} S^2 + \frac{\lambda_S}{4!} S^4 + \frac{\kappa_{HS} v}{2} h S^2 + \frac{\kappa_{HS}}{4} h^2 S^2, \quad (3.16)$$

which written in terms of the scalar masses $m_h = \sqrt{2\lambda_H v^2}$ and $m_S = \sqrt{\mu_S^2 + \kappa_{HS} v^2/2}$, reads as

$$-\mathcal{L}_{\text{SM+RSS}} \supset V(|\Phi|, S) = \frac{1}{2} m_h^2 h^2 + \frac{m_h^2}{2v} h^3 + \frac{m_h^2}{8v^2} h^4 + \frac{1}{2} m_S^2 S^2 + \frac{\lambda_S}{4!} S^4 + \frac{\kappa_{HS} v}{2} h S^2 + \frac{\kappa_{HS}}{4} h^2 S^2. \quad (3.17)$$

The unbroken \mathcal{Z}_2 symmetry ensures that S does not decay (stable particle), thus being a DM candidate. This is shown in Figure 3.2, which presents the Feynman rules for the new interaction vertices that emerge in this SM extension.

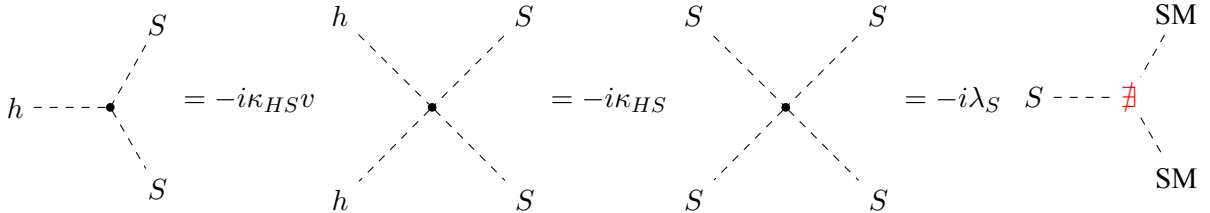


Figure 3.2: Feynman rules for the interaction vertices involving the S dark matter particle candidate. The decays $S \rightarrow \text{SM SM}$ are forbidden by “dark parity” (or \mathcal{Z}_2 charge) conservation, as a consequence of the \mathcal{Z}_2 discrete symmetry.

3.3.1 Parameter Space Scans and Numerical Analysis

The real scalar singlet extension of the SM has three (new) free parameters, but only two of them are relevant at tree-level: the DM mass m_S and the portal interaction coefficient κ_{HS} . The quartic self-interaction coefficient λ_S is only relevant for loop level corrections in perturbation theory, which will not be considered in this work. Hence, we scanned the 2-dimensional free parameter space (relevant at tree-level) of this model with `micrOMEGAs 6.0` [59], a numerical code written in C (C++) designed to compute DM related observables within extensions of the SM. In particular, it solves the Boltzmann equation (3.1) numerically (for a given free parameter space point of the model). We assumed that the scalar DM particle S is a WIMP (as we shall always do in this work), thus having been thermally produced according to the freeze-out mechanism described in Section 3.2.1.

The scans were performed considering all DM experimental constraints described in Section 3.2. The results are shown in Figure 3.3, which displays these constraints in the (m_S, κ_{HS}) plane. The red region represents free parameter space points that reproduce the observed DM relic density $\Omega_{\text{DM}}^{\text{obs}} h^2 = 0.120 \pm 0.001$ from Planck [7] measurements. It forms the line pattern satisfying $\Omega_S(m_S, \kappa_{HS}) h^2 = \Omega_{\text{DM}}^{\text{obs}} h^2$, i.e., displays the $m_S \mapsto \kappa_{HS}$ map that gives the correct abundance.⁸ Conversely, the grey region reproduces an over-density of DM, thus being excluded. The remaining coloured free parameter space regions are all excluded by DM detection experiments: 1) The purple region is excluded by the XENON1T [60], DarkSide-50 [61], PICO-60 [62], CRESST-III [63], PandaX-4T [64] and LUX-ZEPLIN (LZ) [2] direct detection experiments. 2) The green region is experimentally excluded by indirect detection, with the exclusion performed using MADHAT [65, 66], a numerical tool that implements a Fermi-LAT data-driven, model-independent analysis of γ -ray emission from dwarf galaxies due to DM annihilation. 3) As for collider searches, the orange region is experimentally excluded by the ATLAS [67] upper bound on the branching ratio for the Higgs boson decay to “invisible” products, $\text{BR}(h \rightarrow \text{inv}) < 0.107$. Furthermore, no region of the free parameter space was excluded by the mono-jet LHC search routine in `micrOMEGAs 6.0`. We will revisit collider searches in later stages of this work.

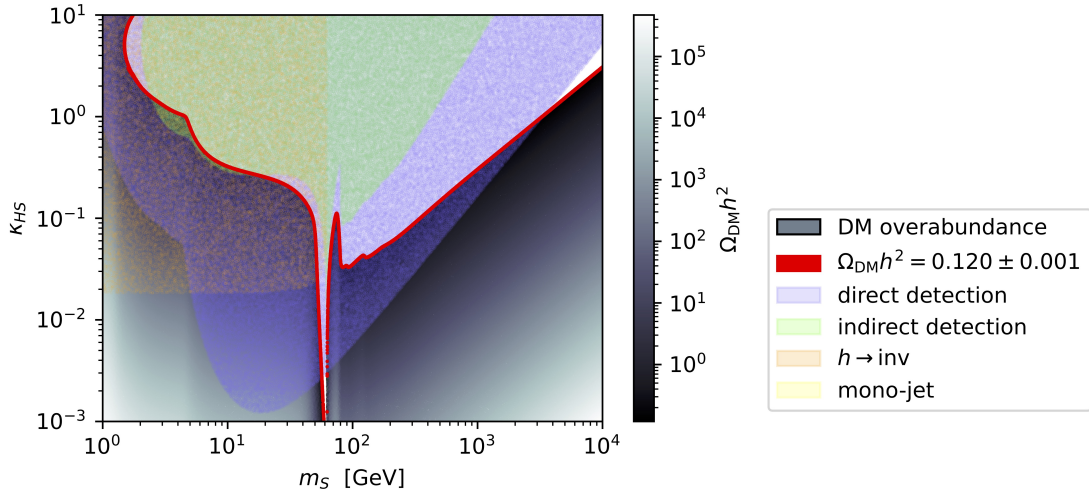


Figure 3.3: Experimental constraints on the SM+RSS model (3.4), obtained by scanning the free parameter space with `micrOMEGAs 6.0` for the freeze-out mechanism. The grey, purple, green and orange regions are respectively excluded by DM relic (over-)density, direct detection, indirect detection and $\text{BR}(h \rightarrow \text{inv})$; while the red region corresponds to the observed DM relic density.

⁸This is a special feature of this model, due to only having two (relevant) free parameters: for a given DM mass m_S , only one value for the portal coefficient κ_{HS} is able to reproduce the observed DM relic density. This will not happen for other DM models, with a higher-dimensional free parameter space.

As explicitly shown in Figure 3.3, nearly all of the free parameter space in the real scalar singlet SM extension is experimentally excluded. Additionally, the combined constraints from the observed relic density and direct detection fully account for all this exclusion (without the need for other experimental constraints). We will not conduct a detailed numerical analysis, as this model is not the primary focus of this work, but rather serves as a motivation for what follows. Nevertheless, we shall make a few relevant observations about the behavior of the relic density, which will prove useful later on.

- For $m_S < m_h/2$, the relic density decreases with m_S ; but for $m_S > m_h/2$, the relic density increases with m_S . Therefore, the relic density increases as $|m_S - m_h/2|$ increases in the entire DM mass range.
- When the mass of the DM reaches half the mass of the Higgs boson (from either lower and higher values), the relic density sharply drops to (roughly) zero: $\Omega_S h^2 \rightarrow 0$ ($m_S \rightarrow m_h/2$).
- When the mass of the DM reaches the mass of a SM particle (from lower values) that can be produced through DM annihilation, the relic density abruptly decreases before quickly resuming its prior behavior.

All theoretical aspects of these observations will be discussed later in Sections 4.2 and 4.4. The important thing to retain from this numerical analysis, aside from the previous remarks, is that this SM+RSS model is excluded for DM masses below 3535 GeV (excluding the resonant scenario).

Chapter 4

The Two-Real-Scalar-Singlet SM Extension

As we just saw in Figure 3.3 of the previous Section 3.3.1, the real scalar singlet SM extension (3.4) with an unbroken \mathcal{Z}_2 discrete symmetry is highly constrained by the observed relic density and direct detection experiments, which exclude this model for DM masses below 3535 GeV. Hence, this SM extension cannot be probed at LHC collider searches targeted at its WIMP candidate (the reason for this will be later explained in Section 4.5).

There are many interesting DM models worth studying (e.g., see Ref. [10] for a review), but we wish to persist with $SU(3)_c \times SU(2)_L \times U(1)_Y$ singlet field extensions for their simplicity. In particular, we are interested in exploring the possibility of extending the SM with a *second* real scalar singlet and respective additional \mathcal{Z}_2 unbroken symmetry.

The S_1, S_2 two-real-scalar-singlet SM extension with a $\mathcal{Z}_2^{(1)} \times \mathcal{Z}_2^{(2)}$ discrete symmetry (where only S_r transforms non-trivially under $\mathcal{Z}_2^{(r)}$, $r = 1, 2$) is treated in Ref. [19], but for the scenario where both symmetries are spontaneously broken, thus leading to two extra Higgs-like particles and zero DM candidates. In contrast, our $\mathcal{Z}_2^{(1)} \times \mathcal{Z}_2^{(2)}$ symmetry shall remain unbroken, thus leading to two DM candidates (and zero extra Higgs-like particles), as explained in this next Section 4.1. Like us, Ref. [20] considers the SM+2RSS model with the same unbroken $\mathcal{Z}_2^{(1)} \times \mathcal{Z}_2^{(2)}$ vacuum configuration, but for the alternative scenario where one of the two DM candidates is a FIMP (produced via freeze-in), rather than a WIMP (produced via freeze-out), as we shall do.

Additionally, in Appendix C we consider imposing a single $\mathcal{Z}_2^{(1,2)}$ unbroken symmetry, under which both singlet fields are odd. In this alternative scenario, the $\mathcal{Z}_2^{(1)} \times \mathcal{Z}_2^{(2)}$ invariant Lagrangian density is extended by four soft-breaking terms, resulting in a distinct phenomenology.

4.1 The SM+2RSS DM Model with an Unbroken $\mathcal{Z}_2^{(1)} \times \mathcal{Z}_2^{(2)}$ Symmetry

We now consider an extension of the Standard Model with two real scalar $SU(3)_c \times SU(2)_L \times U(1)_Y$ singlet fields $S_1(x), S_2(x) \sim (\mathbf{1}, \mathbf{1}, 0)$, and impose (in addition to the SM gauge invariance) an additional symmetry with respect to the discrete direct product group $\mathcal{Z}_2^{(1)} \times \mathcal{Z}_2^{(2)}$, under which the fields transform as

$$\mathcal{Z}_2^{(1)} : S_1(x) \rightarrow -S_1(x), \quad S_2(x) \rightarrow +S_2(x), \quad \text{SM} \rightarrow +\text{SM} \quad (4.1)$$

$$\mathcal{Z}_2^{(2)} : S_1(x) \rightarrow +S_1(x), \quad S_2(x) \rightarrow -S_2(x), \quad \text{SM} \rightarrow +\text{SM}, \quad (4.2)$$

i.e., only $S_r(x)$ is $\mathcal{Z}_2^{(r)}$ -odd, while the remaining fields are $\mathcal{Z}_2^{(r)}$ -even and transform trivially under $\mathcal{Z}_2^{(r)}$, $r = 1, 2$. In other words, the non-trivial transformations under $\mathcal{Z}_2^{(1)} \times \mathcal{Z}_2^{(2)}$ are

$$\mathcal{Z}_2^{(1)} \times \mathcal{Z}_2^{(2)} : S_r(x) \rightarrow -S_r(x), \quad r = 1 \vee r = 2 \vee r = 1, 2. \quad (4.3)$$

The $\mathcal{Z}_2^{(1)}, \mathcal{Z}_2^{(2)}$ charges can be interpreted as two independent *dark* (intrinsic) parity quantum numbers. Therefore, the most general renormalizable Lagrangian density invariant under $\text{SU}(3)_c \times \text{SU}(2)_L \times \text{U}(1)_Y \times \mathcal{Z}_2^{(1)} \times \mathcal{Z}_2^{(2)}$ transformations is given by

$$\begin{aligned} \mathcal{L}_{\text{SM}+2\text{RSS}} = & \mathcal{L}_{\text{SM}} + \frac{1}{2}(\partial_\mu S_1)\partial^\mu S_1 + \frac{1}{2}(\partial_\mu S_2)\partial^\mu S_2 - \frac{1}{2}\mu_1^2 S_1^2 - \frac{1}{2}\mu_2^2 S_2^2 - \frac{\lambda_1}{4!}S_1^4 - \frac{\lambda_2}{4!}S_2^4 \\ & - \underbrace{\frac{\kappa_{H1}}{2}S_1^2\Phi^\dagger\Phi}_{=\mathcal{L}_{\text{portal}(1)}} - \underbrace{\frac{\kappa_{H2}}{2}S_2^2\Phi^\dagger\Phi}_{=\mathcal{L}_{\text{portal}(2)}} - \underbrace{\frac{\lambda_{12}}{4}S_1^2S_2^2}_{=\mathcal{L}_{\text{int}(1,2)}} \supset -V(|\Phi|, S_1, S_2), \end{aligned} \quad (4.4)$$

where $\Phi(x) = \begin{pmatrix} G^+(x) & \phi^0(x) \end{pmatrix}^\top \sim (\mathbf{1}, \mathbf{2}, +1/2)$ is the Higgs doublet, and the scalar potential is now given by

$$V(|\Phi|, S_1, S_2) = \mu_H^2 \Phi^\dagger \Phi + \lambda_H (\Phi^\dagger \Phi)^2 + \sum_{r=1}^2 \left[\frac{1}{2} \mu_r^2 S_r^2 + \frac{\lambda_r}{4!} S_r^4 + \frac{\kappa_{Hr}}{2} S_r^2 \Phi^\dagger \Phi \right] + \frac{\lambda_{12}}{4} S_1^2 S_2^2. \quad (4.5)$$

The singlets $S_1(x)$ and $S_2(x)$ couple to each other through $\mathcal{L}_{\text{int}(1,2)}$, which links both dark sectors to each other, and to the Higgs doublet $\Phi(x)$ through the portal terms $\mathcal{L}_{\text{portal}(1)}$ and $\mathcal{L}_{\text{portal}(2)}$ (resp.), which link both dark sectors to the SM sector.

The vacuum (or ground) state is obtained by the usual minimization procedure

$$\begin{aligned} & \begin{cases} \frac{\partial V}{\partial \Phi} \big|_{\Phi=\langle \Phi \rangle_0, S_r=\langle S_r \rangle_0} = \left(\mu_H^2 + 2\lambda_H \langle \Phi \rangle_0^\dagger \langle \Phi \rangle_0 + \sum_{r=1}^2 \frac{\kappa_{Hr}}{2} \langle S_r \rangle_0^2 \right) \langle \Phi \rangle_0^\dagger = 0 \\ \frac{\partial V}{\partial \Phi^\dagger} \big|_{\Phi=\langle \Phi \rangle_0, S_r=\langle S_r \rangle_0} = \left(\mu_H^2 + 2\lambda_H \langle \Phi \rangle_0^\dagger \langle \Phi \rangle_0 + \sum_{r=1}^2 \frac{\kappa_{Hr}}{2} \langle S_r \rangle_0^2 \right) \langle \Phi \rangle_0 = 0 \\ \frac{\partial V}{\partial S_1} \big|_{\Phi=\langle \Phi \rangle_0, S_r=\langle S_r \rangle_0} = \left(\mu_1^2 + \frac{\lambda_1}{3!} \langle S_1 \rangle_0^2 + \kappa_{H1} \langle \Phi \rangle_0^\dagger \langle \Phi \rangle_0 + \frac{\lambda_{12}}{2} \langle S_2 \rangle_0^2 \right) \langle S_1 \rangle_0 = 0 \\ \frac{\partial V}{\partial S_2} \big|_{\Phi=\langle \Phi \rangle_0, S_r=\langle S_r \rangle_0} = \left(\mu_2^2 + \frac{\lambda_2}{3!} \langle S_2 \rangle_0^2 + \kappa_{H2} \langle \Phi \rangle_0^\dagger \langle \Phi \rangle_0 + \frac{\lambda_{12}}{2} \langle S_1 \rangle_0^2 \right) \langle S_2 \rangle_0 = 0 \end{cases} \quad (4.6) \\ \Leftrightarrow & \left(\langle \Phi \rangle_0 = 0 \vee \langle \Phi \rangle_0^\dagger \langle \Phi \rangle_0 = -\frac{\mu_H^2 + \sum_{r=1}^2 \kappa_{Hr} \langle S_r \rangle_0^2 / 2}{2\lambda_H} \right) \\ & \wedge \left(\langle S_1 \rangle_0 = 0 \vee \langle S_1 \rangle_0^2 = -\frac{\mu_1^2 + \kappa_{H1} \langle \Phi \rangle_0^\dagger \langle \Phi \rangle_0 + \lambda_{12} \langle S_2 \rangle_0^2 / 2}{\lambda_1 / 3!} \right) \\ & \wedge \left(\langle S_2 \rangle_0 = 0 \vee \langle S_2 \rangle_0^2 = -\frac{\mu_2^2 + \kappa_{H2} \langle \Phi \rangle_0^\dagger \langle \Phi \rangle_0 + \lambda_{12} \langle S_1 \rangle_0^2 / 2}{\lambda_2 / 3!} \right), \end{aligned} \quad (4.7)$$

corresponding to eight $\text{SU}(3)_c \times \text{SU}(2)_L \times \text{U}(1)_Y \times \mathcal{Z}_2^{(1)} \times \mathcal{Z}_2^{(2)}$ invariant stationary solution sets (which can be minima by requiring the Hessian matrix to have positive eigenvalues)

$$\langle \Phi \rangle_0 = 0 \quad \bigwedge_{r=1}^2 \quad \langle S_r \rangle_0 = 0, \quad (4.8)$$

$$\langle \Phi \rangle_0^\dagger \langle \Phi \rangle_0 = -\frac{\mu_H^2}{2\lambda_H} \equiv \frac{v^2}{2} \quad \bigwedge_{r=1}^2 \quad \langle S_r \rangle_0 = 0, \quad (4.9)$$

$$\langle \Phi \rangle_0 = 0 \quad \wedge \quad \langle S_r \rangle_0^2 = -\frac{6\mu_r^2}{\lambda_r} \equiv v_r^2 \quad \wedge \quad \langle S_{r'} \rangle_0 = 0, \quad r = 1, 2 \wedge r' \neq r, \quad (4.10)$$

$$\langle \Phi \rangle_0^\dagger \langle \Phi \rangle_0 = -\frac{\mu_H^2 + \kappa_{Hr} v_r'^2/2}{2\lambda_H} \equiv \frac{v'^2}{2} \quad \wedge \quad \langle S_r \rangle_0^2 = -\frac{\mu_r^2 + \kappa_{Hr} v_r'^2/2}{\lambda_r/3!} \equiv v_r'^2 \quad \wedge \quad \langle S_{r'} \rangle_0 = 0, \\ r = 1, 2 \wedge r' \neq r, \quad (4.11)$$

$$\langle \Phi \rangle_0 = 0 \quad \bigwedge_{r=1}^2 \quad \langle S_r \rangle_0^2 = -\frac{\mu_r^2 + \lambda_{12} v_r''^2/2}{\lambda_r/3!} \equiv v_r''^2, \quad r' \neq r, \quad (4.12)$$

$$\langle \Phi \rangle_0^\dagger \langle \Phi \rangle_0 = -\frac{\mu_H^2 + \sum_{r=1}^2 \kappa_{Hr} v_r''^2/2}{2\lambda_H} \equiv \frac{v''^2}{2} \quad \bigwedge_{r=1}^2 \quad \langle S_r \rangle_0^2 = -\frac{\mu_r^2 + \kappa_{Hr} v_r''^2/2 + \lambda_{12} v_r''^2/2}{\lambda_r/3!} \equiv v_r''^2, \\ r' \neq r. \quad (4.13)$$

Let us now analyse these vacuum configurations in more detail. Since the $\Phi(x)$, $S_1(x)$ and $S_2(x)$ fields are $SU(3)_c$ singlets – i.e., they are not coloured and thus transform trivially under this gauge group – the local $SU(3)_c$ symmetry cannot be spontaneously broken. Therefore, it is sufficient to consider only the $SU(2)_L \times U(1)_Y \times \mathcal{Z}_2^{(1)} \times \mathcal{Z}_2^{(2)}$ symmetry for this discussion.

- For the minimum solution sets (4.8), (4.10) and (4.12), the Higgs doublet does not acquire a VEV, i.e. $\langle \Phi \rangle_0 = 0$, and thus electroweak $SU(2)_L \times U(1)_Y \rightarrow U(1)_Q$ SSB does not occur. Consequently, no mass terms for the electroweak gauge bosons and fermions are generated via the SM Higgs mechanism, and therefore, these vacuum configurations do not correspond to what is physically observed in Nature. This leaves us with vacuum configurations (4.9), (4.11) and (4.13) left to consider, where the Higgs doublet acquires a non-zero VEV $\langle \Phi \rangle_0 \neq 0$ (out of the possible $SU(2)_L \times U(1)_Y$ gauge invariant solution set), thus spontaneously breaking the $SU(2)_L \times U(1)_Y$ gauge symmetry of the vacuum down to $U(1)_Q$. Without loss of generality, we can take the conventional VEV

$$\langle \Phi \rangle_0 = \begin{pmatrix} 0 \\ \frac{v}{\sqrt{2}} \end{pmatrix}, \quad \text{so that} \quad \Phi(x) = \begin{pmatrix} G^+(x) \\ \frac{v+h(x)+iG^0(x)}{\sqrt{2}} \end{pmatrix}, \quad (4.14)$$

where $v \in \mathbb{R}^+$ is determined by the choice of vacuum configuration (between (4.9), (4.11) and (4.13)). As usual, the fields $G^0(x)$ and $G^\pm(x)$ are would-be Goldstone bosons that can be “gauged away” into the unitary gauge.

- For the minimum solution set (4.13), both singlets also acquire a non-zero VEV out of the possible $\mathcal{Z}_2^{(r)}$ invariant (discrete) solution set $\langle S_r \rangle_0 = \pm v_r'''$ ($v_r''' \in \mathbb{R}^+$), thus also spontaneously breaking the $\mathcal{Z}_2^{(r)}$ symmetries of the vacuum ($r = 1, 2$). After $SU(2)_L \times U(1)_Y \times \mathcal{Z}_2^{(1)} \times \mathcal{Z}_2^{(2)} \rightarrow U(1)_Q$ SSB, $h(x)$ and the field perturbations $\xi_r(x) \equiv S_r(x) - \langle S_r \rangle_0$ mix in the $hS_r S_r$ ($r = 1, 2$) couplings (contained in the portal terms) and in the $S_1 S_1 S_2 S_2$ coupling. Hence, $h(x)$, $\xi_1(x)$, $\xi_2(x)$ are interaction eigenstates, while the mass eigenstates (physical fields) $h'(x)$, $h_{\xi_1}(x)$, $h_{\xi_2}(x)$ are given by a flavour space rotation of the interaction eigenstates, so that the scalar mass terms are diagonal (without flavour mixing) in the mass basis. In this scenario, h' , h_{ξ_1} and h_{ξ_2} are Higgs-like particles (one of them being the 125 GeV discovered Higgs boson), and therefore, are able to decay (unstable particles). The spontaneously (but not explicitly) broken $\mathcal{Z}_2^{(1)} \times \mathcal{Z}_2^{(2)}$ symmetry is now *hidden* in the Lagrangian density. For the minimum solution set (4.13), the model does not contain a DM particle candidate, and hence, this vacuum configuration does not hold any interest in the context of this work.

- For the minimum solution set (4.11), one of the singlets also acquires a non-zero VEV out of the possible $\mathcal{Z}_2^{(r)}$ invariant (discrete) solution set $\langle S_r \rangle_0 = \pm v'_r$ ($v'_r \in \mathbb{R}^+$), thus also spontaneously breaking the $\mathcal{Z}_2^{(r)}$ symmetry of the vacuum; while the other $\mathcal{Z}_2^{(r')}$ symmetry remains unbroken ($r, r' = 1, 2 \wedge r \neq r'$). After $\text{SU}(2)_L \times \text{U}(1)_Y \times \mathcal{Z}_2^{(1)} \times \mathcal{Z}_2^{(2)} \rightarrow \text{U}(1)_Q \times \mathcal{Z}_2^{(r')}$ SSB, $h(x)$ and the field perturbation $\xi_r(x) \equiv S_r(x) - \langle S_r \rangle_0$ mix in the $hS_r S_r$ coupling (contained in the portal term), but $S_{r'}(x)$ does not mix. Hence, while $S_{r'}(x)$ is a mass eigenstate (physical field), $h(x), \xi_r(x)$ are interaction eigenstates. The two remaining mass eigenstates $h'(x), h_{\xi_r}(x)$ are given by a flavour space rotation of the two interaction eigenstates, so that the scalar mass terms are diagonal (without flavour mixing) in the mass basis. In this scenario, h' and h_{ξ_r} are Higgs-like particles (one of them being the 125 GeV discovered Higgs boson), and therefore, are able to decay (unstable particles). The spontaneously (but not explicitly) broken $\mathcal{Z}_2^{(r)}$ symmetry is now *hidden* in the Lagrangian density. On the other hand, the unbroken $\mathcal{Z}_2^{(r')}$ symmetry ensures that $S_{r'}$ does not decay (stable particle), thus being a DM candidate. For the minimum solution set (4.13), the model contains an extra Higgs-like particle and a DM particle candidate.

We will consider the vacuum configuration (4.9) of this model. For this minimum solution set, both singlets do not acquire a VEV, i.e. $\langle S_r \rangle_0 = 0$ ($r = 1, 2$), so that the $\mathcal{Z}_2^{(1)} \times \mathcal{Z}_2^{(2)}$ symmetry is not spontaneously broken and there is no flavour mixing with $h(x)$. Hence, $h(x), S_1(x)$ and $S_2(x)$ are mass eigenstates – i.e., these fields correspond to physical particles – where h is the Higgs boson and S_r ($r = 1, 2$) are new spin 0 massive particles. Using the minimum condition in (4.9), $v^2 = -\mu_H^2/\lambda_H \Leftrightarrow \mu_H^2 = -\lambda_H v^2$ (the same as that of the SM), the (expanded) scalar potential, in the unitary gauge $\Phi(x) \rightarrow \frac{1}{\sqrt{2}} \begin{pmatrix} 0 & v + h(x) \end{pmatrix}^\top$, is given by

$$V(|\Phi|, S_1, S_2) = \frac{1}{2} \overbrace{(2\lambda_H v^2)}^{=m_h^2} h^2 + \lambda_H v h^3 + \frac{\lambda_H}{4} h^4 + \frac{\lambda_{12}}{4} S_1^2 S_2^2 + \sum_{r=1}^2 \left[\frac{1}{2} \underbrace{\left(\mu_r^2 + \frac{\kappa_{Hr} v^2}{2} \right)}_{=m_{S_r}^2} S_r^2 + \frac{\lambda_r}{4!} S_r^4 + \frac{\kappa_{Hr} v}{2} h S_r^2 + \frac{\kappa_{Hr}}{4} h^2 S_r^2 \right], \quad (4.15)$$

which written in terms of the scalar masses $m_h = \sqrt{2\lambda_H v^2}$ and $m_{S_r} = \sqrt{\mu_r^2 + \kappa_{Hr} v^2/2}$ ($r = 1, 2$), reads as

$$-\mathcal{L}_{\text{SM}+2\text{RSS}} \supset V(|\Phi|, S_1, S_2) = \frac{1}{2} m_h^2 h^2 + \frac{m_h^2}{2v} h^3 + \frac{m_h^2}{8v^2} h^4 + \frac{\lambda_{12}}{4} S_1^2 S_2^2 + \sum_{r=1}^2 \left[\frac{1}{2} m_{S_r}^2 S_r^2 + \frac{\lambda_r}{4!} S_r^4 + \frac{\kappa_{Hr} v}{2} h S_r^2 + \frac{\kappa_{Hr}}{4} h^2 S_r^2 \right]. \quad (4.16)$$

The unbroken $\mathcal{Z}_2^{(1)} \times \mathcal{Z}_2^{(2)}$ symmetry ensures that S_1 and S_2 do not decay (stable particles), thus being DM candidates. This is shown in Figure 4.1, which presents the Feynman rules for the new interaction vertices that emerge in this SM extension.

4.2 Cross Sections for Direct Detection and Relic Density of DM

Let us obtain analytical expressions for the cross sections that will be relevant to the analysis of our future (numerical) results. As discussed in Section 3.3.1, direct detection is – together with the observed

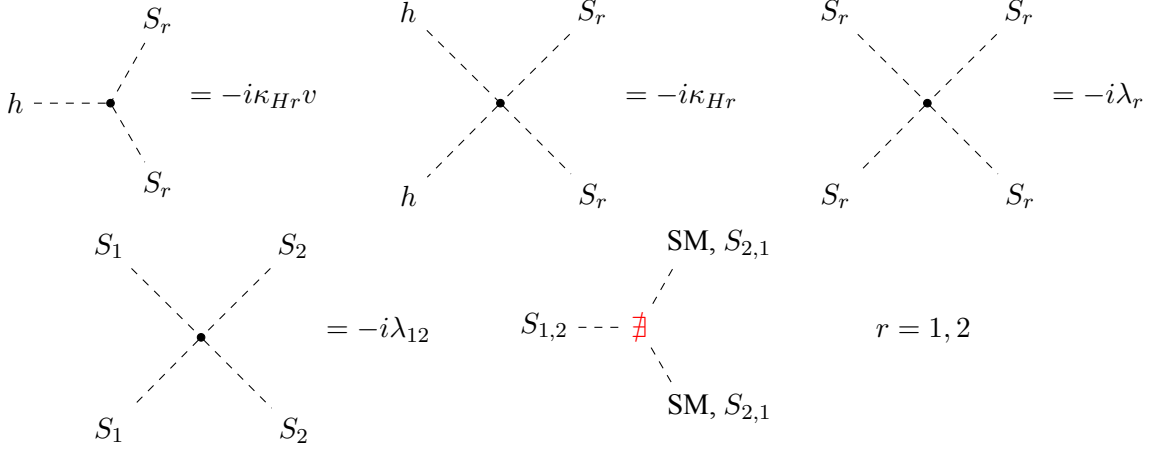


Figure 4.1: Feynman rules for the interaction vertices involving the S_1 and S_2 dark matter particle candidates. The decays $S_{1,2} \rightarrow \text{SM SM}$ and $S_{1,2} \rightarrow S_{2,1} S_{2,1}$ are forbidden by “dark parity” (or $\mathcal{Z}_2^{(r)}$ charge, $r = 1, 2$) conservation, as a consequence of the $\mathcal{Z}_2^{(1)} \times \mathcal{Z}_2^{(2)}$ discrete symmetry.

DM relic density constraint – responsible for all the free parameter space experimental exclusion of the (one) real scalar singlet SM extension, and hence, we should expect it to also play a crucial role in the experimental exclusion of the two-real-scalar-singlet SM extension. For this reason, we start by computing the spin-independent (SI) cross section of DM-nucleon elastic scattering $S_r N \rightarrow S_r N$, $N = p, n$ ($r = 1, 2$). Next, we compute $S_r S_r \rightarrow \text{SM } \overline{\text{SM}}$ ($r = 1, 2$) DM annihilation cross sections, where $\text{SM} = h, W^+, Z, \ell (= e^-, \mu^-, \tau^-), q (= u, d, c, s, t, b)$ are SM (final state) particles which are possible to produce in DM annihilation processes of our SM+2RSS model, i.e., SM particles that couple to the Higgs boson (mediator). These are not only relevant for indirect detection, but also to the DM density/abundance, under the assumption of its time evolution being described by the freeze-out mechanism. We also compute the cross sections for the inter-dark annihilation/creation processes $S_{1,2} S_{1,2} \rightarrow S_{2,1} S_{2,1}$, because (as we shall see in Section 4.4) they are also impactful to the DM relic density.

4.2.1 Spin-Independent Cross Section of DM-Nucleon Elastic Scattering

The standard WIMP-nucleon scattering treatments rely on effective field theory methods, as in e.g. Refs. [68, 69, 70, 71, 72, 73]. We start by constructing the most general effective theory of interactions between DM particles S_r ($r = 1, 2$) and all possible nucleon constituent particles, i.e., the quarks $q = u, d, s, c, b, t$ and the gluon g . The corresponding effective Lagrangian density of interaction is given by the following linear combination of higher-mass-dimensional (effective) operators [71],

$$\begin{aligned} \mathcal{L}_{\text{int}}^{(\text{eff})}[S_r, q, G_\mu^a] = & \sum_q \left[C_q^S m_q S_r^2(x) \bar{q}(x) q(x) + C_q^{T_2} \frac{1}{m_{S_r}^2} S_r(x) i \partial_\mu i \partial_\nu S_r(x) \mathcal{O}_q^{\mu\nu}(x) \right] \\ & + C_g^S \frac{\alpha_s}{\pi} S_r^2(x) \sum_{a=1}^8 G_{\mu\nu}^a(x) G^{a\mu\nu}(x) + C_g^{T_2} \frac{1}{m_{S_r}^2} S_r(x) i \partial_\mu i \partial_\nu S_r(x) \mathcal{O}_g^{\mu\nu}(x), \end{aligned} \quad (4.17)$$

$$(4.18)$$

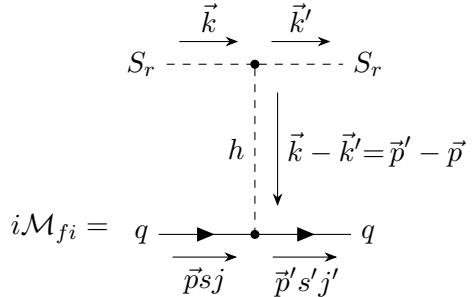
where $\mathcal{O}_{\mu\nu}^q(x)$ and $\mathcal{O}_{\mu\nu}^g(x)$ are the twist-2 operators of quarks and gluon, respectively defined by

$$\mathcal{O}_q^{\mu\nu}(x) \equiv \frac{i}{2} \bar{q}(x) \left(\gamma^\mu D^\nu + \gamma^\nu D^\mu - \frac{1}{2} g^{\mu\nu} \not{D} \right) q(x) \quad (4.19)$$

$$\mathcal{O}_g^{\mu\nu}(x) \equiv \sum_{a=1}^8 \left(G^{a\lambda\mu}(x) G^a_{\lambda\nu}(x) - \frac{1}{4} g^{\mu\nu} G^a_{\lambda\rho}(x) G^{a\lambda\rho}(x) \right). \quad (4.20)$$

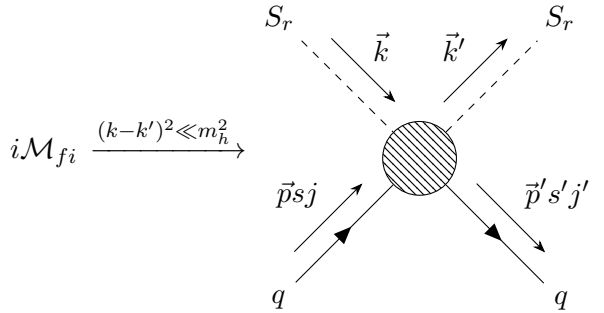
One should notice that there is no spin-dependent effective interactions in the scalar DM case [71]. For the elastic scattering $S_r N \rightarrow S_r N$, the Lagrangian density describing the effective DM-nucleon interaction is obtained by evaluating the matrix elements of the DM effective interaction terms with quarks (4.17) and gluon (4.18) between nucleon states $|N\rangle$ with the same 4-momentum – i.e., in the zero transferred momentum limit. Hence, all Wilson coefficients $C_{q,g}^{S,T_2}$ should also be evaluated in the low transferred momentum regime, to any order of approximation in perturbation theory [71, 73].

We shall not consider loop corrections in the calculation of the Wilson coefficients $C_{q,g}^{S,T_2}$. Hence, at tree-level of approximation in perturbation theory, the only possible process is DM-quark scattering $S_r(\vec{k}) q(\vec{p}, s, j) \rightarrow S_r(\vec{k}') q(\vec{p}', s', j')$, $r = 1, 2$, where s, s' and j, j' are spin and colour indices, respectively. This process has a (reduced) transition amplitude given by



$$i\mathcal{M}_{fi} = c_{j'j}^\dagger \bar{u}_{\vec{p}'s'} \left(-i \frac{m_q}{v} \right) u_{\vec{p}s} c_j \frac{i}{(k - k')^2 - m_h^2} (-i \kappa_{Hr} v) \\ = \delta_{j'j} \bar{u}_{\vec{p}'s'} u_{\vec{p}s} \frac{-i m_q \kappa_{Hr}}{(k - k')^2 - m_h^2}. \quad (4.21)$$

In the low transferred momentum limit $q^\mu \equiv k^\mu - k'^\mu = p'^\mu - p^\mu \approx 0$ ($\Rightarrow |q^2| \approx 0 \ll m_h^2$), the expression for the transition amplitude is simplified to



$$i\mathcal{M}_{fi} \xrightarrow{(k-k')^2 \ll m_h^2} = \delta_{j'j} \bar{u}_{\vec{p}'s'} u_{\vec{p}s} \left(+i \frac{m_q \kappa_{Hr}}{m_h^2} \right), \quad (4.22)$$

which corresponds to an effective quartic coupling $S_r S_r \bar{q} q$ represented by the interaction term

$$\mathcal{L}_{\text{int}}^{(\text{eff})}[S_r, q] = \sum_q + \frac{m_q \kappa_{Hr}}{(2!) m_h^2} S_r^2 \bar{q} q = \sum_q C_q^{S(\text{LO})} m_q S_r^2 \bar{q} q, \quad \text{where} \quad C_q^{S(\text{LO})} \equiv + \frac{\kappa_{Hr}}{2 m_h^2} \quad (4.23)$$

is the Wilson coefficient describing the effective coupling between a DM particle S_r and a quark q in the low transferred momentum regime at leading order (LO). Therefore, at tree-level, the effective Lagrangian density of interaction between a DM particle S_r and a nucleon $N = p, n$ is given by

$$\mathcal{L}_{\text{int}}^{(\text{eff})}[S_r, N] = \langle N(\vec{p}) | \mathcal{L}_{\text{int}}^{(\text{eff})}[S_r, q] | N(\vec{p}) \rangle \bar{N} N = \sum_q C_q^{S(\text{LO})} m_q \langle N(\vec{p}) | \bar{q} q | N(\vec{p}) \rangle S_r^2 \bar{N} N \quad (4.24)$$

$$= \left[\sum_{q'=u,d,s} C_{q'}^{S(\text{LO})} f_{T_{q'}}^{(N)} m_N + \sum_{Q=c,b,t} C_Q^{S(\text{LO})} m_Q \langle N(\vec{p}) | \bar{Q}Q | N(\vec{p}) \rangle \right] S_r^2 \bar{N} N, \quad (4.25)$$

where m_N is the nucleon mass and

$$f_{T_{q'}}^{(N)} \equiv \frac{m_{q'} \langle N(\vec{p}) | \bar{q}' q' | N(\vec{p}) \rangle}{m_N} \quad (4.26)$$

is the fraction of nucleon mass that is attributed to a light quark $q' = u, d, s$.

The following results are essential for proceeding with our effective treatment, and are explained in detail in Appendix B.

- As shown by M. A. Shifman, A. I. Vainshtein and V. I. Zakharov in Ref. [74], the heavy quark contribution to the nucleon mass – under the heavy quark expansion – is given by

$$m_Q \langle N(\vec{p}) | \bar{Q}Q | N(\vec{p}) \rangle = -\frac{2}{3} \frac{\alpha_s}{8\pi} \sum_{a=1}^8 \langle N(\vec{p}) | G_{\mu\nu}^a G^{a\mu\nu} | N(\vec{p}) \rangle + \mathcal{O}(1/(4m_Q^2)), \quad (4.27)$$

$\forall Q = c, b, t$ and hence, the DM-nucleon effective interaction (4.25) can be simplified to

$$\mathcal{L}_{\text{int}}^{(\text{eff})}[S_r, N] \approx \left[\sum_{q'=u,d,s} C_{q'}^{S(\text{LO})} f_{T_{q'}}^{(N)} m_N - \sum_{Q=c,b,t} C_Q^{S(\text{LO})} \frac{2}{3} \frac{\alpha_s}{8\pi} \sum_{a=1}^8 \langle N(\vec{p}) | G_{\mu\nu}^a G^{a\mu\nu} | N(\vec{p}) \rangle \right] \times S_r^2 \bar{N} N. \quad (4.28)$$

Note that effective scalar operators for heavy quarks can be replaced by effective scalar operators for the gluon (and vice-versa), which is why some references omit these heavy quark operators in the effective interactions (4.17). For more details, see e.g. Ref. [70].

- It is possible to show from scale invariance breaking in QCD (see Appendix B for a detailed derivation, in particular Sections B.3 and B.4) that the trace of the QCD energy-momentum tensor¹ is given by²

$$(\partial_\mu j_{\text{scale}}^\mu =) \Theta^\mu_\mu = \sum_q m_q \bar{q}q + \frac{\beta(\alpha_s)}{4\alpha_s} \sum_{a=1}^8 G_{\mu\nu}^a G^{a\mu\nu} \quad (4.29)$$

$$\approx \sum_q m_q \bar{q}q - \beta_0 \frac{\alpha_s}{8\pi} \sum_{a=1}^8 G_{\mu\nu}^a G^{a\mu\nu}, \quad (4.30)$$

to any order in Eq.(4.29) and at 1-loop order of approximation $\beta(\alpha_s) \approx -\beta_0 \frac{\alpha_s^2}{2\pi}$ in Eq. (4.30), with $\beta_0 = \frac{11}{3} N_c - \frac{2}{3} N_f^{(q)} = 7$. The first and second terms in the right-hand side (of both equations) exhibit the scale invariance breaking in QCD at the classical and quantum loop levels, respectively. If quarks were massless, this last term would break the classical scale invariance at the quantum level, thus being called the QCD *trace anomaly*.

- The mass of a nucleon N is given by the matrix element of the trace of the QCD energy-momentum tensor between (appropriately normalized) nucleon states $|N\rangle$ with the same 4-momentum (i.e., in

¹We choose to work with the $\mu \leftrightarrow \nu$ symmetric and $\text{SU}(3)_c$ gauge invariant Belinfante-Rosenfeld EMT (B.23) of QCD, but there are other valid choices (e.g., see Ref. [75]).

²The *non-conserved* Noether current j_{scale}^μ associated to scale transformations is given in Eq. (B.32).

the limit of zero transferred momentum) [76, 73, 31], thus giving

$$m_N = \langle N(\vec{p}) | \Theta^\mu_\mu | N(\vec{p}) \rangle = \sum_q m_q \langle N(\vec{p}) | \bar{q}q | N(\vec{p}) \rangle + \frac{\beta(\alpha_s)}{4\alpha_s} \sum_{a=1}^8 \langle N(\vec{p}) | G^a_{\mu\nu} G^{a\mu\nu} | N(\vec{p}) \rangle$$

$$\approx \sum_q m_q \langle N(\vec{p}) | \bar{q}q | N(\vec{p}) \rangle - \underbrace{\beta_0}_{=7} \frac{\alpha_s}{8\pi} \sum_{a=1}^8 \langle N(\vec{p}) | G^a_{\mu\nu} G^{a\mu\nu} | N(\vec{p}) \rangle \quad (4.31)$$

$$\approx \sum_{q'=u,d,s} m_{q'} \langle N(\vec{p}) | \bar{q}'q' | N(\vec{p}) \rangle - \frac{9\alpha_s}{8\pi} \sum_{a=1}^8 \langle N(\vec{p}) | G^a_{\mu\nu} G^{a\mu\nu} | N(\vec{p}) \rangle, \quad (4.32)$$

where the second line (4.31) is the 1-loop approximation $\beta(\alpha_s) \approx -\beta_0 \frac{\alpha_s}{2\pi}$ and the third line (4.32) is additionally approximated by the heavy quark contribution expression (4.27). Furthermore, with definition (4.26), the nucleon mass (4.32) can be written as

$$m_N = \sum_{q'=u,d,s} f_{T_{q'}}^{(N)} m_N - \frac{9\alpha_s}{8\pi} \sum_{a=1}^8 \langle N(\vec{p}) | G^a_{\mu\nu} G^{a\mu\nu} | N(\vec{p}) \rangle = \left[\sum_{q'=u,d,s} f_{T_{q'}}^{(N)} + f_{T_G}^{(N)} \right] m_N, \quad (4.33)$$

where

$$f_{T_G}^{(N)} \equiv \frac{-\frac{9\alpha_s}{8\pi} \sum_{a=1}^8 \langle N(\vec{p}) | G^a_{\mu\nu} G^{a\mu\nu} | N(\vec{p}) \rangle}{m_N} = 1 - \sum_{q'=u,d,s} f_{T_{q'}}^{(N)} \quad (4.34)$$

is the fraction of nucleon mass that is *not* attributed to light quarks – thus being attributed to the heavy quarks $Q = c, b, t$ and gluon. Finally, with definition (4.34), the DM-nucleon effective interaction (4.28) can be written as

$$\mathcal{L}_{\text{int}}^{(\text{eff})}[S_r, N] = \left[\sum_{q'=u,d,s} C_{q'}^{S(\text{LO})} f_{T_{q'}}^{(N)} + \sum_{Q=c,b,t} C_Q^{S(\text{LO})} \frac{2}{27} f_{T_G}^{(N)} \right] m_N S_r^2 \bar{N} N, \quad (4.35)$$

where the nucleon mass fractions $f_{T_{q'}}^{(N)}$, $q' = u, d, s$ and $f_{T_G}^{(N)}$ are obtained from lattice QCD simulations.

In our particular case, the Wilson coefficients $C_q^{S(\text{LO})} \equiv +\frac{\kappa_{Hr}}{2m_h^2}$ do not depend on the quark flavour $q = u, d, s, c, b, t$. Hence, we can factor them out in Eq. (4.35), thus obtaining

$$\mathcal{L}_{\text{int}}^{(\text{eff})}[S_r, N] = +\frac{\kappa_{Hr}}{2m_h^2} \left[\sum_{q'=u,d,s} f_{T_{q'}}^{(N)} + \frac{6}{27} f_{T_G}^{(N)} \right] m_N S_r^2 \bar{N} N, \quad f_{T_G}^{(N)} = 1 - \sum_{q'=u,d,s} f_{T_{q'}}^{(N)} \quad (4.36)$$

$$= f_N^{(\text{LO})} S_r^2 \bar{N} N, \quad \text{where} \quad f_N^{(\text{LO})} \equiv +\frac{\kappa_{Hr}}{2m_h^2} \left[\frac{21}{27} \sum_{q'=u,d,s} f_{T_{q'}}^{(N)} + \frac{6}{27} \right] m_N \quad (4.37)$$

is the Wilson coefficient describing the effective DM-nucleon coupling, at leading order (LO), in the low transferred momentum regime (i.e., for an elastic scattering $S_r N \rightarrow S_r N$).

Our final task is to compute the DM-nucleon elastic scattering cross section, $\sigma^{\text{SI}}(S_r N \rightarrow S_r N)$. The transition amplitude for the $S_r(\vec{k}) N(\vec{p}, s) \rightarrow S_r(\vec{k}') N(\vec{p}', s')$ elastic scattering follows directly from

the DM-nucleon effective interaction term (4.37), and is given by

$$i\mathcal{M}_{fi} = \overline{u_{p's'}} u_{ps} \left(+ i(2!) f_N^{(LO)} \right), \quad (4.38)$$

so that the spin-averaged squared (transition) amplitude is

$$|\overline{\mathcal{M}_{fi}}|^2 = \frac{1}{2} \sum_{s,s'} \mathcal{M}_{fi}^\dagger \mathcal{M}_{fi} = \frac{1}{2} \times 4 |f_N^{(LO)}|^2 \times \sum_{s,s'} \overline{u_{ps'}} \overline{u_{p's'}} u_{ps} u_{p's} \quad (4.39)$$

$$= \frac{1}{2} \times 4 |f_N^{(LO)}|^2 \times \text{Tr} [(\not{p} + m_N \mathbb{1})(\not{p}' + m_N \mathbb{1})] = 4 |f_N^{(LO)}|^2 (4m_N^2 - t), \quad (4.40)$$

where $t = (p-p')^2$ refers to the Mandelstam variable. The cross section – computed in the center-of-mass reference frame, without loss of generality – is given by the usual $1\,2 \rightarrow 3\,4$ formula,

$$\sigma(i \rightarrow f) = \frac{1}{s!} \frac{1}{64\pi^2} \frac{|\vec{k}_3|}{|\vec{k}_1|_s} \int d\Omega_{k_3} |\overline{\mathcal{M}_{fi}}|^2, \quad (4.41)$$

where $s = 0$ is the number of identical final state particles and $s \equiv (k_1 + k_2)^2 = (p + k)^2$ is the Mandelstam variable which corresponds to the squared total energy in the center-of-mass reference frame.³ Total energy conservation implies $|\vec{k}_1| = |\vec{k}_3| \Leftrightarrow |\vec{p}| = |\vec{p}'|$, thus giving

$$\sigma^{\text{SI}}(S_r N \rightarrow S_r N) = \frac{1}{64\pi^2} \frac{1}{s} \int d\Omega_{p'} 4 |f_N^{(LO)}|^2 (4m_N^2 - t). \quad (4.42)$$

The following low-energy approximations are valid in the non-relativistic regime,

$$4m_N^2 \gg 2\vec{p}^2(1 - \cos\theta_{p'}) = -t (> 0) \quad \Leftrightarrow \quad 4m_N^2 - t \approx 4m_N^2 \quad (4.43)$$

$$s = m_N^2 + m_{S_r}^2 + 2\sqrt{m_N^2 + 2\vec{p}^2} \sqrt{m_{S_r}^2 + 2\vec{p}^2} + 2\vec{p}^2 \approx (m_N + m_{S_r})^2, \quad (4.44)$$

which inserted in Eq. (4.42), give the popular expression for the spin-independent (SI) cross section of DM-nucleon elastic scattering

$$\sigma^{\text{SI}}(S_r N \rightarrow S_r N) = \frac{1}{\pi} \left(\frac{m_N}{m_N + m_{S_r}} \right)^2 |f_N^{(LO)}|^2, \quad (4.45)$$

where the $f_N^{(LO)}$ Wilson coefficient is given in Eq. (4.37).

³We are taking $k_1^\mu = p^\mu$, $k_2^\mu = k^\mu$, $k_3^\mu = p'^\mu$, $k_4^\mu = k'^\mu$ without loss of generality.

4.2.2 Cross Section of Dark Matter Annihilation Processes

We start by computing the cross section for DM annihilation to a Higgs boson pair. At tree-level, the (reduced) transition amplitude for the $S_r(\vec{k}_1) S_r(\vec{k}_2) \rightarrow h(\vec{k}_3) h(\vec{k}_4)$ process is given by

$$i\mathcal{M}_{fi} = \text{[Contact]} + \text{[t-channel]} + \text{[u-channel]} + \text{[s-channel]} \quad (4.46)$$

$$+ \text{[t-channel]} + \text{[u-channel]} + \text{[s-channel]} \quad (4.47)$$

$$= -i\kappa_{Hr} \left[1 + \frac{3m_h^2}{s - m_h^2 + im_h\Gamma_h} + \frac{\kappa_{Hr}v^2}{t - m_{S_r}^2} + \frac{\kappa_{Hr}v^2}{u - m_{S_r}^2} \right], \quad (4.48)$$

where $s \equiv (k_1 + k_2)^2$, $t \equiv (k_1 - k_3)^2$, $u \equiv (k_1 - k_4)^2$ are the Mandelstam variables, and the spin-averaged squared (transition) amplitude gives

$$|\overline{\mathcal{M}_{fi}}|^2 = \mathcal{M}_{fi}^\dagger \mathcal{M}_{fi} = \kappa_{Hr}^2 \left[1 + \frac{9m_h^4}{(s - m_h^2)^2 + m_h^2\Gamma_h^2} + \frac{\kappa_{Hr}^2 v^4}{(t - m_{S_r}^2)^2} + \frac{\kappa_{Hr}^2 v^4}{(u - m_{S_r}^2)^2} \right] \quad (4.49)$$

$$+ \frac{6m_h^2(s - m_h^2)}{(s - m_h^2)^2 + m_h^2\Gamma_h^2} + \frac{2\kappa_{Hr}v^2}{t - m_{S_r}^2} + \frac{2\kappa_{Hr}v^2}{u - m_{S_r}^2} + \frac{2\kappa_{Hr}^2 v^4}{(t - m_{S_r}^2)(u - m_{S_r}^2)} \quad (4.50)$$

$$\left[\frac{6m_h^2\kappa_{Hr}v^2(s - m_h^2)(t - m_{S_r}^2)}{(s - m_h^2)^2(t - m_{S_r}^2)^2 + m_h^2(t - m_{S_r}^2)^2\Gamma_h^2} + \frac{6m_h^2\kappa_{Hr}v^2(s - m_h^2)(u - m_{S_r}^2)}{(s - m_h^2)^2(u - m_{S_r}^2)^2 + m_h^2(u - m_{S_r}^2)^2\Gamma_h^2} \right], \quad (4.51)$$

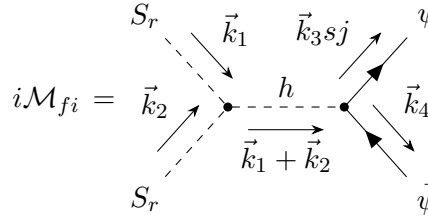
which depends on the 3-momentum polar angle θ_{k_3} through $t, u = -\vec{k}_1^2 - \vec{k}_3^2 \pm 2|\vec{k}_1||\vec{k}_3|\cos\theta_{k_3} = m_{S_r}^2 + m_h^2 - s/2 \pm 2(s/4 - m_{S_r}^2)^{1/2}(s/4 - m_h^2)^{1/2}\cos\theta_{k_3}$ (but not s).⁴ The cross section, computed in the center-of-mass reference frame, is obtained by the usual $1\ 2 \rightarrow 3\ 4$ formula (4.41), thus giving

$$\begin{aligned} \sigma(S_r S_r \rightarrow hh) &= \frac{1}{2!} \frac{1}{64\pi^2} \frac{1}{s} \sqrt{\frac{1 - 4m_h^2/s}{1 - 4m_{S_r}^2/s}} \int d\Omega_{k_3} |\overline{\mathcal{M}_{fi}}|^2 \\ &= \sqrt{\frac{1 - 4m_h^2/s}{1 - 4m_{S_r}^2/s}} \frac{\kappa_{Hr}^2/(32\pi s)}{(s - m_h^2)^2 + m_h^2\Gamma_h^2} \left[(s + 2m_h^2)^2 + m_h^2\Gamma_h^2 \right] \end{aligned} \quad (4.52)$$

⁴We choose to work in the center-of-mass reference frame, where $\vec{k}_{i(f)}^{\text{total}} = \vec{k}_{1(3)} + \vec{k}_{2(4)} = 0$.

$$\begin{aligned}
 & + \frac{2\kappa_{Hr}^2 v^4 [(s - m_h^2)^2 + m_h^2 \Gamma_h^2]}{m_h^4 - 4m_h^2 m_{S_r}^2 + m_{S_r}^2 s} + \frac{8\kappa_{Hr} v^2 \tanh^{-1} \left(\frac{\sqrt{(s-4m_h^2)(s-4m_{S_r}^2)}}{s-2m_h^2} \right)}{(s - 2m_h^2) \sqrt{(s - 4m_h^2)(s - 4m_{S_r}^2)}} \\
 & \times \left\{ \kappa_{Hr} v^2 [(s - m_h^2)^2 + m_h^2 \Gamma_h^2] - (s - 2m_h^2)(s^2 + m_h^2[s - 2m_h^2 + \Gamma_h^2]) \right\} \Bigg]. \quad (4.53)
 \end{aligned}$$

All remaining DM annihilation processes that produce SM particles (i.e., charged fermions $\psi = \ell, q$ and weak gauge bosons W^\pm, Z) are s -channels mediated by a (virtual) Higgs boson. Let us consider fermion anti-fermion pair production. At tree-level, the (reduced) transition amplitude for a $S_r(\vec{k}_1) S_r(\vec{k}_2) \rightarrow \psi(\vec{k}_3, s, j) \bar{\psi}(\vec{k}_4, s', j')$ annihilation process is given by



$$i\mathcal{M}_{fi} = \delta_{jj'} \bar{u}_{\vec{k}_3 s} v_{\vec{k}_4 s'} \frac{-im_\psi \kappa_{Hr}}{s - m_h^2 + im_h \Gamma_h}, \quad (4.54)$$

so that the spin-averaged squared (transition) amplitude is

$$\overline{|\mathcal{M}_{fi}|^2} = \sum_{j,j'} \sum_{s,s'} \mathcal{M}_{fi}^\dagger \mathcal{M}_{fi} = \frac{m_\psi^2 \kappa_{Hr}^2}{(s - m_h^2)^2 + m_h^2 \Gamma_h^2} \sum_{j,j'} \sum_{s,s'} \delta_{jj'} \delta_{jj'} \bar{u}_{\vec{k}_3 s} u_{\vec{k}_3 s'} \bar{v}_{\vec{k}_4 s'} v_{\vec{k}_4 s}, \quad (4.55)$$

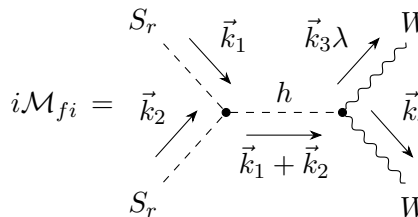
$$= N_c \frac{m_\psi^2 \kappa_{Hr}^2}{(s - m_h^2)^2 + m_h^2 \Gamma_h^2} \text{Tr}[(\not{k}_3 + m_\psi \mathbb{1})(\not{k}_4 - m_\psi \mathbb{1})] = N_c \frac{2m_\psi^2 \kappa_{Hr}^2 (s - 4m_\psi^2)}{(s - m_h^2)^2 + m_h^2 \Gamma_h^2}, \quad (4.56)$$

where N_c is the number of colours, and the cross section (computed in the center-of-mass reference frame) gives

$$\sigma(S_r S_r \rightarrow \psi \bar{\psi}) = \frac{1}{0!} \frac{1}{64\pi^2} \frac{1}{s} \sqrt{\frac{1 - 4m_\psi^2/s}{1 - 4m_{S_r}^2/s}} \int d\Omega_{k_3} \overline{|\mathcal{M}_{fi}|^2} \quad (4.57)$$

$$= \frac{N_c}{8\pi} \sqrt{\frac{(1 - 4m_\psi^2/s)^3}{1 - 4m_{S_r}^2/s}} \frac{m_\psi^2 \kappa_{Hr}^2}{(s - m_h^2)^2 + m_h^2 \Gamma_h^2}, \quad \text{with} \quad N_c = \begin{cases} 1, & \psi = \ell \\ 3, & \psi = q \end{cases}. \quad (4.58)$$

Now considering weak gauge boson pair production, the tree-level (reduced) transition amplitude for the $S_r(\vec{k}_1) S_r(\vec{k}_2) \rightarrow W^+(\vec{k}_3, \lambda) W^-(\vec{k}_4, \lambda')$ annihilation process is given by



$$i\mathcal{M}_{fi} = g_{\mu\nu} \varepsilon_{\vec{k}_3 \lambda}^{*\mu} \varepsilon_{\vec{k}_4 \lambda'}^\nu \frac{+ig_w m_W \kappa_{Hr} v}{s - m_h^2 + im_h \Gamma_h}, \quad (4.59)$$

so that the spin-averaged squared (transition) amplitude is

$$\overline{|\mathcal{M}_{fi}|^2} = \sum_{\lambda, \lambda'} \mathcal{M}_{fi}^\dagger \mathcal{M}_{fi} = \frac{g_w^2 m_W^2 \kappa_{Hr}^2 v^2}{(s - m_h^2)^2 + m_h^2 \Gamma_h^2} \sum_{\lambda, \lambda'} \varepsilon_{\vec{k}_3 \lambda}^\alpha (\varepsilon_{\vec{k}_4 \lambda'}^*)_\alpha \varepsilon_{\vec{k}_3 \lambda}^{*\mu} (\varepsilon_{\vec{k}_4 \lambda'}^\mu)_\mu \quad (4.60)$$

$$= \frac{g_w^2 m_W^2 \kappa_{Hr}^2 v^2}{(s - m_h^2)^2 + m_h^2 \Gamma_h^2} \left(-g^{\alpha\mu} + \frac{k_3^\alpha k_3^\mu}{m_W^2} \right) \left(-g_{\mu\alpha} + \frac{k_{4\mu} k_{4\alpha}}{m_W^2} \right) \quad (4.61)$$

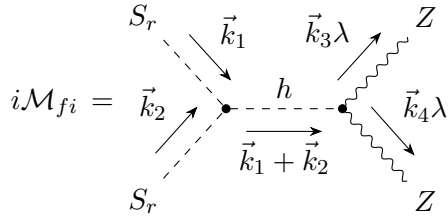
$$= \frac{g_w^2 m_W^2 \kappa_{Hr}^2 v^2}{(s - m_h^2)^2 + m_h^2 \Gamma_h^2} \left[3 + \frac{s^2}{4m_W^4} (1 - 4m_W^2/s) \right], \quad (4.62)$$

and the cross section (computed in the center-of-mass reference frame) gives

$$\sigma(S_r S_r \rightarrow W^+ W^-) = \frac{1}{0!} \frac{1}{64\pi^2} \frac{1}{s} \sqrt{\frac{1 - 4m_W^2/s}{1 - 4m_{S_r}^2/s}} \int d\Omega_{k_3} \overline{|\mathcal{M}_{fi}|^2} \quad (4.63)$$

$$= \frac{1}{16\pi s} \sqrt{\frac{1 - 4m_W^2/s}{1 - 4m_{S_r}^2/s}} \frac{g_w^2 m_W^2 \kappa_{Hr}^2 v^2}{(s - m_h^2)^2 + m_h^2 \Gamma_h^2} \left[3 + \frac{s^2}{4m_W^4} (1 - 4m_W^2/s) \right]. \quad (4.64)$$

The procedure for $S_r(\vec{k}_1) S_r(\vec{k}_2) \rightarrow Z(\vec{k}_3, \lambda) Z(\vec{k}_4, \lambda')$ is almost identical, except for the coupling to the Higgs boson and the two (instead of zero) identical final state particles. At tree-level, the corresponding (reduced) transition amplitude is given by



$$i\mathcal{M}_{fi} = \frac{g_{\mu\nu} \varepsilon_{\vec{k}_3 \lambda}^{*\mu} \varepsilon_{\vec{k}_4 \lambda'}^{*\nu}}{s - m_h^2 + im_h \Gamma_h} + \frac{ig_w(m_Z/\cos\theta_w)\kappa_{Hr}v}{s - m_h^2 + im_h \Gamma_h}, \quad (4.65)$$

so that the spin-averaged squared (transition) amplitude is

$$\overline{|\mathcal{M}_{fi}|^2} = \sum_{\lambda, \lambda'} \mathcal{M}_{fi}^\dagger \mathcal{M}_{fi} = \frac{g_w^2 (m_Z^2/\cos^2\theta_w) \kappa_{Hr}^2 v^2}{(s - m_h^2)^2 + m_h^2 \Gamma_h^2} \sum_{\lambda, \lambda'} \varepsilon_{\vec{k}_3 \lambda}^\alpha (\varepsilon_{\vec{k}_4 \lambda'}^*)_\alpha \varepsilon_{\vec{k}_3 \lambda}^{*\mu} (\varepsilon_{\vec{k}_4 \lambda'}^\mu)_\mu \quad (4.66)$$

$$= \frac{g_w^2 (m_Z^2/\cos^2\theta_w) \kappa_{Hr}^2 v^2}{(s - m_h^2)^2 + m_h^2 \Gamma_h^2} \left(-g^{\alpha\mu} + \frac{k_3^\alpha k_3^\mu}{m_Z^2} \right) \left(-g_{\mu\alpha} + \frac{k_{4\mu} k_{4\alpha}}{m_Z^2} \right) \quad (4.67)$$

$$= \frac{g_w^2 (m_Z^2/\cos^2\theta_w) \kappa_{Hr}^2 v^2}{(s - m_h^2)^2 + m_h^2 \Gamma_h^2} \left[3 + \frac{s^2}{4m_Z^4} (1 - 4m_Z^2/s) \right], \quad (4.68)$$

and the cross section (computed in the center-of-mass reference frame) gives

$$\sigma(S_r S_r \rightarrow ZZ) = \frac{1}{2!} \frac{1}{64\pi^2} \frac{1}{s} \sqrt{\frac{1 - 4m_Z^2/s}{1 - 4m_{S_r}^2/s}} \int d\Omega_{k_3} \overline{|\mathcal{M}_{fi}|^2} \quad (4.69)$$

$$= \frac{1}{32\pi s} \sqrt{\frac{1 - 4m_Z^2/s}{1 - 4m_{S_r}^2/s}} \frac{g_w^2 (m_Z^2/\cos^2\theta_w) \kappa_{Hr}^2 v^2}{(s - m_h^2)^2 + m_h^2 \Gamma_h^2} \left[3 + \frac{s^2}{4m_Z^4} (1 - 4m_Z^2/s) \right]. \quad (4.70)$$

There are two final DM annihilation processes left to consider: the annihilation of a DM particle S_r pair which produces a DM particle $S_{r'}$ pair from (the) other dark sector ($r' \neq r$) and the inverse process. These inter-dark annihilation/production channels $S_{1,2} S_{1,2} \rightarrow S_{2,1} S_{2,1}$ are the only ones that

do not also exist in the (one) real scalar singlet extension of the SM, and they should have an impact on the (total) density of DM in the Universe. At tree-level, the (reduced) transition amplitude for a $S_r(\vec{k}_1) S_r(\vec{k}_2) \rightarrow S_{r'}(\vec{k}_3) S_{r'}(\vec{k}_4)$ annihilation is given by

$$i\mathcal{M}_{fi} = \text{[Diagram 1]} + \text{[Diagram 2]} \quad (4.71)$$

The diagrams represent two tree-level Feynman diagrams for the annihilation process $S_r S_r \rightarrow S_{r'} S_{r'}$. Diagram 1 shows a contact interaction where two incoming scalar lines S_r with momenta \vec{k}_1 and \vec{k}_2 meet at a central vertex, and two outgoing scalar lines $S_{r'}$ with momenta \vec{k}_3 and \vec{k}_4 emerge from the same vertex. Diagram 2 shows an s-channel exchange of a Higgs boson h . Two incoming scalar lines S_r with momenta \vec{k}_1 and \vec{k}_2 meet at a vertex, and a dashed line representing the Higgs boson h with momentum $\vec{k}_1 + \vec{k}_2$ connects this vertex to another vertex from which two outgoing scalar lines $S_{r'}$ with momenta \vec{k}_3 and \vec{k}_4 emerge.

$$= -i \left[\lambda_{12} + \frac{\kappa_{H1} \kappa_{H2} v^2}{s - m_h^2 + i m_h \Gamma_h} \right], \quad (4.72)$$

which is independent of the $i \leftrightarrow f$ “direction” of the process. The same holds true for the spin-averaged squared (transition) amplitude

$$\overline{|\mathcal{M}_{fi}|^2} = \mathcal{M}_{fi}^\dagger \mathcal{M}_{fi} = \lambda_{12}^2 + \kappa_{H1} \kappa_{H2} v^2 \frac{2\lambda_{12}(s - m_h^2) + \kappa_{H1} \kappa_{H2} v^2}{(s - m_h^2)^2 + m_h^2 \Gamma_h^2}, \quad (4.73)$$

but not for the cross section (due to the phase space factor), which computed in the center-of-mass reference frame, gives

$$\sigma(S_r S_r \rightarrow S_{r'} S_{r'}) = \frac{1}{2!} \frac{1}{64\pi^2} \frac{1}{s} \sqrt{\frac{1 - 4m_{S_{r'}}^2/s}{1 - 4m_{S_r}^2/s}} \int d\Omega_{k_3} \overline{|\mathcal{M}_{fi}|^2} \quad (4.74)$$

$$= \frac{1}{32\pi s} \sqrt{\frac{1 - 4m_{S_{r'}}^2/s}{1 - 4m_{S_r}^2/s}} \left[\lambda_{12}^2 + \kappa_{H1} \kappa_{H2} v^2 \frac{2\lambda_{12}(s - m_h^2) + \kappa_{H1} \kappa_{H2} v^2}{(s - m_h^2)^2 + m_h^2 \Gamma_h^2} \right], \quad (4.75)$$

$r, r' = 1, 2 \wedge r' \neq r$. This expression (4.75) explicitly shows that for $m_{S_1} \neq m_{S_2}$ (especially in the low-energy regime), one of the two inter-dark annihilation processes is dominant over the other: the annihilation of the heavier DM particle pair into the lighter DM particle pair.

It should be noted that all (S_r pair) DM annihilation cross sections are either proportional or partially proportional⁵ to $\kappa_{Hr}^2 / [(s - m_h^2)^2 + m_h^2 \Gamma_h^2]$, where the numerator and the denominator arise from the DM-Higgs coupling and the (s-channel) Higgs boson propagator $i/(s - m_h^2 + i m_h \Gamma_h)$, respectively. Hence, the following conclusions are valid in the low-energy regime:

- In the non-relativistic limit $s \approx 4m_{S_r}^2$, an annihilation process $S_r S_r \rightarrow X \bar{X}$ is kinematically impossible for $m_{S_r} < m_X$, and the channel is said to be “closed” (this has nothing to do with the Higgs propagator, but we still mentioned it for its importance).
- In the non-relativistic limit $s \approx 4m_{S_r}^2$, the squared amplitude of the (s-channel) Higgs boson propagator – and consequently, all (kinematically possible) S_r annihilation cross sections – increase (decrease) as $|m_{S_r} - m_h/2|$ decreases (increases).⁶

⁵The Higgs boson pair production $S_r S_r \rightarrow hh$ (4.53) and inter-dark $S_r S_r \rightarrow S_{r'} S_{r'}$ (4.75) annihilation cross sections both contain one point-like interaction term that is not proportional.

⁶This always holds in the low-energy regime, even without taking the non-relativistic limit $s \rightarrow 4m_{S_r}^2$ (but not too far from

- In the non-relativistic limit $s \approx 4m_{S_r}^2$, when the S_r mass actually reaches half of the Higgs boson mass, we hit the resonance pole of the s-channel Higgs propagator, $i/(s - m_h^2 + im_h\Gamma_h) \approx i/(4m_{S_r}^2 - m_h^2 + im_h\Gamma_h) \rightarrow 1/(m_h\Gamma_h)$ ($m_{S_r} \rightarrow m_h/2$). In this resonant scenario, the (virtual) Higgs boson mediator is actually on-shell, since $s \approx m_h^2$. The squared amplitude of the (s-channel) Higgs propagator – and hence, all S_r annihilation cross sections – are maximized.

4.3 Theoretical and Pre-Scan Experimental Constraints

Before conducting a numerical analysis for DM related experimental constraints on the free parameter space of our model, we first must impose the usual theoretical and experimental constraints required of any SM extension.

- **Boundedness from Below Conditions:** To ensure a stable vacuum, the scalar potential must be bounded from below. The boundedness from below conditions are derived by imposing that the potential does not tend to infinitely negative values for any infinite direction in the field space, and are given by [19, 77, 78]:

$$\lambda_H, \lambda_r > 0, \quad r = 1, 2, \quad (4.76)$$

$$\bar{\kappa}_{Hr}/2 \equiv \kappa_{Hr}/2 + \sqrt{\lambda_H \lambda_r}/6 > 0, \quad r = 1, 2, \quad (4.77)$$

$$\bar{\lambda}_{12} \equiv \lambda_{12} + \sqrt{\lambda_1 \lambda_2}/3 > 0, \quad (4.78)$$

$$\kappa_{H1}\sqrt{\lambda_2/6} + \kappa_{H2}\sqrt{\lambda_1/6} + \lambda_{12}\sqrt{\lambda_H} + \sqrt{\lambda_H \lambda_1 \lambda_2}/6 + \sqrt{\bar{\kappa}_{H1}\bar{\kappa}_{H2}\bar{\lambda}_{12}} > 0. \quad (4.79)$$

- **Perturbative Unitarity Conditions:** The conditions for tree-level perturbative unitarity can be obtained by imposing $|\text{Re}(a_0)| < 1/2$ for all the relevant $2 \rightarrow 2$ scalar processes in the high-energy regime $s \gg m_h^2, m_{S_r}^2$, where

$$a_0(s) = \frac{1}{32\pi} \int_{-1}^{+1} \mathcal{M}(s, \cos \theta_{k_3}) d \cos \theta_{k_3} = \frac{1}{16\pi s} \int_{-s}^0 \mathcal{M}(s, t) dt \quad (4.80)$$

is the order $l = 0$ coefficient of the partial-wave expansion (in Legendre polynomials P_l) of a given transition amplitude

$$\mathcal{M}(s, \cos \theta_{k_3}) = 16\pi \sum_{l=0}^{\infty} (2l+1) P_l(\cos \theta_{k_3}) a_l(s), \quad (4.81)$$

$$\text{with } a_l(s) = \frac{1}{32\pi} \int_{-1}^{+1} P_l(\cos \theta_{k_3}) \mathcal{M}(s, \cos \theta_{k_3}) d \cos \theta_{k_3}. \quad (4.82)$$

In the SM+2RSS model, there are six relevant initial/final scalar particle pair states: hh, hS_r, S_1S_2, S_rS_r ($r = 1, 2$). Since all the possible scalar processes have point-like interactions (single-vertex diagrams), then assuming $\cos \theta \neq \pm 1$, $\mathcal{M} = (\text{constant in } s, \theta) + \mathcal{O}(1/s)$ will be independent of $\cos \theta$ (or equivalently, t) in the high-energy regime $s \gg m_h^2, m_{S_r}^2$, which implies $a_l(s) \rightarrow 0$ ($s \gg m_h^2, m_{S_r}^2$) $\forall l \neq 0$.⁷ Hence, the tree-level perturbative unitarity conditions are directly

it either).

⁷This argument relies on the assumption that $|t|, |u| \approx s/2(1 \mp \cos \theta) \gg m_h^2, m_{S_r}^2 \Leftrightarrow \theta \neq 0, \pi$ when $s \gg m_h^2, m_{S_r}^2$. A more rigorous demonstration is to compute $a_0(s)$ in Eq. (4.80) and conclude that only the point-like interaction terms “survive” in the high-energy regime $s \gg m_h^2, m_{S_r}^2$, thus showing that $16\pi|a_0| = |\mathcal{M}|(\theta \neq 0, \pi) < 8\pi$ ($s \gg m_h^2, m_{S_r}^2$).

obtained by

$$16\pi |a_0(hh \rightarrow hh)|_{s \gg m_h^2, m_{S_r}^2} = |\mathcal{M}(hh \rightarrow hh)|_{s \gg m_h^2, m_{S_r}^2}^{(\theta \neq 0, \pi)} = |3m_h^2/v^2| < 8\pi, \quad (4.83)$$

$$16\pi |a_0(S_r S_r \rightarrow S_r S_r)|_{s \gg m_h^2, m_{S_r}^2} = |\mathcal{M}(S_r S_r \rightarrow S_r S_r)|_{s \gg m_h^2, m_{S_r}^2}^{(\theta \neq 0, \pi)} = |\lambda_r| < 8\pi, \quad (4.84)$$

$$16\pi |a_0(i \rightarrow f)|_{s \gg m_h^2, m_{S_r}^2} = |\mathcal{M}(i \rightarrow f)|_{s \gg m_h^2, m_{S_r}^2}^{(\theta \neq 0, \pi)} = |\kappa_{Hr}| < 8\pi, \quad (4.85)$$

$$16\pi |a_0(i' \rightarrow f')|_{s \gg m_h^2, m_{S_r}^2} = |\mathcal{M}(i' \rightarrow f')|_{s \gg m_h^2, m_{S_r}^2}^{(\theta \neq 0, \pi)} = |\lambda_{12}| < 8\pi, \quad (4.86)$$

$$\forall i \rightarrow f = hh \rightarrow S_r S_r, h S_r \rightarrow h S_r, S_r S_r \rightarrow hh,$$

$$\forall i' \rightarrow f' = S_1 S_1 \rightarrow S_2 S_2, S_1 S_2 \rightarrow S_1 S_2, S_2 S_2 \rightarrow S_1 S_1,$$

with $r = 1, 2$. Also, extra conditions can be derived through a coupled-channel analysis [79], by requiring the eigenvalues of the scalar⁸ coupled-channel (symmetric) matrix $(a_0)_{2 \rightarrow 2}$ in the high-energy regime $s \gg m_h^2, m_{S_r}^2$ to be smaller (in magnitude) than $1/2$ (or impose a limit of 8π on the magnitude of the eigenvalues of $\mathcal{M}_{2 \rightarrow 2}$). These extra tree-level perturbative unitarity conditions are given in Ref. [19].

- **Higgs Invisible Decay BR Upper Limit:** The $h S_r S_r$ coupling allows the Higgs boson to decay to a DM particle pair, $h \rightarrow S_r S_r$ ($r = 1, 2$) for $m_{S_r} < m_h/2$ (when it is kinematically possible), and the corresponding (tree-level) decay rate is given by

$$\Gamma(h \rightarrow S_r S_r) = \frac{1}{2!} \frac{1}{32\pi^2} \frac{|\vec{k}|}{m_h^2} \int d\Omega_k |\overline{\mathcal{M}_{fi}}|^2 = \frac{\kappa_{Hr}^2 v^2}{32\pi m_h} \sqrt{1 - 4m_{S_r}^2/m_h^2}, \quad (4.87)$$

which must agree with the ATLAS [67] upper bound on the branching ratio of the Higgs boson decay to “invisible” products, $\text{BR}(h \rightarrow \text{inv}) < 0.107$. Hence, our model predictions must satisfy

$$\frac{\sum_{r=1,2} \Gamma(h \rightarrow S_r S_r)}{\Gamma_h^{(\text{total})}} = \frac{\sum_{r=1,2} \Gamma(h \rightarrow S_r S_r)}{\sum_{X \in \text{SM}} \Gamma(h \rightarrow X \bar{X}) + \sum_{r=1,2} \Gamma(h \rightarrow S_r S_r)} < 0.107. \quad (4.88)$$

- **Electroweak Precision Measurements:** Any SM extension must agree with the precise measurements of electroweak observables. Since we are considering the vacuum configuration (4.9), both singlets do not acquire a VEV (the $\mathcal{Z}_2^{(1)} \times \mathcal{Z}_2^{(2)}$ symmetry remains unbroken) and there is no mixing with the Higgs field. Hence, the electroweak sector remains unchanged relative to that of the SM, and our DM model is therefore in agreement with all electroweak precision measurements. In particular, the tree-level SM+2RSS model prediction for the

$$\rho \equiv \frac{m_W^2}{m_Z^2 \cos^2 \theta_w} = \frac{\sum_{\varphi} [I_w^{(\varphi)} (I_w^{(\varphi)} + 1) - (I_{w3}^{(\varphi)})^2] v_{\varphi}^2}{2 \sum_{\varphi} (I_{w3}^{(\varphi)})^2 v_{\varphi}^2} \quad (4.89)$$

parameter (where φ are $\text{SU}(2)_L$ scalar multiplets of isospin numbers $I_w^{(\varphi)}$ and $I_{w3}^{(\varphi)}$ with VEV v_{φ}) is $\rho_{\text{SM}+2\text{RSS}} = \rho_{\text{SM}} = 1$, in agreement with the experimental [38] value $\rho_0 = 1.00031 \pm 0.00019$. Similarly, the model predictions for the S, T and U oblique parameters [80] are $(S, T, U)_{\text{SM}+2\text{RSS}} = (S, T, U)_{\text{SM}} = (0, 0, 0)$, in agreement with the experimental [38] values $(-0.04 \pm 0.10, 0.01 \pm 0.12, -0.01 \pm 0.09)$.

⁸The weak gauge bosons (could have been included, but) are neither considered here nor in Ref. [19].

4.4 Parameter Space Scans and Numerical Analysis

The two-real-scalar-singlet extension of the SM has seven (new) free parameters, but only five of them are relevant at tree-level: the DM masses m_{S_1} and m_{S_2} , the portal coefficients κ_{H1} and κ_{H2} , and the λ_{12} interaction coefficient. The two quartic self-interaction coefficients λ_1 and λ_2 are only relevant for loop corrections in perturbation theory. Hence, we scanned the 5-dimensional free parameter space (relevant at tree-level) of this model with `micrOMEGAs 6.0` [59], assuming both scalar DM particles were thermally produced according to the freeze-out mechanism. The scans were performed considering the DM relic density and direct detection exclusion, motivated by the fact that these experimental constraints completely define the allowed free parameter space of the (one) real scalar singlet SM extension (Figure 3.3). The (relic density and direct detection) experimental constraints on the SM+2RSS model (4.4) are shown in Figures 4.2 and 4.3, which only display allowed (i.e., not experimentally excluded) free parameter space points. In both figures, the left panel displays the scanned free parameter space points that correspond to the observed DM relic density $\Omega_{\text{DM}}^{\text{obs}} h^2 = 0.120 \pm 0.001$ from Planck [7] measurements, and the right panel displays the free parameter space points which (in addition to giving the observed relic density) are *also* not excluded by the XENON1T [60], DarkSide-50 [61], PICO-60 [62], CRESST-III [63], PandaX-4T [64] and LUX-ZEPLIN (LZ) [2] direct detection experiments. Figure 4.2 presents several projections with m_{S_1} on the x -axis and the four remaining free parameters (relevant at tree-level) m_{S_2} , κ_{H1} , κ_{H2} and λ_{12} on the y -axis and colour bars. Figure 4.3 presents (only) the projection in the (m_{S_1}, m_{S_2}) plane, and the colour bar displays the relic density of S_1 .

Before proceeding to the numerical analysis, one should notice from Figures 4.2 and 4.3 that – as already expected from the Lagrangian density (4.4) describing our theory – the model is $S_1 \leftrightarrow S_2$ symmetric. With that being said, we do not distinguish between cases that only differ by a $S_1 \leftrightarrow S_2$ re-naming, and hence, there are only three (main) allowed free parameter space regions that can be identified from Figures 4.2 and 4.3:

1. The $\mathbf{m}_{S_{1,2}} \sim \mathbf{m}_{S_{2,1}} > 1 \text{ TeV}$ case, where both DM particles (S_1 and S_2) are heavy. In this scenario, the model cannot be probed at the LHC, since the phase space of final state particles in any DM production process is highly suppressed, resulting in low cross sections, and thus, a negligible number of DM production events. As shown in Figure 4.2, both portal coupling constants κ_{H1} and κ_{H2} take high values, while λ_{12} can take the full range of values.
2. The $\mathbf{m}_h/2 < \mathbf{m}_{S_{1,2}} < 1 \text{ TeV} < \mathbf{m}_{S_{2,1}}$ case, where one DM particle ($S_{2,1}$) is heavy, *but* the other one ($S_{1,2}$) is *lighter*. In this scenario, the model can be probed through LHC searches targeted at the lighter DM particle. As shown in Figure 4.2, both portal coupling constants κ_{H1} and κ_{H2} take high values, but the portal coupling of the lighter DM particle is always higher than that of the heavier one.
3. The $\mathbf{m}_h/2 \approx \mathbf{m}_{S_{1,2}} < \mathbf{m}_{S_{2,1}}$ (resonant) case, where one of the DM particles ($S_{1,2}$) has a mass that – in the non-relativistic limit $\sqrt{s} \approx 2m_{S_{1,2}}$ of two DM particles $S_{1,2}$ annihilating – gives a center-of-mass energy $\sqrt{s} = m_h$ in the resonance pole of the s -channel Higgs propagator, so that

$$\frac{i}{s - m_h^2 + im_h\Gamma_h} \approx \frac{i}{4m_{S_{1,2}}^2 - m_h^2 + im_h\Gamma_h} \rightarrow \frac{1}{m_h\Gamma_h} \left(m_{S_{1,2}} \rightarrow \frac{m_h}{2} \right). \quad (4.90)$$

In this resonant scenario, the (virtual) s -channel Higgs mediator with 4-momentum $k_1^\mu + k_2^\mu$ is actually on-shell, since $(k_1 + k_2)^2 \equiv s \approx 4m_{S_{1,2}}^2 := m_h^2$, and the squared amplitude of the s -channel Higgs propagator is maximized. This results in extremely high $S_{1,2}$ annihilation cross

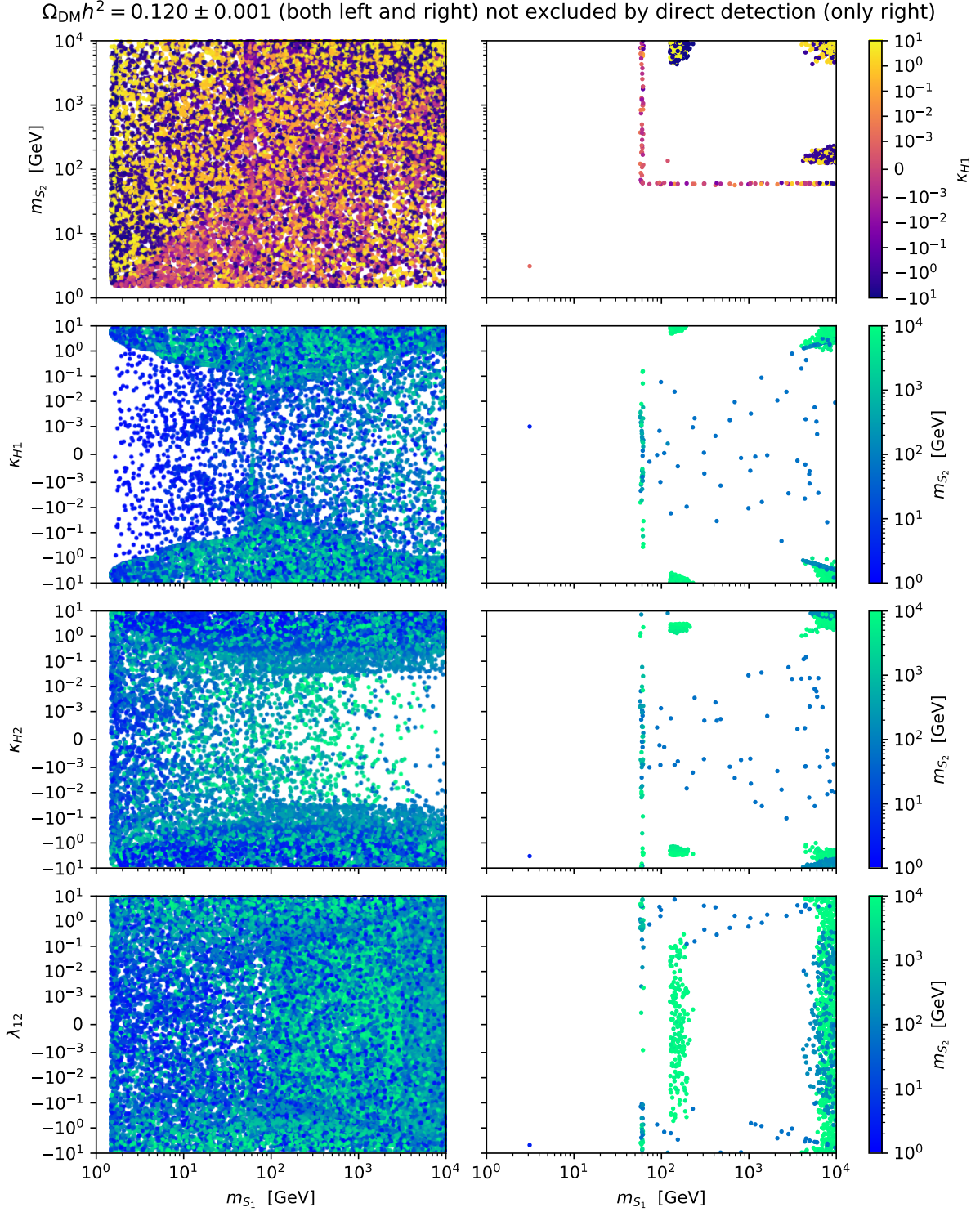


Figure 4.2: Experimental constraints on the SM+2RSS model (4.4), obtained by scanning the free parameter space with micrOMEGAs 6.0 for the freeze-out mechanism. The left panel shows parameter space points that correspond to the observed DM relic density, and the right panel displays the points that are *also* not excluded by direct detection. Columns share the x -axis, and rows share the y -axis and the colour bar.

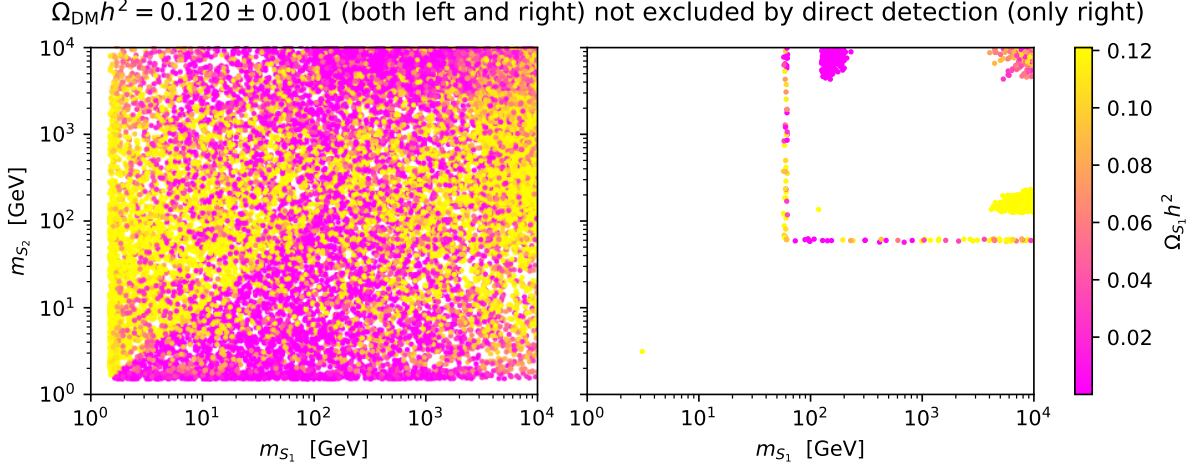


Figure 4.3: Experimental constraints on the SM+2RSS model (4.4), obtained by scanning the free parameter space with micrOMEGAS 6.0 for the freeze-out mechanism. The left panel shows parameter space points that correspond to the observed DM relic density, and the right panel displays the points that are *also* not excluded by direct detection. The y -axis and the colour bar are shared. The figure is similar to the first row of Figure 4.2, but here the colour bar displays the relic density of the DM particle S_1 .

sections – since all $S_{1,2}$ annihilation processes feature Higgs mediated s -channels, as shown in Section 4.2.2 – which drastically decreases the relic density of $S_{1,2}$. Therefore, in this $m_h/2 \approx m_{S_{1,2}} (< m_{S_{2,1}})$ case, the remaining free parameters can take a wide range of values, as shown in Figure 4.2.

In the first scenario, both DM particles are too heavy to be produced (in non-negligible numbers) at the LHC, which is analogous to what happens in the (one) real scalar singlet SM extension. The third scenario is also viable in the SM+RSS model, where a DM mass lies at the resonance pole of the s -channel Higgs propagator, drastically reducing the corresponding DM relic density. Therefore, although all three scenarios correspond to equally valid allowed regions, we are only interested in the second one – i.e., the $(m_h/2 <) \mathbf{m}_{S_{1,2}} (< 1 \text{ TeV}) < \mathbf{m}_{S_{2,1}}$ case – since it is the only one that is not also featured in the (one) real scalar singlet SM extension, providing us a lighter DM particle that can be searched for at the LHC (thus justifying the study of this two-real-scalar-singlet SM extension).

4.4.1 Analysis of the $(m_h/2 <) \mathbf{m}_{S_1} < \mathbf{m}_{S_2}$ Case

Let us now focus on the $m_{S_1} \neq m_{S_2}$ case, with both DM masses outside the resonance pole of the s -channel Higgs propagator (in the non-relativistic limit, i.e., so that $m_{S_{1,2}} \approx \sqrt{s}/2 \neq m_h/2$). From now on, we will take S_1 (S_2) as the lighter (heavier) DM particle, without loss of generality (due to the $S_1 \leftrightarrow S_2$ symmetry of our model). This $m_{S_1} < m_{S_2}$ case (as we shall refer to it from now on, for the sake of simplicity) is highlighted in Figure 4.4, which shows all the scanned points that are allowed by relic density and direct detection – i.e., the same points that are present in the right panel of Figure 4.2 – but where only $m_{S_1} < m_{S_2}$ case points are coloured, while the remaining allowed free parameter space points are displayed in shades of grey. Additionally, all coupling constants are now taken to be positive (without loss of generality), both in this figure and in the discussions that will follow.

For this $(m_h/2 <) m_{S_1} < m_{S_2}$ case (coloured points of Figure 4.4), the allowed mass ranges are $m_{S_1} \in [124.8, 230.0] \text{ GeV}$ and $m_{S_2} \in [4321.0, 9977.0] \text{ GeV}$ – which considerably suppresses the phase space of LHC events that produce the heavier DM particle S_2 – and the allowed coupling constant ranges

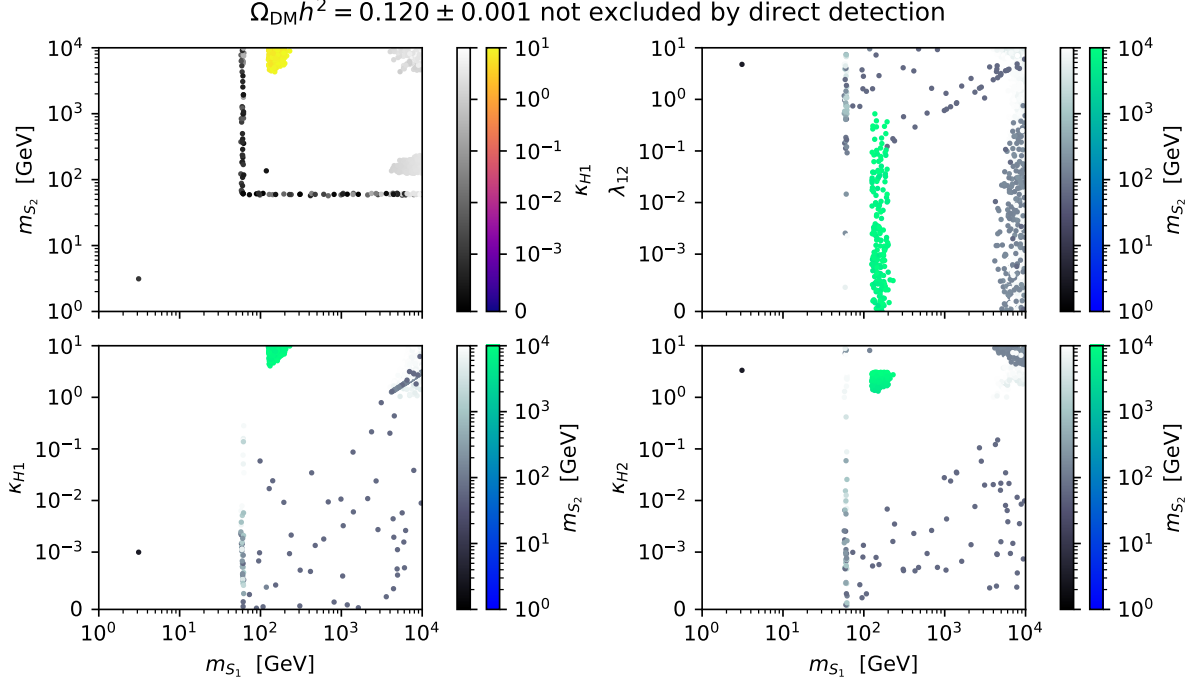


Figure 4.4: Scanned free parameter space points that correspond to the observed DM relic density and are not excluded by direct detection, just like in the right panel of Figure 4.2 (except here all coupling constants are taken as positive). The $m_{S_1} < m_{S_2}$ case points are coloured, while the other allowed parameter space points are grey (each colour bar has its grey version “twin”). Columns share the x -axis.

are $\kappa_{H1} \in [4.066, 9.986]$, $\kappa_{H2} \in [1.321, 3.074]$ and $\lambda_{12} \in [2.940 \times 10^{-6}, 0.7093]$ – the portal coupling constant is larger (in magnitude) for the lighter DM particle S_1 than for the heavier DM particle S_2 . Also, as shown in Figure 4.3, the lighter DM particle S_1 corresponds to a very small fraction of the observed relic density $\Omega_{S_1} h^2 \sim [10^{-8}, 10^{-7}]$, so that $\Omega_{DM} h^2 = (\Omega_{S_1} + \Omega_{S_2}) h^2 \approx \Omega_{S_2} h^2$.

We now want to analyse this small allowed region of free parameter space in more detail. In particular, we aim to understand why it has so well-defined boundaries and allows for a lighter DM candidate. In order to do so, we must comprehend how the relic density and direct detection exclusion are affected by each one of the free parameters, i.e., the exclusion behaviour in the free parameter space. This cannot be done based on Figures 4.2, 4.3 and 4.4 alone. Hence, several new scans were performed around benchmark points of this $m_{S_1} < m_{S_2}$ allowed region, in which we scanned one free parameter at a time. Figure 4.5 shows m_{S_1} scans on the $(m_{S_1}, \Omega_{S_1} h^2)$ (left panel) and $(m_{S_1}, \Omega_{DM} h^2)$ (right panel) planes, where in each row, one of the remaining parameters m_{S_2} , κ_{H1} , κ_{H2} or λ_{12} takes five different fixed values. Additionally, each point that is not excluded by direct detection is displayed in green. Figure 4.6, on the other hand, shows a (one) parameter scan per row, for all five (relevant at tree-level) free parameters. Each row shows how $\Omega_{S_1} h^2$ (left panel) and $\Omega_{DM} h^2$ (right panel) change with the scanned parameter, with the remaining parameters fixed. Just like in Figure 4.5, only green points are allowed by direct detection. Notice that, unlike previous Figures 4.2, 4.3 and 4.4, these ones (4.5 and 4.6) do not “filter” out excluded points.

Let us start by analysing the relic density behaviour in this region. It is clear from Figures 4.5 and 4.6 that the total relic density $\Omega_{DM} h^2 = (\Omega_{S_1} + \Omega_{S_2}) h^2$, although dependent on all five free parameters m_{S_1} , m_{S_2} , κ_{H1} , κ_{H2} and λ_{12} , is only strongly affected by three of them: m_{S_2} , κ_{H2} and λ_{12} . This was already expected, since $\Omega_{DM} h^2 \approx \Omega_{S_2} h^2$ is determined by the relic density of the heavier DM particle S_2 . In particular, $\Omega_{DM} h^2$ increases with m_{S_2} and decreases with κ_{H2} and λ_{12} , which can be respectively

explained by the following reasons:

- As shown in Section 4.2.2, all S_2 annihilation cross sections are proportional or partially proportional (both $S_2 S_2 \rightarrow hh$ and $S_2 S_2 \rightarrow S_1 S_1$ annihilation cross sections contain one point-like interaction term that is not proportional) to the squared amplitude of the (s-channel) Higgs boson propagator

$$\left| \frac{i}{s - m_h^2 + im_h \Gamma_h} \right|^2 = \frac{1}{(s - m_h^2)^2 + m_h^2 \Gamma_h^2}, \quad (4.91)$$

and hence, in the low-energy regime, all S_2 annihilation cross sections decrease as $|m_{S_2} - m_h/2|$ increases – which in our case, corresponds to $m_{S_2} > m_h/2$ increasing. Therefore, for the freeze-out mechanism, the S_2 relic density $\Omega_{S_2} h^2 \approx \Omega_{\text{DM}} h^2$ increases with m_{S_2} (for $m_{S_2} > m_h/2$). This was already shown for the SM+RSS model in Figure 3.3, where for $m_{S_2} > m_h/2$, the DM relic density always increases with the DM particle mass, except when an annihilation channel opens (i.e., becomes kinematically possible in the non-relativistic limit).

- Similarly (see Section 4.2.2), all S_2 annihilation cross sections (but the $S_2 S_2 \rightarrow S_1 S_1$ annihilation cross section, which contains one proportional and one non-proportional term) are proportional to κ_{H2}^2 , thus increasing with $|\kappa_{H2}|$. Therefore, for the freeze-out mechanism, the S_2 relic density $\Omega_{S_2} h^2 \approx \Omega_{\text{DM}} h^2$ decreases with $|\kappa_{H2}|$ (also shown for the SM+RSS model in Figure 3.3).
- The inter-dark $S_{2,1} S_{2,1} \rightarrow S_{1,2} S_{1,2}$ annihilation cross sections are given in Eq. (4.75), and explicitly increase with $|\lambda_{12}|$. Since $m_{S_1} < m_{S_2}$, then $S_2 S_2 \rightarrow S_1 S_1$ is dominant over the inverse process, which means that the S_2 relic density $\Omega_{S_2} h^2 \approx \Omega_{\text{DM}} h^2$ decreases with $|\lambda_{12}|$.

All these arguments rely on the fact that $\Omega_{\text{DM}} h^2 = (\Omega_{S_1} + \Omega_{S_2}) h^2 \approx \Omega_{S_2} h^2$. One should note that we did not try to explain this feature, but rather took it as a result from our first scan in Figure 4.3.

We now turn our attention to the direct detection (DD) exclusion. Let us remember from Section 4.2.1 that, at leading order, the spin-independent (SI) cross section for the elastic scattering of a DM particle S_r off a nucleon $N = p, n$ is given by

$$\sigma^{\text{SI}}(S_r N \rightarrow S_r N) = \frac{1}{\pi} \left(\frac{m_N}{m_N + m_{S_r}} \right)^2 |f_N^{(\text{LO})}|^2, \quad r = 1, 2, \quad (4.92)$$

where

$$\begin{aligned} f_N^{(\text{LO})} &= \left[\sum_{q'=u,d,s} C_{q'}^{S(\text{LO})} f_{T_{q'}}^{(N)} + \sum_{Q=c,b,t} C_Q^{S(\text{LO})} \times \frac{2}{27} f_{T_G}^{(N)} \right] m_N, \quad f_{T_G}^{(N)} = 1 - \sum_{q'=u,d,s} f_{T_{q'}}^{(N)} \\ &= + \frac{\kappa_{Hr}}{2m_h^2} \left[\frac{21}{27} \sum_{q'=u,d,s} f_{T_{q'}}^{(N)} + \frac{6}{27} \right] m_N \end{aligned} \quad (4.93)$$

is the DM-nucleon effective coupling and $f_{T_{q'}}^{(N)} \equiv \langle N(\vec{p}) | m_{q'} \bar{q}' q' | N(\vec{p}) \rangle / m_N$ represents the fraction of nucleon mass attributed to a light quark $q' = u, d, s$ contribution (obtained from lattice QCD simulations). Thus, $\sigma^{\text{SI}}(S_r N \rightarrow S_r N)$ decreases with m_{S_r} and increases with κ_{Hr} ($r = 1, 2$). However, one must avoid the mistake of assuming that high DM masses $m_{S_{1,2}}$ and low portal coupling constants $\kappa_{H1,2}$ promote direct detection non-exclusion – as shown in Figures 4.5 and 4.6, this is only partially true – due to the fact that our model has two DM particles (instead of just one). Direct detection experiments set an upper bound on the DM-nucleon elastic scattering cross section under the assumption of that DM

4.4. Parameter Space Scans and Numerical Analysis

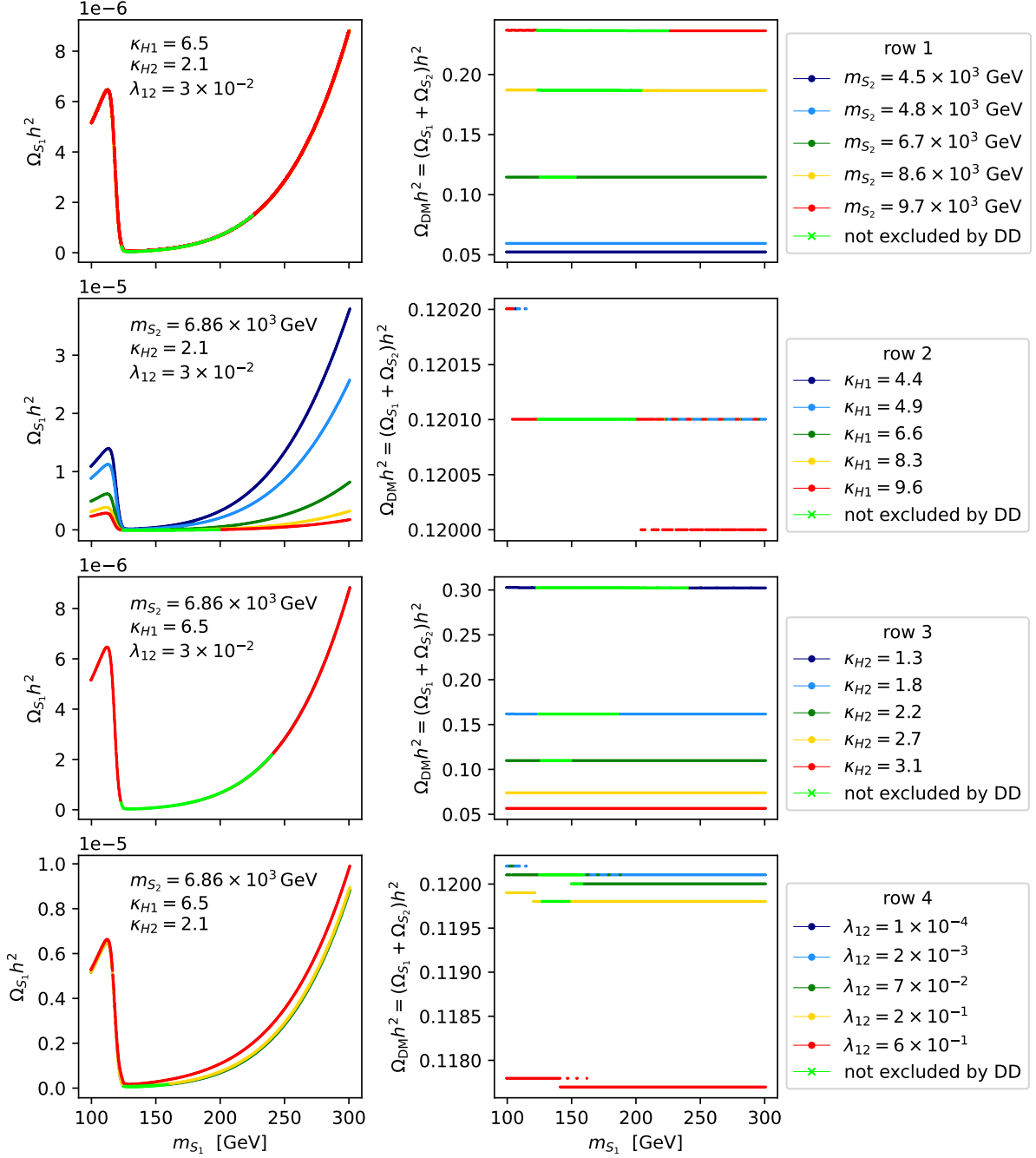


Figure 4.5: Analysis of the $m_{S_1} < m_{S_2}$ case with all parameters but m_{S_1} (light DM mass) fixed. Each row shows one fixed parameter – between m_{S_2} , κ_{H1} , κ_{H2} and λ_{12} – taking five different fixed values. Only green points are not excluded by direct detection. Columns share the x -axis.

particle being responsible for all the observed relic density $\Omega_{DM}^{obs} h^2 = 0.120 \pm 0.001$ (thus responsible for all the local DM number density). In other words, for a model with more than one DM candidate – and assuming that the contribution of each DM particle to the local DM number density is the same as its contribution to the observed DM relic density – DD experiments can only set upper bounds on

$$\sigma^{SI}(DM_r N \rightarrow DM_r N) \frac{\Omega_r}{\Omega_{DM}}, \quad \text{with} \quad \Omega_{DM} h^2 = \sum_r \Omega_r h^2 := 0.120 \pm 0.001. \quad (4.94)$$

Hence, in a model with multiple DM particles, DD exclusion is not only determined by the cross sections

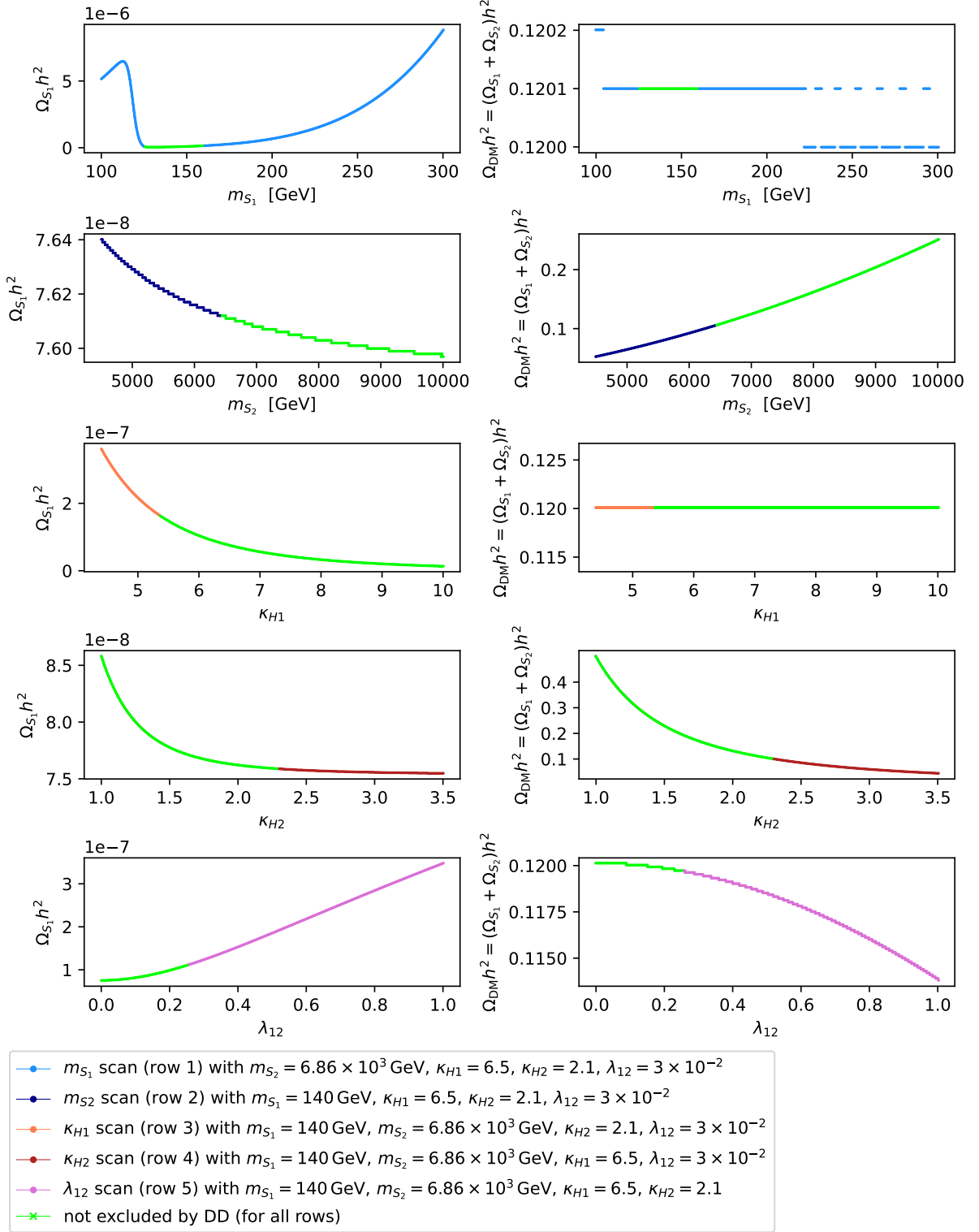


Figure 4.6: Analysis of the $m_{S_1} < m_{S_2}$ case with all parameters (but one) fixed. Each row scans one parameter – m_{S_1} , m_{S_2} , κ_{H1} , κ_{H2} and λ_{12} , in this order – with all the remaining parameters fixed. Only green points are not excluded by direct detection.

$\sigma^{\text{SI}}(\text{DM}_r N \rightarrow \text{DM}_r N)$, but also by the corresponding fractions $\Omega_r/\Omega_{\text{DM}}$ ($r = 1, 2, \dots$).

For the heavier DM particle S_2 – which is responsible for almost all the observed relic density, i.e. $\Omega_{S_2}/\Omega_{\text{DM}} \approx 1$ – the respective DD exclusion is completely determined by $\sigma^{\text{SI}}(S_2 N \rightarrow S_2 N)$; which must not surpass the upper bound set by DD experiments. This means that by increasing m_{S_2} and decreasing κ_{H2} we are promoting DD non-exclusion; however, we are also increasing $\Omega_{S_2} h^2 \approx \Omega_{\text{DM}} h^2$, thus simultaneously promoting relic over-density. There is a “tension” between relic density and direct detection, in the sense that m_{S_2} and κ_{H2} must be sufficiently high and low (respectively) so that the points are not excluded by DD, but also sufficiently low and high (respectively) so that the points are not excluded by relic over-density. It is therefore fully understood why m_{S_2} and κ_{H2} are together (i.e., inter-dependently) constrained, exhibiting well-defined allowed ranges, both bounded from below and from above, when the other parameter is fixed.⁹

The same assumptions are no longer valid for the lighter DM particle S_1 – which (virtually) does not contribute to the observed relic density, i.e. $\Omega_{S_1} h^2 \ll \Omega_{\text{DM}} h^2$ – since the respective DD exclusion is not (mainly) determined by $\sigma^{\text{SI}}(S_1 N \rightarrow S_1 N)$. This happens because (as explained above) DD experiments can only set upper-bounds on $\sigma^{\text{SI}}(S_r N \rightarrow S_r N) \times \Omega_{S_r}/\Omega_{\text{DM}}$ ($r = 1, 2$), which for $\Omega_{S_1}/\Omega_{\text{DM}} \ll 1$ will result in an extremely high upper-bound on $\sigma^{\text{SI}}(S_1 N \rightarrow S_1 N)$. Hence, DD exclusion due to the lighter DM particle S_1 is mainly determined by $\Omega_{S_1} h^2$ – as opposed to what happens with S_2 , for which it is fully determined by the (respective) cross section – in the sense that it can only occur for parameter space configurations that increase $\Omega_{S_1} h^2$, which (for $m_{S_1} > 125$ GeV) are characterized by high m_{S_1} , low κ_{H1} and high λ_{12} (Figures 4.5 and 4.6). Equivalently, by decreasing m_{S_1} , increasing κ_{H1} and decreasing λ_{12} we are promoting DD non-exclusion; which explains the well-defined upper, lower and upper bounds exhibited by m_{S_1} , κ_{H1} and λ_{12} , respectively. Furthermore, there is an important feature that is clearly shown in Figures 4.5 and 4.6. For $m_{S_1} < m_h = 125$ GeV, the $S_1 S_1 \rightarrow hh$ annihilation process is kinematically impossible in the non-relativistic limit $\sqrt{s} \approx 2m_{S_1}$, i.e., the channel is closed. The relic density of S_1 is too high in this region, thus being excluded by DD. However, when m_{S_1} reaches 125 GeV = m_h (from lower values), the $S_1 S_1 \rightarrow hh$ annihilation channel opens and $\Omega_{S_1} h^2$ drastically decreases to a local minimum, allowing for DD non-exclusion. This explains why, in addition to the upper bound, m_{S_1} also exhibits a well-defined lower bound at 125 GeV. DD non-exclusion is promoted as m_{S_1} decreases towards the Higgs boson mass (from higher values), i.e., as $m_{S_1} \rightarrow m_h^+ = 125^+$ GeV with $m_{S_1} > m_h$. Finally, it should be noted that the boundaries of the allowed ranges for m_{S_1} , κ_{H1} , and λ_{12} are solely determined by DD exclusion related to S_1 . This makes sense for m_{S_1} and κ_{H1} , as they (virtually) have no influence on the (total) relic density. However, decreasing λ_{12} , in addition to promoting DD non-exclusion – and hence the upper bound, as previously discussed – also increases $\Omega_{S_2} h^2 \approx \Omega_{\text{DM}} h^2$, simultaneously promoting relic over-density. For this reason, one could argue that λ_{12} should also exhibit a well-defined lower bound – but this does not occur, as shown in Figures 4.4 and 4.6, where λ_{12} can decrease to 0 without exclusion. The reason for this is clear from Figures 4.5 and 4.6: m_{S_2} and κ_{H2} have a stronger influence on the (total) relic density than λ_{12} . Hence, a small over-density produced by decreasing λ_{12} can be countered by a slight variation in m_{S_2} (decrease) and κ_{H2} (increase) which lowers $\Omega_{\text{DM}} h^2$ without DD exclusion related to S_2 .

Let us now summarize the conclusions of our analysis. m_{S_2} and κ_{H2} exhibited allowed ranges that are both bounded from below and from above, due to the “tension” between relic over-density and direct detection exclusion related to S_2 (with the latter being determined by the corresponding cross section

⁹Notice that m_{S_2} does not exhibit an upper bound in Figures 4.2, 4.3 and 4.4, as the relic over-density can be counteracted by increasing κ_{H2} , without it leading to DD exclusion because the upper limits on the WIMP-nucleon cross section are weak (i.e., high) for large DM masses. Hence, κ_{H2} only exhibits an upper limit because we did not scan for m_{S_2} above 10 TeV.

Parameter	Constraint responsible for lower bound	Constraint responsible for upper bound
m_{S_1}	DD exclusion related to S_1 (determined by $\Omega_{S_1}/\Omega_{\text{DM}}$)	DD exclusion related to S_1 (determined by $\Omega_{S_1}/\Omega_{\text{DM}}$)
m_{S_2}	DD exclusion related to S_2 (determined by $\sigma^{\text{SI}}(S_2 N \rightarrow S_2 N)$)	relic over-density
κ_{H1}	DD exclusion related to S_1 (determined by $\Omega_{S_1}/\Omega_{\text{DM}}$)	—
κ_{H2}	relic over-density	DD exclusion related to S_2 (determined by $\sigma^{\text{SI}}(S_2 N \rightarrow S_2 N)$)
λ_{12}	—	DD exclusion related to S_1 (determined by $\Omega_{S_1}/\Omega_{\text{DM}}$)

Table 4.1: Experimental constraints responsible for each boundary of the free parameters’ allowed ranges in the $m_{S_1} < m_{S_2}$ case region. If a particular boundary does not exist, the corresponding table entry displays “—”. The m_{S_2} and κ_{H2} parameters are interdependently constrained by the relic-DD “tension”, and the grey bounds on m_{S_2} (κ_{H2}) are only exhibited for fixed κ_{H2} (m_{S_2}) values.

$\sigma^{\text{SI}}(S_2 N \rightarrow S_2 N)$). On the other hand, m_{S_1} , κ_{H1} and λ_{12} exhibited allowed ranges that are, respectively, bounded from both below and above, just bounded from below and just bounded from above; where all this boundaries are solely due to direct detection exclusion related to S_1 (which is determined by the corresponding fraction $\Omega_{S_1}/\Omega_{\text{DM}}$, or equivalently, by $\Omega_{S_1} h^2$). Table 4.1 links each mentioned boundary to the respective experimental constraint (relic over-density and DD exclusion related to S_1 , S_2) that is responsible for its existence.

4.4.2 LZ 2024 Results and Future Prospects for Direct Detection

During the course of this work (2024), new results [3] from the LUX-ZEPLIN experiment came out. These LZ 2024 results [3] provide the most stringent (i.e., the lowest) upper limits on the WIMP-nucleon elastic scattering spin-independent cross section of any direct detection experiment (so far), including the previous (i.e., the first) LZ 2022 results [2]. However, the new LZ 2024 results are not (yet) included in the micrOMEGAs 6.0 code, and consequently, are not taken into account in our previous numerical analysis. This means that we need to perform the corresponding DD exclusion (for the LZ 2024 results) separately.

As already explained in Section 4.4.1, for multi DM particle models, direct detection experiments can only set upper limits on $\sigma^{\text{SI}}(\text{DM}_r N \rightarrow \text{DM}_r N) \times \Omega_r/\Omega_{\text{DM}}$, with $\Omega_{\text{DM}} h^2 = 0.120 \pm 0.001$ (which for a single DM particle model, simply corresponds to an upper limit on the SI cross section $\sigma^{\text{SI}}(\text{DM} N \rightarrow \text{DM} N)$). We computed the $\sigma^{\text{SI}}(S_r N \rightarrow S_r N) \times \Omega_{S_r}/\Omega_{\text{DM}}$, $r = 1, 2$ quantities for all the $m_{S_1} < m_{S_2}$ case free parameter space points that were not experimentally excluded by relic density and direct detection (without considering the LZ 2024 results) in the numerical analysis (i.e., the coloured points of Figure 4.4). These results are shown – for both the lighter S_1 (left panel) and heavier S_2 (right panel) DM particles – in Figure 4.7, which also displays the former 2022 (blue solid line) and new 2024 (green solid line) LZ upper limits on the SI cross section of WIMP-nucleon elastic scattering. As expected, the model-predicted $\sigma^{\text{SI}}(S_r N \rightarrow S_r N) \times \Omega_{S_r}/\Omega_{\text{DM}}$ ($r = 1, 2$) values for the $m_{S_1} < m_{S_2}$ case points are below the LZ 2022 upper limit for both DM particles. However, the same cannot be said regarding the LZ 2024 upper limit, above which all model-predicted values fall for both DM particles. Nevertheless, for a big part of the $m_{S_1} < m_{S_2}$ case points, the model predictions lay inside the experimental LZ 2024 uncertainty band (shaded green region) – to be precise, this happens for parameter space points featuring

any S_1 (lighter DM) mass (in the m_{S_1} allowed range) and any S_2 (heavier DM) mass above (roughly) 6700 GeV. Although for $m_{S_1} < m_{S_2}$ case points with a mass m_{S_1} around (roughly) 140 GeV and a high portal coefficient $\kappa_{H1} (\gtrsim 9)$, the predicted $\sigma^{\text{SI}}(S_1 N \rightarrow S_1 N) \times \Omega_{S_1}/\Omega_{\text{DM}}$ values fall in the actual LZ 2024 upper limit, the respective predicted $\sigma^{\text{SI}}(S_2 N \rightarrow S_2 N) \times \Omega_{S_2}/\Omega_{\text{DM}} \approx \sigma^{\text{SI}}(S_2 N \rightarrow S_2 N)$ values fall above it. Naturally, it only takes one (of the two) prediction values $\sigma^{\text{SI}}(S_r N \rightarrow S_r N) \times \Omega_{S_r}/\Omega_{\text{DM}}$ ($r = 1, 2$) to be above the LZ 2024 upper limit for the experimental DD exclusion of the corresponding parameter space point.

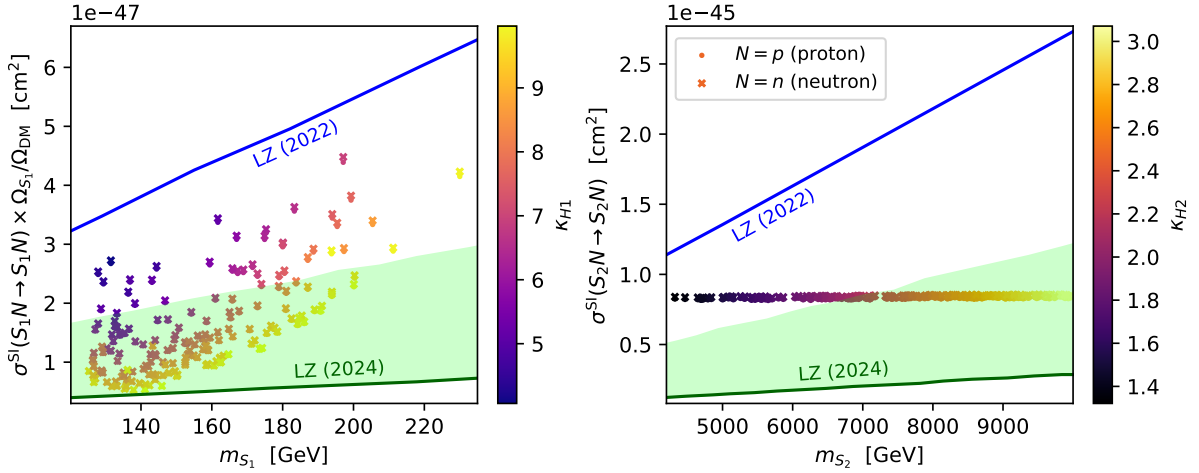


Figure 4.7: Spin-independent cross section of DM-nucleon elastic scattering $S_r N \rightarrow S_r N$ ($N = p, n$) multiplied by the corresponding fraction of DM relic density $\Omega_{S_r}/\Omega_{\text{DM}}$ ($r = 1, 2$), for both the lighter S_1 (left panel) and the heavier S_2 (right panel) DM particle candidates. The presented points correspond to the model's theoretical predictions for the $m_{S_1} < m_{S_2}$ case points, for both proton (p) and neutron (n) elastic scattering. The blue and green (solid) lines correspond to the LUX-ZEPLIN (LZ) experimental upper limits on the WIMP-nucleon elastic scattering spin-independent cross section from 2022 [2] and 2024 [3] results, respectively. The (shaded green) experimental uncertainty band from the LZ 2024 results is displayed. The legend is shared by both panels.

None of the $m_{S_1} < m_{S_2}$ case points' model predictions fall below the (new) LZ 2024 [3] upper limit, but a big part of them lay inside the corresponding experimental uncertainty band – thus not being definitely excluded (but almost). Nevertheless, one should note that if we take the LZ 2024 upper limit (green solid line) as the definitive DD exclusion criteria, all $m_{S_1} < m_{S_2}$ case free parameter space points that were allowed by the numerical analysis are, in fact, experimentally excluded. In the remaining of this Chapter 4, we shall continue to consider all the $m_{S_1} < m_{S_2}$ case allowed points of our numerical analysis (i.e., the coloured points of Figure 4.4); however, aware of the insights that were drawn from the new LZ 2024 upper limit in this Section 4.4.2.

4.5 Searches for the Lighter DM Particle at the LHC

Arguably one of the most interesting features of this model, and in particular, of this $m_{S_1} < m_{S_2}$ case we are focusing on, is that although the heavier DM particle S_2 is responsible for almost all the observed DM relic density, only the lightest DM particle S_1 can (in principle) be searched for at the LHC. This happens because the LHC (does not and) will never run at a center-of-mass energy higher than $\sqrt{s} = 14$ TeV, and since $m_{S_2} \in [4321.0, 9977.0]$ GeV, the phase space of final state particles in S_2 production processes at the LHC is considerably suppressed – which results in very low cross sections, and hence, in a negligible number of S_2 production events. Therefore, until a collider that can operate at a center-of-mass energy much higher than that of the LHC is built, we cannot search for a DM particle with a mass in the range

of $m_{S_2} \in [4321.0, 9977.0]$ GeV. On the other hand, producing the lighter DM particle S_1 at the LHC should not present any problem, given its mass range of $m_{S_1} \in [124.8, 230.0]$ GeV, which is well below 1 TeV. Therefore, as already stated in Section 4.4, this two-real-scalar-singlet extension of the SM can be probed in LHC searches targeted at the lighter DM particle S_1 .

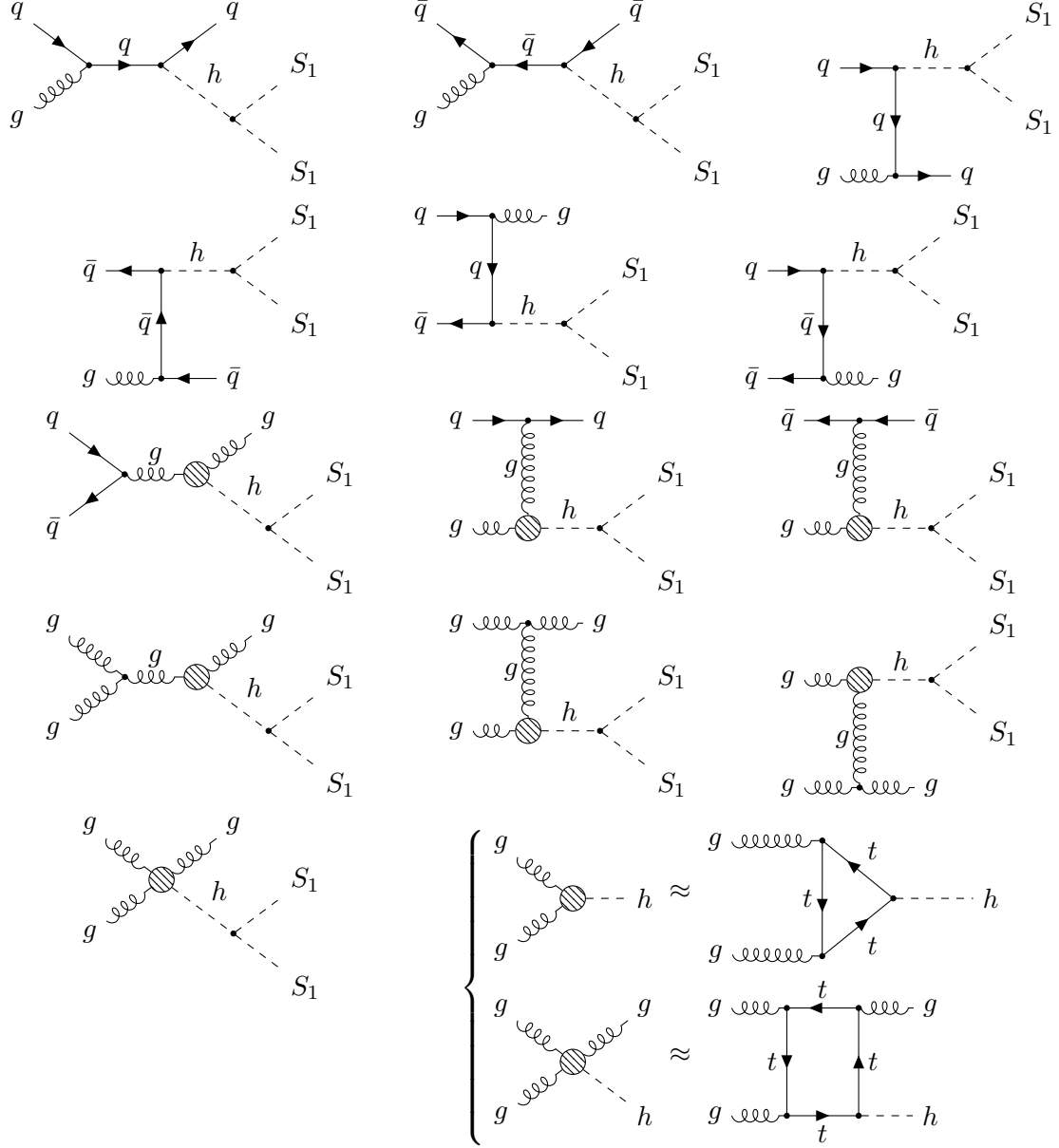


Figure 4.8: Feynman diagrams contributing to mono-jet production processes $pp \rightarrow S_1 S_1 j$ at tree-level, where $j = q, \bar{q}, b, \bar{b}, g$ are jets and $q = u, d, c, s$ are light quarks. The vertices for the ggh and $gggh$ effective couplings arise from top quark loops in gluon fusion processes (in the heavy top quark limit, $m_t^2 \gg s$).

We now must compare theoretical predictions of our model with LHC experiments to determine whether the $m_{S_1} < m_{S_2}$ case (allowed) points are experimentally excluded by collider searches. Since DM particles cannot be directly detected at the LHC (or any other collider), we must consider processes that, in addition to invisible/undetectable DM particle(s), also include visible/detectable SM particle(s) in the final state. The collider events associated with such processes are the so-called *missing energy* events, since their occurrence is observed through detection of final state (visible) SM particle(s), while the final state's energy-momentum that is “missing” for energy-momentum conservation signals the presence

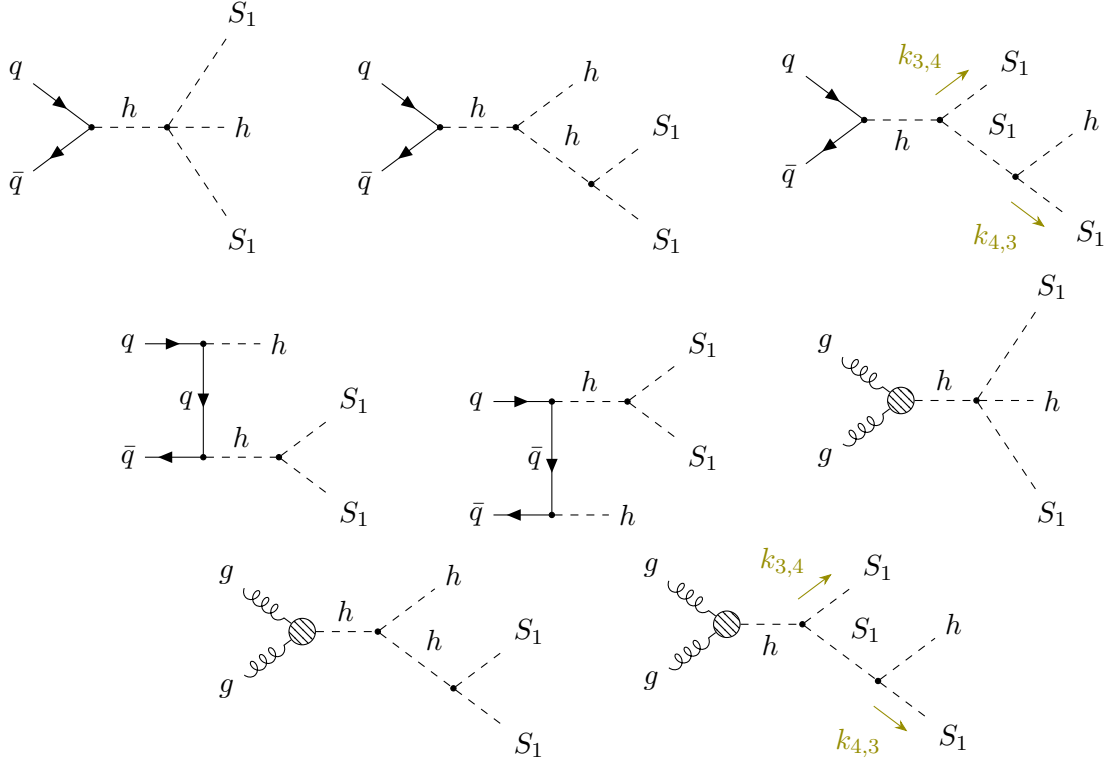


Figure 4.9: Feynman diagrams contributing to the mono-Higgs production process $pp \rightarrow S_1 S_1 h$ at tree-level, where $q = u, d, c, s$ are light quarks. The third and last diagrams each represent two distinct contributions, due to the interchange of the external legs with coloured four-momenta $k_{3,4}^\mu$ and $k_{4,3}^\mu$. The vertex for the ggh effective coupling (arising from the top quark loop in gluon fusion) is explicitly shown in Figure 4.8.

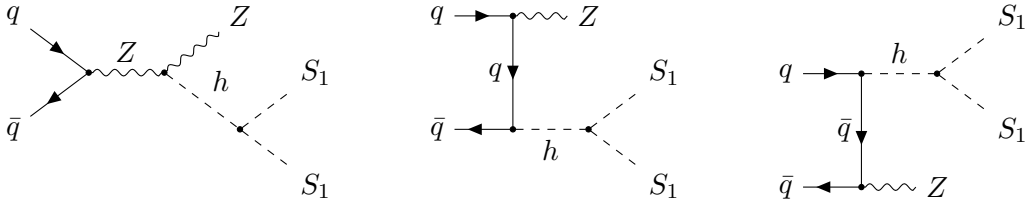


Figure 4.10: Feynman diagrams contributing to the mono-Z production process $pp \rightarrow S_1 S_1 Z$ at tree-level, where $q = u, d, c, s$ are light quarks.

of undetected final state particles (i.e., the 4-momentum of the initial and final states does not match, $p_i^\mu \neq p_f^\mu$ with $E_i > E_f$, because not all final state particles are detected/accounted for). At the LHC, these processes are $pp \rightarrow X + \cancel{E}_T$, where X and $\cancel{E}_T \equiv E_T^{\text{miss}}$ stand for SM (visible) particles and missing transverse energy (MET), respectively. The MET – or equivalently, the missing transverse momentum (p_T^{miss}) – could be due to undetected DM particles, naturally.

It is now time to select the LHC searches to probe our model. In order to do this, we first need to identify the S_1 production processes predicted by the model and, more importantly, determine whether the corresponding cross sections are sufficiently large to yield a significant number of events by the end of the current and/or future LHC runs (or even throughout the entire LHC operation). We start by computing the cross sections and event numbers of the so-called mono- X processes (where X is a single SM particle), for six benchmark $m_{S_1} < m_{S_2}$ case points, with MadGraph5_aMC@NLO [81, 82]. The computations were performed for center-of-mass energies (\sqrt{s}) of 13 TeV, 13.6 TeV and 14 TeV, with corresponding integrated luminosities (\mathcal{L}) of 190 fb^{-1} , 450 fb^{-1} and 3000 fb^{-1} . These three (\sqrt{s}, \mathcal{L})

4. The Two-Real-Scalar-Singlet SM Extension

configurations correspond to the LHC's setups at the end of the previous Run 2, the current Run 3 and the future High-Luminosity (HL-LHC) stage, respectively [83]. We have considered the mono-jet, mono-Higgs and mono- Z processes

$$pp \rightarrow S_1 S_1 X, \quad X = j, h, Z, \quad (4.95)$$

where $j = q, \bar{q}, b, \bar{b}, g$ are jets and $q = u, d, c, s$ are light quarks. The corresponding tree-level Feynman diagrams are presented in Figures 4.8, 4.9 and 4.10, respectively. Additionally, we also considered the di-jet process of bottom/anti-bottom pair production $pp \rightarrow S_1 S_1 b\bar{b}$, for which the tree-level Feynman diagrams are omitted due to their large number.

m_{S_1} [GeV]	κ_{H1}	$\sqrt{s} = 13$ TeV		$\sqrt{s} = 13.6$ TeV		$\sqrt{s} = 14$ TeV	
		σ [fb]	NE	σ [fb]	NE	σ [fb]	NE
124.8	8.821	346.800	65892	386.000	173700	412.100	1236300
140.0	5.700	82.800	15732	92.320	41544	99.090	297270
155.0	8.398	110.400	20976	123.500	55575	132.800	398400
170.4	8.191	66.460	12627	74.690	33610	80.310	240930
185.3	8.350	46.310	8799	52.070	23431	56.190	168570
201.9	9.548	40.030	7606	45.190	20335	48.840	146520

Table 4.2: Model predictions of the cross section $\sigma(pp \rightarrow S_1 S_1 j)$ and corresponding number of events (NE) for six benchmark $m_{S_1} < m_{S_2}$ case points, at three distinct center-of-mass energies. The NE's were computed for the following integrated luminosities: $L = 190 \text{ fb}^{-1}$ at $\sqrt{s} = 13$ TeV, $L = 450 \text{ fb}^{-1}$ at $\sqrt{s} = 13.6$ TeV and $L = 3000 \text{ fb}^{-1}$ at $\sqrt{s} = 14$ TeV.

m_{S_1} [GeV]	κ_{H1}	$\sqrt{s} = 13$ TeV		$\sqrt{s} = 13.6$ TeV		$\sqrt{s} = 14$ TeV	
		σ [fb]	NE	σ [fb]	NE	σ [fb]	NE
124.8	8.821	18.500	3515	20.760	9342	22.340	67020
140.0	5.700	2.337	444	2.629	1183	2.835	8505
155.0	8.398	6.477	1231	7.318	3293	7.907	23721
170.4	8.191	3.958	752	4.477	2015	4.843	14529
185.3	8.350	2.950	560	3.348	1507	3.628	10884
201.9	9.548	3.317	630	3.774	1698	4.093	12279

Table 4.3: Model predictions of the cross section $\sigma(pp \rightarrow S_1 S_1 h)$ and corresponding number of events (NE) for six benchmark $m_{S_1} < m_{S_2}$ case points, at three distinct center-of-mass energies. The NE's were computed for the following integrated luminosities: $L = 190 \text{ fb}^{-1}$ at $\sqrt{s} = 13$ TeV, $L = 450 \text{ fb}^{-1}$ at $\sqrt{s} = 13.6$ TeV and $L = 3000 \text{ fb}^{-1}$ at $\sqrt{s} = 14$ TeV.

m_{S_1} [GeV]	κ_{H1}	$\sqrt{s} = 13$ TeV		$\sqrt{s} = 13.6$ TeV		$\sqrt{s} = 14$ TeV	
		σ [fb]	NE	σ [fb]	NE	σ [fb]	NE
124.8	8.821	2.887	548	3.119	1403	3.270	1471
140.0	5.700	0.557	106	0.603	271	0.634	285
155.0	8.398	0.615	117	0.672	302	0.705	317
170.4	8.191	0.316	60	0.345	155	0.364	164
185.3	8.350	0.190	36	0.208	93	0.220	99
201.9	9.548	0.140	27	0.154	69	0.163	73

Table 4.4: Model predictions of the cross section $\sigma(pp \rightarrow S_1 S_1 Z)$ and corresponding number of events (NE) for six benchmark $m_{S_1} < m_{S_2}$ case points, at three distinct center-of-mass energies. The NE's were computed for the following integrated luminosities: $L = 190 \text{ fb}^{-1}$ at $\sqrt{s} = 13$ TeV, $L = 450 \text{ fb}^{-1}$ at $\sqrt{s} = 13.6$ TeV and $L = 3000 \text{ fb}^{-1}$ at $\sqrt{s} = 14$ TeV.

4.5. Searches for the Lighter DM Particle at the LHC

m_{S_1} [GeV]	κ_{H1}	$\sqrt{s} = 13$ TeV		$\sqrt{s} = 13.6$ TeV		$\sqrt{s} = 14$ TeV	
		σ [fb]	NE	σ [fb]	NE	σ [fb]	NE
124.8	8.821	31.180	5924	34.940	15723	37.510	112530
140.0	5.700	4.834	918	5.414	2436	5.810	17430
155.0	8.398	9.951	1891	11.210	5044	12.070	36210
170.4	8.191	5.911	1123	6.672	3002	7.216	21648
185.3	8.350	4.258	809	4.825	2171	5.214	15642
201.9	9.548	4.474	850	5.086	2289	5.512	16536

Table 4.5: Model predictions of the cross section $\sigma(pp \rightarrow S_1 S_1 b\bar{b})$ and corresponding number of events (NE) for six benchmark $m_{S_1} < m_{S_2}$ case points, at three distinct center-of-mass energies. The NE's were computed for the following integrated luminosities: $L = 190 \text{ fb}^{-1}$ at $\sqrt{s} = 13$ TeV, $L = 450 \text{ fb}^{-1}$ at $\sqrt{s} = 13.6$ TeV and $L = 3000 \text{ fb}^{-1}$ at $\sqrt{s} = 14$ TeV.

The results for the mono-jet, mono-Higgs, mono- Z and di-jet $b\bar{b}$ pair production are presented in Tables 4.2, 4.3, 4.4 and 4.5, respectively. Since these results were obtained for the same six benchmark $m_{S_1} < m_{S_2}$ case points and the same three (\sqrt{s}, L) LHC configurations, they offer a clear idea of which S_1 production processes are most relevant for DM searches at the LHC.

- The Feynman diagrams containing ggh effective vertices – which arise from top quark loops in gluon fusion (see Fig. 4.8), the dominant Higgs production mechanism at the LHC [84, 85] – are the main contributors to the cross sections of the mono-jet, mono-Higgs and di-jet processes. On the other hand, all Feynman diagrams for the mono- Z process also feature a Higgs mediator, but (at tree-level) do not contain the dominant ggh effective vertex. Hence, the mono- Z cross sections (and numbers of events) are lower than for the previous processes, as shown in Tables 4.2–4.5.
- The past Run 2 of the LHC operated at a center-of-mass energy of 13 TeV, and reached an integrated luminosity of 190 fb^{-1} . As shown in Table 4.4, the mono- Z numbers of events are still (low, i.e.) of order 10^1 – 10^2 , so the corresponding signal would be difficult to detect (by the end of Run 2). Conversely, the remaining signals could already be detectable, since the mono-jet (see Table 4.2) numbers of events are of order 10^3 – 10^4 , and the mono-Higgs (see Table 4.3) and di-jet $b\bar{b}$ (see Table 4.5) numbers of events are of order 10^2 – 10^3 .
- The current Run 3 of the LHC operates at a center-of-mass energy of 13.6 TeV and is expected to reach an integrated luminosity of 450 fb^{-1} , leading to a substantial increase (by at least a factor of 2) in the number of events for all considered S_1 production processes, as shown in Tables 4.2–4.5. In particular, this (\sqrt{s}, L) LHC configuration is more promising for the detection of mono- Z signals (especially for low S_1 masses¹⁰), as shown in Table 4.4.
- Finally, the future HL-LHC stage will operate at a center-of-mass energy of 14 TeV with an integrated luminosity of 3000 fb^{-1} , further increasing the number of events for all S_1 production processes, and ensuring the possibility of detecting any of these signals (including the mono- Z in the low S_1 mass range, as previously discussed) by the end of the entire LHC operation.

In summary, all previously discussed S_1 production processes are suitable for probing the two-real-scalar-singlet extension of the SM in LHC searches. The next step is to identify the LHC experimental results that meet our requirements and compare them with the theoretical predictions of this model. We

¹⁰But not any lower than $m_h = 125 \text{ GeV}$, which is the lower bound on m_{S_1} due to the DD exclusion related to S_1 (determined by $\Omega_{S_1}/\Omega_{\text{DM}}$), as discussed in Section 4.4.1 (see Table 4.1).

focus on the ATLAS analyses [4, 5, 6], which provide model-independent upper limits, rather than the similar – but exclusively model-dependent – CMS analyses [86, 87, 88].

4.5.1 Jet Searches

In Ref. [4], the ATLAS Collaboration established model-independent upper limits at the 95% confidence level (CL) on the visible cross section of DM production processes with one to four (final state) jets $j = q, \bar{q}, b, \bar{b}, g$, where $q = u, d, c, s$, at a center-of-mass energy of $\sqrt{s} = 13$ TeV. This visible cross section is defined as

$$\sum_{N=1}^4 \sigma^{\text{vis}}(pp \rightarrow Nj + \text{DM}) \equiv \sum_{N=1}^4 \sigma(pp \rightarrow Nj + \text{DM}) \times A \times \epsilon, \quad (4.96)$$

where A (<1) is the kinematic acceptance and ϵ (<1) is the experimental (detection) efficiency. Since both factors are positive and smaller than one, the visible cross section is lower than the cross section, i.e., $\sigma^{\text{vis}} \equiv \sigma \times A \times \epsilon < \sigma$. These upper limits are set as a function of the *cut* on the missing transverse momentum, so that p_T^{miss} is larger than the considered p_T^{miss} cut (or lower bound).¹¹ The cross sections are lower with missing transverse momentum cuts – which suppress the phase space of final state particles – compared to without them.

These limits were obtained from an analysis of data recorded by the ATLAS detector at the LHC during (the 2015-2018 time period of) Run 2 – corresponding to an integrated luminosity of $L = 139 \text{ fb}^{-1}$ at a center-of-mass energy of $\sqrt{s} = 13$ TeV – and are part of a broader search for BSM new physics phenomena in events with a final state containing (one to four) jets and large missing transverse momentum in proton-proton collisions. The final states of selected events for this BSM phenomena search [4] were required to meet the following criteria:

- large missing transverse momentum, $p_T^{\text{miss}} > 200 \text{ GeV}$;
- a leading jet with transverse momentum $p_T > 150 \text{ GeV}$ and pseudorapidity¹² $|\eta| < 2.4$, along with none to three additional (non-leading) jets with transverse momenta $p_T > 30 \text{ GeV}$ and pseudorapidities $|\eta| < 2.8$;
- azimuthal angle separations $\Delta\phi(\vec{p}_T^{\text{miss}}, \vec{p}^{j_i}) \equiv \phi(\vec{p}_T^{\text{miss}}) - \phi(\vec{p}^{j_i})$ between the missing transverse 3-momentum \vec{p}_T^{miss} and the 3-momentum \vec{p}^{j_i} of each jet j_i , $i = 1, \dots, N$ (with $N \in \{1, 2, 3, 4\}$), satisfying

$$\Delta\phi(\vec{p}_T^{\text{miss}}, \vec{p}^{j_i}) > \begin{cases} 0.4 \text{ rad}, & p_T^{\text{miss}} > 250 \text{ GeV} \\ 0.6 \text{ rad}, & 200 \text{ GeV} < p_T^{\text{miss}} \leq 250 \text{ GeV} \end{cases}. \quad (4.97)$$

The above criteria correspond to additional 3-momentum cuts that must be considered when computing the cross sections for the SM+2RSS model processes $pp \rightarrow S_1 S_1 + Nj$ ($N = 1, 2, 3, 4$), in order to test our theoretical model against the ATLAS experimental upper limits. However, one should remember the following: 1) visible cross sections are necessarily lower than the corresponding (defining, i.e., without cuts) cross sections; 2) momentum cuts necessarily lower cross sections. Hence, one can respectively conclude that: 1) if the model-predicted cross section for a given $m_{S_1} < m_{S_2}$ case point does not exceed the ATLAS upper limit on the visible cross section (4.96), then that point is necessarily not excluded by

¹¹One should notice that, in the center-of-mass reference frame, the missing 3-momentum must be the symmetric of the sum of the 3-momenta of the $N \in \{1, 2, 3, 4\}$ jets, i.e., $\vec{p}^{\text{miss}} = -\sum_{i=1}^N \vec{p}^{j_i}$, thus having the same magnitude.

¹²Pseudorapidity is defined as $\eta \equiv -\ln[\tan(\theta/2)]$, where θ is the 3-momentum polar angle.

this bound; 2) following the same reasoning, if the model-predicted cross section without part (or all) of the momentum cuts for a given $m_{S_1} < m_{S_2}$ case point does not exceed the ATLAS upper limit on the visible cross section, then that point is necessarily not excluded by this bound. Conversely, in both 1) and 2) cases, if the model-predicted cross section for a given $m_{S_1} < m_{S_2}$ case point does exceed the ATLAS upper limit on the visible cross section (4.96), nothing can be concluded unless the model prediction refers specifically to the *visible* cross section, with *all* momentum cuts applied in accordance with those used in the experimental upper bound.

Using MadGraph5_aMC@NLO [81, 82], we computed the cross section $\sum_{N=1}^4 \sigma(pp \rightarrow S_1 S_1 + Nj)$ of S_1 pair plus (one to four) jet production processes in our SM+2RSS model at a center-of-mass energy of $\sqrt{s} = 13$ TeV. The Feynman diagrams of the mono-jet production processes are (once again) shown in Figure 4.8. The remaining $N = 2, 3, 4$ multi-jet diagrams are not displayed, for being too numerous. Since Ref. [4] does not provide the acceptances A or efficiencies ϵ corresponding to the ATLAS upper limits on the visible cross section – each determined for a distinct missing transverse momentum cut – we are unable to convert these upper limits on the visible cross section into upper limits on the (defining) cross section, nor can we convert our model-predicted cross sections into visible cross sections.

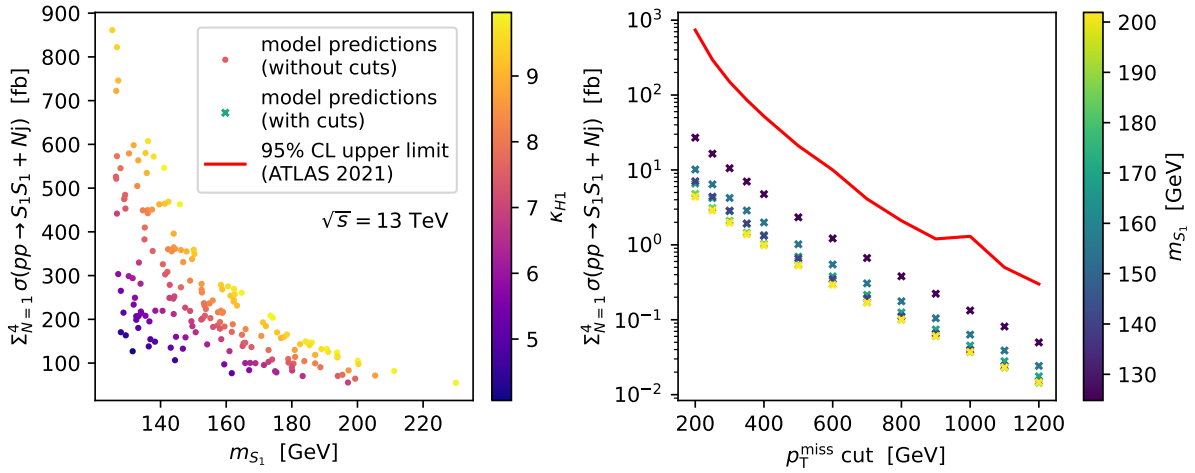


Figure 4.11: Cross section of jet production processes $pp \rightarrow S_1 S_1 + Nj$ ($N = 1, 2, 3, 4$), where $j = q, \bar{q}, b, \bar{b}, g$ and $q = u, d, c, s$, at a center-of-mass energy of $\sqrt{s} = 13$ TeV. The presented points correspond to the model’s theoretical predictions for the $m_{S_1} < m_{S_2}$ case points, and the red (solid) line is the ATLAS (2021) [4] model-independent experimental upper limit on the visible cross section (σ^{vis}) of $pp \rightarrow Nj + \text{DM}$ ($N = 1, 2, 3, 4$) processes. Left panel: model predictions of the cross section for all $m_{S_1} < m_{S_2}$ case points without momentum cuts. Right panel: model predictions of the cross section for six benchmark $m_{S_1} < m_{S_2}$ case points with different missing transverse momentum (p_T^{miss}) cuts, along with the corresponding ATLAS upper limits. The legend is shared by both panels.

The results are shown in Figure 4.11, which displays the theoretical predictions of the cross section $\sum_{N=1}^4 \sigma(pp \rightarrow S_1 S_1 + Nj)$ for the $m_{S_1} < m_{S_2}$ case points of our model – represented as dots (left panel) or crosses (right panel) – and the ATLAS upper limit on the visible cross section (4.96) for distinct missing transverse momentum cuts, represented by a solid red line (right panel). The left panel shows the model predictions for the cross section without any momentum cuts across all $m_{S_1} < m_{S_2}$ case points, plotted as a function of the mass m_{S_1} (x -axis) and the portal coupling constant κ_{H1} (colour bar) of S_1 . The right panel presents the ATLAS upper limits on the visible cross section (4.96) as a function of the missing transverse momentum cut (x -axis), alongside the model predictions for six benchmark $m_{S_1} < m_{S_2}$ case points of the cross section with the same momentum cuts – not only on the missing transverse momentum but also on the jet momenta, as required by the event selection criteria – ensuring consistency with the

ATLAS upper limits. One can easily conclude that all $m_{S_1} < m_{S_2}$ case free parameter space points are not experimentally excluded by this LHC search. In particular, the right panel alone shows that these points are at least (because these model predictions refer to the cross section $\sigma > \sigma^{\text{vis}}$) roughly one (to two) order(s) of magnitude away from exclusion.

4.5.2 Mono-Higgs Searches

In Ref. [5], the ATLAS Collaboration established model-independent upper limits at the 95% CL on the visible cross section of DM production processes with a (final state) Higgs boson, at a center-of-mass energy of $\sqrt{s} = 13$ TeV. This visible cross section is defined as

$$\sigma^{\text{vis}}(pp \rightarrow h + \text{DM}) \equiv \sigma(pp \rightarrow h + \text{DM}) \times A \times \epsilon \times \text{BR}(h \rightarrow b\bar{b}), \quad (4.98)$$

where A is the acceptance, ϵ is the efficiency and the branching ratio for the hadronic Higgs boson decay is (defined as, and) given by

$$\text{BR}(h \rightarrow b\bar{b}) \equiv \frac{\Gamma(h \rightarrow b\bar{b})}{\Gamma_h^{\text{(total)}}} \approx 0.58, \quad (4.99)$$

Since all three factors are positive and smaller than one, the visible cross section is lower than the cross section, i.e., $\sigma^{\text{vis}} \equiv \sigma \times A \times \epsilon \times \text{BR}(h \rightarrow b\bar{b}) < \sigma$. These upper limits are set as a function of the missing transverse momentum *range*, where p_T^{miss} is both bounded from below and from above.¹³ The selected p_T^{miss} ranges translate into (not only lower, but also upper) p_T^{miss} cuts in the cross section, which suppress the phase space of final state particles, thus lowering the cross section value.

These limits were obtained from an analysis of data recorded by the ATLAS detector at the LHC during (the 2015-2018 time period of) Run 2 – corresponding to an integrated luminosity of $L = 139 \text{ fb}^{-1}$ at a center-of-mass energy of $\sqrt{s} = 13$ TeV – and are part of a broader search for DM particles produced in mono-Higgs events; in particular, events with a final state containing b -tagged jets consistent with a (single) Higgs boson h and large missing transverse momentum in proton-proton collisions. The event selection can be consulted in (section 5 of) Ref. [5].

Using MadGraph5_aMC@NLO [81, 82], we computed the cross section $\sigma(pp \rightarrow S_1 S_1 h)$ of the S_1 pair plus mono-Higgs production process in our SM+2RSS model at a center-of-mass energy of $\sqrt{s} = 13$ TeV. The corresponding Feynman diagrams are (once again) shown in Figure 4.9. Analogously to what happened in Section 4.5.1 with the jet search analysis [4], this mono-Higgs search analysis [5] does not provide the acceptances A or efficiencies ϵ corresponding to the ATLAS upper limits on the visible cross section – each determined for a distinct missing transverse momentum range – and once again, we are unable to convert these upper limits on the visible cross section into upper limits on the (defining) cross section, nor can we convert our model-predicted cross sections into visible cross sections.

The results are shown in Figure 4.12, which displays the theoretical predictions of the cross section $\sigma(pp \rightarrow S_1 S_1 h)$ for the $m_{S_1} < m_{S_2}$ case points of our model – represented as dots (left panel) or crosses (right panel) – and the ATLAS upper limit on $\sigma^{\text{vis}}/\text{BR}(h \rightarrow b\bar{b}) \equiv \sigma \times A \times \epsilon (< \sigma)$ for distinct missing transverse momentum ranges, represented by a solid red line (right panel). The left panel shows the model predictions for the cross section without any momentum cuts across all $m_{S_1} < m_{S_2}$ case points, plotted as a function of the mass m_{S_1} (x -axis) and the portal coupling constant κ_{H1} (colour bar) of S_1 . The right panel presents the ATLAS upper limits on $\sigma^{\text{vis}}/\text{BR}(h \rightarrow b\bar{b}) \equiv \sigma \times A \times \epsilon$ as a function of the missing transverse momentum range (x -axis), alongside the model predictions for six benchmark $m_{S_1} < m_{S_2}$

¹³In the center-of-mass reference frame, the missing 3-momentum is the symmetric of the Higgs boson 3-momentum, i.e., $\vec{p}^{\text{miss}} = -\vec{p}^h$, thus having the same magnitude.

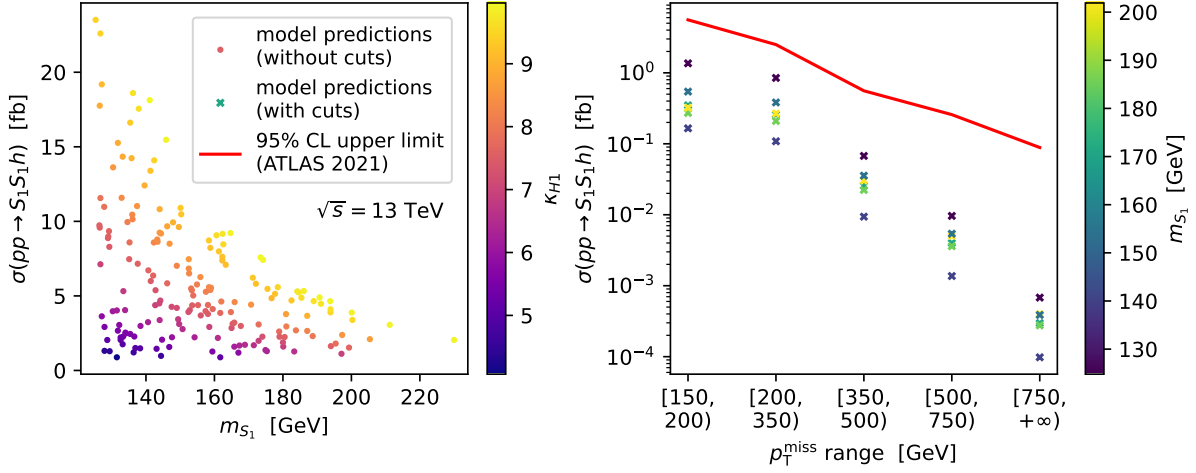


Figure 4.12: Cross section of mono-Higgs production processes $pp \rightarrow S_1 S_1 h$ at a center-of-mass energy of $\sqrt{s} = 13$ TeV. The presented points correspond to the model's theoretical predictions for the $m_{S_1} < m_{S_2}$ case points, and the red (solid) line is the ATLAS (2021) [5] model-independent experimental upper limit on $\sigma^{\text{vis}}/\text{BR}(h \rightarrow b\bar{b}) \equiv \sigma \times A \times \epsilon$ of $pp \rightarrow Z + \text{DM}$ processes. Left panel: model predictions of the cross section for all $m_{S_1} < m_{S_2}$ case points without momentum cuts. Right panel: model predictions of the cross section for six benchmark $m_{S_1} < m_{S_2}$ case points with different missing transverse momentum (p_T^{miss}) ranges, along with the corresponding ATLAS upper limits. The legend is shared by both panels.

case points of the cross section with the same momentum cuts (ensuring consistency with the ATLAS upper limits). One can easily conclude that all $m_{S_1} < m_{S_2}$ case free parameter space points are not experimentally excluded by this LHC search. In particular, the right panel alone shows that these points are at least (because these model predictions refer to the cross section $\sigma > \sigma \times A \times \epsilon$) roughly one order of magnitude away from exclusion.

4.5.3 Mono- Z Searches

In Ref. [6], the ATLAS Collaboration established model-independent upper limits at the 95% CL on the visible cross section of DM production processes with a (final state) Z boson, at a center-of-mass energy of $\sqrt{s} = 13$ TeV. This visible cross section is defined as

$$\sigma^{\text{vis}}(pp \rightarrow Z + \text{DM}) \equiv \sigma(pp \rightarrow Z + \text{DM}) \times A \times \epsilon \times \sum_q \text{BR}(Z \rightarrow q\bar{q}), \quad (4.100)$$

where A is the acceptance, ϵ is the efficiency and the branching ratio for the hadronic Z boson decay is (defined as, and) given by

$$\sum_q \text{BR}(Z \rightarrow q\bar{q}) \equiv \frac{\sum_q \Gamma(Z \rightarrow q\bar{q})}{\Gamma_Z^{\text{(total)}}} = \frac{(1.664 \pm 3.3 \times 10^{-5}) \text{ GeV}}{(2.412 \pm 3.5 \times 10^{-5}) \text{ GeV}} \approx 0.69, \quad (4.101)$$

where the sum is performed over all quarks $q = u, d, c, s, b$ (although the top quark t does not contribute, because the decay $Z \rightarrow t\bar{t}$ is kinematically impossible to occur). Since all three factors are positive and smaller than one, the visible cross section is lower than the cross section, i.e., $\sigma^{\text{vis}} \equiv \sigma \times A \times \epsilon \times \sum_q \text{BR}(Z \rightarrow q\bar{q}) < \sigma$. These upper limits are set as a function of the missing transverse momentum range, where p_T^{miss} is both bounded from below and from above.¹⁴ The selected p_T^{miss} ranges translate

¹⁴In the center-of-mass reference frame, the missing 3-momentum is the symmetric of the Z boson 3-momentum, i.e., $\vec{p}^{\text{miss}} = -\vec{p}^Z$, thus having the same magnitude.

into (not only lower, but also upper) p_T^{miss} cuts in the cross section, which suppress the phase space of final state particles, thus lowering the cross section value.

These limits were obtained from an analysis of data recorded by the ATLAS detector at the LHC during (a 2015-2016 time period of) Run 2 – corresponding to an integrated luminosity of $L = 36.1 \text{ fb}^{-1}$ at a center-of-mass energy of $\sqrt{s} = 13 \text{ TeV}$ – and are part of a broader search for DM particles produced in mono- W^\pm/Z events, i.e., events with a final state containing a (single) weak gauge boson W^\pm or Z and large missing transverse momentum in proton-proton collisions. The event selection can be consulted in (section 6 of) Ref. [6].

Using MadGraph5_aMC@NLO [81, 82], we computed the cross section $\sigma(pp \rightarrow S_1 S_1 Z)$ of the S_1 pair plus mono- Z production process in our SM+2RSS model at a center-of-mass energy of $\sqrt{s} = 13 \text{ TeV}$. The corresponding Feynman diagrams are (once again) shown in Figure 4.10. In contrast to what happened in Sections 4.5.1 and 4.5.2 with the jet and mono-Higgs search analyses [4, 5] (respectively), this mono- W^\pm/Z search analysis [6] provides both the acceptances A and the efficiencies ϵ corresponding to the ATLAS upper limits on the visible cross section – each determined for a distinct missing transverse momentum range – thus enabling us to convert these upper limits on the visible cross section into upper limits on the (defining) cross section through Eq. (4.100).

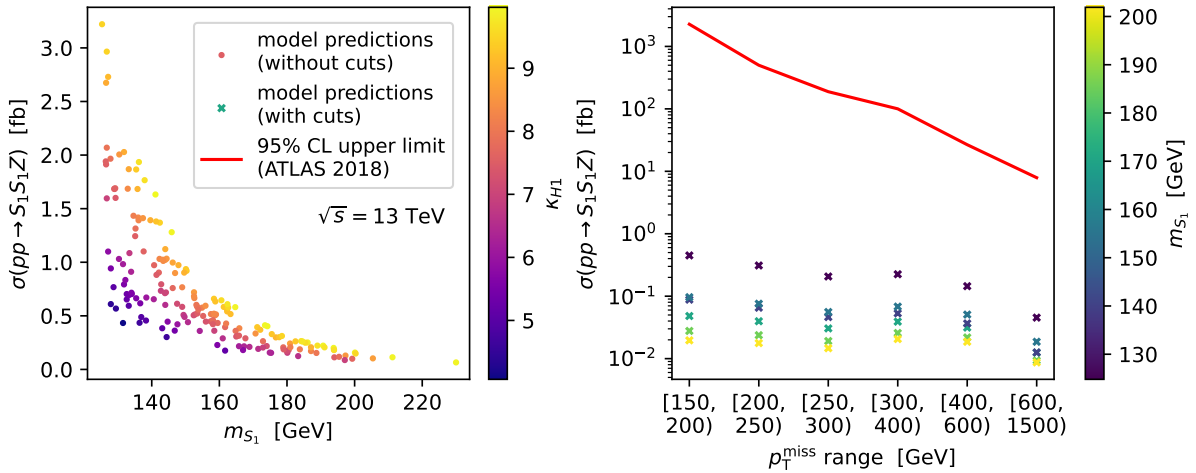


Figure 4.13: Cross section of mono- Z production processes $pp \rightarrow S_1 S_1 Z$ at a center-of-mass energy of $\sqrt{s} = 13 \text{ TeV}$. The presented points correspond to the model’s theoretical predictions for the $m_{S_1} < m_{S_2}$ case points, and the red (solid) line is the ATLAS (2018) [6] model-independent experimental upper limit on the cross section (σ) of $pp \rightarrow Z + \text{DM}$ processes. Left panel: model predictions of the cross section for all $m_{S_1} < m_{S_2}$ case points without momentum cuts. Right panel: model predictions of the cross section for six benchmark $m_{S_1} < m_{S_2}$ case points with different missing transverse momentum (p_T^{miss}) ranges, along with the corresponding ATLAS upper limits. The legend is shared by both panels.

The results are shown in Figure 4.13, which displays the theoretical predictions of the cross section $\sigma(pp \rightarrow S_1 S_1 Z)$ for the $m_{S_1} < m_{S_2}$ case points of our model – represented as dots (left panel) or crosses (right panel) – and the ATLAS upper limit on the cross section (4.100) for distinct missing transverse momentum ranges, represented by a solid red line (right panel). The left panel shows the model predictions for the cross section without any momentum cuts across all $m_{S_1} < m_{S_2}$ case points, plotted as a function of the mass m_{S_1} (x -axis) and the portal coupling constant κ_{H1} (colour bar) of S_1 . The right panel presents the ATLAS upper limits on the cross section as a function of the missing transverse momentum range (x -axis), alongside the model predictions for six benchmark $m_{S_1} < m_{S_2}$ case points of the cross section with the same momentum cuts (ensuring consistency with the ATLAS upper limits). One can easily conclude that all $m_{S_1} < m_{S_2}$ case free parameter space points are far from being experimentally

excluded by this LHC search. In particular, the right panel alone shows that these points are roughly two to five orders of magnitude away from exclusion. Furthermore, as shown in the left panel, the model predictions of the cross section – even without any momentum cuts – are lower than the ATLAS upper limits on the cross section for all missing transverse momentum ranges; for all $m_{S_1} < m_{S_2}$ case points, thereby ensuring that none of these points is excluded.

Chapter 5

The Three-Real-Scalar-Singlet SM Extension

The two-real-scalar-singlet SM extension (4.4) with an unbroken $\mathcal{Z}_2^{(1)} \times \mathcal{Z}_2^{(2)}$ discrete symmetry that was studied in the previous Chapter 4 provided us an experimentally allowed free parameter space region – the (one-light-one-heavy) $m_{S_1} < m_{S_2}$ case allowed region – where the heavier DM particle S_2 is responsible for (virtually) all the observed DM relic density, but more importantly, the lighter DM particle S_1 can be searched for at the LHC – something that was impossible for the (one) real scalar singlet SM extension (3.4) with an unbroken \mathcal{Z}_2 discrete symmetry that was studied in Chapter 3, which is experimentally excluded for DM masses below 3535 GeV.

However, as discussed in Section 4.4.2, the new LZ 2024 results [3] practically exclude all $m_{S_1} < m_{S_2}$ case free parameter space points, since the respective $\sigma^{\text{SI}}(S_r N \rightarrow S_r N) \times \Omega_{S_r}/\Omega_{\text{DM}}$ ($r = 1, 2$) predicted values fall above the corresponding (LZ 2024) upper limit on the WIMP-nucleon elastic scattering SI cross section, with part of them laying inside the experimental uncertainty band (for both DM particles) – thus not being definitely excluded (but almost).

We shall now investigate what happens (i.e., which new features arise, if any) if we extend the SM with a *third* real scalar singlet S_3 (and respective $\mathcal{Z}_2^{(3)}$ discrete symmetry), in the same spirit of our transition from one to two real scalar singlets in Chapter 4.

5.1 The SM+3RSS DM Model with an Unbroken $\mathcal{Z}_2^{(1)} \times \mathcal{Z}_2^{(2)} \times \mathcal{Z}_2^{(3)}$ Symmetry

We now consider an extension of the Standard Model with three real scalar $\text{SU}(3)_c \times \text{SU}(2)_L \times \text{U}(1)_Y$ singlet fields $S_1(x), S_2(x), S_3(x) \sim (\mathbf{1}, \mathbf{1}, 0)$, and impose (in addition to the SM gauge invariance) an additional symmetry with respect to the discrete direct product group $\mathcal{Z}_2^{(1)} \times \mathcal{Z}_2^{(2)} \times \mathcal{Z}_2^{(3)}$, under which the fields transform as

$$\mathcal{Z}_2^{(1)} : S_1(x) \rightarrow -S_1(x), \quad S_2(x) \rightarrow +S_2(x), \quad S_3(x) \rightarrow +S_3(x), \quad \text{SM} \rightarrow +\text{SM} \quad (5.1)$$

$$\mathcal{Z}_2^{(2)} : S_1(x) \rightarrow +S_1(x), \quad S_2(x) \rightarrow -S_2(x), \quad S_3(x) \rightarrow +S_3(x), \quad \text{SM} \rightarrow +\text{SM} \quad (5.2)$$

$$\mathcal{Z}_2^{(3)} : S_1(x) \rightarrow +S_1(x), \quad S_2(x) \rightarrow +S_2(x), \quad S_3(x) \rightarrow -S_3(x), \quad \text{SM} \rightarrow +\text{SM}, \quad (5.3)$$

5.1. The SM+3RSS DM Model with an Unbroken $\mathcal{Z}_2^{(1)} \times \mathcal{Z}_2^{(2)} \times \mathcal{Z}_2^{(3)}$ Symmetry

i.e., only $S_r(x)$ is $\mathcal{Z}_2^{(r)}$ -odd, while the remaining fields are $\mathcal{Z}_2^{(r)}$ -even and transform trivially under $\mathcal{Z}_2^{(r)}$, $r = 1, 2, 3$. In other words, the non-trivial transformations under $\mathcal{Z}_2^{(1)} \times \mathcal{Z}_2^{(2)} \times \mathcal{Z}_2^{(3)}$ are

$$\mathcal{Z}_2^{(1)} \times \mathcal{Z}_2^{(2)} \times \mathcal{Z}_2^{(3)} : S_r(x) \rightarrow -S_r(x), \quad r = 1 \vee r = 2 \vee r = 3 \vee r = 1, 2 \vee r = 2, 3 \vee r = 3, 1 \vee r = 1, 2, 3.$$

The $\mathcal{Z}_2^{(r)}$ ($r = 1, 2, 3$) charges can be interpreted as three independent *dark* (intrinsic) parity quantum numbers. Therefore, the most general renormalizable Lagrangian density invariant under $\text{SU}(3)_c \times \text{SU}(2)_L \times \text{U}(1)_Y \times \mathcal{Z}_2^{(1)} \times \mathcal{Z}_2^{(2)} \times \mathcal{Z}_2^{(3)}$ transformations is given by

$$\begin{aligned} \mathcal{L}_{\text{SM+3RSS}} = \mathcal{L}_{\text{SM}} + \sum_{r=1}^3 \left[\frac{1}{2} (\partial_\mu S_r) \partial^\mu S_r - \frac{1}{2} \mu_r^2 S_r^2 - \frac{\lambda_r}{4!} S_r^4 - \underbrace{\frac{\kappa_{Hr}}{2} S_r^2 \Phi^\dagger \Phi}_{=\mathcal{L}_{\text{portal}(r)}} \right] \\ - \underbrace{\frac{\lambda_{12}}{4} S_1^2 S_2^2}_{=\mathcal{L}_{\text{int}(1,2)}} - \underbrace{\frac{\lambda_{23}}{4} S_2^2 S_3^2}_{=\mathcal{L}_{\text{int}(2,3)}} - \underbrace{\frac{\lambda_{31}}{4} S_3^2 S_1^2}_{=\mathcal{L}_{\text{int}(3,1)}} \supset -V(|\Phi|, S_1, S_2, S_3), \end{aligned} \quad (5.4)$$

where $\Phi(x) = \begin{pmatrix} G^+(x) & \phi^0(x) \end{pmatrix}^\top \sim (\mathbf{1}, \mathbf{2}, +1/2)$ is the Higgs doublet, and the scalar potential is now given by

$$\begin{aligned} V(|\Phi|, S_1, S_2, S_3) = \mu_H^2 \Phi^\dagger \Phi + \lambda_H (\Phi^\dagger \Phi)^2 + \sum_{r=1}^3 \left[\frac{1}{2} \mu_r^2 S_r^2 + \frac{\lambda_r}{4!} S_r^4 + \frac{\kappa_{Hr}}{2} S_r^2 \Phi^\dagger \Phi \right] \\ + \frac{\lambda_{12}}{4} S_1^2 S_2^2 + \frac{\lambda_{23}}{4} S_2^2 S_3^2 + \frac{\lambda_{31}}{4} S_3^2 S_1^2. \end{aligned} \quad (5.5)$$

The singlets $S_r(x)$ couple to each other through the interaction terms $\mathcal{L}_{\text{int}(r,r')}$, which link the (three) dark sectors between them, and to the Higgs doublet $\Phi(x)$ through the portal terms $\mathcal{L}_{\text{portal}(r)}$, which link the dark sectors to the SM sector ($r, r' = 1, 2, 3 \wedge r \neq r'$).

The vacuum (or ground) state is obtained by the usual minimization procedure

$$\begin{aligned} \begin{cases} \frac{\partial V}{\partial \Phi} \big|_{\Phi=\langle \Phi \rangle_0, S_r=\langle S_r \rangle_0} = \left(\mu_H^2 + 2\lambda_H \langle \Phi \rangle_0^\dagger \langle \Phi \rangle_0 + \sum_{r=1}^3 \frac{\kappa_{Hr}}{2} \langle S_r \rangle_0^2 \right) \langle \Phi \rangle_0^\dagger = 0 \\ \frac{\partial V}{\partial \Phi^\dagger} \big|_{\Phi=\langle \Phi \rangle_0, S_r=\langle S_r \rangle_0} = \left(\mu_H^2 + 2\lambda_H \langle \Phi \rangle_0^\dagger \langle \Phi \rangle_0 + \sum_{r=1}^3 \frac{\kappa_{Hr}}{2} \langle S_r \rangle_0^2 \right) \langle \Phi \rangle_0 = 0 \\ \frac{\partial V}{\partial S_1} \big|_{\Phi=\langle \Phi \rangle_0, S_r=\langle S_r \rangle_0} = \left(\mu_1^2 + \frac{\lambda_1}{3!} \langle S_1 \rangle_0^2 + \kappa_{H1} \langle \Phi \rangle_0^\dagger \langle \Phi \rangle_0 + \frac{\lambda_{12}}{2} \langle S_2 \rangle_0^2 + \frac{\lambda_{31}}{2} \langle S_3 \rangle_0^2 \right) \langle S_1 \rangle_0 = 0 \\ \frac{\partial V}{\partial S_2} \big|_{\Phi=\langle \Phi \rangle_0, S_r=\langle S_r \rangle_0} = \left(\mu_2^2 + \frac{\lambda_2}{3!} \langle S_2 \rangle_0^2 + \kappa_{H2} \langle \Phi \rangle_0^\dagger \langle \Phi \rangle_0 + \frac{\lambda_{23}}{2} \langle S_3 \rangle_0^2 + \frac{\lambda_{12}}{2} \langle S_1 \rangle_0^2 \right) \langle S_2 \rangle_0 = 0 \\ \frac{\partial V}{\partial S_3} \big|_{\Phi=\langle \Phi \rangle_0, S_r=\langle S_r \rangle_0} = \left(\mu_3^2 + \frac{\lambda_3}{3!} \langle S_3 \rangle_0^2 + \kappa_{H3} \langle \Phi \rangle_0^\dagger \langle \Phi \rangle_0 + \frac{\lambda_{31}}{2} \langle S_1 \rangle_0^2 + \frac{\lambda_{23}}{2} \langle S_2 \rangle_0^2 \right) \langle S_3 \rangle_0 = 0 \end{cases} \\ \Leftrightarrow \begin{pmatrix} \langle \Phi \rangle_0 = 0 \vee \langle \Phi \rangle_0^\dagger \langle \Phi \rangle_0 = -\frac{\mu_H^2 + \sum_{r=1}^3 \kappa_{Hr} \langle S_r \rangle_0^2 / 2}{2\lambda_H} \end{pmatrix} \\ \bigwedge_{r=1}^3 \begin{pmatrix} \langle S_r \rangle_0 = 0 \vee \langle S_r \rangle_0^2 = -\frac{\mu_r^2 + \kappa_{Hr} \langle \Phi \rangle_0^\dagger \langle \Phi \rangle_0 + \sum_{r' \neq r} \lambda_{rr'} \langle S_{r'} \rangle_0^2 / 2}{\lambda_r / 3!} \end{pmatrix}, \end{aligned} \quad (5.6)$$

corresponding to sixteen $\text{SU}(3)_c \times \text{SU}(2)_L \times \text{U}(1)_Y \times \mathcal{Z}_2^{(1)} \times \mathcal{Z}_2^{(2)} \times \mathcal{Z}_2^{(3)}$ invariant stationary solution sets (which can be minima by requiring the Hessian matrix to have positive eigenvalues)

$$\langle \Phi \rangle_0 = 0 \quad \bigwedge_{r=1}^3 \quad \langle S_r \rangle_0 = 0, \quad (5.7)$$

$$\langle \Phi \rangle_0^\dagger \langle \Phi \rangle_0 = -\frac{\mu_H^2}{2\lambda_H} \equiv \frac{v^2}{2} \bigwedge_{r=1}^3 \langle S_r \rangle_0 = 0, \quad (5.8)$$

$$\langle \Phi \rangle_0 = 0 \quad \wedge \quad \langle S_r \rangle_0^2 = -\frac{6\mu_r^2}{\lambda_r} \equiv v_r^2 \bigwedge_{r' \neq r} \langle S_{r'} \rangle_0 = 0, \quad r = 1, 2, 3, \quad (5.9)$$

$$\langle \Phi \rangle_0^\dagger \langle \Phi \rangle_0 = -\frac{\mu_H^2 + \kappa_{Hr} v_r'^2/2}{2\lambda_H} \equiv \frac{v'^2}{2} \quad \wedge \quad \langle S_r \rangle_0^2 = -\frac{\mu_r^2 + \kappa_{Hr} v'^2/2}{\lambda_r/3!} \equiv v_r'^2 \bigwedge_{r' \neq r} \langle S_{r'} \rangle_0 = 0, \quad r = 1, 2, 3, \quad (5.10)$$

$$\langle \Phi \rangle_0 = 0 \quad \wedge \quad \langle S_r \rangle_0 = 0 \quad \bigwedge_{r' \neq r} \langle S_{r'} \rangle_0^2 = -\frac{\mu_{r'}^2 + \lambda_{r'm} v_m''^2/2}{\lambda_{r'}/3!} \equiv v_{r'}''^2, \quad r = 1, 2, 3 \wedge m \neq r, r', \quad (5.11)$$

$$\langle \Phi \rangle_0^\dagger \langle \Phi \rangle_0 = -\frac{\mu_H^2 + \sum_{r' \neq r} \kappa_{Hr'} v_{r'}'''^2/2}{2\lambda_H} \equiv \frac{v'''^2}{2} \quad \wedge \quad \langle S_r \rangle_0 = 0 \quad \bigwedge_{r' \neq r} \langle S_{r'} \rangle_0^2 = -\frac{\mu_{r'}^2 + \kappa_{Hr'} v''^2/2 + \lambda_{r'm} v_m'''^2/2}{\lambda_{r'}/3!} \equiv v_{r'}'''^2, \quad r = 1, 2, 3 \wedge m \neq r, r', \quad (5.12)$$

$$\langle \Phi \rangle_0 = 0 \quad \bigwedge_{r=1}^3 \langle S_r \rangle_0 = -\frac{\mu_r^2 + \sum_{r' \neq r} \lambda_{rr'} v_{r'}'''^2/2}{\lambda_r/3!} \equiv v_r'''^2, \quad (5.13)$$

$$\langle \Phi \rangle_0^\dagger \langle \Phi \rangle_0 = -\frac{\mu_H^2 + \sum_{r=1}^3 \kappa_{Hr} v_r'''^2/2}{2\lambda_H} \equiv \frac{v'''^2}{2} \quad \bigwedge_{r=1}^3 \langle S_r \rangle_0^2 = -\frac{\mu_r^2 + \kappa_{Hr} v'''^2/2 + \sum_{r' \neq r} \lambda_{rr'} v_{r'}'''^2/2}{\lambda_r/3!} \equiv v_r'''^2. \quad (5.14)$$

Once again, let us analyse these vacuum configurations in more detail. Since the $\Phi(x)$ and $S_r(x)$ ($r = 1, 2, 3$) fields are $SU(3)_c$ singlets – i.e., they are not coloured and thus transform trivially under this gauge group – the local $SU(3)_c$ symmetry cannot be spontaneously broken. Therefore, it is sufficient to consider only the $SU(2)_L \times U(1)_Y \times \mathcal{Z}_2^{(1)} \times \mathcal{Z}_2^{(2)} \times \mathcal{Z}_2^{(3)}$ symmetry for this discussion.

- For the minimum solution sets (5.7), (5.9), (5.11) and (5.13) the Higgs doublet does not acquire a VEV, i.e. $\langle \Phi \rangle_0 = 0$, and thus electroweak $SU(2)_L \times U(1)_Y \rightarrow U(1)_Q$ SSB does not occur. Consequently, no mass terms for the electroweak gauge bosons and fermions are generated via the SM Higgs mechanism, and therefore, these vacuum configurations do not correspond to what is physically observed in Nature. We are left with vacuum configurations (5.8), (5.10), (5.12) and (5.14), where the Higgs doublet acquires a non-zero VEV $\langle \Phi \rangle_0 \neq 0$ (out of the possible $SU(2)_L \times U(1)_Y$ gauge invariant solution set), thus spontaneously breaking the $SU(2)_L \times U(1)_Y$ gauge symmetry of the vacuum down to $U(1)_Q$. Without loss of generality, we can take the conventional VEV

$$\langle \Phi \rangle_0 = \begin{pmatrix} 0 \\ \frac{v}{\sqrt{2}} \end{pmatrix}, \quad \text{so that} \quad \Phi(x) = \begin{pmatrix} G^+(x) \\ \frac{v+h(x)+iG^0(x)}{\sqrt{2}} \end{pmatrix}, \quad (5.15)$$

where $v \in \mathbb{R}^+$ is determined by the choice of vacuum configuration (between (5.8), (5.10), (5.12) and (5.14)). As usual, the fields $G^0(x)$ and $G^\pm(x)$ are would-be Goldstone bosons that can be “gauged away” into the unitary gauge.

- For minimum solution sets (5.8), (5.10), (5.12), (5.14), $n = 0, 1, 2, 3$ (resp.) singlets $S_r(x)$ also acquire a non-zero VEV out of the possible $\mathcal{Z}_2^{(r)}$ invariant (discrete) solution set $\langle S_r \rangle_0 = \pm v_r$

($v_r \in \mathbb{R}^+$), thus also spontaneously breaking the $\mathcal{Z}_2^{(r)}$ symmetries of the vacuum; while the other $3 - n$ symmetries $\mathcal{Z}_2^{(r')}$ remain unbroken. After $SU(2)_L \times U(1)_Y \times \mathcal{Z}_2^{(1)} \times \mathcal{Z}_2^{(2)} \times \mathcal{Z}_2^{(3)} \rightarrow U(1)_Q \times_{r'} \mathcal{Z}_2^{(r')}$ SSB, $h(x)$ and the n field perturbations $\xi_r(x) \equiv S_r(x) - \langle S_r \rangle_0$ mix in the hS_rS_r couplings (contained in the portal terms) and in the $S_rS_rS_mS_m$ couplings¹ (contained in the inter-dark sector terms), but the $3 - n$ fields $S_{r'}(x)$ do not mix. Hence, while $S_{r'}(x)$ are $3 - n$ mass eigenstates (physical fields), $h(x), \xi_r(x)$ are $1+n$ interaction eigenstates. The $1+n$ remaining mass eigenstates $h'(x), h_{\xi_r}(x)$ are given by a flavour space rotation of the $1+n$ interaction eigenstates, so that the scalar mass terms are diagonal (without flavour mixing) in the mass basis. In this scenario, h', h_{ξ_r} are Higgs-like particles (one of them being the 125 GeV discovered Higgs boson), and therefore, are able to decay (unstable particles). The n spontaneously (but not explicitly) broken $\mathcal{Z}_2^{(r)}$ symmetries are now *hidden* in the Lagrangian density. On the other hand, the $3 - n$ unbroken $\mathcal{Z}_2^{(r')}$ symmetries ensure that $S_{r'}$ do not decay (stable particles), thus being DM candidates. In summary, for minimum solution sets (5.8), (5.10), (5.12), (5.14), the model contains $n = 0, 1, 2, 3$ extra Higgs-like particles and $3 - n$ DM particle candidates, respectively.

We will consider the vacuum configuration (5.8) of this model. For this minimum solution set, the (three) singlets do not acquire a VEV, i.e. $\langle S_r \rangle_0 = 0$ ($r = 1, 2, 3$), so that the $\mathcal{Z}_2^{(1)} \times \mathcal{Z}_2^{(2)} \times \mathcal{Z}_2^{(3)}$ symmetry is not spontaneously broken and there is no flavour mixing with $h(x)$. Hence, $h(x)$ and $S_r(x)$ ($r = 1, 2, 3$) are mass eigenstates – i.e., these fields correspond to physical particles – where h is the Higgs boson and S_r ($r = 1, 2, 3$) are new spin 0 massive particles. Using the minimum condition in (5.8), $v^2 = -\mu_H^2/\lambda_H \Leftrightarrow \mu_H^2 = -\lambda_H v^2$ (the same as that of the SM), the (expanded) scalar potential, in the unitary gauge $\Phi(x) \rightarrow \frac{1}{\sqrt{2}} \begin{pmatrix} 0 & v + h(x) \end{pmatrix}^\top$, is given by

$$V(|\Phi|, S_1, S_2, S_3) = \frac{1}{2} \overbrace{(2\lambda_H v^2)}^{=m_h^2} h^2 + \lambda_H v h^3 + \frac{\lambda_H}{4} h^4 + \frac{\lambda_{12}}{4} S_1^2 S_2^2 + \frac{\lambda_{23}}{4} S_2^2 S_3^2 + \frac{\lambda_{31}}{4} S_3^2 S_1^2 + \sum_{r=1}^3 \left[\frac{1}{2} \underbrace{\left(\mu_r^2 + \frac{\kappa_{Hr} v^2}{2} \right)}_{=m_{S_r}^2} S_r^2 + \frac{\lambda_r}{4!} S_r^4 + \frac{\kappa_{Hr} v}{2} h S_r^2 + \frac{\kappa_{Hr}}{4} h^2 S_r^2 \right], \quad (5.16)$$

which written in terms of the scalar masses $m_h = \sqrt{2\lambda_H v^2}$ and $m_{S_r} = \sqrt{\mu_r^2 + \kappa_{Hr} v^2/2}$ ($r = 1, 2, 3$), reads as

$$-\mathcal{L}_{\text{SM+3RSS}} \supset V(|\Phi|, S_1, S_2, S_3) = \frac{1}{2} m_h^2 h^2 + \frac{m_h^2}{2v} h^3 + \frac{m_h^2}{8v^2} h^4 + \frac{\lambda_{12}}{4} S_1^2 S_2^2 + \frac{\lambda_{23}}{4} S_2^2 S_3^2 + \frac{\lambda_{31}}{4} S_3^2 S_1^2 + \sum_{r=1}^3 \left[\frac{1}{2} m_{S_r}^2 S_r^2 + \frac{\lambda_r}{4!} S_r^4 + \frac{\kappa_{Hr} v}{2} h S_r^2 + \frac{\kappa_{Hr}}{4} h^2 S_r^2 \right]. \quad (5.17)$$

The unbroken $\mathcal{Z}_2^{(1)} \times \mathcal{Z}_2^{(2)} \times \mathcal{Z}_2^{(3)}$ symmetry ensures that S_r ($r = 1, 2, 3$) do not decay (stable particles), thus being DM candidates. This is shown in Figure 5.1, which presents the Feynman rules for the new interaction vertices that emerge in this SM extension.

¹Here, in addition to $\mathcal{Z}_2^{(r)}$ (as already established), $\mathcal{Z}_2^{(m)}$ must also be one of the n spontaneously broken symmetries. On the other hand, $\mathcal{Z}_2^{(r')}$ always refers to one of the $3 - n$ unbroken symmetries (in this item/point).

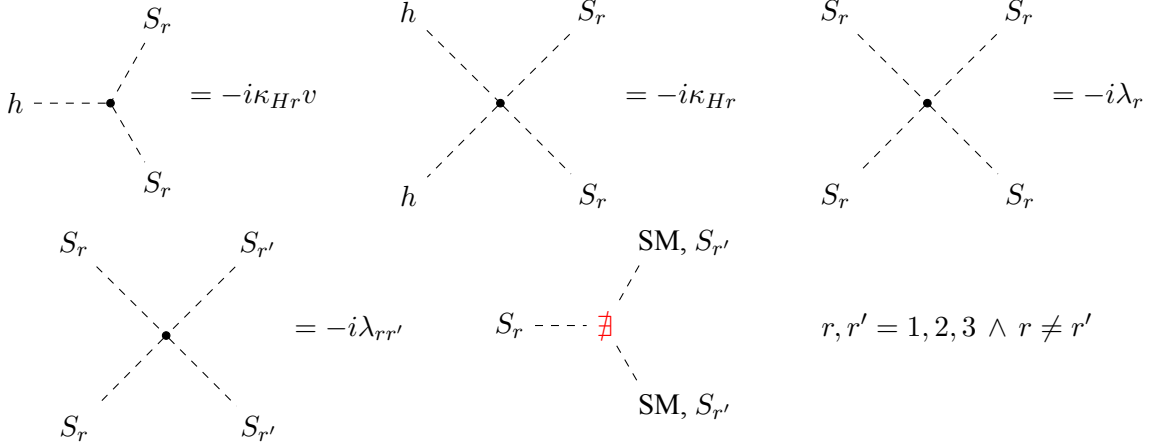


Figure 5.1: Feynman rules for the interaction vertices involving the S_r ($r = 1, 2, 3$) dark matter particle candidates. The decays $S_r \rightarrow \text{SM SM}$ and $S_r \rightarrow S_{r'} S_{r'}$ ($r' \neq r$) are forbidden by “dark parity” (or $\mathbb{Z}_2^{(r)}$ charge) conservation, as a consequence of the $\mathbb{Z}_2^{(1)} \times \mathbb{Z}_2^{(2)} \times \mathbb{Z}_2^{(3)}$ discrete symmetry.

5.2 Cross Sections for Direct Detection and Relic Density of DM

The analytical expressions of the relevant cross sections were already obtained in Section 4.2 for the SM+2RSS model. The only difference is that the SM+3RSS model contains three singlet DM particles S_r ($r = 1, 2, 3$) instead of two, but the generalizations are straightforward. The spin-independent cross section of DM-nucleon elastic scattering $S_r N \rightarrow S_r N$, with $N = p, n$ is given in Eq. (4.45). Similarly, the cross sections of all DM annihilation processes which create SM particles $S_r S_r \rightarrow \text{SM SM}$, with $\text{SM} = h, W^+, Z, \psi$ ($= \ell, q$) are given in Section 4.2.2; and the cross section of inter-dark annihilation processes is the trivial generalization of Eq. (4.75), i.e.

$$\sigma(S_r S_r \rightarrow S_{r'} S_{r'}) = \frac{1}{32\pi s} \sqrt{\frac{1 - 4m_{S_{r'}}^2/s}{1 - 4m_{S_r}^2/s}} \left[\lambda_{rr'}^2 + \kappa_{Hr} \kappa_{Hr'} v^2 \frac{2\lambda_{rr'}(s - m_h^2) + \kappa_{Hr} \kappa_{Hr'} v^2}{(s - m_h^2)^2 + m_h^2 \Gamma_h^2} \right], \quad (5.18)$$

$r, r' = 1, 2, 3 \wedge r' \neq r$. Once again, the annihilation of a heavier DM particle pair into a lighter DM particle pair is dominant over the inverse process.

5.3 Theoretical and Pre-Scan Experimental Constraints

Once again, the theoretical and experimental constraints (from particle physics) are already derived in Section 4.3 for the SM+2RSS model, and can be generalized for the SM+3RSS model. The generalization of the boundedness from below conditions can be obtained by following the (same) procedure based on the copositivity criteria that is described in Refs. [77, 78]. For the perturbative unitary conditions, the generalization from six to ten scalar particle pair states $hh, hS_r, S_r S_{r'}, S_r S_r$ ($r, r' = 1, 2, 3 \wedge r' \neq r$) is straightforward. In particular, the inter-dark annihilations give

$$16\pi |a_0(i \rightarrow f)|_{s \gg m_h^2, m_{S_r}^2} = |\mathcal{M}(i \rightarrow f)|_{s \gg m_h^2, m_{S_r}^2}^{(\theta \neq 0, \pi)} = |\lambda_{rr'}| < 8\pi, \quad (5.19)$$

$\forall i \rightarrow f = S_r S_r \rightarrow S_{r'} S_{r'}, S_r S_{r'} \rightarrow S_r S_{r'}$, with $r, r' = 1, 2, 3 \wedge r' \neq r$. If additionally, one performs a complementary coupled-channel analysis, one obtains ten (instead of six) conditions, one for each eigenvalue of the scalar coupled-channel matrix $(a_0)_{2 \rightarrow 2}$. Now moving from theoretical to experimental

constraints, the decay rate of $h \rightarrow S_r S_r$ ($r = 1, 2, 3$) is given in Eq. (4.87), and the generalization of the condition (4.88) associated to the experimental limit $\text{BR}(h \rightarrow \text{inv}) < 0.107$ is trivial. Finally, the $\mathcal{Z}_2^{(1)} \times \mathcal{Z}_2^{(2)} \times \mathcal{Z}_2^{(3)}$ symmetry remains unbroken, so that all three singlets do not acquire VEVs and there is no mixing with the Higgs field. Once more, the electroweak sector remains unchanged relative to that of the SM, and therefore, the SM+3RSS agrees with all electroweak precision measurements (such as the parameters ρ and S, T, U).

5.4 Parameter Space Scans and Numerical Analysis

The three-real-scalar-singlet extension of the SM has twelve (new) free parameters (i.e., five more than the two-real-scalar-singlet extension), but only nine of them are relevant at tree-level: the DM masses m_{S_1} , m_{S_2} and m_{S_3} , the portal coefficients κ_{H1} , κ_{H2} and κ_{H3} , and the inter-dark coefficients λ_{12} , λ_{23} and λ_{31} . The three quartic self-interaction coefficients λ_1 , λ_2 and λ_3 are only relevant at the loop level in perturbation theory. Hence, we scanned the 9-dimensional free parameter space (relevant at tree-level) of this model with `micrOMEGAs 6.1` [59], assuming all (three) scalar DM particles were thermally produced according to the freeze-out mechanism during the expansion of the Universe. Once again, the scans were performed considering the DM relic density and direct detection exclusion, but in a different manner from the ones of Section 4.4 for the SM+2RSS model.

The scans of the two-real-scalar-singlet SM extension in Section 4.4 are global, covering the entire 5-dimensional free parameter space (relevant at tree-level) of the model. Moreover, at a preliminary phase, the full domain was scanned exhaustively and uniformly (for an appropriate choice of scales, either taken as linear or logarithmic), which (in principle) allowed us to identify all (DD and relic density) non-excluded free parameter space regions. However, this was not the methodology used (here) for the three-real-scalar-singlet SM extension. The first reason for this is the SM+3RSS model having nine free parameters that are relevant at tree-level, thus requiring a considerably larger computational effort and time to perform global scans (in the 9-dimensional parameter space of the SM+3RSS model, in comparison to scanning the 5-dimensional parameter space of the SM+2RSS model, which was already computationally demanding). The second reason is that we are particularly interested in extending the (one heavy and one light) $m_{S_1} < m_{S_2}$ case of the SM+2RSS model – which is almost excluded by the new LZ 2024 results, hence our motivation for doing it – with a third scalar singlet DM particle S_3 that is either light or heavy, ensuring we end up with similar cases where two or one (respectively) light DM particles can be searched for at colliders. Hence, (after some unfruitful global scans) we locally scanned over two distinct free parameter space regions of the SM+3RSS model:

- the two light (masses below 1 TeV) and one heavy (mass above 1 TeV) case region, where S_3 is the additional light DM particle;
- the one light (mass below 1 TeV) and two heavy (masses above 1 TeV) case region, where S_3 is the additional heavy DM particle.

We imposed $m_{S_3} < m_{S_1} < m_{S_2}$ for the two-light-one-heavy case and $m_{S_1} < m_{S_2} < m_{S_3}$ for the one-light-two-heavy case regions prior to the local scans, so that (the SM+2RSS “pre-existing” S_1/S_2 take the usual light/heavy roles, and) S_3 is respectively taken as the lighter and heavier DM particle (out of the three).² The coupling constants can take the usual values, but we focused on parameter configurations

²Due to the $S_r \leftrightarrow S_{r'}$ ($r, r' = 1, 2, 3 \wedge r' \neq r$) symmetry of our model, the choice of mass hierarchy is arbitrary.

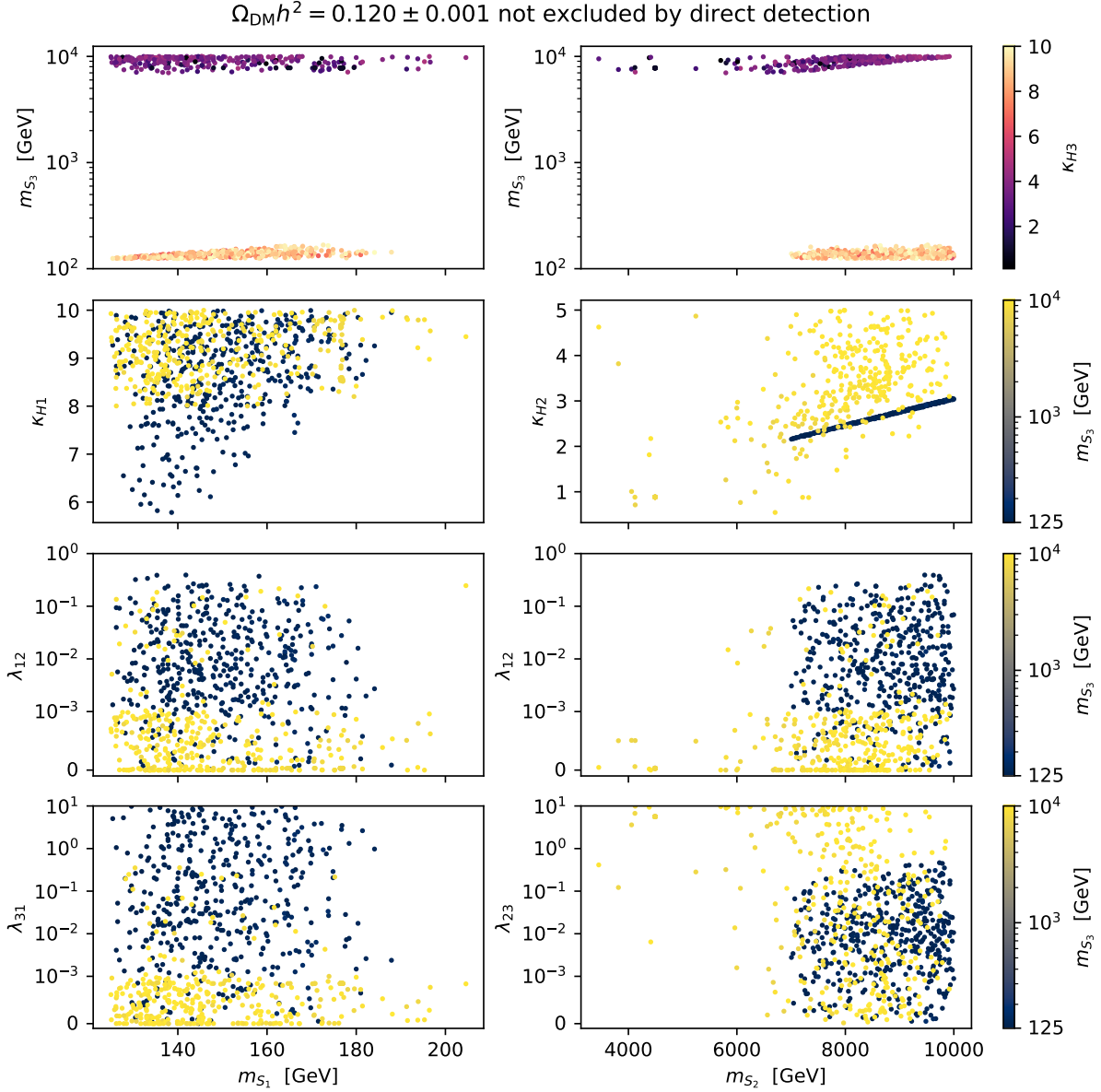


Figure 5.2: Experimental constraints on the SM+3RSS model (5.4), obtained by scanning the free parameter space with `micrOMEGAs 6.1` for the freeze-out mechanism. Both panels show free parameter space points that correspond to the observed DM relic density and are not excluded by direct detection. Columns share the x -axis, and rows share the colour bar.

that could potentially be allowed by the observed relic density and DD experiments (inspired by our previous numerical analysis in Section 4.4.1).

The (relic density and direct detection) experimental constraints on the SM+3RSS model (5.4) are shown in Figures 5.2 and 5.3, which only display allowed (i.e., not experimentally excluded) free parameter space points. Both figures display the scanned free parameter space points that correspond to the observed DM relic density $\Omega_{\text{DM}}^{\text{obs}} h^2 = 0.120 \pm 0.001$ from Planck [7] measurements and are also not excluded by the XENON1T [60], DarkSide-50 [61], PICO-60 [62], CRESST-III [63], PandaX-4T [64] and LUX-ZEPLIN (LZ) [2] direct detection experiments.³ Figure 5.2 presents several projections with m_{S_1}

³It should be noted that this LZ constraint refers to the former 2022 results [2]. The new LZ 2024 results [3] are not (yet) included in `micrOMEGAs 6.1`, thus not being taken into account in this numerical analysis – once again, we will have to perform the corresponding DD exclusion separately, later in Section 5.4.1.

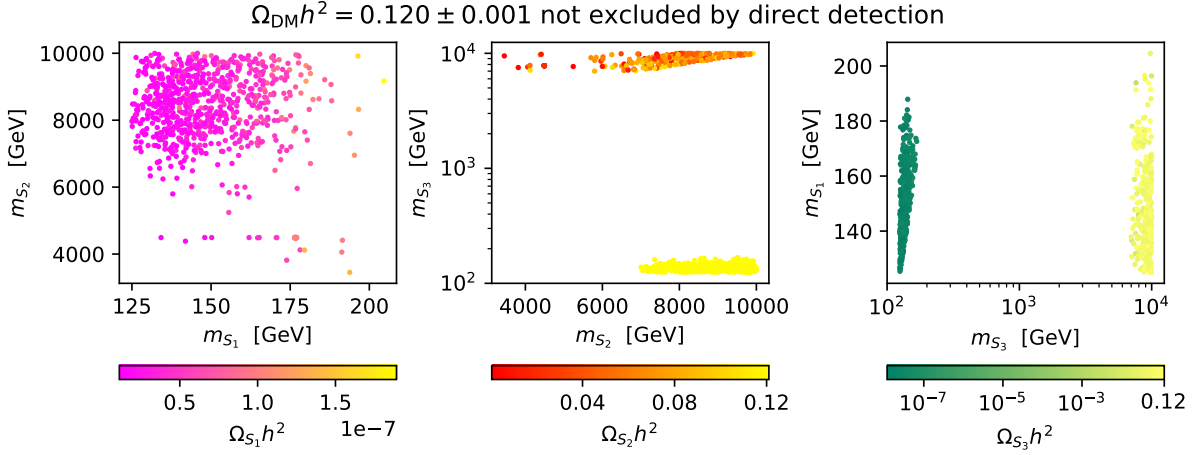


Figure 5.3: Experimental constraints on the SM+3RSS model (5.4), obtained by scanning the free parameter space with micrOMEGAs 6.1 for the freeze-out mechanism. All panels show free parameter space points that correspond to the observed DM relic density and are not excluded by direct detection. Each colour bar displays the relic density of one of the DM particles S_r ($r = 1, 2, 3$).

and m_{S_2} on the x -axis of the left and right panels, respectively; and the seven remaining free parameters (relevant at tree-level) m_{S_3} , κ_{H1} , κ_{H2} , κ_{H3} , λ_{12} , λ_{23} and λ_{31} on the y -axis and colour bars. Figure 5.3 presents the projections in the (m_{S_1}, m_{S_2}) , (m_{S_2}, m_{S_3}) and (m_{S_3}, m_{S_1}) planes, with the colour bars displaying the relic density of S_1 , S_2 and S_3 , respectively. One should notice that, for all plots of both Figures 5.2 and 5.3, the free parameter space points of the two-light-one-heavy $m_{S_3} < m_{S_1} < m_{S_2}$ and one-light-two-heavy $m_{S_1} < m_{S_2} < m_{S_3}$ case allowed regions can be easily distinguished.

Let us now proceed to the analysis of the results that were obtained in our local free parameter space scans. We shall treat both (two-light-one-heavy $m_{S_3} < m_{S_1} < m_{S_2}$ and one-light-two-heavy $m_{S_1} < m_{S_2} < m_{S_3}$) case allowed regions separately.

- The **two-light-one-heavy** $m_{S_3} < m_{S_1} < m_{S_2}$ case allowed region closely resembles the SM+2RSS (one-light-one-heavy) $m_{S_1} < m_{S_2}$ case allowed region, except for the additional lighter DM particle S_3 . As expected (from the SM+2RSS numerical analysis of Section 4.4) for a lighter DM particle, the S_3 relic density – just like for the S_1 “pre-existing” (in the context of the SM+2RSS model) lighter DM particle – is negligible, $\Omega_{S_3} h^2 \sim 10^{-7}$ ($\sim \Omega_{S_1} h^2$), as shown in Figure 5.3, and the (single) heavier DM particle S_2 is (once again) responsible for all the observed DM relic density, i.e. $\Omega_{\text{DM}} h^2 = \sum_{r=1}^3 \Omega_{S_r} h^2 \approx \Omega_{S_2} h^2$. The consequences to this are analogous to the ones of the SM+2RSS (one-light-one-heavy) $m_{S_1} < m_{S_2}$ case, as shown in Figure 5.2. The lighter DM particle $S_{3,1}$ related DD exclusion is determined by the corresponding $S_{3,1}$ relic density fractions in $\sigma^{\text{SI}}(S_{3,1} N \rightarrow S_{3,1} N) \times \Omega_{S_{3,1}} / \Omega_{\text{DM}}$, which must be sufficiently low for DD non-exclusion, thus constraining $m_{S_{3,1}}$ ($> m_h = 125$ GeV) from above, $\kappa_{H3,1}$ from below and $\lambda_{23}, \lambda_{12}$ from above. On the other hand, m_{S_2} and κ_{H2} are highly constrained⁴ (from both below and above) due to the “tension” between relic over-density and DD exclusion related to S_2 , the latter being now determined by the corresponding SI cross section $\sigma^{\text{SI}}(S_2 N \rightarrow S_2 N) \times \Omega_{S_2} / \Omega_{\text{DM}} \approx \sigma^{\text{SI}}(S_2 N \rightarrow S_2 N)$. The detailed explanations for these last two statements can be re-consulted in Section 4.4.1 (or simply check Table 4.1 for a brief summary).

- The **one-light-two-heavy** $m_{S_1} < m_{S_2} < m_{S_3}$ case allowed region, in contrast, exhibits differences

⁴To be more precise, for a fixed m_{S_2} allowed value, the (very short) κ_{H2} allowed range is bounded from both below and above; and vice-versa (see Figure 5.2, second row of second column).

from the SM+2RSS (one-light-one-heavy) $m_{S_1} < m_{S_2}$ case allowed region beyond the inclusion of an additional (this time, heavier) DM particle S_3 . As expected, the relic density of the (now, single) “pre-existing” (in the context of the SM+2RSS model) lighter DM particle S_1 is negligible ($\Omega_{S_1} h^2 \sim 10^{-7}$), as shown in Figure 5.3; but the two heavier DM particles S_2 and S_3 are (simultaneously) responsible for the observed DM relic density, i.e.

$$(0.120 \pm 0.001 =) \Omega_{\text{DM}} h^2 = \sum_{r=1}^3 \Omega_{S_r} h^2 \approx (\Omega_{S_2} + \Omega_{S_3}) h^2, \quad \text{with} \quad \Omega_{S_2} h^2 \sim \Omega_{S_3} h^2. \quad (5.20)$$

In addition to the shared responsibility between the two heavier DM particles $S_{2,3}$ for the total DM relic density, the DD exclusion related to the heavy DM particles $S_{2,3}$ is now determined not only by the SI cross sections, but also by the DM relic density fractions in $\sigma^{\text{SI}}(S_{2,3} N \rightarrow S_{2,3} N) \times \Omega_{S_{2,3}} / \Omega_{\text{DM}}$. Consequently, the “tension” between relic over-density and DD exclusion related to the heavy DM particles $S_{2,3}$ is “alleviated”, which translates into the weakening of the (up until now, extremely stringent) constraints on the heavier DM particle masses $m_{S_{2,3}}$ and portal coefficients $\kappa_{H2,3}$ allowed values (see Figure 5.2, second row of second column for a comparison).

Finally, it should be noted that since our SM+3RSS numerical scans were performed locally, i.e., within targeted free parameter space regions, one must not focus (or draw any invalid conclusions) on the boundaries of the (relic density and DD) allowed free parameter space regions. Nevertheless, the conclusions that were drawn from the SM+2RSS global scans in Section 4.4 (in particular, with respect to the $m_{S_1} < m_{S_2}$ case allowed region in Section 4.4.1, summarized in Table 4.1) still provided valuable insights on both ($m_{S_3} < m_{S_1} < m_{S_2}$ and $m_{S_1} < m_{S_2} < m_{S_3}$) case allowed regions of this SM+3RSS model.

5.4.1 LZ 2024 Results and Future Prospects for Direct Detection

As already stated, the new LZ 2024 results [3] (unlike the former LZ 2022 results [2]) are not (yet) included in the micrOMEGAs 6.1 code, and consequently, are not taken into account in our previous numerical analysis. Just like we did in Section 4.4.2 for the two-real-scalar-singlet SM extension, we need to perform the corresponding DD exclusion (for the LZ 2024 results) of the three-real-scalar-singlet SM extension separately.

We computed the $\sigma^{\text{SI}}(S_r N \rightarrow S_r N) \times \Omega_{S_r} / \Omega_{\text{DM}}$, $r = 1, 2, 3$ quantities ($\Omega_{\text{DM}} h^2 = 0.120 \pm 0.001$) for all the free parameter space points that were not experimentally excluded by relic density and direct detection (without considering the LZ 2024 results) in the numerical analysis (i.e., all points of Figure 5.2). The results for the (two-light-one-heavy) $m_{S_3} < m_{S_1} < m_{S_2}$ and (one-light-two-heavy) $m_{S_1} < m_{S_2} < m_{S_3}$ cases are respectively shown – for all three DM particles, lighter one(s) at the top panel and heavier one(s) at the bottom panel – in Figures 5.4 and 5.5, which also display the former 2022 (blue solid line) and new 2024 (green solid line) LZ upper limits on the SI cross section of WIMP-nucleon elastic scattering. As expected, the model-predicted $\sigma^{\text{SI}}(S_r N \rightarrow S_r N) \times \Omega_{S_r} / \Omega_{\text{DM}}$ ($r = 1, 2, 3$) values for the points of both ($m_{S_3} < m_{S_1} < m_{S_2}$ and $m_{S_1} < m_{S_2} < m_{S_3}$) cases are below the LZ 2022 upper limit for all (three) DM particles. However, the same cannot be said regarding the LZ 2024 upper limit. One should remember that if one, two or three (out of the three) prediction values $\sigma^{\text{SI}}(S_r N \rightarrow S_r N) \times \Omega_{S_r} / \Omega_{\text{DM}}$ ($r = 1, 2, 3$) is above the LZ 2024 upper limit, the corresponding parameter space point is experimentally DD excluded. We shall analyse both ($m_{S_3} < m_{S_1} < m_{S_2}$ and $m_{S_1} < m_{S_2} < m_{S_3}$) cases separately, since they yield (apparently similar, yet) different results.

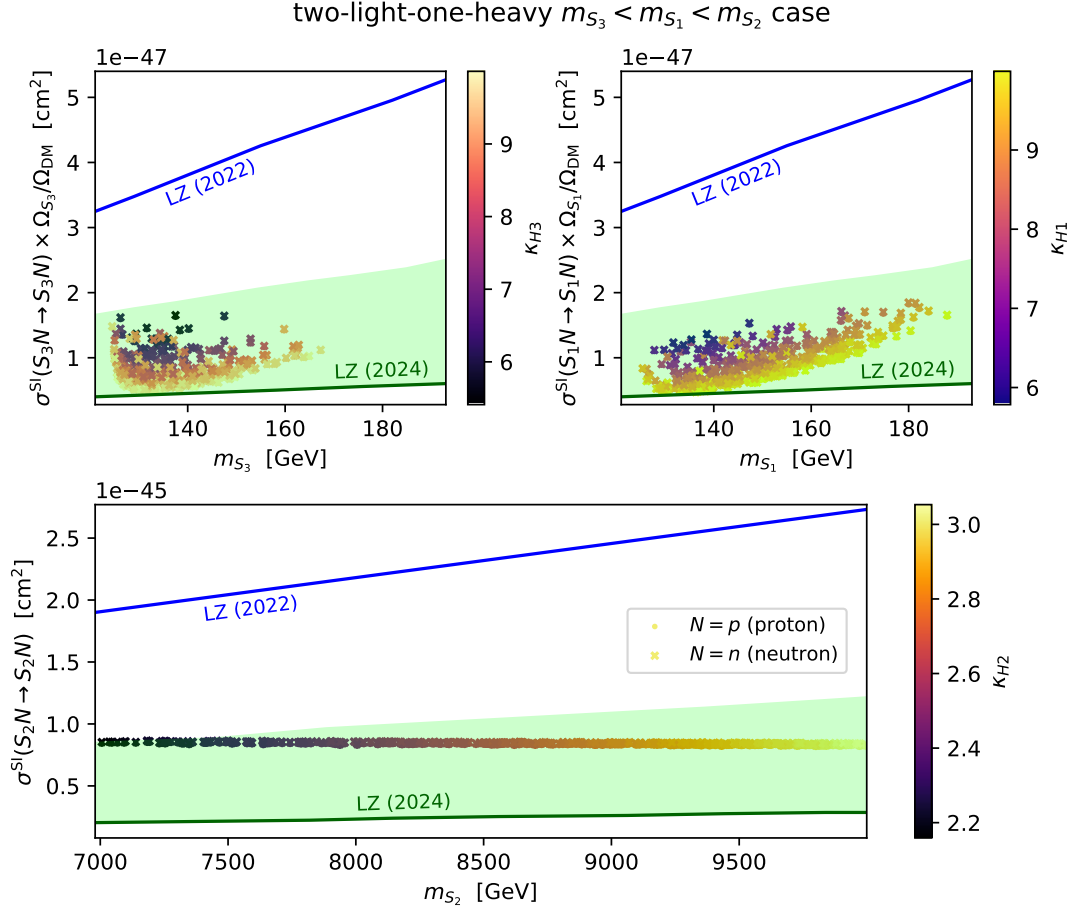


Figure 5.4: Spin-independent cross section of DM-nucleon elastic scattering $S_r N \rightarrow S_r N$ ($N = p, n$) multiplied by the corresponding fraction of DM relic density $\Omega_{S_r}/\Omega_{\text{DM}}$ ($r = 1, 2, 3$). The presented points correspond to the model's theoretical predictions for the $m_{S_3} < m_{S_1} < m_{S_2}$ (two light one two heavy) case points of Figure 5.2, for both proton (p) and neutron (n) elastic scattering. The blue and green (solid) lines correspond to the LUX-ZEPLIN (LZ) experimental upper limits on the WIMP-nucleon elastic scattering spin-independent cross section from 2022 [2] and 2024 [3] results, respectively. The (shaded green) experimental uncertainty band from the LZ 2024 results is displayed. The legend is shared by both panels.

- The **two-light-one-heavy** $m_{S_3} < m_{S_1} < m_{S_2}$ case results are shown in Figure 5.4, for the lighter S_3, S_1 (top panel) and heavier S_2 (bottom panel) DM particles. One should note that, just like in the (one-light-one-heavy) $m_{S_1} < m_{S_2}$ case of the SM+2RSS model, the (single) heavier DM particle S_2 is responsible for (virtually) all DM relic density, i.e. $\sigma^{\text{SI}}(S_2 N \rightarrow S_2 N) \times \Omega_{S_2}/\Omega_{\text{DM}} \approx \sigma^{\text{SI}}(S_2 N \rightarrow S_2 N)$, with the (now, two) lighter DM particles $S_{3,1}$ having negligible relic densities of $\Omega_{S_{3,1}} h^2 \sim 10^{-7}$. Once again, the $\sigma^{\text{SI}}(S_r N \rightarrow S_r N) \times \Omega_{S_r}/\Omega_{\text{DM}}$ ($r = 1, 2, 3$) predicted values (and corresponding parameter space points' DD exclusion) are solely determined by the SI cross section $\sigma^{\text{SI}}(S_2 N \rightarrow S_2 N)$ of the heavier DM particle S_2 and fraction $\Omega_{S_{3,1}}/\Omega_{\text{DM}}$ of the lighter DM particles $S_{3,1}$. Furthermore, the allowed mass and portal coefficient values are similar to the ones of the SM+2RSS model's $m_{S_1} < m_{S_2}$ case, for both heavier and lighter DM particles. Hence, it is no surprise that the (two-light-one-heavy) $m_{S_3} < m_{S_1} < m_{S_2}$ case results of the SM+3RSS model – despite having two lighter DM particles, instead of just one – are similar to the (one-light-one-heavy) $m_{S_1} < m_{S_2}$ case results of the SM+2RSS model, as one can check by comparing Figures 5.4 and 4.7 (respectively). For (two-light-one-heavy) $m_{S_3} < m_{S_1} < m_{S_2}$ case points with lighter DM particle masses $m_{S_{3,1}} \sim [135, 140]$ GeV and high portal coefficients $\kappa_{H3,1} (\gtrsim 9)$, the

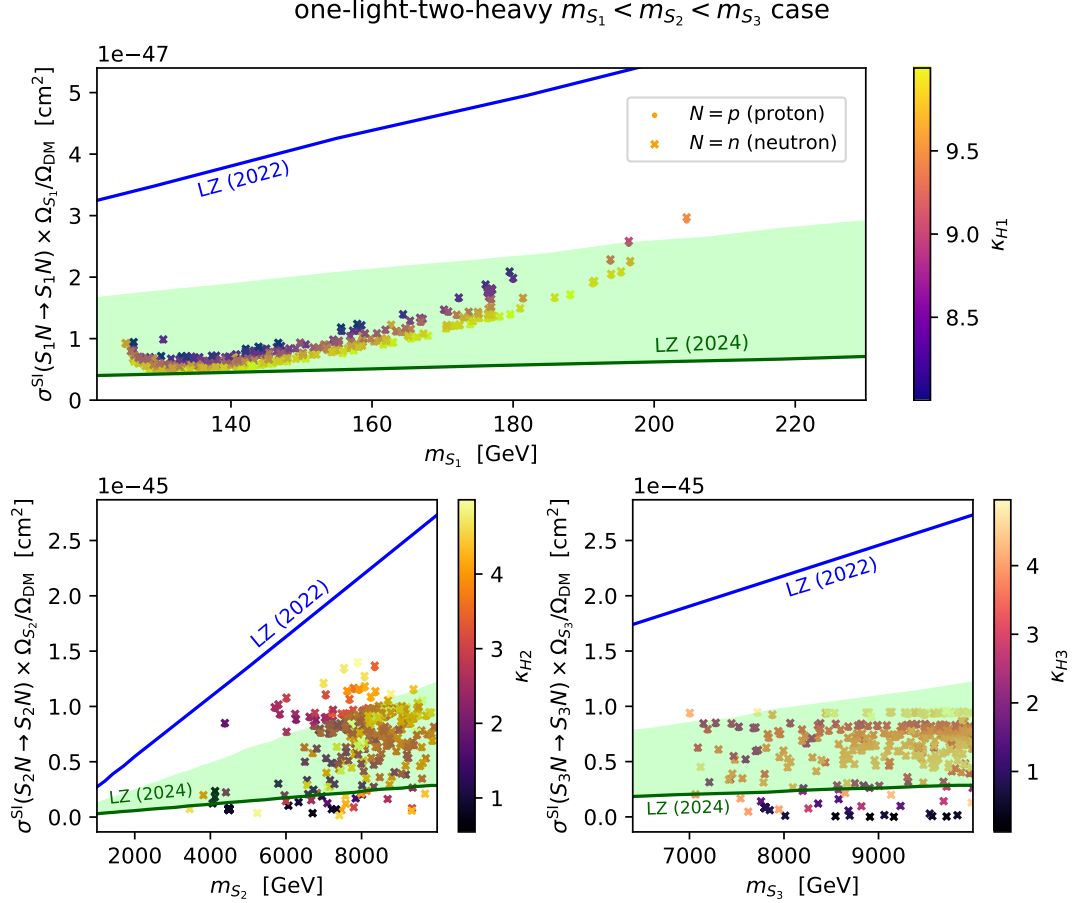


Figure 5.5: Spin-independent cross section of DM-nucleon elastic scattering $S_r N \rightarrow S_r N$ ($N = p, n$) multiplied by the corresponding fraction of DM relic density $\Omega_{S_r}/\Omega_{\text{DM}}$ ($r = 1, 2, 3$). The presented points correspond to the model’s theoretical predictions for the $m_{S_1} < m_{S_2} < m_{S_3}$ (one-light-two-heavy) case points of Figure 5.2, for both proton (p) and neutron (n) elastic scattering. The blue and green (solid) lines correspond to the LUX-ZEPLIN (LZ) experimental upper limits on the WIMP-nucleon elastic scattering spin-independent cross section from 2022 [2] and 2024 [3] results, respectively. The (shaded green) experimental uncertainty band from the LZ 2024 results is displayed. The legend is shared by all panels.

$\sigma^{\text{SI}}(S_{3,1} N \rightarrow S_{3,1} N) \times \Omega_{S_{3,1}}/\Omega_{\text{DM}}$ predicted values fall in the actual LZ 2024 upper limit, but the respective $\sigma^{\text{SI}}(S_2 N \rightarrow S_2 N) \times \Omega_{S_2}/\Omega_{\text{DM}} \approx \sigma^{\text{SI}}(S_2 N \rightarrow S_2 N)$ predicted values fall above it – nevertheless, inside the (LZ 2024) experimental uncertainty band.

- The **one-light-two-heavy** $m_{S_1} < m_{S_2} < m_{S_3}$ case results are shown in Figure 5.5, for the lighter S_1 (top panel) and heavier S_2, S_3 (bottom panel) DM particles. Similarly to what happens in the two-light-one-heavy $m_{S_3} < m_{S_1} < m_{S_2}$ case (and the one-light-one-heavy $m_{S_1} < m_{S_2}$ case of the SM+2RSS model), the (single) lighter DM particle S_1 has a negligible relic density of $\Omega_{S_1} h^2 \sim 10^{-7}$, and hence, the $\sigma^{\text{SI}}(S_1 N \rightarrow S_1 N) \times \Omega_{S_1}/\Omega_{\text{DM}}$ predicted values are solely determined by the $\Omega_{S_1}/\Omega_{\text{DM}}$ fraction. Once more, for (one-light-two-heavy) $m_{S_1} < m_{S_2} < m_{S_3}$ case points with lighter DM particle mass $m_{S_1} \sim [135, 140]$ GeV and high portal coefficient $\kappa_{H1} (\gtrsim 9)$, the predicted $\sigma^{\text{SI}}(S_1 N \rightarrow S_1 N) \times \Omega_{S_1}/\Omega_{\text{DM}}$ values fall in the actual LZ 2024 upper limit. However, this allowed free parameter space region has the distinguishing feature of having (not one, but) two heavier DM particles S_2 and S_3 which share the “responsibility” for all DM relic density, i.e., $\Omega_{\text{DM}} = \sum_{r=1}^3 \Omega_{S_r} \approx \Omega_{S_2} + \Omega_{S_3}$ with $\Omega_{S_2} \sim \Omega_{S_3}$. Consequently, for the first time (in comparison to the previously discussed allowed parameter space regions), the pre-

dicted $\sigma^{\text{SI}}(S_{2,3}N \rightarrow S_{2,3}N) \times \Omega_{S_{2,3}}/\Omega_{\text{DM}}$ values for the heavier DM particles $S_{2,3}$ are not solely determined by the SI cross sections $\sigma^{\text{SI}}(S_{2,3}N \rightarrow S_{2,3}N)$, but also by the respective fractions $\Omega_{S_{2,3}}/\Omega_{\text{DM}} \neq 1$. These $\Omega_{S_{2,3}}/\Omega_{\text{DM}} < 1$ fractions (now also relevant for DD exclusion related to the heavier DM particles) are able to lower the $\sigma^{\text{SI}}(S_{2,3}N \rightarrow S_{2,3}N) \times \Omega_{S_{2,3}}/\Omega_{\text{DM}}$ values down to the point where they can fall below the LZ 2024 upper limit. In particular, this happens with part of the (one-light-two-heavy) $m_{S_1} < m_{S_2} < m_{S_3}$ case points with lighter DM particle mass $m_{S_1} \sim [135, 140]$ GeV and high portal coefficient $\kappa_{H1} (\gtrsim 9)$, which not only have the $\sigma^{\text{SI}}(S_1N \rightarrow S_1N) \times \Omega_{S_1}/\Omega_{\text{DM}}$ predicted values falling in the actual LZ 2024 upper limit, but also have the respective $\sigma^{\text{SI}}(S_{2,3}N \rightarrow S_{2,3}N) \times \Omega_{S_{2,3}}/\Omega_{\text{DM}}$ predicted values (simultaneously) falling below it.

The SM+3RSS model predictions for both the (two-light-one-heavy) $m_{S_3} < m_{S_1} < m_{S_2}$ and the (one-light-two-heavy) $m_{S_1} < m_{S_2} < m_{S_3}$ case allowed points are, for the lighter DM particles, similar to the SM+2RSS model predictions for the (one-light-one-heavy) $m_{S_1} < m_{S_2}$ case allowed points (see Figures 5.4 (top panel), 5.5 (top panel) and 4.7 (left panel), respectively), which for masses around (roughly) 135-140 GeV and high portal coefficients ($\gtrsim 9$) of the lighter DM particle(s), fall exactly in the LZ 2024 upper limit. The same holds true for the SM+3RSS model predictions of the (two-light-one-heavy) $m_{S_3} < m_{S_1} < m_{S_2}$ case allowed points for the heavy DM particle, since they fall above the LZ 2024 upper limit, even if inside the experimental uncertainty band. However, the SM+3RSS model predictions of some of the (one-light-two-heavy) $m_{S_1} < m_{S_2} < m_{S_3}$ case allowed points for both heavy DM particles (simultaneously) fall below the LZ 2024 upper limit – contrary to what happens with the (two-light-one-heavy) $m_{S_3} < m_{S_1} < m_{S_2}$ case SM+3RSS model predictions and the (one-light-one-heavy) $m_{S_1} < m_{S_2}$ case SM+2RSS model predictions (see Figures 5.5 (bottom panel), 5.4 (bottom panel) and 4.7 (right panel), respectively) – because there are two heavier DM particles contributing to the (total) DM relic density, instead of just one (as previously explained).

In conclusion, the three-real-scalar-singlet SM extension (5.4) provides an allowed free parameter space region – the (one-light-two-heavy) $m_{S_1} < m_{S_2} < m_{S_3}$ case allowed region – which for some of its points, the $\sigma^{\text{SI}}(S_rN \rightarrow S_rN) \times \Omega_{S_r}/\Omega_{\text{DM}}$ model predictions (simultaneously) do not fall above the LZ 2024 upper limit for all three DM particles S_r ($r = 1, 2, 3$), thus (definitely) not being DD excluded by this new LZ 2024 results. This could not be achieved with the (two-light-one-heavy) $m_{S_3} < m_{S_1} < m_{S_2}$ case allowed region, which – besides the unnecessary extra lighter DM particle – does not offer any new feature over the two-real-scalar-singlet SM extension (4.4).

5.5 Searches for the Lighter DM Particle(s) at the LHC

Same as the two-real-scalar-singlet SM extension, the three-real-scalar-singlet SM extension can also be probed at the LHC. The allowed free parameter space regions for both ($m_{S_3} < m_{S_1} < m_{S_2}$ and $m_{S_1} < m_{S_2} < m_{S_3}$) cases provide one and two (respectively) heavier DM particles that are responsible for (virtually) all the observed DM relic density, but more importantly, two and one (respectively) lighter DM particles that can be searched for at the LHC.⁵

In analogy to our treatment in Section 4.5 for the SM+2RSS model, we now must compare theoretical predictions of the SM+3RSS model with LHC experiments to determine whether the ($m_{S_3} < m_{S_1} < m_{S_2}$ and $m_{S_1} < m_{S_2} < m_{S_3}$) case allowed points are experimentally excluded by collider searches. The appropriate LHC experimental results were already identified as Refs. [4, 5, 6], where the ATLAS

⁵The reason for this was already explained in Section 4.5 for the SM+2RSS model (and the generalization is trivial).

Collaboration established model-independent upper limits at the 95% confidence level on the visible cross section of DM production processes with: one to four final state jets $j = q, \bar{q}, b, \bar{b}, g$, with $q = u, d, c, s$ (Section 4.5.1), a (single) final state Higgs boson (Section 4.5.2) and a (single) final state Z gauge boson (Section 4.5.3), respectively; at a center-of-mass energy of $\sqrt{s} = 13$ TeV.

This comparative analysis does not require the re-computation of the SM+3RSS model-predicted cross sections for all the allowed points. Instead, we can simply use the results that were obtained in Section 4.5 for the SM+2RSS model. The cross section of all (lighter) DM production processes at the LHC are maximized for: 1) low lighter DM particle masses ($\rightarrow 125^+$ GeV, which is the Higgs boson mass, the minimum value for these allowed case regions); 2) high lighter DM particle portal coefficients ($\rightarrow 10^-$, which is the maximum value that was considered in the numerical analyses). However, even for free parameter space points with this (maximizing) features, the corresponding cross sections are at least (roughly) one order of magnitude away from being excluded by the upper limits set by the experimental analyses [4, 5, 6], as respectively shown in Figures 4.11–4.13. Therefore, it is safe to conclude that LHC (collider) searches are not able to experimentally exclude a single free parameter space point of the SM+3RSS model.

Chapter 6

Conclusions

In this work, we have studied $n = 1, 2, 3$ multi-real-scalar-singlet SM extensions with unbroken $\times_{r=1}^n \mathcal{Z}_2^{(r)} \equiv \mathcal{Z}_2^{(1)} \times \dots \times \mathcal{Z}_2^{(n)}$ discrete symmetries, which provided $n = 1, 2, 3$ stable DM particle candidates (and zero extra Higgs-like particles). Our starting point was the $n = 1$ real scalar singlet SM extension, a well-known DM model that had already been extensively studied. Nevertheless, by imposing the most recent DM related experimental constraints on the SM+RSS model's free parameter space, we were able to conclude that this model is experimentally excluded for DM masses below 3535 GeV. This makes it impossible to probe through collider searches at the LHC, which operates at a center-of-mass energy of $\sqrt{s} = 13.6$ TeV (Run 3), and will never surpass a maximum value of $\sqrt{s} = 14$ TeV (Run 4). This was the main motivation behind the following investigation.

We then proceeded to study the two-real-scalar-singlet SM extension ($n = 2$). The combined constraints from the observed relic density and direct detection experiments fully accounted for all the excluded free parameter space of the SM+RSS model. Hence, after imposing the particle physics related (theoretical and experimental) limits, we scanned the free parameter space with `micrOMEGAs 6.0` for this two DM related (relic density and DD) constraints. Taking S_1 (S_2) as the lighter (heavier) WIMP, we found three main allowed regions: 1) the $m_{S_1} \sim m_{S_2} > 1$ TeV case, where both DM particles are heavy; 2) the $m_h/2 < m_{S_1} < 1$ TeV $< m_{S_2}$ case, where one of the DM particles is lighter (than 1 TeV); 3) the $m_h/2 \approx m_{S_1} < m_{S_2}$ resonant case. Among these, only the $m_h/2 < m_{S_1} < 1$ TeV $< m_{S_2}$ case allowed region was not already (analogously) present in the SM+RSS model. Moreover, by providing a lighter DM particle that can be searched for at the LHC, this parameter space region became our focus of interest. Our numerical analysis showed that, in this allowed region, the heavier DM particle S_2 is responsible for (almost) all the observed DM relic density, and consequently, its mass m_{S_2} and portal coefficient κ_{H2} are (together) highly constrained (from both below and above) due to the “tension” between relic over-density and DD exclusion related to S_2 , the latter being determined by the SI cross section in $\sigma^{\text{SI}}(S_2 N \rightarrow S_2 N) \times \Omega_{S_2}/\Omega_{\text{DM}} \approx \sigma^{\text{SI}}(S_2 N \rightarrow S_2 N)$. In contrast, the lighter DM particle S_1 makes a negligible contribution of $\Omega_{S_1} h^2 \sim 10^{-7}$ to the total DM relic density, so that m_{S_1} and κ_{H1} are only constrained (from below and above, and from below, respectively) due to DD exclusion related to S_1 , which is determined by the abundance fraction in $\sigma^{\text{SI}}(S_1 N \rightarrow S_1 N) \times \Omega_{S_1}/\Omega_{\text{DM}}$. We also concluded that the inter-dark coefficient λ_{12} regulating the $S_2 S_2 \rightarrow S_1 S_1$ annihilation does not influence the total DM relic density as significantly as m_{S_2} and κ_{H2} , and is therefore not constrained by it. But since it affects the S_1 fraction $\Omega_{S_1}/\Omega_{\text{DM}}$, it is bounded from above due to DD exclusion related to S_1 .

However, this one-light-one-heavy $m_{S_1} < m_{S_2}$ case allowed region turned out to be almost excluded by the new LUX-ZEPLIN results of 2024. This recent constraints are not incorporated in `micrOMEGAs 6.0`, and we had to perform the corresponding DD exclusion separately from the numerical analysis. The

$\sigma^{\text{SI}}(S_r N \rightarrow S_r N) \times \Omega_{S_r}/\Omega_{\text{DM}}$ ($r = 1, 2$) model predictions of the $m_{S_1} < m_{S_2}$ case points exceed the LZ 2024 upper limit on the WIMP-nucleon elastic scattering SI cross section, with part of them falling inside the experimental uncertainty band for both particles.

This led us to study the three-real-scalar-singlet SM extension ($n = 3$). By performing a similar analysis (but through local scans on targeted parameter space regions), we found two allowed regions of interest: 1) the two-light-one-heavy $m_{S_3} < m_{S_1} < 1 \text{ TeV} < m_{S_2}$ case, where S_3 takes the role of an additional light DM particle; 2) the one-light-two-heavy $m_{S_1} < 1 \text{ TeV} < m_{S_2} < m_{S_3}$ case, where S_3 takes the role of an additional heavy DM particle. The first case is identical to the SM+2RSS (one-light-one-heavy) $m_{S_1} < m_{S_2}$ case, except for the unnecessary extra light DM particle (with identical characteristics to the “pre-existing” one). The second case, however, has the key feature of having two heavy DM particles simultaneously accounting for the observed relic density, so that $\sum_{r=1}^3 \Omega_{S_r} \approx \Omega_{S_2} + \Omega_{S_3}$, with $\Omega_{S_2} \sim \Omega_{S_3}$. Additionally, the DD exclusion related to the heavy DM particles $S_{2,3}$ is now determined also by the abundance fractions $\Omega_{S_{2,3}}/\Omega_{\text{DM}} \neq 1$, and not just the SI cross sections. Therefore, the “tension” between relic over-density and DD exclusion related to the heavy DM particles $S_{2,3}$ is “alleviated”, weakening the usually stringent constraints on the heavy DM particle masses $m_{S_{2,3}}$ and portal coefficients $\kappa_{H2,3}$ allowed values. As a result, this one-light-two-heavy $m_{S_1} < m_{S_2} < m_{S_3}$ case region contains free parameter space points that are able to predict $\sigma^{\text{SI}}(S_r N \rightarrow S_r N) \times \Omega_{S_r}/\Omega_{\text{DM}}$ values which do not fall above the LZ 2024 upper limit for all three DM particles ($r = 1, 2, 3$).

Finally, we selected the most relevant LHC experiments to determine whether our (relic density and direct detection) allowed points were experimentally excluded by collider searches. These included jet, mono-Higgs and mono- Z searches performed with the ATLAS detector during Run 2, which established model-independent upper limits on the visible cross section for the corresponding DM production processes. However, our model predictions for the visible cross sections are at least (roughly) one order of magnitude away from being excluded by any of these three experimental analyses, across all allowed parameter space points for both ($n = 2, 3$) extension models. Nevertheless, the cross sections for some allowed points are within one order of magnitude (or less) of being excluded by the jet and mono-Higgs searches (both conducted during Run 2). This suggests that a scalar WIMP of this type could be detected during the remainder of the LHC operation, particularly in the HL-LHC stage.

In conclusion, we have shown that the $n = 2, 3$ multi-real-scalar-singlet SM extensions with unbroken $\times_{r=1}^n \mathcal{Z}_2^{(r)} \equiv \mathcal{Z}_2^{(1)} \times \cdots \times \mathcal{Z}_2^{(n)}$ discrete symmetries, unlike the $n = 1$ case, can provide experimentally allowed free parameter space regions (by relic density and direct detection) where a lighter DM particle (with mass $\lesssim 200 \text{ GeV}$) may be searched for at the LHC or future colliders. However, the exclusion of these multi-real-scalar-singlet SM extensions will most likely be determined by upcoming direct detection experiments, rather than collider DM searches.

Bibliography

- [1] Maria Gonçalves, Margarete Mühlleitner, Rui Santos, and Tomás Trindade. Dark Matter in Multi-Singlet Extensions of the Standard Model. 5 2025.
- [2] J. Aalbers et al. First Dark Matter Search Results from the LUX-ZEPLIN (LZ) Experiment. *Phys. Rev. Lett.*, 131(4):041002, 2023. doi: 10.1103/PhysRevLett.131.041002.
- [3] Scott Haselschwardt. New Dark Matter Search Results from the LUX-ZEPLIN (LZ) Experiment. TeV Particle Astrophysics (TeVPA) 2024, Chicago, 8 2024. Presented on behalf of the LZ Collaboration on August 26, 2024. url: <https://indico.uchicago.edu/event/427/contributions/1325/>.
- [4] Georges Aad et al. Search for new phenomena in events with an energetic jet and missing transverse momentum in pp collisions at $\sqrt{s}=13$ TeV with the ATLAS detector. *Phys. Rev. D*, 103(11):112006, 2021. doi: 10.1103/PhysRevD.103.112006.
- [5] Georges Aad et al. Search for dark matter produced in association with a Standard Model Higgs boson decaying into b-quarks using the full Run 2 dataset from the ATLAS detector. *JHEP*, 11:209, 2021. doi: 10.1007/JHEP11(2021)209.
- [6] M. Aaboud et al. Search for dark matter in events with a hadronically decaying vector boson and missing transverse momentum in pp collisions at $\sqrt{s} = 13$ TeV with the ATLAS detector. *JHEP*, 10:180, 2018. doi: 10.1007/JHEP10(2018)180.
- [7] N. Aghanim et al. Planck 2018 results. VI. Cosmological parameters. *Astron. Astrophys.*, 641:A6, 2020. doi: 10.1051/0004-6361/201833910. [Erratum: *Astron. Astrophys.* 652, C4 (2021)].
- [8] Gianfranco Bertone, Dan Hooper, and Joseph Silk. Particle dark matter: Evidence, candidates and constraints. *Phys. Rept.*, 405:279–390, 2005. doi: 10.1016/j.physrep.2004.08.031.
- [9] Jonathan L. Feng. Dark Matter Candidates from Particle Physics and Methods of Detection. *Ann. Rev. Astron. Astrophys.*, 48:495–545, 2010. doi: 10.1146/annurev-astro-082708-101659.
- [10] Marco Cirelli, Alessandro Strumia, and Jure Zupan. Dark matter, 2024.
- [11] C. P. Burgess, Maxim Pospelov, and Tonnies ter Veldhuis. The Minimal model of nonbaryonic dark matter: A Singlet scalar. *Nucl. Phys. B*, 619:709–728, 2001. doi: 10.1016/S0550-3213(01)00513-2.
- [12] Vernon Barger, Paul Langacker, Mathew McCaskey, Michael J. Ramsey-Musolf, and Gabe Shaughnessy. LHC Phenomenology of an Extended Standard Model with a Real Scalar Singlet. *Phys. Rev. D*, 77:035005, 2008. doi: 10.1103/PhysRevD.77.035005.

- [13] Wan-Lei Guo and Yue-Liang Wu. The Real singlet scalar dark matter model. *JHEP*, 10:083, 2010. doi: 10.1007/JHEP10(2010)083.
- [14] Vernon Barger, Paul Langacker, Mathew McCaskey, Michael Ramsey-Musolf, and Gabe Shaughnessy. Complex Singlet Extension of the Standard Model. *Phys. Rev. D*, 79:015018, 2009. doi: 10.1103/PhysRevD.79.015018.
- [15] Giorgio Arcadi, Abdelhak Djouadi, and Martti Raidal. Dark Matter through the Higgs portal. *Phys. Rept.*, 842:1–180, 2020. doi: 10.1016/j.physrep.2019.11.003.
- [16] Giorgio Arcadi, Abdelhak Djouadi, and Marumi Kado. The Higgs-portal for dark matter: effective field theories versus concrete realizations. *Eur. Phys. J. C*, 81(7):653, 2021. doi: 10.1140/epjc/s10052-021-09411-2.
- [17] Juan Carlos Criado, Abdelhak Djouadi, Manuel Perez-Victoria, and Jose Santiago. A complete effective field theory for dark matter. *JHEP*, 07:081, 2021. doi: 10.1007/JHEP07(2021)081.
- [18] Giorgio Arcadi, David Cabo-Almeida, Maira Dutra, Pradipta Ghosh, Manfred Lindner, Yann Mambrini, Jacinto P. Neto, Mathias Pierre, Stefano Profumo, and Farinaldo S. Queiroz. The Waning of the WIMP: Endgame? 3 2024.
- [19] Tania Robens, Tim Stefaniak, and Jonas Wittbrodt. Two-real-scalar-singlet extension of the SM: LHC phenomenology and benchmark scenarios. *Eur. Phys. J. C*, 80(2):151, 2020. doi: 10.1140/epjc/s10052-020-7655-x.
- [20] Rodrigo Capucha, Karim Elyaouti, Margarete Mühlleitner, Johann Plotnikov, and Rui Santos. Freeze-in as a complementary process to freeze-out. *JHEP*, 09:113, 2024. doi: 10.1007/JHEP09(2024)113.
- [21] Franz Mandl and Graham Shaw. *QUANTUM FIELD THEORY*. 1985.
- [22] Michele Maggiore. *A Modern introduction to quantum field theory*. Oxford Master Series in Physics. 2005. ISBN 978-0-19-852074-0.
- [23] Michael E. Peskin and Daniel V. Schroeder. *An Introduction to quantum field theory*. Addison-Wesley, Reading, USA, 1995. ISBN 978-0-201-50397-5, 978-0-429-50355-9, 978-0-429-49417-8. doi: 10.1201/9780429503559.
- [24] Matthew D. Schwartz. *Quantum Field Theory and the Standard Model*. Cambridge University Press, 3 2014. ISBN 978-1-107-03473-0, 978-1-107-03473-0.
- [25] Jorge Crispim Romão and João Paulo Silva. Quantum field theory. Lecture notes, unpublished, 2022. URL <https://porthos.tecnico.ulisboa.pt/Public/textos/qft.pdf>.
- [26] Jorge Crispim Romão. Advanced quantum field theory. Lecture notes, unpublished, 2020. URL <https://porthos.tecnico.ulisboa.pt/Public/textos/tca.pdf>.
- [27] Luís Filipe Bento. Lectures on quantum field theory, 2022/2023. Master’s in Physics and Astrophysics, Faculty of Sciences, University of Lisbon.
- [28] Wu-Ki Tung. *Group Theory in Physics*. 8 1985. doi: 10.1142/0097.

- [29] Howard Georgi. *Lie Algebras In Particle Physics : from Isospin To Unified Theories*. Taylor & Francis, Boca Raton, 2000. ISBN 978-0-429-96776-4, 978-0-367-09172-9, 978-0-429-49921-0, 978-0-7382-0233-4. doi: 10.1201/9780429499210.
- [30] E. Leader and E. Predazzi. *An Introduction to gauge theories and modern particle physics. Vol. 1: Electroweak interactions, the new particles and the parton model*. Cambridge University Press, 4 2011. ISBN 978-0-511-88573-0, 978-0-521-46840-4.
- [31] John F. Donoghue, Eugene Golowich, and Barry R. Holstein. *Dynamics of the Standard Model: Second edition*. Cambridge University Press, 11 2022. ISBN 978-1-009-29100-2, 978-1-009-29101-9, 978-1-009-29103-3. doi: 10.1017/9781009291033.
- [32] Paul Langacker. *The Standard Model and Beyond*. Taylor & Francis, 2017. ISBN 978-1-4987-6322-6, 978-1-4987-6321-9, 978-0-367-57344-7, 978-1-315-17062-6. doi: 10.1201/b22175.
- [33] Filipe R. Joaquim. Lectures on standard model, 2022/2023. Master’s in Technological Engineering Physics, Instituto Superior Técnico, University of Lisbon.
- [34] Luís Lavoura. Standard model. Lecture notes, unpublished, 2020.
- [35] C. Itzykson and J. B. Zuber. *Quantum Field Theory*. International Series In Pure and Applied Physics. McGraw-Hill, New York, 1980. ISBN 978-0-486-44568-7.
- [36] Georges Aad et al. Observation of a new particle in the search for the Standard Model Higgs boson with the ATLAS detector at the LHC. *Phys. Lett. B*, 716:1–29, 2012. doi: 10.1016/j.physletb.2012.08.020.
- [37] Serguei Chatrchyan et al. Observation of a New Boson at a Mass of 125 GeV with the CMS Experiment at the LHC. *Phys. Lett. B*, 716:30–61, 2012. doi: 10.1016/j.physletb.2012.08.021.
- [38] S. Navas et al. Review of particle physics. *Phys. Rev. D*, 110(3):030001, 2024. doi: 10.1103/PhysRevD.110.030001.
- [39] Mariangela Lisanti. Lectures on Dark Matter Physics. In *Theoretical Advanced Study Institute in Elementary Particle Physics: New Frontiers in Fields and Strings*, pages 399–446, 2017. doi: 10.1142/9789813149441_0007.
- [40] Martin Bauer and Tilman Plehn. *Yet Another Introduction to Dark Matter: The Particle Physics Approach*, volume 959 of *Lecture Notes in Physics*. Springer, 2019. doi: 10.1007/978-3-030-16234-4.
- [41] Stefano Profumo, Leonardo Giani, and Oliver F. Piattella. An Introduction to Particle Dark Matter. *Universe*, 5(10):213, 2019. doi: 10.3390/universe5100213.
- [42] Rui Santos. Lectures on dark matter, phase transitions and gravitational waves, 2022/2023. Master’s in Physics and Astrophysics, Faculty of Sciences, University of Lisbon.
- [43] Carlo Giunti and Chung W. Kim. *Fundamentals of Neutrino Physics and Astrophysics*. 2007. ISBN 978-0-19-850871-7. doi: 10.1093/acprof:oso/9780198508717.001.0001.
- [44] Jose W. F. Valle and Jorge C. Romao. *Neutrinos in high energy and astroparticle physics*. Physics textbook. Wiley-VCH, Weinheim, 2015. ISBN 978-3-527-41197-9, 978-3-527-67102-1.

- [45] R. D. Peccei. The Strong CP problem and axions. *Lect. Notes Phys.*, 741:3–17, 2008. doi: 10.1007/978-3-540-73518-2_1.
- [46] Gustavo C. Branco, Luis Lavoura, and Joao P. Silva. *CP Violation*, volume 103. 1999. ISBN 978-1-383-02075-5, 978-0-19-850399-6. doi: 10.1093/oso/9780198503996.001.0001.
- [47] R. D. Peccei and Helen R. Quinn. CP Conservation in the Presence of Instantons. *Phys. Rev. Lett.*, 38:1440–1443, 1977. doi: 10.1103/PhysRevLett.38.1440.
- [48] R. D. Peccei and Helen R. Quinn. Constraints Imposed by CP Conservation in the Presence of Instantons. *Phys. Rev. D*, 16:1791–1797, 1977. doi: 10.1103/PhysRevD.16.1791.
- [49] Frank Wilczek. Problem of Strong P and T Invariance in the Presence of Instantons. *Phys. Rev. Lett.*, 40:279–282, 1978. doi: 10.1103/PhysRevLett.40.279.
- [50] Steven Weinberg. A New Light Boson? *Phys. Rev. Lett.*, 40:223–226, 1978. doi: 10.1103/PhysRevLett.40.223.
- [51] Bryce S. DeWitt and Giampiero Esposito. An Introduction to quantum gravity. *Int. J. Geom. Meth. Mod. Phys.*, 5:101–156, 2008. doi: 10.1142/S0219887808002679.
- [52] Giampiero Esposito. An Introduction to quantum gravity. 8 2011.
- [53] A. D. Sakharov. Violation of CP Invariance, C asymmetry, and baryon asymmetry of the universe. *Pisma Zh. Eksp. Teor. Fiz.*, 5:32–35, 1967. doi: 10.1070/PU1991v034n05ABEH002497.
- [54] Laurent Canetti, Marco Drewes, and Mikhail Shaposhnikov. Matter and Antimatter in the Universe. *New J. Phys.*, 14:095012, 2012. doi: 10.1088/1367-2630/14/9/095012.
- [55] Mark Thomson. *Modern particle physics*. Cambridge University Press, New York, 10 2013. ISBN 978-1-107-03426-6, 978-1-139-52536-7. doi: 10.1017/CBO9781139525367.
- [56] Michael E. Peskin. *Concepts of Elementary Particle Physics*. Oxford Master Series in Physics. Oxford University Press, 9 2019. ISBN 978-0-19-881218-0, 978-0-19-881219-7. doi: 10.1093/oso/9780198812180.001.0001.
- [57] Scott Dodelson and Fabian Schmidt. *Modern Cosmology*. Academic Press, 2020. doi: 10.1016/C2017-0-01943-2.
- [58] Daniel Baumann. *Cosmology*. Cambridge University Press, 7 2022. ISBN 978-1-108-93709-2, 978-1-108-83807-8. doi: 10.1017/9781108937092.
- [59] G. Alguero, G. Belanger, F. Boudjema, S. Chakraborti, A. Goudelis, S. Kraml, A. Mjallal, and A. Pukhov. micrOMEGAs 6.0: N-component dark matter. *Comput. Phys. Commun.*, 299:109133, 2024. doi: 10.1016/j.cpc.2024.109133.
- [60] E. Aprile et al. Dark Matter Search Results from a One Ton-Year Exposure of XENON1T. *Phys. Rev. Lett.*, 121(11):111302, 2018. doi: 10.1103/PhysRevLett.121.111302.
- [61] P. Agnes et al. Low-Mass Dark Matter Search with the DarkSide-50 Experiment. *Phys. Rev. Lett.*, 121(8):081307, 2018. doi: 10.1103/PhysRevLett.121.081307.

- [62] C. Amole et al. Dark Matter Search Results from the Complete Exposure of the PICO-60 C_3F_8 Bubble Chamber. *Phys. Rev. D*, 100(2):022001, 2019. doi: 10.1103/PhysRevD.100.022001.
- [63] A. H. Abdelhameed et al. First results from the CRESST-III low-mass dark matter program. *Phys. Rev. D*, 100(10):102002, 2019. doi: 10.1103/PhysRevD.100.102002.
- [64] Yue Meng et al. Dark Matter Search Results from the PandaX-4T Commissioning Run. *Phys. Rev. Lett.*, 127(26):261802, 2021. doi: 10.1103/PhysRevLett.127.261802.
- [65] Kimberly K. Boddy, Stephen Hill, Jason Kumar, Pearl Sandick, and Barmak Shams Es Haghi. MADHAT: Model-Agnostic Dark Halo Analysis Tool. *Comput. Phys. Commun.*, 261:107815, 2021. doi: 10.1016/j.cpc.2020.107815.
- [66] Kimberly Boddy, Jason Kumar, Danny Marfatia, and Pearl Sandick. Model-independent constraints on dark matter annihilation in dwarf spheroidal galaxies. *Phys. Rev. D*, 97(9):095031, 2018. doi: 10.1103/PhysRevD.97.095031.
- [67] Georges Aad et al. Combination of searches for invisible decays of the Higgs boson using 139 fb $^{-1}$ of proton-proton collision data at $\sqrt{s}=13$ TeV collected with the ATLAS experiment. *Phys. Lett. B*, 842:137963, 2023. doi: 10.1016/j.physletb.2023.137963.
- [68] Gerard Jungman, Marc Kamionkowski, and Kim Griest. Supersymmetric dark matter. *Phys. Rept.*, 267:195–373, 1996. doi: 10.1016/0370-1573(95)00058-5.
- [69] Hai-Yang Cheng and Cheng-Wei Chiang. Revisiting Scalar and Pseudoscalar Couplings with Nucleons. *JHEP*, 07:009, 2012. doi: 10.1007/JHEP07(2012)009.
- [70] Junji Hisano, Koji Ishiwata, and Natsumi Nagata. Gluon contribution to the dark matter direct detection. *Phys. Rev. D*, 82:115007, 2010. doi: 10.1103/PhysRevD.82.115007.
- [71] Junji Hisano, Ryo Nagai, and Natsumi Nagata. Effective Theories for Dark Matter Nucleon Scattering. *JHEP*, 05:037, 2015. doi: 10.1007/JHEP05(2015)037.
- [72] Junji Hisano. Effective theory approach to direct detection of dark matter. 12 2017. doi: 10.1093/oso/9780198855743.003.0011.
- [73] Eugenio Del Nobile. The Theory of Direct Dark Matter Detection: A Guide to Computations. 4 2021. doi: 10.1007/978-3-030-95228-0.
- [74] Mikhail A. Shifman, A. I. Vainshtein, and Valentin I. Zakharov. Remarks on Higgs Boson Interactions with Nucleons. *Phys. Lett. B*, 78:443–446, 1978. doi: 10.1016/0370-2693(78)90481-1.
- [75] Curtis G. Callan, Jr., Sidney R. Coleman, and Roman Jackiw. A New improved energy - momentum tensor. *Annals Phys.*, 59:42–73, 1970. doi: 10.1016/0003-4916(70)90394-5.
- [76] Cédric Lorcé, Andreas Metz, Barbara Pasquini, and Simone Rodini. Energy-momentum tensor in QCD: nucleon mass decomposition and mechanical equilibrium. *JHEP*, 11:121, 2021. doi: 10.1007/JHEP11(2021)121.
- [77] Kristjan Kannike. Vacuum Stability Conditions From Copositivity Criteria. *Eur. Phys. J. C*, 72: 2093, 2012. doi: 10.1140/epjc/s10052-012-2093-z.

- [78] Kristjan Kannike. Vacuum Stability of a General Scalar Potential of a Few Fields. *Eur. Phys. J. C*, 76(6):324, 2016. doi: 10.1140/epjc/s10052-016-4160-3. [Erratum: *Eur.Phys.J.C* 78, 355 (2018)].
- [79] Heather E. Logan. Lectures on perturbative unitarity and decoupling in Higgs physics. 7 2022.
- [80] Michael E. Peskin and Tatsu Takeuchi. Estimation of oblique electroweak corrections. *Phys. Rev. D*, 46:381–409, 1992. doi: 10.1103/PhysRevD.46.381.
- [81] Johan Alwall, Michel Herquet, Fabio Maltoni, Olivier Mattelaer, and Tim Stelzer. MadGraph 5 : Going Beyond. *JHEP*, 06:128, 2011. doi: 10.1007/JHEP06(2011)128.
- [82] J. Alwall, R. Frederix, S. Frixione, V. Hirschi, F. Maltoni, O. Mattelaer, H. S. Shao, T. Stelzer, P. Torrielli, and M. Zaro. The automated computation of tree-level and next-to-leading order differential cross sections, and their matching to parton shower simulations. *JHEP*, 07:079, 2014. doi: 10.1007/JHEP07(2014)079.
- [83] Markus Zerlauth and Oliver Brüning. Status and prospects of the HL-LHC project. *PoS, EPS-HEP2023*:615, 2024. doi: 10.22323/1.449.0615.
- [84] H. M. Georgi, S. L. Glashow, M. E. Machacek, and Dimitri V. Nanopoulos. Higgs Bosons from Two Gluon Annihilation in Proton Proton Collisions. *Phys. Rev. Lett.*, 40:692, 1978. doi: 10.1103/PhysRevLett.40.692.
- [85] M. Spira, A. Djouadi, D. Graudenz, and P. M. Zerwas. Higgs boson production at the LHC. *Nucl. Phys. B*, 453:17–82, 1995. doi: 10.1016/0550-3213(95)00379-7.
- [86] Armen Tumasyan et al. Search for new particles in events with energetic jets and large missing transverse momentum in proton-proton collisions at $\sqrt{s} = 13$ TeV. *JHEP*, 11:153, 2021. doi: 10.1007/JHEP11(2021)153.
- [87] Albert M Sirunyan et al. Search for dark matter particles produced in association with a Higgs boson in proton-proton collisions at $\sqrt{s} = 13$ TeV. *JHEP*, 03:025, 2020. doi: 10.1007/JHEP03(2020)025.
- [88] Albert M Sirunyan et al. Search for dark matter produced in association with a leptonically decaying Z boson in proton-proton collisions at $\sqrt{s} = 13$ TeV. *Eur. Phys. J. C*, 81(1):13, 2021. doi: 10.1140/epjc/s10052-020-08739-5. [Erratum: *Eur.Phys.J.C* 81, 333 (2021)].
- [89] Emmy Noether. Invariant Variation Problems. *Gott. Nachr.*, 1918:235–257, 1918. doi: 10.1080/00411457108231446.
- [90] Kerson Huang. *Quantum field theory: From operators to path integrals*. 1998.
- [91] Daniel N. Blaschke, Francois Gieres, Meril Reboud, and Manfred Schweda. The energy–momentum tensor(s) in classical gauge theories. *Nucl. Phys. B*, 912:192–223, 2016. doi: 10.1016/j.nuclphysb.2016.07.001.
- [92] F.J. Belinfante. On the spin angular momentum of mesons. *Physica*, 6(7):887–898, 1939. ISSN 0031-8914. doi: [https://doi.org/10.1016/S0031-8914\(39\)90090-X](https://doi.org/10.1016/S0031-8914(39)90090-X). URL <https://www.sciencedirect.com/science/article/pii/S003189143990090X>.

BIBLIOGRAPHY

- [93] F.J. Belinfante. On the current and the density of the electric charge, the energy, the linear momentum and the angular momentum of arbitrary fields. *Physica*, 7(5):449–474, 1940. ISSN 0031-8914. doi: [https://doi.org/10.1016/S0031-8914\(40\)90091-X](https://doi.org/10.1016/S0031-8914(40)90091-X). URL <https://www.sciencedirect.com/science/article/pii/S003189144090091X>.

Appendix A

Principles in Field Theory

This appendix provides a didactic theoretical background to the main principles that govern field theory, namely the variational principle of least action, which leads to the Euler-Lagrange equations of motion, and the local gauge symmetry principle, which formulates our theories of interactions. Hence, it serves not only as a theoretical complement to Chapter 2, but also to the rest of this work.

A.1 The Variational Principle of Least Action

The transition from non-relativistic classical mechanics to relativistic classical field theory is achieved by replacing the generalized coordinates $q_j(t)$, which are functions of time, by fields $\varphi_r(x^\mu) \equiv \varphi_r(t, \vec{x})$, which are functions of space-time. The action is then defined by

$$S \equiv \int_{t_1}^{t_2} dt L(t) \equiv \int_{V_4} d^4x \mathcal{L}(\varphi_r, \partial_\mu \varphi_r), \quad (\text{A.1})$$

where $L(t) \equiv \int_{V_3} d^3x \mathcal{L}(\varphi_r, \partial_\mu \varphi_r)$ is the Lagrangian and $\mathcal{L}(\varphi_r, \partial_\mu \varphi_r)$ is the Lagrangian density, which is a functional of the fields $\varphi_r(x)$ and their space-time partial derivatives $\partial_\mu \varphi_r \equiv \frac{\partial \varphi_r}{\partial x^\mu} = (\frac{\partial \varphi_r}{\partial t}, \vec{\nabla} \varphi_r)$. The *variational principle of least action* states that the space-time evolution of the fields, which have fixed values (and thus, null variation) on the boundary surface $\Sigma_3 = \partial V_4$ of the 4-dimensional space-time volume V_4 , is determined by the requirement that the action be an extremum (a minimum), i.e.,

$$\underbrace{\delta S[\mathcal{L}(\varphi_r, \partial_\mu \varphi_r)] = 0}_{\text{stationary action}}, \quad \text{with} \quad \underbrace{\delta \varphi_r(x) = 0, \forall x^\mu \in \Sigma_3 = \partial V_4}_{\text{boundary condition (BC)}}. \quad (\text{A.2})$$

Computing the variation of the action, this variational principle leads to

$$0 = \delta S = \delta \int_{V_4} d^4x \mathcal{L}(\varphi_r, \partial_\mu \varphi_r) = \int_{V_4} d^4x \delta \mathcal{L}(\varphi_r, \partial_\mu \varphi_r) \quad (\text{A.3})$$

$$= \sum_{\varphi_r} \int_{V_4} d^4x \left[\frac{\partial \mathcal{L}}{\partial \varphi_r} \delta \varphi_r + \frac{\partial \mathcal{L}}{\partial (\partial_\mu \varphi_r)} \delta (\partial_\mu \varphi_r) \right], \quad \delta (\partial_\mu \varphi_r) = \partial_\mu (\delta \varphi_r) \quad (\text{A.4})$$

$$= \sum_{\varphi_r} \int_{V_4} d^4x \left[\frac{\partial \mathcal{L}}{\partial \varphi_r} \delta \varphi_r + \partial_\mu \left[\frac{\partial \mathcal{L}}{\partial (\partial_\mu \varphi_r)} \delta \varphi_r \right] - \left[\partial_\mu \frac{\partial \mathcal{L}}{\partial (\partial_\mu \varphi_r)} \right] \delta \varphi_r \right] \quad (\text{A.5})$$

$$= \sum_{\varphi_r} \int_{V_4} d^4x \left[\frac{\partial \mathcal{L}}{\partial \varphi_r} - \partial_\mu \frac{\partial \mathcal{L}}{\partial (\partial_\mu \varphi_r)} \right] \delta \varphi_r + \sum_{\varphi_r} \oint_{\Sigma_3 = \partial V_4} dS n_\mu \frac{\partial \mathcal{L}}{\partial (\partial_\mu \varphi_r)} \underbrace{\delta \varphi_r}_{=0 \text{ (BC)}} \quad (\text{A.6})$$

$$= \sum_{\varphi_r} \int_{V_4} d^4x \left[\frac{\partial \mathcal{L}}{\partial \varphi_r} - \partial_\mu \frac{\partial \mathcal{L}}{\partial (\partial_\mu \varphi_r)} \right] \delta \varphi_r, \quad (\text{A.7})$$

which implies the so-called Euler-Lagrange equations of motion,

$$\Rightarrow \partial_\mu \frac{\partial \mathcal{L}}{\partial (\partial_\mu \varphi_r)} - \frac{\partial \mathcal{L}}{\partial \varphi_r} = 0, \quad \forall \varphi_r. \quad (\text{A.8})$$

It should be noted that the Lagrangian density is not uniquely defined. One can define alternative Lagrangian densities of the form $\mathcal{L}' = \mathcal{L} + \partial_\mu F^\mu(\varphi_r, \partial_\mu \varphi_r)$, i.e., by adding a total 4-divergence term, so that the action $S' = \int_{V_4} d^4x \mathcal{L}' = \int_{V_4} d^4x \mathcal{L} + \int_{V_4} d^4x \partial_\mu F^\mu = S + \oint_{\Sigma_3=\partial V_4} dS n_\mu F^\mu$ is only changed by a constant boundary term that does not affect the Euler-Lagrange equations of motion (since its variation is null), thus leaving the theory unchanged. Furthermore, for an infinite 4-dimensional space-time volume V_4 , the boundary term vanishes under the assumption of the field configurations going to zero sufficiently fast at infinity [22]. For example, the (hermitian) Dirac Lagrangian density

$$\mathcal{L}_D(\psi, \bar{\psi}, \partial_\mu \psi, \partial_\mu \bar{\psi}) = \frac{i}{2} \bar{\psi} \gamma^\mu \partial_\mu \psi - \frac{i}{2} (\partial_\mu \bar{\psi}) \gamma^\mu \psi - m \bar{\psi} \psi \equiv \bar{\psi} \left(\frac{i}{2} \gamma^\mu \overleftrightarrow{\partial}_\mu - m \right) \psi, \quad (\text{A.9})$$

with $\overleftrightarrow{\partial}_\mu \equiv \overrightarrow{\partial}_\mu - \overleftarrow{\partial}_\mu$, describes a free spinor field $\psi(x)$, and the corresponding Euler-Lagrange equation of motion is the (free) Dirac equation,

$$\begin{cases} \partial_\mu \frac{\partial \mathcal{L}_D}{\partial (\partial_\mu \bar{\psi})} - \frac{\partial \mathcal{L}_D}{\partial \bar{\psi}} = 0 \Leftrightarrow i(\partial_\mu \bar{\psi}) \gamma^\mu + m \bar{\psi} \equiv \bar{\psi} (i \gamma^\mu \overleftarrow{\partial}_\mu + m) = 0 \\ \partial_\mu \frac{\partial \mathcal{L}_D}{\partial (\partial_\mu \psi)} - \frac{\partial \mathcal{L}_D}{\partial \psi} = 0 \Leftrightarrow (i \gamma^\mu \partial_\mu - m) \psi = 0 \end{cases}. \quad (\text{A.10})$$

Since $\mathcal{L}_D = \bar{\psi} (i \gamma^\mu \partial_\mu - m) \psi + \partial_\mu (-\frac{i}{2} \bar{\psi} \gamma^\mu \psi)$, one can consider the (popular) alternative non-hermitian Lagrangian density $\mathcal{L}'_D = \mathcal{L}_D + \partial_\mu (-\frac{i}{2} \bar{\psi} \gamma^\mu \psi) = \bar{\psi} (i \gamma^\mu \partial_\mu - m) \psi$ (or equivalently, the alternative action $S'_D = S_D + \oint_{\Sigma_3=\partial V_4} dS n_\mu \frac{i}{2} \bar{\psi} \gamma^\mu \psi$), which leads to the same Euler-Lagrange (Dirac) equation of motion.

A.2 The Gauge Symmetry Principle and Non-Abelian Gauge Theories

Consider a fermion \tilde{n} -dimensional multiplet field $\Psi(x) = \begin{pmatrix} \psi_1(x) & \dots & \psi_{\tilde{n}}(x) \end{pmatrix}^\top \sim \tilde{\mathbf{n}}$ which transforms under the \tilde{n} -dimensional representation $U(\vec{\alpha}) = e^{-i \sum_{a=1}^{d_G} \alpha^a T_a} \mapsto \tilde{U}(\vec{\alpha}) = e^{-i \sum_{a=1}^{d_G} \alpha^a \tilde{T}_a}$, with $\tilde{T}_a \in \mathbb{C}^{\tilde{n} \times \tilde{n}}$, of a non-Abelian d_G -dimensional Lie group of algebra $[T_a, T_b] = i \sum_{c=1}^{d_G} f_{abc} T_c$, where T_a are the generators and f_{abc} are the structure constants, $a, b, c = 1, \dots, d_G$, so that

$$\Psi \rightarrow \Psi' = \tilde{U}(\vec{\alpha}) \Psi = e^{-i \sum_{a=1}^{d_G} \alpha^a \tilde{T}_a} \Psi \approx \left(\mathbb{1} - i \sum_{a=1}^{d_G} \alpha^a \tilde{T}_a \right) \Psi, \quad (\text{A.11})$$

or equivalently, $\psi_i \rightarrow \psi'_i = \sum_{j=1}^{\tilde{n}} \tilde{U}_{ij}(\vec{\alpha}) \psi_j \approx \sum_{j=1}^{\tilde{n}} (\mathbb{1} - i \sum_{a=1}^{d_G} \alpha^a \tilde{T}_a)_{ij} \psi_j$ in component form. The Lagrangian density of the free massive fermion multiplet field $\Psi(x) \sim \tilde{\mathbf{n}}$,

$$\mathcal{L}_D^{(\Psi)} = \bar{\Psi} (i \gamma^\mu \partial_\mu - m) \Psi = \sum_{i=1}^{\tilde{n}} \bar{\psi}_i (i \gamma^\mu \partial_\mu - m) \psi_i \quad (\text{A.12})$$

$$\xrightarrow{\text{global}} \mathcal{L}_D^{(\Psi)} = \bar{\Psi} \tilde{U}^\dagger(\vec{\alpha}) (i \gamma^\mu \partial_\mu - m) \tilde{U}(\vec{\alpha}) \Psi = \sum_{i,j,k=1}^{\tilde{n}} \bar{\psi}_j \tilde{U}_{ij}^*(\vec{\alpha}) (i \gamma^\mu \partial_\mu - m) \tilde{U}_{ik}(\vec{\alpha}) \psi_k, \quad (\text{A.13})$$

is invariant under *global* transformations of the group, provided these are unitary.¹ However, under *local* transformations $\Psi \rightarrow \Psi' = \tilde{U}[\vec{\alpha}(x)]\Psi = e^{-i\sum_{a=1}^{d_G} \alpha^a(x)\hat{T}_a}\Psi$, where $\vec{\alpha} = \vec{\alpha}(x)$ depends on the space-time coordinates, one has

$$\mathcal{L}_D^{(\Psi)} \xrightarrow{\text{local}} \mathcal{L}_D'^{(\Psi)} = \bar{\Psi}\tilde{U}^\dagger[\vec{\alpha}(x)](i\gamma^\mu\partial_\mu - m)\tilde{U}[\vec{\alpha}(x)]\Psi = \bar{\Psi}(i\gamma^\mu[\partial_\mu + \tilde{U}^\dagger\partial_\mu\tilde{U}] - m)\Psi \quad (\text{A.14})$$

$$\neq \mathcal{L}_D^{(\Psi)}, \quad \forall \vec{\alpha}(x) \neq \text{space-time constant}, \quad (\text{A.15})$$

where $\tilde{U} = \tilde{U}[\vec{\alpha}(x)]$. Imposing invariance under local transformations of this group requires replacing the partial derivative ∂_μ , in the Lagrangian density,² with another differential operator D_μ of the form

$$D_\mu = \partial_\mu + ig\tilde{G}_\mu(x), \quad \text{with} \quad \tilde{G}_\mu(x) \in \mathbb{C}^{\tilde{n} \times \tilde{n}}, \quad (\text{A.16})$$

where g is an arbitrary real constant. This replacement procedure $\partial_\mu \hookrightarrow D_\mu$ is called *minimal coupling*, and the “new” Lagrangian density $\mathcal{L}_{D+\text{int}}^{(\Psi)} = \bar{\Psi}(i\gamma^\mu D_\mu - m)\Psi$ now locally transforms as

$$\mathcal{L}_{D+\text{int}}^{(\Psi)} \xrightarrow{\text{local}} \mathcal{L}_{D+\text{int}}'^{(\Psi)} = \bar{\Psi}\tilde{U}^\dagger[\vec{\alpha}(x)](i\gamma^\mu D'_\mu - m)\tilde{U}[\vec{\alpha}(x)]\Psi, \quad D'_\mu = \partial_\mu + ig\tilde{G}'_\mu(x) \quad (\text{A.17})$$

$$= \bar{\Psi}(i\gamma^\mu[\partial_\mu + \tilde{U}^\dagger(\partial_\mu + ig\tilde{G}'_\mu)\tilde{U}] - m)\Psi, \quad (\text{A.18})$$

thus being invariant under local transformations if $\tilde{U}^\dagger(\partial_\mu + ig\tilde{G}'_\mu)\tilde{U} = +ig\tilde{G}_\mu$, i.e., provided that $\tilde{G}_\mu(x)$ transforms as

$$\tilde{G}_\mu \xrightarrow{\text{local}} \tilde{G}'_\mu = \tilde{U}\tilde{G}_\mu\tilde{U}^\dagger + \frac{i}{g}(\partial_\mu\tilde{U})\tilde{U}^\dagger = \tilde{U}\tilde{G}_\mu\tilde{U}^\dagger - \frac{i}{g}\tilde{U}\partial_\mu\tilde{U}^\dagger \quad (\text{A.19})$$

$$= \tilde{U}\tilde{G}_\mu\tilde{U}^\dagger + \sum_{a=1}^{d_G} \frac{\partial_\mu\alpha^a(x)}{g}\tilde{T}_a. \quad (\text{A.20})$$

One can directly check, by applying two consecutive transformations $\tilde{G}_\mu \xrightarrow{U_1} \tilde{G}'_\mu \xrightarrow{U_2} \tilde{G}''_\mu$, that this transformation constitutes a representation of the group. It is possible to show that $\tilde{G}_\mu(x) = \vec{G}_\mu(x) \cdot \vec{T} = \sum_{a=1}^{d_G} G_\mu^a(x)\tilde{T}_a$, where $G_\mu^a(x)$, $a = 1, \dots, d_G$ globally transform as components of a d_G -dimensional multiplet $\vec{G}_\mu(x) = \left(G_\mu^1(x) \dots G_\mu^{d_G}(x)\right)^\top \sim \mathbf{d}_G$ which transforms under the adjoint representation of the group, $T_a \mapsto \hat{T}_a$ with $(\hat{T}_a)_{bc} \equiv -if_{abc}$, so that

$$\begin{aligned} G_\mu^a \xrightarrow{\text{global}} G_\mu'^a &= \sum_{c=1}^{d_G} \left(e^{-i\sum_{b=1}^{d_G} \alpha^b \hat{T}_b} \right)_{ac} G_\mu^c \approx \sum_{c=1}^{d_G} \left(\mathbb{1} - i \sum_{b=1}^{d_G} \alpha^b \hat{T}_b \right)_{ac} G_\mu^c = \sum_{c=1}^{d_G} \left[\delta_{ac} - i \sum_{b=1}^{d_G} \alpha^b (\hat{T}_b)_{ac} \right] G_\mu^c \\ &= \sum_{c=1}^{d_G} \left[\delta_{ac} - \sum_{b=1}^{d_G} \alpha^b f_{bac} \right] G_\mu^c = G_\mu^a + \sum_{b,c=1}^{d_G} f_{abc} \alpha^b G_\mu^c. \end{aligned} \quad (\text{A.21})$$

This can be verified by inserting $\tilde{G}_\mu(x) = \sum_{a=1}^{d_G} G_\mu^a(x)\tilde{T}_a$ in Eq. (A.20), leading to

$$\sum_{a=1}^{d_G} G_\mu^a \tilde{T}_a \xrightarrow{\text{local}} \tilde{U} \sum_{a=1}^{d_G} G_\mu^a \tilde{T}_a \tilde{U}^\dagger + \sum_{a=1}^{d_G} \frac{\partial_\mu\alpha^a(x)}{g} \tilde{T}_a \quad (\text{A.22})$$

¹By definition, $f_{abc} = -f_{bac}$. One can show that: unitary transformations $U^\dagger = U^{-1} \Leftrightarrow$ hermitian generators $T_a^\dagger = T_a \Leftrightarrow$ real structure constants $f_{abc} \in \mathbb{R} \Rightarrow$ fully anti-symmetric structure constants $f_{abc} = -f_{bac} = +f_{bca} = -f_{cba} = \dots$

²Or equivalently, it requires the introduction of an interaction term of the form $-g\bar{\Psi}\gamma^\mu\tilde{G}_\mu\Psi = -g\sum_{i,j=1}^{\tilde{n}} \bar{\psi}_i\gamma^\mu(\tilde{G}_\mu)_{ij}\psi_j$, with $\tilde{G}_\mu \in \mathbb{C}^{\tilde{n} \times \tilde{n}}$, as we shall later see in Eq. (A.28).

$$= e^{-i \sum_{b=1}^{d_G} \alpha^b(x) \tilde{T}_b} \sum_{a=1}^{d_G} G_\mu^a \tilde{T}_a e^{+i \sum_{c=1}^{d_G} \alpha^c(x) \tilde{T}_c} + \sum_{a=1}^{d_G} \frac{\partial_\mu \alpha^a(x)}{g} \tilde{T}_a \quad (\text{A.23})$$

$$\approx \left(\mathbb{1} - i \sum_{b=1}^{d_G} \alpha^b(x) \tilde{T}_b \right) \sum_{a=1}^{d_G} G_\mu^a \tilde{T}_a \left(\mathbb{1} + i \sum_{c=1}^{d_G} \alpha^c(x) \tilde{T}_c \right) + \sum_{a=1}^{d_G} \frac{\partial_\mu \alpha^a(x)}{g} \tilde{T}_a \quad (\text{A.24})$$

$$\begin{aligned} &= \sum_{a=1}^{d_G} G_\mu^a \tilde{T}_a - i \sum_{a,b=1}^{d_G} \alpha^b(x) G_\mu^a [\tilde{T}_b, \tilde{T}_a] + \sum_{a,b,c=1}^{d_G} \alpha^b(x) \alpha^c(x) G_\mu^a \tilde{T}_b \tilde{T}_a \tilde{T}_c + \sum_{a=1}^{d_G} \frac{\partial_\mu \alpha^a(x)}{g} \tilde{T}_a \\ &= \sum_{a=1}^{d_G} \left[G_\mu^a + \sum_{b,c=1}^{d_G} f_{bca} \alpha^b(x) G_\mu^c + \mathcal{O}(\tilde{\alpha}^2) + \frac{\partial_\mu \alpha^a(x)}{g} \right] \tilde{T}_a, \end{aligned} \quad (\text{A.25})$$

which implies that, under infinitesimal local transformations of the group,

$$G_\mu^a \xrightarrow{\text{local}} G_\mu'^a \approx G_\mu^a + \sum_{b,c=1}^{d_G} f_{bca} \alpha^b(x) G_\mu^c + \frac{\partial_\mu \alpha^a(x)}{g}. \quad (\text{A.26})$$

Notice that, unlike $\tilde{G}_\mu(x) = \sum_{a=1}^{d_G} G_\mu^a(x) \tilde{T}_a$, the transformation of $G_\mu^a(x)$ is independent of the representation $\tilde{\mathbf{n}}$ of the fermion multiplet field $\Psi(x) \sim \tilde{\mathbf{n}}$ to which the covariant derivative is applied – it only depends on the Lie algebra of the group. Hence, provided that $G_\mu^a(x)$ transforms as in Eq. (A.26), the (minimally coupled) Lagrangian density

$$\mathcal{L}_{\text{D+int}}^{(\Psi)} = \bar{\Psi}(i\gamma^\mu D_\mu - m)\Psi, \quad D_\mu = \partial_\mu + ig \sum_{a=1}^{d_G} G_\mu^a(x) \tilde{T}_a \quad (\text{A.27})$$

$$= \bar{\Psi}(i\gamma^\mu \partial_\mu - m)\Psi - g \sum_{a=1}^{d_G} G_\mu^a \bar{\Psi} \gamma^\mu \tilde{T}_a \Psi \quad (\text{A.28})$$

is invariant under local (or gauge) transformations of the group. A gauge interaction term emerged, $-g \sum_{a=1}^{d_G} G_\mu^a \bar{\Psi} \gamma^\mu \tilde{T}_a \Psi = -g \sum_{i,j=1}^{\tilde{n}} \sum_{a=1}^{d_G} G_\mu^a \bar{\psi}_i \gamma^\mu (\tilde{T}_a)_{ij} \psi_j$, mediated by the d_G gauge bosons $G_\mu^a(x)$, $a = 1, \dots, d_G$ associated to the local (or gauge) symmetry with respect to the d_G -dimensional Lie group.

Additionally, the gauge boson fields $G_\mu^a(x)$ are not external/auxiliary, but rather dynamical fields, thus requiring kinetic terms. If our theory is constructed based on a gauge symmetry criteria, all local gauge invariant terms must be introduced. One can show that $\tilde{G}_{\mu\nu} \rightarrow \tilde{U} \tilde{G}_{\mu\nu} \tilde{U}^\dagger$, with

$$\tilde{G}_{\mu\nu} \equiv \partial_\mu \tilde{G}_\nu - \partial_\nu \tilde{G}_\mu + ig [\tilde{G}_\mu, \tilde{G}_\nu] = \sum_{a=1}^{d_G} G_{\mu\nu}^a \tilde{T}_a, \quad (\text{A.29})$$

$$\text{where } G_{\mu\nu}^a \equiv \partial_\mu G_\nu^a - \partial_\nu G_\mu^a - g \sum_{b,c=1}^{d_G} f_{bca} G_\mu^b G_\nu^c \quad (\text{A.30})$$

are the so-called field strength tensors. Therefore, the kinetic terms of $G_\mu^a(x)$ must be contained in a term that is proportional the gauge invariant quantity

$$\text{Tr}(\tilde{G}_{\mu\nu} \tilde{G}^{\mu\nu}) = \sum_{a,b=1}^{d_G} G_{\mu\nu}^a G^{b\mu\nu} \underbrace{\text{Tr}(\tilde{T}_a \tilde{T}_b)}_{= \tilde{k} \delta_{ab}} = \tilde{k} \sum_{a=1}^{d_G} G_{\mu\nu}^a G^{a\mu\nu} \quad (\text{A.31})$$

$$\rightarrow \text{Tr}(\tilde{U} \tilde{G}_{\mu\nu} \tilde{U}^\dagger \tilde{U} \tilde{G}^{\mu\nu} \tilde{U}^\dagger) = \text{Tr}(\tilde{G}_{\mu\nu} \tilde{G}^{\mu\nu} \tilde{U}^\dagger \tilde{U}) = \text{Tr}(\tilde{G}_{\mu\nu} \tilde{G}^{\mu\nu}), \quad (\text{A.32})$$

where the cyclic property of traces was used, and $\text{Tr}(\tilde{T}_a \tilde{T}_b) = \tilde{k} \delta_{ab}$ depends on the representation (e.g., $k = 1/2$ for the fundamental representation). We choose a factor of $-1/4$, like in the $U(1)_Q$ Abelian case of electromagnetism, in order to obtain the correct equations of motion. Hence, the so-called “pure gauge” terms are given by

$$\mathcal{L}_{\text{gauge}} = -\frac{1}{4} \sum_{a=1}^{d_G} G_{\mu\nu}^a G^{a\mu\nu}, \quad G_{\mu\nu}^a \equiv \partial_\mu G_\nu^a - \partial_\nu G_\mu^a - g \sum_{b,c=1}^{d_G} f_{bca} G_\mu^b G_\nu^c \quad (\text{A.33})$$

$$= -\frac{1}{2} \sum_{a=1}^{d_G} [(\partial_\mu G_\nu^a) \partial^\mu G^{a\nu} - (\partial_\mu G_\nu^a) \partial^\nu G^{a\mu}] \quad (\text{A.34})$$

$$+ g \sum_{a,b,c=1}^{d_G} f_{bca} (\partial^\mu G^{a\nu}) G_\mu^b G_\nu^c - \frac{g^2}{4} \sum_{a,b,c,d,e=1}^{d_G} f_{bca} f_{dea} G_\mu^b G_\nu^c G^{d\mu} G^{e\nu}, \quad (\text{A.35})$$

where (A.34) are the usual real vector field kinetic terms, and (A.35) are the gauge boson self-interaction terms (for the special case of an Abelian group, $f_{abc} = 0$ and the gauge bosons do not self-interact).

Finally, there are no more local gauge invariant (and renormalizable) terms, and the final gauge theory is described by the Lagrangian density

$$\mathcal{L} = \mathcal{L}_{\text{D+int}}^{(\Psi)} + \mathcal{L}_{\text{gauge}} = \bar{\Psi}(i\gamma^\mu D_\mu - m)\Psi - \frac{1}{4} \sum_{a=1}^{d_G} G_{\mu\nu}^a G^{a\mu\nu} \quad (\text{A.36})$$

$$= \bar{\Psi}(i\gamma^\mu \partial_\mu - m)\Psi - g \sum_{a=1}^{d_G} G_\mu^a \bar{\Psi} \gamma^\mu \tilde{T}_a \Psi - \frac{1}{2} \sum_{a=1}^{d_G} [(\partial_\mu G_\nu^a) \partial^\mu G^{a\nu} - (\partial_\mu G_\nu^a) \partial^\nu G^{a\mu}]$$

$$+ g \sum_{a,b,c=1}^{d_G} f_{bca} (\partial^\mu G^{a\nu}) G_\mu^b G_\nu^c - \frac{g^2}{4} \sum_{a,b,c,d,e=1}^{d_G} f_{bca} f_{dea} G_\mu^b G_\nu^c G^{d\mu} G^{e\nu}. \quad (\text{A.37})$$

One should note that gauge boson mass terms $+\frac{1}{2}m_G^2 G_\mu^a G^{a\mu}$ explicitly break the gauge symmetry of the Lagrangian density, thus not being allowed (by themselves) in a gauge theory. Our findings can be summarized as follows: 1) Imposing local (or gauge) invariance under transformations of a d_G -dimensional Lie group on a theory that is globally invariant leads to the emergence of an interaction, mediated by d_G introduced (real vector) gauge bosons. 2) Requiring the introduction of all gauge invariant terms leads to the dynamics (i.e., kinetic terms) and self-interactions of the introduced gauge bosons, and also forbids gauge boson mass terms. This is the *local gauge symmetry principle*, which describes interactions as being deeply connected to gauge symmetries. Additionally, for $\mathcal{L} = \sum_i c_i \hat{\mathcal{O}}_i(x)$ with $[\hat{\mathcal{O}}_i(x)] = [m]^{D \leq 4}$ (operators with $D \leq 4$ mass dimensions), a gauge theory is renormalizable.

CONVENTION	$\Psi \rightarrow \Psi' = e^{-i \sum_a \alpha^a \tilde{T}_a} \Psi$ (active)	$\Psi \rightarrow \Psi' = e^{+i \sum_a \alpha^a \tilde{T}_a} \Psi$ (passive)
$D_\mu = \partial_\mu + ig \sum_a G_\mu^a \tilde{T}_a$	$G_\mu^a \rightarrow G_\mu'^a = G_\mu^a + \sum_{b,c} f_{bca} \alpha^b G_\mu^c + \frac{\partial_\mu \alpha^a}{g}$ $G_{\mu\nu}^a \equiv \partial_\mu G_\nu^a - \partial_\nu G_\mu^a - g \sum_{b,c} f_{bca} G_\mu^b G_\nu^c$	$G_\mu^a \rightarrow G_\mu'^a = G_\mu^a - \sum_{b,c} f_{bca} \alpha^b G_\mu^c - \frac{\partial_\mu \alpha^a}{g}$ $G_{\mu\nu}^a \equiv \partial_\mu G_\nu^a - \partial_\nu G_\mu^a - g \sum_{b,c} f_{bca} G_\mu^b G_\nu^c$
$D_\mu = \partial_\mu - ig \sum_a G_\mu^a \tilde{T}_a$	$G_\mu^a \rightarrow G_\mu'^a = G_\mu^a + \sum_{b,c} f_{bca} \alpha^b G_\mu^c - \frac{\partial_\mu \alpha^a}{g}$ $G_{\mu\nu}^a \equiv \partial_\mu G_\nu^a - \partial_\nu G_\mu^a + g \sum_{b,c} f_{bca} G_\mu^b G_\nu^c$	$G_\mu^a \rightarrow G_\mu'^a = G_\mu^a - \sum_{b,c} f_{bca} \alpha^b G_\mu^c + \frac{\partial_\mu \alpha^a}{g}$ $G_{\mu\nu}^a \equiv \partial_\mu G_\nu^a - \partial_\nu G_\mu^a + g \sum_{b,c} f_{bca} G_\mu^b G_\nu^c$

Table A.1: Summary of the different gauge theory conventions found in the literature, both for active/passive transformations (which are inverse to each other, with their correspondence obtained through a change of sign in the $\vec{\alpha}$ parameters) and for the sign of the gauge coupling constant in the covariant derivative.

In general, a gauge theory of real scalar multiplets $\varphi_r(x) \sim \mathbf{n}_r$, complex scalar multiplets $\Phi_s(x) \sim \mathbf{n}_s$

and fermion multiplets $\Psi_t(x) \sim \mathbf{n}_t$ is described by the Lagrangian density

$$\mathcal{L} = \sum_{\varphi_r} \left[\frac{1}{2} (D_\mu \varphi_r)^\dagger D^\mu \varphi_r - \frac{1}{2} m_{\varphi_r}^2 \varphi_r^\top \varphi_r \right] + \sum_{\Phi_s} \left[(D_\mu \Phi_s)^\dagger D^\mu \Phi_s - m_{\Phi_s}^2 \Phi_s^\dagger \Phi_s \right] \quad (\text{A.38})$$

$$+ \sum_{\Psi_t} \bar{\Psi}_t (i\gamma^\mu D_\mu - m_{\Psi_t}) \Psi_t - \frac{1}{4} \sum_{a=1}^{d_G} G_{\mu\nu}^a G^{a\mu\nu}, \quad (\text{A.39})$$

where the covariant derivative $D_\mu \equiv \partial_\mu + ig \sum_{a=1}^{d_G} G_\mu^a(x) T_a$ sits in the representation of the multiplet field to which it is applied,

$$D_\mu \varphi_r = [\partial_\mu + ig \sum_{a=1}^{d_G} G_\mu^a T_a^{(\mathbf{n}_r)}] \varphi_r, \quad D_\mu \Phi_s = [\partial_\mu + ig \sum_{a=1}^{d_G} G_\mu^a T_a^{(\mathbf{n}_s)}] \Phi_s, \quad D_\mu \Psi_t = [\partial_\mu + ig \sum_{a=1}^{d_G} G_\mu^a T_a^{(\mathbf{n}_t)}] \Psi_t.$$

Example: Quantum Electrodynamics is a gauge theory with respect to the Abelian 1-dimensional Lie group $U(1)_Q$, generated by the electric charge Q (in units of the positron electric charge $e = |e|$),

$$\mathcal{L}_{\text{QED}} = \bar{\psi} (i\gamma^\mu D_\mu - m) \psi - \frac{1}{4} F_{\mu\nu} F^{\mu\nu}, \quad D_\mu = \partial_\mu + ieQ A_\mu \quad (\text{A.40})$$

$$= \bar{\psi} (i\gamma^\mu \partial_\mu - m) \psi - eQ^{(\psi)} A_\mu \bar{\psi} \gamma^\mu \psi - \frac{1}{2} [(\partial_\mu A_\nu) \partial^\mu A^\nu - (\partial_\mu A_\nu) \partial^\nu A^\mu], \quad (\text{A.41})$$

where e is the electromagnetic coupling constant, $F_{\mu\nu} = \partial_\mu A_\nu - \partial_\nu A_\mu$ is the field strength tensor, A_μ is the photon field and ψ are fermion fields with electric charge $Q^{(\psi)}$.

Example: Quantum Chromodynamics is a gauge theory with respect to the non-Abelian $3^2 - 1 = 8$ dimensional Lie group $SU(3)_c$, generated by T_a^s , $a = 1, \dots, 8$,

$$\mathcal{L}_{\text{QCD}} = \bar{q} (i\gamma^\mu D_\mu - m) q - \frac{1}{4} \sum_{a=1}^8 G_{\mu\nu}^a G^{a\mu\nu}, \quad D_\mu = \partial_\mu + ig_s \sum_{a=1}^8 G_\mu^a T_a^s \quad (\text{A.42})$$

$$= \bar{q} (i\gamma^\mu \partial_\mu - m) q - g_s \sum_{a=1}^8 G_\mu^a \bar{q} \gamma^\mu \frac{\lambda_a}{2} q - \frac{1}{2} \sum_{a=1}^8 [(\partial_\mu G_\nu^a) \partial^\mu G^{a\nu} - (\partial_\mu G_\nu^a) \partial^\nu G^{a\mu}] \\ + g_s \sum_{a,b,c=1}^8 f_{bca} (\partial^\mu G^{a\nu}) G_\mu^b G_\nu^c - \frac{g_s^2}{4} \sum_{a,b,c,d,e=1}^8 f_{bca} f_{dea} G_\mu^b G_\nu^c G^{d\mu} G^{e\nu}, \quad (\text{A.43})$$

where g_s is the strong coupling constant, $G_{\mu\nu}^a = \partial_\mu G_\nu^a - \partial_\nu G_\mu^a - g_s \sum_{b,c=1}^8 f_{bca} G_\mu^b G_\nu^c$ are the field strength tensors, G_μ^a are the gluon fields, and $q \sim \mathbf{3}$ are the quark (triplet) fields, which transform under the fundamental $\mathbf{3}$ representation $T_a^s \mapsto \lambda_a/2$ of $SU(3)_c$.

Appendix B

Scale Invariance Breaking and the Trace Anomaly in QCD

This appendix provides a didactic theoretical background to many of the concepts and results that are used in effective field theory methods to compute WIMP-nucleon elastic scattering cross sections, which are relevant for direct detection. Hence, it constitutes a theoretical complement to Section 4.2.1.

B.1 A Generalization of Noether's Theorem

The variation of the Lagrangian density $\mathcal{L}(\varphi_r, \partial_\mu \varphi_r)$ of a general theory of fields $\varphi_r(x)$ is given by

$$\delta\mathcal{L}(\varphi_r, \partial_\mu \varphi_r) = \sum_{\varphi_r} \left[\frac{\partial\mathcal{L}}{\partial\varphi_r} \delta\varphi_r + \frac{\partial\mathcal{L}}{\partial(\partial_\mu \varphi_r)} \delta(\partial_\mu \varphi_r) \right] = \sum_{\varphi_r} \left[\frac{\partial\mathcal{L}}{\partial\varphi_r} \delta\varphi_r + \frac{\partial\mathcal{L}}{\partial(\partial_\mu \varphi_r)} \partial_\mu (\delta\varphi_r) \right] \quad (\text{B.1})$$

$$= \sum_{\varphi_r} \left[\frac{\partial\mathcal{L}}{\partial\varphi_r} \delta\varphi_r + \partial_\mu \left[\frac{\partial\mathcal{L}}{\partial(\partial_\mu \varphi_r)} \delta\varphi_r \right] - \left[\partial_\mu \frac{\partial\mathcal{L}}{\partial(\partial_\mu \varphi_r)} \right] \delta\varphi_r \right] \quad (\text{B.2})$$

$$= \sum_{\varphi_r} \left(\underbrace{\left[\frac{\partial\mathcal{L}}{\partial\varphi_r} - \partial_\mu \frac{\partial\mathcal{L}}{\partial(\partial_\mu \varphi_r)} \right]}_{=0} \delta\varphi_r + \partial_\mu \left[\frac{\partial\mathcal{L}}{\partial(\partial_\mu \varphi_r)} \delta\varphi_r \right] \right), \quad (\text{B.3})$$

where from the variational principle of least action (i.e., using the Euler-Lagrange equations of motion), the first term in Eq. (B.3) is null, thus giving

$$\Rightarrow \quad \delta\mathcal{L}(\varphi_r, \partial_\mu \varphi_r) = \sum_{\varphi_r} \partial_\mu \left[\frac{\partial\mathcal{L}}{\partial(\partial_\mu \varphi_r)} \delta\varphi_r \right]. \quad (\text{B.4})$$

A generalization of Noether's Theorem I [89] for (both symmetric and) non-symmetric theories under a given continuous transformation follows directly from this result (B.4).

Theorem 2 (Generalization of Noether's Theorem I) *Consider an arbitrary continuous transformation, under which the Lagrangian density $\mathcal{L}(\varphi_r, \partial_\mu \varphi_r)$ of a general field theory transforms (infinitesimally) as $\mathcal{L} \rightarrow \mathcal{L}' \approx \mathcal{L} + \delta\mathcal{L}$, with*

$$\delta\mathcal{L}(\varphi_r, \partial_\mu \varphi_r) = \partial_\mu F^\mu(\varphi_r, \partial_\mu \varphi_r) + \Delta(\varphi_r, \partial_\mu \varphi_r), \quad (\text{B.5})$$

where $\Delta(\varphi_r, \partial_\mu \varphi_r) \neq \partial_\mu G^\mu(\varphi_r, \partial_\mu \varphi_r)$ is not a total 4-divergence. Then, the Noether 4-current associ-

ated to this continuous transformation, defined by

$$j^\mu \equiv \sum_{\varphi_r} \frac{\partial \mathcal{L}}{\partial(\partial_\mu \varphi_r)} \delta \varphi_r - F^\mu, \quad (\text{B.6})$$

satisfies the following non-homogeneous continuity equation: $\partial_\mu j^\mu = \Delta$.

Proof. Using Eq. (B.4), one directly obtains

$$\sum_{\varphi_r} \partial_\mu \left[\frac{\partial \mathcal{L}}{\partial(\partial_\mu \varphi_r)} \delta \varphi_r \right] = \delta \mathcal{L}(\varphi_r, \partial_\mu \varphi_r) := \partial_\mu F^\mu + \Delta \Leftrightarrow \partial_\mu \left(\sum_{\varphi_r} \frac{\partial \mathcal{L}}{\partial(\partial_\mu \varphi_r)} \delta \varphi_r - F^\mu \right) := \Delta. \quad \square$$

Noether's Theorem I [89] is the particular case of Theorem 2 where the theory is invariant under this continuous transformation,¹ i.e. $\Delta = 0 \Leftrightarrow \delta \mathcal{L} = \partial_\mu F^\mu$ (*symmetry*), so that the corresponding Noether current (B.6) satisfies the homogeneous continuity equation $\partial_\mu j^\mu = 0$ (*conservation law*), and is said to be conserved. Furthermore, defining the corresponding Noether charge as $Q(t) \equiv \int d^3x j^0$, the homogeneous continuity equation directly implies that its time variation is given by

$$\frac{\partial Q}{\partial t} \equiv \int_{V_3} d^3x \frac{\partial j^0}{\partial t} = - \int_{V_3} d^3x \vec{\nabla} \cdot \vec{j} = - \oint_{\Sigma_2=\partial V_3} dS \vec{n} \cdot \vec{j}, \quad (\text{B.7})$$

i.e., by a (constant) boundary term representing a (constant) net flux, which – under the assumption of the field configurations going to zero sufficiently fast at infinity – vanishes for an infinite 3-dimensional space volume V_3 , so that $Q(t)$ is conserved in time [22].

Remark. If the continuous transformation is parametrized by d constant parameters α^a , $a = 1, \dots, d$ (e.g., a d -dimensional Lie group transformation), then the Noether 4-current (B.6) is actually given by a sum $j^\mu = \sum_{a=1}^d j^{a\mu} \delta \alpha^a$, where $\delta \alpha^a$ are the infinitesimal constant parameters and

$$j^{a\mu} = \frac{j^\mu}{\delta \alpha^a} \equiv \sum_{\varphi_r} \frac{\partial \mathcal{L}}{\partial(\partial_\mu \varphi_r)} \frac{\delta \varphi_r}{\delta \alpha^a} - \frac{F^\mu}{\delta \alpha^a}, \quad a = 1, \dots, d \quad (\text{B.8})$$

are the d independent Noether 4-currents associated to the transformation (one for each parameter, or direction), each satisfying the non-homogeneous continuity equation $\partial_\mu j^{a\mu} = \Delta / \delta \alpha^a$. Naturally, for a theory that is invariant under these transformations ($\Delta = 0 \Leftrightarrow \delta \mathcal{L} = \partial_\mu F^\mu$), each Noether 4-current satisfies the homogeneous continuity equation $\partial_\mu j^{a\mu} = 0$ and has a corresponding Noether charge $Q^a(t) = Q(t) / \delta \alpha^a \equiv \int d^3x j^0 / \delta \alpha^a = \int d^3x j^{a0}$ ($a = 1, \dots, d$) that is conserved in time ($\partial_t Q^a(t) = 0$).

¹If $\delta \mathcal{L} = \partial_\mu F^\mu$, the Lagrangian density itself is (in general, i.e. for $F^\mu \neq 0$) not invariant under the continuous transformation, but the action transforms as $S \rightarrow S' \approx S + \delta S$, where $\delta S = \int_{V_4} d^4x \partial_\mu F^\mu = \oint_{\Sigma_3=\partial V_4} dS n_\mu F^\mu$ is a (constant) boundary term that does not affect the Euler-Lagrange equations of motion (since its variation is null), and the theory is therefore said to be invariant (or symmetric) under this continuous transformation. Furthermore, for an infinite 4-dimensional space-time volume V_4 , the boundary term vanishes under the assumption of the field configurations going to zero sufficiently fast at infinity [22].

B.2 Canonical EMT and the Belinfante Symmetrization Procedure

Under an infinitesimal space-time translation $x^\mu \rightarrow x'^\mu = x^\mu + \epsilon^\mu$ ($|\epsilon| \ll 1$), a field (of any spin) $\varphi_r(x)$ (actively) transforms as²

$$\varphi'_r(x' = x + \epsilon) = \varphi_r(x) \quad \Leftrightarrow \quad \varphi_r(x) \rightarrow \varphi'_r(x) = \varphi_r(x - \epsilon) \approx \varphi_r(x) \underbrace{-\epsilon^\mu \partial_\mu \varphi_r(x)}_{=\delta\varphi_r(x)}. \quad (\text{B.9})$$

If a Lagrangian density $\mathcal{L}(\varphi_r, \partial_\mu \varphi_r)$ does not explicitly depend on the space-time coordinates (but only implicitly, through its dependence on the fields), then it transforms like a regular scalar field under space-time translations, i.e.

$$\mathcal{L}(x) \rightarrow \mathcal{L}'(x) = \mathcal{L}(x - \epsilon) \approx \mathcal{L}(x) \underbrace{-\epsilon^\mu \partial_\mu \mathcal{L}(x)}_{=\delta\mathcal{L}(x)}. \quad (\text{B.10})$$

Since $\delta\mathcal{L} = -\epsilon^\mu \partial_\mu \mathcal{L} := \partial_\mu F^\mu$, with $F^\mu := -\epsilon^\mu \mathcal{L}$, then Noether's Theorem ensures that the Noether current (B.6) associated to the invariance under space-time translations,

$$j_{\text{translation}}^\mu = \sum_{\varphi_r} \frac{\partial \mathcal{L}}{\partial(\partial_\mu \varphi_r)} \delta\varphi_r - F^\mu = \sum_{\varphi_r} \frac{\partial \mathcal{L}}{\partial(\partial_\mu \varphi_r)} (-\epsilon^\nu \partial_\nu \varphi_r) - (-\epsilon^\mu \mathcal{L}) \quad (\text{B.11})$$

$$= -\epsilon_\nu \left[\sum_{\varphi_r} \frac{\partial \mathcal{L}}{\partial(\partial_\mu \varphi_r)} \partial^\nu \varphi_r - g^{\mu\nu} \mathcal{L} \right], \quad (\text{B.12})$$

is a conserved current, i.e. $\partial_\mu j_{\text{translation}}^\mu = 0$. Since ϵ_ν ($\nu = 0, 1, 2, 3$) are four arbitrary constant parameters, this result implies four conserved currents

$$(j_{\text{translation}}^\nu)^\mu = \sum_{\varphi_r} \frac{\partial \mathcal{L}}{\partial(\partial_\mu \varphi_r)} \partial^\nu \varphi_r - g^{\mu\nu} \mathcal{L} \equiv T^{\mu\nu}, \quad \nu = 0, 1, 2, 3, \quad (\text{B.13})$$

so that $\partial_\mu (j_{\text{translation}}^\nu)^\mu = \partial_\mu T^{\mu\nu} = 0$, $\forall \nu = 0, 1, 2, 3$. The quantity $T^{\mu\nu}$ defined in Eq. (B.13) is the *canonical* energy-momentum tensor (EMT), and (by definition) is the component μ of the Noether current $\nu = 0, 1, 2, 3$ associated to the $x^\nu \rightarrow x^\nu + \epsilon^\nu$ space-time translational symmetry. Furthermore, the four corresponding Noether charges

$$Q_{\text{translation}}^\nu = \int d^3x T^{0\nu} \equiv P^\nu = (E, \vec{P})^\nu, \quad \nu = 0, 1, 2, 3 \quad (\text{B.14})$$

are conserved in time, and represent the total 4-momentum components of the field configuration.

However, the energy-momentum tensor is not uniquely defined. One can define alternative energy-momentum tensors – other than the canonical EMT of Eq. (B.13) – of the form

$$\Theta^{\mu\nu} = T^{\mu\nu} + \frac{1}{2} \partial_\lambda X^{\lambda\mu\nu}, \quad \text{where} \quad X^{\lambda\mu\nu} = -X^{\mu\lambda\nu} \quad (\text{B.15})$$

is anti-symmetric in $\lambda \leftrightarrow \mu$, so that $\partial_\mu \partial_\lambda X^{\lambda\mu\nu} = 0$, and hence $\partial_\mu T^{\mu\nu} = \partial_\mu \Theta^{\mu\nu}$. This way, $T^{\mu\nu}$ and $\Theta^{\mu\nu}$ satisfy the same balance equation, which for a theory that is invariant under space-time translations, is simply $\partial_\mu T^{\mu\nu} = \partial_\mu \Theta^{\mu\nu} = 0$. Choosing the new EMT to be symmetric in $\mu \leftrightarrow \nu$ (i.e., imposing

²One should recall that a finite transformation can be obtained by applying $N \rightarrow +\infty$ successive infinitesimal transformations. Under finite space-time translations, $\varphi_r(x) \rightarrow \varphi'_r(x) = \lim_{N \rightarrow +\infty} \left(1 - \frac{\epsilon^\mu}{N} \partial_\mu\right)^N \varphi_r(x) = e^{-\epsilon^\mu \partial_\mu} \varphi_r(x)$.

$\Theta^{\mu\nu} = \Theta^{\nu\mu}$) leads to the necessary condition [90, 91]

$$X^{\lambda\mu\nu} = \mathcal{S}^{\lambda\mu\nu} - \mathcal{S}^{\mu\lambda\nu} - \mathcal{S}^{\nu\lambda\mu}, \quad \text{with} \quad \mathcal{S}^{\lambda\mu\nu} \equiv -i \sum_{\varphi_r} \frac{\partial \mathcal{L}}{\partial(\partial_\lambda \varphi_r)} \mathcal{S}^{\mu\nu} \varphi_r = -\mathcal{S}^{\lambda\nu\mu}, \quad (\text{B.16})$$

where $\mathcal{S}^{\mu\nu} = -\mathcal{S}^{\nu\mu}$ are the internal $\text{SO}(3, 1)$ Lorentz group generators.³ This method is known as the Belinfante-Rosenfeld symmetrization procedure [92, 93]. Directly inserting Eq. (B.16) in Eq. (B.15), and then using $T^{\mu\nu} - T^{\nu\mu} = -\partial_\lambda \mathcal{S}^{\lambda\mu\nu}$, the Belinfante-Rosenfeld energy-momentum tensor can be written as

$$\Theta^{\mu\nu} = T^{\mu\nu} + \frac{1}{2} \partial_\lambda \underbrace{(\mathcal{S}^{\lambda\mu\nu} - \mathcal{S}^{\mu\lambda\nu} - \mathcal{S}^{\nu\lambda\mu})}_{= X^{\lambda\mu\nu}} = \frac{1}{2} (T^{\mu\nu} + T^{\nu\mu}) - \frac{1}{2} \partial_\lambda (\mathcal{S}^{\mu\lambda\nu} + \mathcal{S}^{\nu\lambda\mu}). \quad (\text{B.17})$$

For future applications, let us consider the theory of Quantum Chromodynamics (QCD), whose Lagrangian density is given by

$$\mathcal{L}_{\text{QCD}} = \sum_q \bar{q}(i\gamma^\mu D_\mu - m_q)q - \frac{1}{4} \sum_{a=1}^8 G_{\mu\nu}^a G^{a\mu\nu}, \quad (\text{B.18})$$

where $D_\mu \equiv \partial_\mu + ig_s \sum_{a=1}^8 \frac{\lambda_a}{2} G_\mu^a$ and $G_{\mu\nu}^a \equiv \partial_\mu G_\nu^a - \partial_\nu G_\mu^a - g_s \sum_{b,c=1}^8 f_{abc} G_\mu^b G_\nu^c$ are the $\text{SU}(3)_c$ covariant derivative (in its fundamental **3** representation) and strength tensor field of QCD, respectively. The canonical energy-momentum tensor (B.13) of QCD is then given by

$$T_{\text{QCD}}^{\mu\nu} \equiv \sum_q \left[\frac{\partial \mathcal{L}_{\text{QCD}}}{\partial(\partial_\mu q)} \partial^\nu q + (\partial^\nu \bar{q}) \frac{\partial \mathcal{L}_{\text{QCD}}}{\partial(\partial_\mu \bar{q})} \right] + \sum_{a=1}^8 \frac{\partial \mathcal{L}_{\text{QCD}}}{\partial(\partial_\mu G_\lambda^a)} \partial^\nu G_\lambda^a - g^{\mu\nu} \mathcal{L}_{\text{QCD}} \quad (\text{B.19})$$

$$= \sum_q \bar{q} i \gamma^\mu \partial^\nu q - \sum_{a=1}^8 G^{a\mu\lambda} \partial^\nu G_\lambda^a - g^{\mu\nu} \mathcal{L}_{\text{QCD}}, \quad (\text{B.20})$$

which is not symmetric in $\mu \leftrightarrow \nu$ (and also not $\text{SU}(3)_c$ gauge invariant). Since QCD is a space-time translational invariant theory, $\partial_\mu T_{\text{QCD}}^{\mu\nu} = 0$. Now computing

$$\mathcal{S}^{\lambda\mu\nu} \equiv -i \sum_q \left[\frac{\partial \mathcal{L}_{\text{QCD}}}{\partial(\partial_\lambda q)} \mathcal{S}_{(s=1/2)}^{\mu\nu} q + \bar{q} \mathcal{S}_{(s=1/2)}^{\mu\nu} \frac{\partial \mathcal{L}_{\text{QCD}}}{\partial(\partial_\lambda \bar{q})} \right] - i \sum_{a=1}^8 \frac{\partial \mathcal{L}_{\text{QCD}}}{\partial(\partial_\lambda G_\gamma^a)} (\mathcal{S}_{(s=1)}^{\mu\nu})_\gamma^\rho G_\rho^a \quad (\text{B.21})$$

$$= + \sum_q \bar{q} \gamma^\lambda \frac{i}{4} [\gamma^\mu, \gamma^\nu] q - \sum_{a=1}^8 (G^{a\lambda\mu} G^{a\nu} - G^{a\lambda\nu} G^{a\mu}), \quad (\text{B.22})$$

the Belinfante-Rosenfeld energy-momentum tensor of QCD (which satisfies the same balance equation, $\partial_\mu \Theta^{\mu\nu} = 0$) follows directly from Eq. (B.17),

$$\Theta^{\mu\nu} = T_{\text{QCD}}^{\mu\nu} + \partial_\lambda \left(+ \frac{1}{2} \sum_q \bar{q} \frac{i}{2} \underbrace{(\gamma^\lambda \gamma^\mu \gamma^\nu + g^{\mu\nu} \gamma^\lambda - g^{\lambda\nu} \gamma^\mu - g^{\lambda\mu} \gamma^\nu)}_{= \frac{1}{2} (\gamma^\lambda [\gamma^\mu, \gamma^\nu] - \gamma^\mu [\gamma^\lambda, \gamma^\nu] - \gamma^\nu [\gamma^\lambda, \gamma^\mu])} q - \sum_{a=1}^8 G^{a\lambda\mu} G^{a\nu} \right) \quad (\text{B.23})$$

³A field $\varphi_r(x)$ transforms as $\varphi'_r(x') = \Lambda x = S(\Lambda) \varphi_r(x) \Leftrightarrow \varphi_r(x) \rightarrow \varphi'_r(x) = S(\Lambda) \varphi_r(\Lambda^{-1} x)$ under $\text{SO}(3, 1)$ Lorentz transformations $x^\mu \rightarrow x'^\mu = \Lambda^\mu_\nu x^\nu$, where $\Lambda^\mu_\nu = e^{\omega^\mu_\nu}$ and $S(\Lambda) = e^{-\frac{i}{2} \omega^{\mu\nu} \mathcal{S}_{\mu\nu}}$. The spin $s = 0, 1/2, 1$ representations $\mathcal{S}_{\mu\nu} \mapsto \mathcal{S}_{\mu\nu}^{(s)}$ are $\mathcal{S}_{\mu\nu}^{(s=0)} = 0$, $\mathcal{S}_{\mu\nu}^{(s=1/2)} = \frac{i}{4} [\gamma_\mu, \gamma_\nu] \equiv \frac{\sigma_{\mu\nu}}{2}$ and $(\mathcal{S}_{\mu\nu}^{(s=1)})^\alpha_\beta = i(g^\alpha_\mu g_{\nu\beta} - g^\alpha_\nu g_{\mu\beta})$, respectively.

$$\begin{aligned}
 &= \frac{1}{2}(T_{\text{QCD}}^{\mu\nu} + T_{\text{QCD}}^{\nu\mu}) - \frac{1}{2}\partial_\lambda \left(+ \sum_q \bar{q} \frac{i}{2} \underbrace{(g^{\lambda\nu}\gamma^\mu + g^{\lambda\mu}\gamma^\nu - 2g^{\mu\nu}\gamma^\lambda)}_{=\frac{1}{2}(\gamma^\mu[\gamma^\lambda, \gamma^\nu] + \gamma^\nu[\gamma^\lambda, \gamma^\mu])} q - \sum_{a=1}^8 (G^{a\mu\lambda}G^{a\nu} + G^{a\nu\lambda}G^{a\mu}) \right) \\
 &= -g^{\mu\nu}\mathcal{L}_{\text{QCD}} + \frac{1}{2}\sum_q i\bar{q}(\gamma^\mu D^\nu + \gamma^\nu D^\mu)q - \sum_{a=1}^8 G^{a\lambda\mu}G^{a\lambda\nu} - \frac{i}{4}\sum_q [\partial^\nu(\bar{q}\gamma^\mu q) + \partial^\mu(\bar{q}\gamma^\nu q)] .
 \end{aligned}$$

The last (i.e., third) equality was obtained from the previous (i.e., second) one with the aid of the Euler-Lagrange equations of motion, and explicitly shows that the Belinfante-Rosenfeld EMT of QCD is symmetric in $\mu \leftrightarrow \nu$ (as expected). Additionally, it is also $\text{SU}(3)_c$ gauge invariant.

B.3 Dilatations and Scale Invariance in QCD

Under an infinitesimal scale transformation (or dilatation) $x^\mu \rightarrow x'^\mu = \lambda x^\mu \equiv e^\rho x^\mu \approx x^\mu + \rho x^\mu$ ($|\lambda - 1| \ll 1 \Leftrightarrow |\rho| \ll 1$),⁴ a field $\varphi_r(x)$ with D_φ mass dimensions (i.e., so that $[\varphi_r(x)] = [m]^{D_\varphi}$) (actively) transforms as⁵

$$\begin{aligned}
 \varphi'_r(x') &= e^\rho \varphi_r(x) = e^{-D_\varphi \rho} \varphi_r(x) \\
 \Leftrightarrow \varphi_r(x) &\rightarrow \varphi'_r(x) = e^{-D_\varphi \rho} \varphi_r(e^{-\rho} x) \approx \varphi_r(x) - \underbrace{\rho(D_\varphi + x^\mu \partial_\mu) \varphi_r(x)}_{=\delta\varphi_r(x)} .
 \end{aligned} \tag{B.24}$$

A field theory is scale invariant *if and only if* the Lagrangian density transforms like a regular field with $D_\varphi = 4$ mass dimensions (would) under scale transformations, i.e.

$$\mathcal{L}(x) \rightarrow \mathcal{L}'(x) = e^{-4\rho} \mathcal{L}(e^{-\rho} x) \approx \mathcal{L}(x) - \rho(4 + x^\mu \partial_\mu) \mathcal{L}(x) = \mathcal{L}(x) - \rho(g^\mu_\mu + x^\mu \partial_\mu) \mathcal{L}(x) \tag{B.25}$$

$$= \mathcal{L}(x) - \rho([\partial_\mu x^\mu] + x^\mu \partial_\mu) \mathcal{L}(x) = \mathcal{L}(x) - \underbrace{\rho \partial_\mu (x^\mu \mathcal{L}(x))}_{=\delta\mathcal{L}(x)} , \tag{B.26}$$

so that $\delta\mathcal{L} = \partial_\mu F^\mu$, with $F^\mu = -\rho x^\mu \mathcal{L}$. Let us now see if QCD is a scale invariant theory. Under scale transformations, the QCD Lagrangian density (B.18) transforms as

$$\begin{aligned}
 \mathcal{L}_{\text{QCD}}(x) \rightarrow \mathcal{L}'_{\text{QCD}}(x) &= e^{-4\rho} \left[\sum_q i\bar{q}(e^{-\rho} x) \gamma^\mu D_\mu q(e^{-\rho} x) - \frac{1}{4} \sum_{a=1}^8 G_{\mu\nu}^a(e^{-\rho} x) G^{a\mu\nu}(e^{-\rho} x) \right] \\
 &\quad - e^{-3\rho} \sum_q m_q \bar{q}(e^{-\rho} x) q(e^{-\rho} x)
 \end{aligned} \tag{B.27}$$

$$\begin{aligned}
 &\approx \mathcal{L}_{\text{QCD}}(x) - \rho(4 + x^\mu \partial_\mu) \left[\sum_q i\bar{q}(x) \gamma^\mu D_\mu q(x) - \frac{1}{4} \sum_{a=1}^8 G_{\mu\nu}^a(x) G^{a\mu\nu}(x) \right] \\
 &\quad + \rho(3 + x^\mu \partial_\mu) \sum_q m_q \bar{q}(x) q(x)
 \end{aligned} \tag{B.28}$$

$$\begin{aligned}
 &= \mathcal{L}_{\text{QCD}}(x) - \rho \partial_\mu (x^\mu \mathcal{L}_{\text{QCD}}(x)) - \rho \sum_q m_q \bar{q}(x) q(x) . \\
 &\quad \underbrace{\hspace{10em}}_{=\delta\mathcal{L}(x)}
 \end{aligned} \tag{B.29}$$

⁴The choice of (the single) parameter $\lambda \equiv e^\rho \approx 1 + \rho \Leftrightarrow \rho \equiv \ln \lambda \approx \lambda - 1$ to parametrize dilatations is arbitrary.

⁵We recall that the finite transformation is obtained by applying $N \rightarrow +\infty$ successive infinitesimal transformations. Under finite scale translations, $\varphi_r(x) \rightarrow \varphi'_r(x) = \lim_{N \rightarrow +\infty} [1 - \frac{\rho}{N}(D_\varphi + x^\mu \partial_\mu)]^N \varphi_r(x) = e^{-\rho(D_\varphi + x^\mu \partial_\mu)} \varphi_r(x)$.

Since $\delta\mathcal{L}_{\text{QCD}} = \partial_\mu F^\mu + \Delta$, with $F^\mu = -\rho x^\mu \mathcal{L}_{\text{QCD}}$ and $\Delta = -\rho \sum_q m_q \bar{q}q$, QCD is not scale invariant due to the quark mass terms, and (the generalization of Noether's) Theorem 2 states that the non-homogeneous continuity equation $\partial_\mu j^\mu = \Delta$ is satisfied by the non-conserved Noether current

$$j^\mu = \sum_q \left[\frac{\partial\mathcal{L}_{\text{QCD}}}{\partial(\partial_\mu q)} \delta q + \delta \bar{q} \frac{\partial\mathcal{L}_{\text{QCD}}}{\partial(\partial_\mu \bar{q})} \right] + \sum_{a=1}^8 \frac{\partial\mathcal{L}_{\text{QCD}}}{\partial(\partial_\mu G_\lambda^a)} \delta G_\lambda^a - F^\mu \quad (\text{B.30})$$

$$\begin{aligned} &= -\rho \sum_q \left[\frac{\partial\mathcal{L}_{\text{QCD}}}{\partial(\partial_\mu q)} \left(\frac{3}{2} + x^\nu \partial_\nu \right) q + \left(\frac{3}{2} + x^\nu \partial_\nu \right) \bar{q} \frac{\partial\mathcal{L}_{\text{QCD}}}{\partial(\partial_\mu \bar{q})} \right] - \rho \sum_{a=1}^8 \frac{\partial\mathcal{L}_{\text{QCD}}}{\partial(\partial_\mu G_\lambda^a)} (1 + x^\nu \partial_\nu) G_\lambda^a + \rho x^\mu \mathcal{L}_{\text{QCD}} \\ &= -\rho \left(x_\nu \left\{ \sum_q \left[\frac{\partial\mathcal{L}_{\text{QCD}}}{\partial(\partial_\mu q)} \partial^\nu q + (\partial^\nu \bar{q}) \frac{\partial\mathcal{L}_{\text{QCD}}}{\partial(\partial_\mu \bar{q})} \right] + \sum_{a=1}^8 \frac{\partial\mathcal{L}_{\text{QCD}}}{\partial(\partial_\mu G_\lambda^a)} \partial^\nu G_\lambda^a - g^{\mu\nu} \mathcal{L}_{\text{QCD}} \right\} \right. \\ &\quad \left. + \frac{3}{2} \sum_q \left[\frac{\partial\mathcal{L}_{\text{QCD}}}{\partial(\partial_\mu q)} q + \bar{q} \frac{\partial\mathcal{L}_{\text{QCD}}}{\partial(\partial_\mu \bar{q})} \right] + \sum_{a=1}^8 \frac{\partial\mathcal{L}_{\text{QCD}}}{\partial(\partial_\mu G_\lambda^a)} G_\lambda^a \right) \quad (\text{B.31}) \end{aligned}$$

$$= -\rho \left(x_\nu T_{\text{QCD}}^{\mu\nu} + \frac{3}{2} \sum_q i \bar{q} \gamma^\mu q - \sum_{a=1}^8 G^{a\mu\lambda} G_\lambda^a \right) \equiv -\rho j_{\text{scale}}^\mu, \quad (\text{B.32})$$

where $T_{\text{QCD}}^{\mu\nu}$ is the QCD canonical EMT (B.20). Since ρ is an arbitrary constant parameter, $j_{\text{scale}}^\mu \equiv j^\mu / (-\rho)$ is an equally valid (non-conserved) Noether current associated to scale transformations, satisfying an equivalent (non-homogeneous) continuity equation $\partial_\mu j_{\text{scale}}^\mu = \Delta / (-\rho)$. By direct computation (and using the balance equation, $\partial_\mu T_{\text{QCD}}^{\mu\nu} = 0$), one obtains $\partial_\mu j_{\text{scale}}^\mu = (T_{\text{QCD}})^\mu_\mu + \frac{3}{2} \partial_\mu \sum_q i \bar{q} \gamma^\mu q - \partial_\mu \sum_{a=1}^8 G^{a\mu\lambda} G_\lambda^a = \Theta^\mu_\mu$, where $\Theta^{\mu\nu}$ is the QCD Belinfante-Rosenfeld EMT (B.23). Hence, the non-homogeneous continuity equation can be simply written as

$$\partial_\mu j_{\text{scale}}^\mu = \Theta^\mu_\mu = \sum_q m_q \bar{q}q. \quad (\text{B.33})$$

If quarks were massless, QCD would be invariant under scale transformations and the corresponding Noether current (B.32) would be conserved, so that $\partial_\mu j_{\text{scale}}^\mu = \Theta^\mu_\mu \rightarrow 0$ ($m_q \rightarrow 0$). However, as we just saw, the quark mass terms explicitly break the scale invariance in QCD (at the classical level), and the corresponding Noether current is not conserved.

B.4 The Trace Anomaly of QCD

In perturbation theory, loop corrections can be incorporated into effective coupling constants – known as *running couplings* – which depend on the energy scale. The Renormalization Group Equation (RGE) of QCD, $\beta(\alpha_s) = \mu \frac{d\alpha_s}{d\mu} = \frac{d\alpha_s}{d(\ln \mu)}$, describes the running strong coupling $\alpha_s \equiv \frac{g_s^2}{4\pi}$ dependence on the energy scale μ . At the 1-loop order of approximation, the QCD beta function is $\beta(\alpha_s) \approx -\beta_0 \frac{\alpha_s^2}{2\pi}$, and the RGE yields the solution

$$\alpha_s(\mu) = \frac{1}{\frac{\beta_0}{2\pi} \ln\left(\frac{\mu}{\Lambda_{\text{QCD}}}\right)}, \quad \text{with} \quad \beta_0 = \frac{11}{3} N_c - \frac{2}{3} N_f^{(q)}, \quad (\text{B.34})$$

where $N_c = 3$ and $N_f^{(q)} = 6$ are the quark number of colours and flavours (respectively), and Λ_{QCD} is the QCD scale parameter (energy scale below which QCD becomes non-perturbative, so that $\alpha_s(\mu \leq \Lambda_{\text{QCD}}) \rightarrow +\infty$), also known as Landau pole [24].

Since the energy scale μ transforms as $\mu \rightarrow \mu' = e^{-\rho} \mu$ under scale transformations, when quantum loop corrections are taken into account, the (energy scale dependent) running strong coupling transforms (infinitesimally) as

$$\alpha_s \rightarrow \alpha'_s \approx \alpha_s + \delta\alpha_s, \quad \text{with} \quad \delta\alpha_s = \rho \left[\frac{\partial \alpha'_s}{\partial \rho} \right]_{\rho=0} = \rho \left[\frac{\partial \mu'}{\partial \rho} \frac{\partial \alpha'_s}{\partial \mu'} \right]_{\rho=0} = -\rho\beta(\alpha_s) \quad (\text{B.35})$$

to any order in perturbation theory, and hence, quantum loop corrections will affect scale transformations in QCD. The simplest way to see this [23, 31] (although not as rigorous as loop level perturbative computation or path integral treatments) is by rescaling the gluon (vector) field, i.e. $\underline{G}_\mu^a \equiv g_s G_\mu^a$ and $\underline{G}_{\mu\nu}^a \equiv g_s G_{\mu\nu}^a$, so that the QCD Lagrangian density (B.18) can be written as

$$\mathcal{L}_{\text{QCD}} = \sum_q \left(i\bar{q}\gamma^\mu \partial_\mu q - \sum_{a=1}^8 \underline{G}_\mu^a \bar{q}\gamma^\mu \frac{\lambda_a}{2} q \right) - \frac{1}{16\pi\alpha_s} \sum_{a=1}^8 \underline{G}_{\mu\nu}^a \underline{G}^{a\mu\nu}. \quad (\text{B.36})$$

It was shown in Eq. (B.29) that, at the classical level, $\delta\mathcal{L}_{\text{QCD}} = -\rho\partial_\mu(x^\mu \mathcal{L}_{\text{QCD}}) - \rho \sum_q m_q \bar{q}q$. Then, taking into account (loop corrections in perturbation theory, and consequentially) the scale dependence of the running strong coupling, the variation is quantum loop corrected to

$$\delta\mathcal{L}_{\text{QCD}} = -\rho\partial_\mu(x^\mu \mathcal{L}_{\text{QCD}}) - \rho \sum_q m_q \bar{q}q + \delta\alpha_s \frac{\partial \mathcal{L}_{\text{QCD}}}{\partial \alpha_s} \quad (\text{B.37})$$

$$= -\rho\partial_\mu(x^\mu \mathcal{L}_{\text{QCD}}) - \rho \sum_q m_q \bar{q}q - \rho\beta(\alpha_s) \frac{1}{16\pi\alpha_s^2} \sum_{a=1}^8 \underline{G}_{\mu\nu}^a \underline{G}^{a\mu\nu} \quad (\text{B.38})$$

$$= \underbrace{-\rho\partial_\mu(x^\mu \mathcal{L}_{\text{QCD}})}_{=\partial_\mu F^\mu} - \underbrace{\rho \sum_q m_q \bar{q}q - \rho \frac{\beta(\alpha_s)}{4\alpha_s} \sum_{a=1}^8 \underline{G}_{\mu\nu}^a \underline{G}^{a\mu\nu}}_{=\Delta}, \quad (\text{B.39})$$

and hence – performing the same derivation of the previous section – the (non-conserved) Noether current associated to scale transformations is still given by Eq. (B.32), and satisfies the same (non-homogeneous) continuity equation $\partial_\mu j_{\text{scale}}^\mu = \Delta/(-\rho)$, but with a quantum loop correction in the non-homogeneous term, i.e. $\Delta = \Delta_{\text{classical}} - \rho \frac{\beta(\alpha_s)}{4\alpha_s} \sum_{a=1}^8 \underline{G}_{\mu\nu}^a \underline{G}^{a\mu\nu}$. In summary, the non-homogeneous continuity equation (B.33) is quantum loop corrected to

$$\partial_\mu j_{\text{scale}}^\mu = \Theta^\mu_\mu = \sum_q m_q \bar{q}q + \frac{\beta(\alpha_s)}{4\alpha_s} \sum_{a=1}^8 \underline{G}_{\mu\nu}^a \underline{G}^{a\mu\nu} \quad (\text{B.40})$$

$$\approx \sum_q m_q \bar{q}q - \beta_0 \frac{\alpha_s}{8\pi} \sum_{a=1}^8 \underline{G}_{\mu\nu}^a \underline{G}^{a\mu\nu}, \quad (\text{B.41})$$

to any order in Eq.(B.40) and at 1-loop order $\beta(\alpha_s) \approx -\beta_0 \frac{\alpha_s^2}{2\pi}$ in Eq. (B.41). The first and second terms in the right-hand side (of both equations) exhibit the scale invariance breaking in QCD at the classical and quantum loop levels, respectively. If quarks were massless, this last term would break the classical scale invariance at the quantum level, thus being called the QCD *trace anomaly*.

B.5 Nucleon Mass and the Heavy Quark Contribution

The mass of a nucleon N is given by the matrix element of the trace of the QCD energy-momentum tensor⁶ between (appropriately normalized) nucleon states $|N\rangle$ with the same 4-momentum (i.e., in the limit of zero transferred momentum) [76, 73, 31], thus giving

$$m_N = \langle N(\vec{p}) | \Theta^\mu_\mu | N(\vec{p}) \rangle = \sum_q m_q \langle N(\vec{p}) | \bar{q}q | N(\vec{p}) \rangle + \frac{\beta(\alpha_s)}{4\alpha_s} \sum_{a=1}^8 \langle N(\vec{p}) | G^a_{\mu\nu} G^{a\mu\nu} | N(\vec{p}) \rangle \quad (\text{B.42})$$

$$\approx \sum_q m_q \langle N(\vec{p}) | \bar{q}q | N(\vec{p}) \rangle - \beta_0 \frac{\alpha_s}{8\pi} \sum_{a=1}^8 \langle N(\vec{p}) | G^a_{\mu\nu} G^{a\mu\nu} | N(\vec{p}) \rangle, \quad (\text{B.43})$$

to any order in Eq.(B.42) and at 1-loop order of approximation $\beta(\alpha_s) \approx -\beta_0 \frac{\alpha_s^2}{2\pi}$ in Eq. (B.43), with $\beta_0 = \frac{11}{3}N_c - \frac{2}{3}N_f^{(q)} = 7$.

As shown by M. A. Shifman, A. I. Vainshtein and V. I. Zakharov in Ref. [74], the heavy quark contribution to the nucleon mass – under the heavy quark expansion – is given by

$$m_Q \langle N(\vec{p}) | \bar{Q}Q | N(\vec{p}) \rangle = -\frac{2}{3} \frac{\alpha_s}{8\pi} \sum_{a=1}^8 \langle N(\vec{p}) | G^a_{\mu\nu} G^{a\mu\nu} | N(\vec{p}) \rangle + \mathcal{O}(1/(4m_Q^2)), \quad \forall Q = c, b, t \quad (\text{B.44})$$

and hence, the nucleon mass (B.43) can be further simplified to

$$m_N = \langle N(\vec{p}) | \Theta^\mu_\mu | N(\vec{p}) \rangle \approx \sum_{q'=u,d,s} m_{q'} \langle N(\vec{p}) | \bar{q}'q' | N(\vec{p}) \rangle - \frac{9\alpha_s}{8\pi} \sum_{a=1}^8 \langle N(\vec{p}) | G^a_{\mu\nu} G^{a\mu\nu} | N(\vec{p}) \rangle. \quad (\text{B.45})$$

Denoting $f_{T_{q'}}^{(N)} \equiv \frac{m_{q'} \langle N(\vec{p}) | \bar{q}'q' | N(\vec{p}) \rangle}{m_N}$ as the fraction of nucleon mass that is attributed to a light quark $q' = u, d, s$, the nucleon mass (B.45) can be written as

$$m_N = \sum_{q'=u,d,s} f_{T_{q'}}^{(N)} m_N - \frac{9\alpha_s}{8\pi} \sum_{a=1}^8 \langle N(\vec{p}) | G^a_{\mu\nu} G^{a\mu\nu} | N(\vec{p}) \rangle = \left[\sum_{q'=u,d,s} f_{T_{q'}}^{(N)} + f_{T_G}^{(N)} \right] m_N, \quad (\text{B.46})$$

where $f_{T_G}^{(N)} \equiv \frac{-\frac{9\alpha_s}{8\pi} \sum_{a=1}^8 \langle N(\vec{p}) | G^a_{\mu\nu} G^{a\mu\nu} | N(\vec{p}) \rangle}{m_N} = 1 - \sum_{q'=u,d,s} f_{T_{q'}}^{(N)}$ is the fraction of nucleon mass that is *not* attributed to light quarks (thus being attributed to the heavy quarks $Q = c, b, t$ and gluon).

⁶We choose to work with the $\mu \leftrightarrow \nu$ symmetric and $\text{SU}(3)_c$ gauge invariant Belinfante-Rosenfeld EMT (B.23) of QCD, but there are other valid choices (e.g., see Ref. [75]).

Appendix C

Explicit $\mathcal{Z}_2^{(1)} \times \mathcal{Z}_2^{(2)} \rightarrow \mathcal{Z}_2^{(1,2)}$ Symmetry Breaking in the Two-Real-Scalar-Singlet

Chapter 4 is devoted to the study of the two-real-scalar-singlet SM extension with an unbroken $\mathcal{Z}_2^{(1)} \times \mathcal{Z}_2^{(2)}$ discrete symmetry, which provides two stable DM particle candidates. However, besides considering another vacuum configuration (as explained in Section 4.1), one may also impose a different symmetry. In this appendix, we explicitly break the $\mathcal{Z}_2^{(1)} \times \mathcal{Z}_2^{(2)}$ symmetry down to $\mathcal{Z}_2^{(1,2)}$, which leads to a different phenomenology.

C.1 The SM+2RSS DM Model with an Unbroken $\mathcal{Z}_2^{(1,2)}$ Symmetry

We now discuss the two-real-scalar-singlet SM extension with a single $\mathcal{Z}_2^{(1,2)}$ symmetry, under which both singlet fields $S'_1, S'_2 \sim (\mathbf{1}, \mathbf{1}, 0)$ are odd: $S'_1 \rightarrow -S'_1, S'_2 \rightarrow -S'_2, \text{SM} \rightarrow +\text{SM}$. The most general renormalizable and $\text{SU}(3)_c \times \text{SU}(2)_L \times \text{U}(1)_Y \times \mathcal{Z}_2^{(1,2)}$ invariant Lagrangian density is given by

$$\begin{aligned} \mathcal{L}'_{\text{SM+2RSS}} = & \mathcal{L}_{\text{SM}} + \frac{1}{2}(\partial_\mu S'_1)\partial^\mu S'_1 - \frac{1}{2}\mu_1^2 S'^2_1 + \frac{1}{2}(\partial_\mu S'_2)\partial^\mu S'_2 - \frac{1}{2}\mu_2^2 S'^2_2 - \frac{\lambda_1}{4!}S'^4_1 - \frac{\lambda_2}{4!}S'^4_2 \\ & - \frac{\kappa_{H1}}{2}S'^2_1 \Phi^\dagger \Phi - \frac{\kappa_{H2}}{2}S'^2_2 \Phi^\dagger \Phi - \frac{\lambda_{12}}{4}S'^2_1 S'^2_2 \\ & - \mu_{12}^2 S'_1 S'_2 - \frac{\lambda_3}{3!}S'^3_1 S'_2 - \frac{\lambda_4}{3!}S'_1 S'^3_2 - \kappa_{H12} S'_1 S'_2 \Phi^\dagger \Phi, \end{aligned} \quad (\text{C.1})$$

i.e., the previous $\text{SU}(3)_c \times \text{SU}(2)_L \times \text{U}(1)_Y \times \mathcal{Z}_2^{(1)} \times \mathcal{Z}_2^{(2)}$ invariant SM+2RSS Lagrangian density (4.4) is extended by the last four $\mathcal{Z}_2^{(1)} \times \mathcal{Z}_2^{(2)}$ soft-breaking terms in (C.1). We consider the vacuum configuration

$$\langle \Phi \rangle_0^\dagger \langle \Phi \rangle_0 = -\frac{\mu_H^2}{2\lambda_H} \equiv \frac{v^2}{2} \quad \bigwedge_{r=1}^2 \quad \langle S_r \rangle_0 = 0, \quad (\text{C.2})$$

and take $\langle \Phi \rangle_0 = \begin{pmatrix} 0 & v/\sqrt{2} \end{pmatrix}^\top$ as the Higgs doublet VEV, so that $\Phi = \begin{pmatrix} G^+ & (v+h+iG^0)/\sqrt{2} \end{pmatrix}^\top$. Hence, the $\text{SU}(2)_L \times \text{U}(1)_Y$ gauge symmetry is spontaneously broken down to $\text{U}(1)_Q$, while the $\mathcal{Z}_2^{(1,2)}$ discrete symmetry remains unbroken (preventing $S'_i h$ flavour mixing). However, expanding the scalar mass terms reveals that the new $\mathcal{Z}_2^{(1)} \times \mathcal{Z}_2^{(2)}$ soft-breaking terms induce $S'_1 S'_2$ flavour mixing,

$$\mathcal{L}'_{\text{SM+2RSS}} \supset \mathcal{L}_{\text{mass}}^{(S'_r)} = -\frac{1}{2}\left(\mu_1^2 + \frac{\kappa_{H1}v^2}{2}\right)S'^2_1 - \left(\mu_{12}^2 + \frac{\kappa_{H12}v^2}{2}\right)S'_1 S'_2 - \frac{1}{2}\left(\mu_2^2 + \frac{\kappa_{H2}v^2}{2}\right)S'^2_2 \quad (\text{C.3})$$

$$= -\frac{1}{2} \begin{pmatrix} S'_1 & S'_2 \end{pmatrix} \underbrace{\begin{pmatrix} \mu_1^2 + \frac{\kappa_{H1}v^2}{2} & \mu_{12}^2 + \frac{\kappa_{H12}v^2}{2} \\ \mu_{12}^2 + \frac{\kappa_{H12}v^2}{2} & \mu_2^2 + \frac{\kappa_{H2}v^2}{2} \end{pmatrix}}_{=M^2} \begin{pmatrix} S'_1 \\ S'_2 \end{pmatrix}, \quad (\text{C.4})$$

implying that S'_1, S'_2 are interaction eigenstates (non-physical fields). The symmetric non-diagonal scalar squared-mass matrix $M^2 \in \mathbb{R}^{2 \times 2}$ can be diagonalized by a single matrix

$$U(\alpha) = \begin{pmatrix} \cos \alpha & \sin \alpha \\ -\sin \alpha & \cos \alpha \end{pmatrix} \in \text{SO}(2), \quad \text{with} \quad \tan(2\alpha) = \frac{2(\mu_{12}^2 + \frac{\kappa_{H12}v^2}{2})}{(\mu_2^2 - \mu_1^2) + \frac{(\kappa_{H2} - \kappa_{H1})v^2}{2}} \quad (\text{C.5})$$

through a change of basis (or rotation) in flavour space, from the interaction eigenstate basis to the mass eigenstate basis, so that $U^\top(\alpha)M^2U(\alpha) = \text{diag}(m_{\chi_1}^2, m_{\chi_2}^2) \equiv \mathcal{D}^2$ is diagonal with real positive elements. The scalar mass terms are diagonal (without flavour mixing) in the mass eigenstate basis,

$$\mathcal{L}_{\text{mass}}^{(S'_r)} = -\frac{1}{2} \begin{pmatrix} S'_1 & S'_2 \end{pmatrix} M^2 \begin{pmatrix} S'_1 \\ S'_2 \end{pmatrix} = -\frac{1}{2} \begin{pmatrix} S'_1 & S'_2 \end{pmatrix} U(\alpha)U^\top(\alpha)M^2U(\alpha)U^\top(\alpha) \begin{pmatrix} S'_1 \\ S'_2 \end{pmatrix} \quad (\text{C.6})$$

$$= -\frac{1}{2} \begin{pmatrix} \chi_1 & \chi_2 \end{pmatrix} \mathcal{D}^2 \begin{pmatrix} \chi_1 \\ \chi_2 \end{pmatrix} = -\frac{1}{2} m_{\chi_1}^2 \chi_1^2 - \frac{1}{2} m_{\chi_2}^2 \chi_2^2, \quad (\text{C.7})$$

where $\begin{pmatrix} \chi_1 & \chi_2 \end{pmatrix}^\top = U^\top(\alpha) \begin{pmatrix} S'_1 & S'_2 \end{pmatrix}^\top \Leftrightarrow \chi_r = \sum_{r'} U_{rr'}^\top(\alpha) S'_{r'}$ are the so-called mass eigenstates (physical fields), and the masses of the corresponding particles are given by

$$m_{\chi_{1,2}}^2 = \frac{\sum_{r=1}^2 (\mu_r^2 + \frac{\kappa_{Hr}v^2}{2}) \mp \sqrt{(\mu_2^2 - \mu_1^2 + \frac{(\kappa_{H2} - \kappa_{H1})v^2}{2})^2 + 4(\mu_{12}^2 + \frac{\kappa_{H12}v^2}{2})^2}}{2}. \quad (\text{C.8})$$

Finally, in the mass eigenstate basis, the (expanded) Lagrangian density in the unitary gauge reads

$$\begin{aligned} \mathcal{L}'_{\text{SM+2RSS}} = \mathcal{L}_{\text{SM}} &+ \sum_{r=1}^2 \left[\frac{1}{2} (\partial_\mu \chi_r) \partial^\mu \chi_r - \frac{1}{2} m_{\chi_r}^2 \chi_r^2 - \frac{\bar{\lambda}_r}{4!} \chi_r^4 \right] - \frac{\bar{\lambda}_{12}}{4} \chi_1^2 \chi_2^2 - \frac{\bar{\lambda}_3}{3!} \chi_1^3 \chi_2 - \frac{\bar{\lambda}_4}{3!} \chi_1 \chi_2^3 \\ &- \sum_{r=1}^2 \left[\frac{\bar{\kappa}_{Hr}v}{2} h \chi_r^2 + \frac{\bar{\kappa}_{Hr}}{4} h^2 \chi_r^2 \right] - \bar{\kappa}_{H12} v h \chi_1 \chi_2 - \frac{\bar{\kappa}_{H12}}{2} h^2 \chi_1 \chi_2, \end{aligned} \quad (\text{C.9})$$

where the redefined coupling constants for the physical fields are given by

$$\bar{\lambda}_1 = \lambda_1 c_\alpha^4 + \lambda_2 s_\alpha^4 + 6\lambda_{12} s_\alpha^2 c_\alpha^2 - 4(\lambda_3 c_\alpha^2 + \lambda_4 s_\alpha^2) s_\alpha c_\alpha \quad (\text{C.10})$$

$$\bar{\lambda}_2 = \lambda_1 s_\alpha^4 + \lambda_2 c_\alpha^4 + 6\lambda_{12} s_\alpha^2 c_\alpha^2 + 4(\lambda_3 s_\alpha^2 + \lambda_4 c_\alpha^2) s_\alpha c_\alpha \quad (\text{C.11})$$

$$\bar{\lambda}_{12} = (\lambda_1 + \lambda_2) s_\alpha^2 c_\alpha^2 + \lambda_{12} (1 - 6s_\alpha^2 c_\alpha^2) + 2(\lambda_3 - \lambda_4) s_\alpha c_\alpha (1 - 2s_\alpha^2) \quad (\text{C.12})$$

$$\bar{\lambda}_3 = (\lambda_1 c_\alpha^2 - \lambda_2 s_\alpha^2) s_\alpha c_\alpha + 3\lambda_{12} s_\alpha c_\alpha (1 - 2c_\alpha^2) + \lambda_3 c_\alpha^2 (1 - 4s_\alpha^2) + \lambda_4 s_\alpha^2 (4c_\alpha^2 - 1) \quad (\text{C.13})$$

$$\bar{\lambda}_4 = (\lambda_1 s_\alpha^2 - \lambda_2 c_\alpha^2) s_\alpha c_\alpha - 3\lambda_{12} s_\alpha c_\alpha (1 - 2c_\alpha^2) + \lambda_3 s_\alpha^2 (4c_\alpha^2 - 1) + \lambda_4 c_\alpha^2 (1 - 4s_\alpha^2) \quad (\text{C.14})$$

$$\bar{\kappa}_{H1} = \kappa_{H1} c_\alpha^2 + \kappa_{H2} s_\alpha^2 - 2\kappa_{H12} s_\alpha c_\alpha \quad (\text{C.15})$$

$$\bar{\kappa}_{H2} = \kappa_{H1} s_\alpha^2 + \kappa_{H2} c_\alpha^2 + 2\kappa_{H12} s_\alpha c_\alpha \quad (\text{C.16})$$

$$\bar{\kappa}_{H12} = (\kappa_{H1} - \kappa_{H2}) s_\alpha c_\alpha + \kappa_{H12} (1 - 2s_\alpha^2), \quad (\text{C.17})$$

with $s_\alpha \equiv \sin \alpha$, $c_\alpha \equiv \cos \alpha$. Figure C.1 presents the Feynman rules for the new interaction vertices of this SM extension, including the $h\chi_1\chi_2$ trilinear vertex that emerges upon $\mathcal{Z}_2^{(1)} \times \mathcal{Z}_2^{(2)} \rightarrow \mathcal{Z}_2^{(1,2)}$

explicit symmetry breaking. Taking χ_1 (χ_2) as the lighter (heavier) scalar particle – without loss of generality, due to the $\chi_1 \leftrightarrow \chi_2$ symmetry of the model – the heavier scalar χ_2 is unstable, as it decays via $\chi_2 \rightarrow \chi_1 h$ ($\rightarrow \chi_1 \text{ SM } \overline{\text{SM}}$). On the other hand, the decays $\chi_1 \rightarrow \chi_2 h$ ($\rightarrow \chi_2 \text{ SM } \overline{\text{SM}}$) are kinematically forbidden, since $m_{\chi_1} < m_{\chi_2}$. Therefore, only the lighter scalar χ_1 is stable, thus being the sole DM particle candidate of this model.

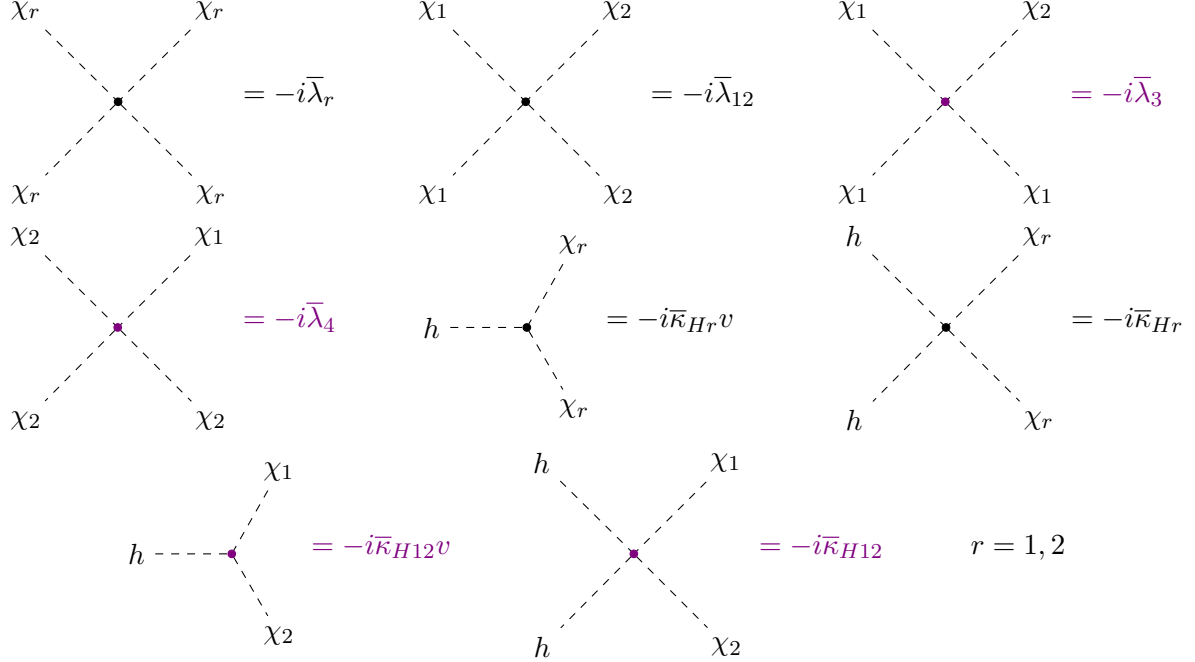


Figure C.1: Feynman rules of the SM+2RSS model for the interaction vertices involving the χ_1, χ_2 scalar particles. The **coloured** vertices emerge upon $\mathcal{Z}_2^{(1)} \times \mathcal{Z}_2^{(2)} \rightarrow \mathcal{Z}_2^{(1,2)}$ explicit symmetry breaking.

C.2 Parameter Space Scans and Numerical Analysis

The $\mathcal{Z}_2^{(1,2)}$ invariant two-real-scalar-singlet extension of the SM has now eleven (new) free parameters¹: the physical scalar masses m_{χ_1} and m_{χ_2} , the coupling constants $\lambda_1, \lambda_2, \lambda_{12}, \lambda_3, \lambda_4, \kappa_{H1}, \kappa_{H2}$ and κ_{H12} , and the scalar mixing angle α . The former (original) eight coupling constants can be replaced by the re-defined interaction coefficients of the physical fields (C.10)–(C.17). We scanned the 11-dimensional free parameter space of this model with `micrOMEGAs 6.1` [59], assuming both scalar particles were thermally produced according to the freeze-out mechanism. The scans were performed considering the DM relic density and direct detection exclusion. The (relic density and direct detection) experimental constraints on this model (C.1) are shown in Figure C.2, which only displays experimentally allowed free parameter space points, through several projections with m_{χ_1} on the x -axis and other free parameters (relevant at tree-level) on the y -axis and colour bars. This figure displays the scanned free parameter space points that correspond to the observed DM relic density $\Omega_{\text{DM}}^{\text{obs}} h^2 = 0.120 \pm 0.001$ from Planck [7] measurements and are also not excluded by the XENON1T [60], DarkSide-50 [61], PICO-60 [62], CRESST-III [63], PandaX-4T [64] and LUX-ZEPLIN (LZ) [2] direct detection experiments.²

What is new in this $\mathcal{Z}_2^{(1,2)}$ invariant model (compared to the $\mathcal{Z}_2^{(1)} \times \mathcal{Z}_2^{(2)}$ invariant model of Chapter 4)

¹Four of which emerge upon $\mathcal{Z}_2^{(1)} \times \mathcal{Z}_2^{(2)} \rightarrow \mathcal{Z}_2^{(1,2)}$ explicit symmetry breaking: $\kappa_{H12}, \lambda_3, \lambda_4$ and α .

²This LZ constraint refers to the former 2022 results [2]. The new LZ 2024 constraint [3] is not considered in Figure C.2 (it is not included in `micrOMEGAs 6.1`), and we will have to perform the corresponding DD exclusion separately (Figure C.3).

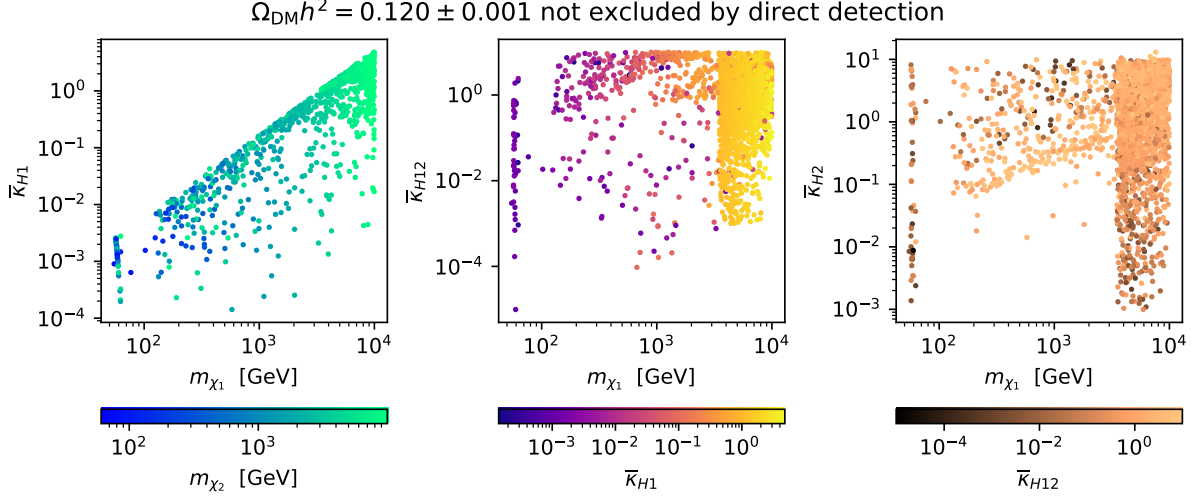


Figure C.2: Experimental constraints on the $\mathcal{Z}_2^{(1,2)}$ invariant SM+2RSS model (C.1), obtained by scanning the free parameter space with micrOMEGAS 6.1 for the freeze-out mechanism. All panels show the parameter space points that correspond to the observed DM relic density and are not excluded by direct detection.

is that (for a fixed DM mass m_{χ_1}), while $\bar{\kappa}_{H1}$ is the only coupling regulating the DD exclusion, the DM relic density is determined by nearly all couplings, namely $\bar{\kappa}_{H1}$, $\bar{\kappa}_{H2}$ and $\bar{\kappa}_{H12}$ (most relevant). Hence, $\bar{\kappa}_{H1}$ remains bounded from above due to DD exclusion (upper bound that increases with m_{χ_1}), but contrary to the $\mathcal{Z}_2^{(1)} \times \mathcal{Z}_2^{(2)}$ invariant scenario, $\bar{\kappa}_{H1}$ can now take low values (respecting the DD constraints) and avoid DM relic over-density through sufficiently high values of the other relevant couplings $\bar{\kappa}_{H2}$ and $\bar{\kappa}_{H12}$. This behaviour is shown in Figure C.2, where parameter space points with low values of $\bar{\kappa}_{H1}$, in order to reproduce the observed relic density, also feature high enough values of $\bar{\kappa}_{H2}$ or $\bar{\kappa}_{H12}$ (or both).

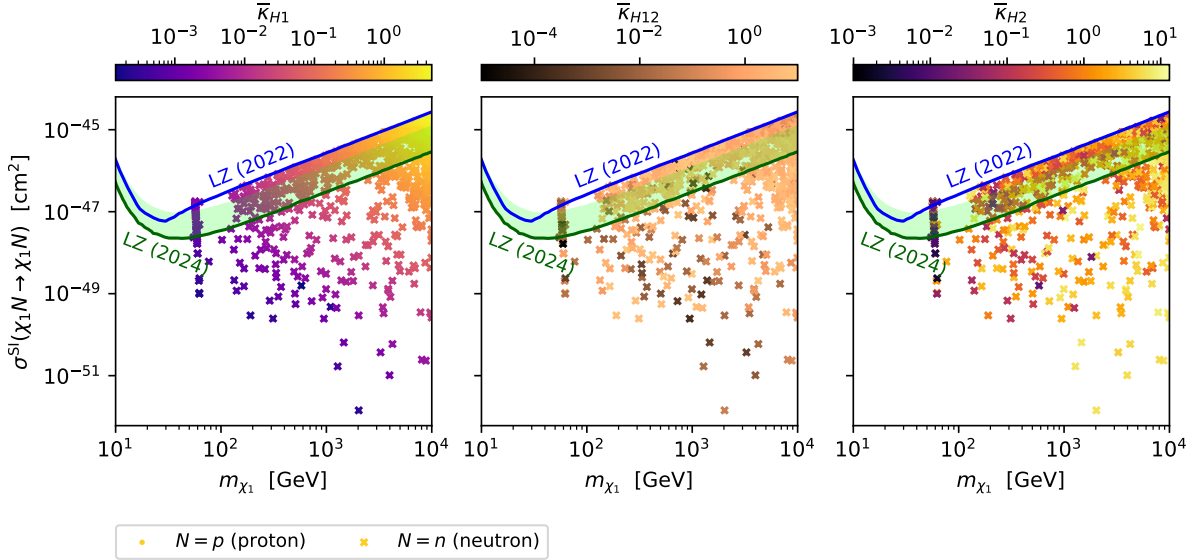


Figure C.3: Spin-independent cross section of DM-nucleon elastic scattering $\chi_1 N \rightarrow \chi_1 N$ ($N = p, n$). The presented points correspond to the model's theoretical predictions for the points of Figure C.2, for both proton (p) and neutron (n) elastic scattering. The blue and green (solid) lines correspond to the LUX-ZEPLIN (LZ) experimental upper limits on the WIMP-nucleon elastic scattering spin-independent cross section from 2022 [2] and 2024 [3] results, respectively. The (shaded green) experimental uncertainty band from the LZ 2024 results is displayed. The legend is shared by all panels, which differ only in the colour bar.

As already stated, the new LZ 2024 results [3] are not (yet) included in the `micrOMEGAs 6.1` code (not taken into account in Figure C.2), and we need to separately apply this DD constraint in our model. We computed the SI cross section of DM-nucleon elastic scattering $\sigma^{\text{SI}}(\chi_1 N \rightarrow \chi_1 N)$ for all parameter space points (of Figure C.2, i.e.) that were not excluded by the observed relic density and direct detection experiments (excluding the LZ 2024). The results are shown in Figure C.3, which also displays the former 2022 (blue solid line) and new 2024 (green solid line) LZ upper limits on the SI cross section. Each of the three panels shows the same plot with a different colour bar – between $\bar{\kappa}_{H1}$, $\bar{\kappa}_{H2}$ and $\bar{\kappa}_{H12}$ – thus confirming that $\bar{\kappa}_{H1}$ is the only coupling relevant for DD exclusion. Since $\bar{\kappa}_{H1}$ can take low values (still reproducing the observed relic density), which results in low SI cross sections, there are parameter space points that are not excluded by the LZ 2024 upper limit (or any other DD experimental result) for any DM mass $m_{\chi_1} (\gtrsim 100 \text{ GeV})$.